

Novel X-ray Diffraction and the Remote Analysis of Mars

Thesis submitted for the degree of
Doctor of Philosophy
at the University of Leicester

by

Stuart Matthew Robert Turner MPhys
Department of Physics & Astronomy
University of Leicester

February 2017

Novel X-ray Diffraction and the Remote Analysis of Mars

Stuart Matthew Robert Turner

Abstract

The scientific exploration of Mars is currently being undertaken with the goals: to determine if Mars ever supported life; to understand the past and present climate; and to understand the evolution of its surface and interior. To achieve these goals, orbital and in-situ exploration of Mars is required. Detailed orbital high-resolution hyperspectral, image and topographic datasets enable the identification of areas of scientific interest on the surface of Mars. In-situ measurements are then taken by planetary landers and rovers to characterise the environment in great detail.

This thesis has used orbital datasets to investigate impact craters on Mars, and has also focused on the development of a novel X-ray diffraction instrument technique that could be used to characterise the surface of Mars in-situ.

The study of post-Noachian impact craters with hyperspectral data returned by the Compact Reconnaissance Imaging Spectrometer for Mars (CRISM), highlighted two impact craters that may have hosted an impact-induced hydrothermal system. One of these impact craters shows spectral evidence for the presence of the mineral prehnite ($\text{Ca}_2\text{Al}_2\text{Si}_3\text{O}_{10}(\text{OH})_2$) that likely formed as a result of impact-induced hydrothermal activity, and might have provided a habitable environment for microbial life.

A novel back-reflection X-ray diffraction technique that is uniquely insensitive to sample morphology, facilitating the analysis of unprepared whole-rock samples, was successfully tested on a range of samples from rock-forming minerals to carbonates, sulphates and phyllosilicates. A range of experimental facilities were utilised in this work, including a beamline at the Diamond Light Source synchrotron facility where the technique was further validated in a high-resolution configuration.

The work presented in this thesis exemplifies the identification of an area of scientific interest on Mars, and the extensive testing and development of an instrument technique that could be used to geologically characterise such an identified area in-situ.

Declaration

I hereby declare that no part of this thesis has been previously submitted to this or any other university as part of the requirement for a higher degree. The work described herein was conducted solely by the undersigned except for those colleagues and other workers acknowledged in the text.

Stuart Matthew Robert Turner

28th February 2017

Acknowledgements

I would like to thank many people who have made this thesis possible. Firstly I'd like to thank my parents and for their support, and use of their washing machine and tumble dryer, along with my sister for the occasional phone conversation, and the slow cooker.

Special thanks to all those that have inspired me to pursue science as a career: from my mother, who took me to museums in London every school holiday, to my GCSE and A level Physics teachers (Mr Crumpton, Mrs Compton and Mr W.P.).

I'd like to thank my good friends Chris, Michael, Burt and the rest of the Essex crowd for their part in keeping me sane! From long phone conversations, parties and getaways; you've given me many amusing (and scarring) memories. Long may it continue!

Special thanks to Alex, Kat, Charlie, Ceri, Belinda, Mike, Peter, Matt and Hannah along with all my Leicester friends and various housemates over the years. From good conversations to meals, parties, FIFA tournaments; you've all helped write this thesis.

I would also like to thank my supervisors John, Graeme and Stephen for their help and guidance with this thesis. My studies have been supported by the Science and Technology Facilities Council and the British Geological Survey, for which I am very grateful. Special thanks go to Bethany Ehlmann for her help and guidance with CRISM analysis. Thank you David Vernon for showing me the way around the lab, and thank you John Holt and Tony Crawford for helping out when the equipment broke! To Cheryl and Nick, thank you for running samples and for showing a physicist how to process geological samples.

I would also like to acknowledge the inventors of coffee and oat-based biscuits.

Table of Contents

Abstract.....	1
Declaration.....	2
Acknowledgements.....	3
Table of Contents.....	4
List of Figures.....	9
List of Tables.....	13
List of Abbreviations.....	14
1. Introduction.....	15
1.1 Overview and Exploration of Mars.....	15
1.1.1 Mars from Orbit.....	16
1.1.2 Mars from the Surface.....	21
1.1.3 Martian Meteorites.....	21
1.2 Future Exploration of Mars.....	22
1.3 Thesis Focus and Outline.....	23
2. Reflectance Spectroscopy for Remote Mineral Identification.....	25
2.1 Reflectance Spectroscopy.....	25
2.1.1 Electronic Transitions: Crystal Field Transitions and Charge Transfers.....	27
2.1.2 Vibrational Processes.....	27
2.1.3 Atmospheric Effects.....	28
2.1.4 Grain Size.....	29
2.2 Spectral Absorptions in the 1.0 – 2.6 μm Region of Mineralogical Interest.....	29
2.2.1 Mafic Minerals.....	29
2.2.2 Phyllosilicate Minerals.....	30
2.2.3 Sulphate Minerals.....	32
2.2.4 Carbonate Minerals.....	34
2.3 Remote mineral identification using reflectance spectroscopy.....	34

Table of Contents

2.3.1 The CRISM Instrument	35
2.4 Ancillary Data	39
2.4.1 HiRISE and CTX.....	39
2.4.2 MOLA	40
3. Theory and Application of X-ray Diffraction.....	42
3.1 Derivation of Bragg’s Law and Summary of Crystal Structures	43
3.2 Angle-Dispersive X-ray Diffraction	47
3.3 Energy-Dispersive X-ray Diffraction.....	51
3.4 Detector Technology	52
3.5 Generation of X-rays and X-ray Fluorescence.....	54
3.6 Back-Reflection Energy-Dispersive X-ray Diffraction	56
3.6.1 Pre-existing CCD Facility	59
3.6.2 Bespoke SDD Facility	61
3.7 High-Resolution Back-Reflection XRD at the Diamond Light Source	62
3.8 X-ray Diffraction Instruments on Space Missions.....	65
4. Hydrothermal Activity Recorded in Post Noachian-aged Impact Craters on Mars 67	
4.1 Introduction	67
4.1.1 Remote Sensing of Mars with OMEGA and CRISM	68
4.1.2 Theory of Impact-Induced Hydrothermal Activity	70
4.1.3 Evidence for Impact-Induced Hydrothermal Activity on Mars	70
4.1.4 This Study.....	73
4.2 Methods.....	73
4.2.1 The CRISM, HiRISE, CTX and MOLA Instruments	73
4.2.2 Identification of Candidate Craters	74
4.2.3 CRISM Data Processing and Spectral Identification of Minerals.....	74
4.2.4 Definition of a “Null” Result.....	76
4.3 Results	76

Table of Contents

4.3.1 Unnamed Ismenius Lacus Impact Crater	77
4.3.2 Unnamed Elysium Impact Crater	81
4.3.3 Stokes Impact Crater	83
4.4 Discussion	86
4.4.1 Unnamed Ismenius Lacus Impact Crater	86
4.4.2 Unnamed Elysium Impact Crater	88
4.4.3 Stokes Impact Crater	88
4.4.4 Comparisons with previous studies	89
4.4.5 Low abundance of Impact-Induced Hydrothermal Systems	90
4.4.6 Technical limitations of this study	91
4.4.7 Relevance to the Nakhrites	91
4.5 Conclusions	92
5. Back-Reflection Energy-Dispersive X-ray Diffraction: Application and Analysis	93
5.1 Samples for Analysis.....	93
5.1.1 Oxide and Feldspar Minerals.....	93
5.1.2 Carbonate minerals.....	94
5.1.3 Sulphate Minerals.....	94
5.1.4 Phyllosilicate Minerals	95
5.2 Experimental Summary.....	95
5.3 Data Analysis Approach	96
5.4 Sample Results and Analysis	97
5.4.1 Group A: Oxide and feldspar Samples.....	101
5.4.2 Group B: Carbonate Samples	113
5.4.3 Group C: Sulphates.....	118
5.4.4 Group D: Phyllosilicates.....	129
5.5 Discussion	134
5.5.1 Oxides and Feldspars.....	134

Table of Contents

5.5.2 Carbonates	137
5.5.3 Sulphates.....	137
5.5.4 Phyllosilicates.....	138
5.5.5 Comparison of the two facilities.....	139
5.5.6 Avenues of future work and applications.....	140
5.6 Conclusions	141
6. High-Resolution Back-Reflection Energy-Dispersive X-ray Diffraction	143
6.1 Analytical Procedure	143
6.2 Results	147
6.2.1 Quartz	147
6.2.2 Dolomite	148
6.2.3 Siderite.....	150
6.2.4 Kaolinite	151
6.2.5 Mica.....	153
6.2.6 Talc	155
6.3 Discussion	157
6.3.1 Quartz, dolomite and siderite pellets	157
6.3.2 Clay pellets	159
6.3.3 Experimental Method and Data Processing	161
6.4 Conclusions	162
7. Synthesis and Conclusions	163
7.1 Remote Sensing of Young Impact Craters on Mars.....	164
7.1.1 Considerations for Future Orbital Instrumentation	166
7.2 Capability of Back-Reflection X-ray Diffraction	166
7.3 Final Comments	170
Appendix A: Hydrothermal Activity Recorded in Post Noachian-aged Impact Craters on Mars	171

Table of Contents

Appendix B: Back-Reflection Energy-Dispersive X-ray Diffraction.....	185
B.1 Quartz	185
B.2 Goethite	186
B.3 Hematite	186
B.4 Evje.....	187
B.5 Iveland.....	187
B.6 Brastad.....	188
B.7 Hope	188
B.8 BastilleA	190
B.9 MindelA.....	192
B.10 MindelB.....	194
B.11 JDo-1	196
B.12 WatchetB	198
B.13 WatchetC	204
B.14 Thackaringa	210
B.15 Wave Hill.....	210
B.16 Mica.....	211
Appendix C: High-Resolution Back-Reflection Energy-Dispersive X-ray Diffraction	212
C.1 Quartz	212
C.2 Dolomite	213
C.3 Siderite.....	214
C.4 Kaolinite	215
C.5 Mica.....	216
C.6 Talc	217
Appendix D: Publications List.....	219
References.....	222

List of Figures

Figure 1.1. Viking image mosaic of Mars	15
Figure 1.2. Global image map of Mars	17
Figure 1.3. MOLA map of Mars with locations landers and rovers marked	18
Figure 1.4. The Hartmann and Neukum Martian Chronology Model	19
Figure 1.5. Map of the Mars stratigraphic epochs superimposed on a MOLA map	20
Figure 1.6. Global distribution of aqueous minerals on Mars	21
Figure 2.1. Common mineral spectral absorptions and their wavelength positions	25
Figure 2.2. CRISM RELAB spectra of mafic minerals	30
Figure 2.3. Phyllosilicate mineral structures	32
Figure 2.4. CRISM RELAB spectra of phyllosilicate minerals	32
Figure 2.5. CRISM RELAB spectra of sulphate minerals	33
Figure 2.6. CRISM RELAB spectra of carbonate minerals.	34
Figure 2.7. Photographs and configuration of the CRISM instrument	35
Figure 2.8. Photographs of HiRISE and CTX instruments	39
Figure 2.9. HiRISE CCD layout on the focal plane array	39
Figure 2.10. Colourised and shaded MOLA map of Mars	41
Figure 3.1. Illustration of Bragg's Law	43
Figure 3.2. Geometric projections of the unit cells of the 14 possible Bravais lattices..	46
Figure 3.3. Angle-dispersive X-ray powder diffraction	48
Figure 3.4. Example powder diffraction plot	49
Figure 3.5. Cylindrical silicon drift detector cross section	53
Figure 3.6. X-ray spectra of molybdenum	54
Figure 3.7. X-ray fluorescence diagram of $K\alpha$ and $K\beta$ fluorescence	55
Figure 3.8. Resolution of the back-reflection method	58
Figure 3.9. Photographs of the pre-existing CCD back-reflection facility	59
Figure 3.10. Diagram of the pre-existing CCD back-reflection facility	60
Figure 3.11. Photograph of the bespoke SDD back-reflection facility	62
Figure 3.12. Back-reflection geometry in a high-resolution configuration at the Diamond Light Source	64
Figure 3.13. CheMin instrument geometry	66
Figure 4.1. Greyscale MOLA map showing the impact craters analysed in this study ..	77
Figure 4.2. 20 km complex impact crater located in the Ismenius Lacus quadrangle	78

Figure 4.3. CRISM spectra of the 20 km complex impact crater located in the Ismenius Lacus quadrangle	79
Figure 4.4. ~51 km diameter unnamed complex impact crater located in the Elysium quadrangle.....	81
Figure 4.5. CRISM spectra of eroded crater fill in Elysium impact crater.....	83
Figure 4.6. Complex impact crater Stokes.....	84
Figure 4.7. Comparisons of CRISM spectra covering Stokes impact crater	85
Figure 5.1. Feldspar solution series	94
Figure 5.2. Quartz pellet datasets obtained with the pre-existing CCD and bespoke SDD back-reflection facilities	102
Figure 5.3. The bespoke SDD quartz pellet dataset compared to quartz model.....	102
Figure 5.4. Photographs of goethite and hematite rock samples	103
Figure 5.5. Fe-suppression dataset for goethite pellet sample compared to goethite model	104
Figure 5.6. Fe-suppression dataset for goethite rock sample compared to goethite model	105
Figure 5.7. Fe-suppression dataset for hematite pellet sample compared to hematite model	106
Figure 5.8. Fe-suppression dataset for hematite rock sample compared to hematite model	107
Figure 5.9. Photograph of orthoclase feldspar rock sample	108
Figure 5.10. K-suppression dataset for orthoclase pellet sample compared to models	108
Figure 5.11. Photograph of plagioclase feldspar rock sample.....	109
Figure 5.12. Ca-suppression dataset for plagioclase feldspar pellet sample compared to models.....	109
Figure 5.13. Ca-suppression dataset for plagioclase feldspar pellet sample compared to models.....	110
Figure 5.14. Ca-suppression dataset for plagioclase feldspar pellet sample compared to refined model	111
Figure 5.15. Photograph of magnetite rock sample	112
Figure 5.16. Ca-suppression dataset for magnetite rock sample compared to magnetite model	112
Figure 5.17. Photograph of carbonate rock samples.....	113

Figure 5.18. Ca-suppression datasets acquired of limestone rock samples compared to calcite diffraction model	114
Figure 5.19. Ca-suppression datasets acquired of limestone rock samples compared to dolomite diffraction model	115
Figure 5.20. Ca-suppression dataset for the Japanese dolomite standard JDo-1 compared to 90% dolomite and 10% calcite diffraction and fluorescence models.....	116
Figure 5.21. JDo-1 Ca-suppression spectra acquired at various sample angles to show variation in the (104) diffraction peak, which experimentally illustrates a preferred orientation effect	117
Figure 5.22. Photographs of sulphate samples	118
Figure 5.23. S-suppression dataset acquired of WatchetB compared to PoDFluX models for gypsum.....	119
Figure 5.24. S-suppression dataset acquired of the second WatchetB pellet compared to diffraction model for gypsum	120
Figure 5.25. S-suppression dataset acquired of the second WatchetB pellet compared to PoDFluX model for Anhydrite-III.....	121
Figure 5.26. S-suppression dataset acquired of WatchetB compared to models for gypsum.....	122
Figure 5.27. WatchetC pellet S-suppression dataset compared to bassanite diffraction model	123
Figure 5.28. Second WatchetC pellet S-suppression dataset compared to gypsum model	124
Figure 5.29. S-suppression dataset acquired of WatchetC compared to models for gypsum.....	125
Figure 5.30. S-suppression dataset of WatchetB whole rock sample obtained using the bespoke SDD back-reflection laboratory facility compared to gypsum model.....	126
Figure 5.31. S-suppression dataset of WatchetC whole rock sample obtained using the bespoke SDD back-reflection laboratory facility compared to gypsum model.....	127
Figure 5.32. Photograph of jarosite rock sample	128
Figure 5.33. K-suppression dataset acquired of jarosite whole rock sample compared to jarosite model.....	129
Figure 5.34. Photograph of prehnite rock sample.....	130
Figure 5.35. Ca-suppression dataset of prehnite whole rock sample obtained using the bespoke SDD back-reflection laboratory facility compared to prehnite model	131

Figure 5.36. K-suppression dataset of mica pellet obtained using the bespoke SDD laboratory facility compared to muscovite (mica) model. 132

Figure 5.37. X-ray diffraction and X-ray fluorescence spectra of pressed powder pellet of M26 Norwegian Talc with Fe-suppression fluorescence and diffraction talc model included for comparison. 133

Figure 5.38. X-ray diffraction and X-ray fluorescence spectra of pressed powder pellet of Kaolin compared to 8 kV kaolinite model 133

Figure 5.39. X-ray diffraction and X-ray fluorescence spectra of pressed powder pellet of China Clay (kaolin) compared to Fe-suppression kaolinite model..... 134

Figure 5.40. Goethite Fe suppression datasets for whole rock and pellet samples..... 135

Figure 5.41. Hematite Fe suppression datasets for whole rock and pellet samples..... 135

Figure 6.1. Plot of monochromator step size against monochromator energy 144

Figure 6.2. Plot of Kaolin PP dataset at various stages of IDL processing 145

Figure 6.3. Quartz PP processed dataset compared to peak positions calculated using the fitted unit cell for quartz in table 6.1 148

Figure 6.4. Dolomite (JDo-1) processed dataset compared to peak positions calculated using the fitted unit cells for dolomite and calcite in tables 6.2 and 6.3, respectively . 149

Figure 6.5. Siderite PP dataset compared to peak positions calculated using the fitted unit cells for siderite and hematite in table 6.4 and 6.5, respectively 151

Figure 6.6. Kaolin PP and China Clay PP datasets compared to calculated peak positions using the fitted unit cell for kaolinite in table 6.7 152

Figure 6.7. Mica PP dataset compared to peak positions calculated using the fitted unit cells for mica and quartz detailed in tables 6.9 and 6.10, respectively..... 154

Figure 6.8. Talc PP dataset compared to calculated peak positions using the fitted unit peaks for talc and magnesite details in tables 6.12 and 6.13, respectively 156

Figure 6.9. Unit-cell dimension distribution plot for carbonate minerals from the 2015 release of the ICDD powder diffraction database. The unit cells for carbonate minerals identified in JDo-1, Siderite PP and Talc PP are shown for comparison 158

List of Tables

Table 1.1. General characteristics of Mars	16
Table 2.1. CRISM targeted imaging modes.	36
Table 2.2. Key CRISM summary parameters and their formulae.	38
Table 3.1. The 14 possible Bravais lattices and their geometric properties.	47
Table 4.1. Amazonian impact craters with phyllosilicates found in this study	76
Table 5.1. Table of samples analysed using the back-reflection technique.....	98
Table 5.2. Table comparing full width at half maximum values for specific XRF peaks for both the pre-existing CCD and bespoke SDD laboratory facilities.	140
Table 6.1. Calculated unit cell for quartz.....	147
Table 6.2. Calculated unit cell for dolomite.	149
Table 6.3. Calculated unit cell for calcite.	149
Table 6.4. Calculated unit cell for siderite.....	150
Table 6.5. Calculated unit cell for hematite.....	150
Table 6.6. Extracted basal peak positions for the Kaolin PP dataset.....	152
Table 6.7. Calculated unit cell for kaolinite.....	153
Table 6.8. Extracted basal peak positions for the Mica PP dataset	154
Table 6.9. Calculated unit cell for muscovite.	154
Table 6.10. Calculated unit cell for quartz.....	155
Table 6.11. Extracted basal and (060) peak positions for the Talc PP dataset	156
Table 6.12. Calculated unit cell for talc.....	157
Table 6.13. Calculated unit cell for magnesite.	157
Table 6.14. Calculated unit cell for dolomite.	157

List of Abbreviations

ADXRD	Angle-Dispersive X-ray Diffraction
AMCSD	American Mineralogist Crystal Structure Database
CRISM	Compact Reconnaissance Imaging Spectrometer for Mars
CTX	Context Camera
EDXRD	Energy-Dispersive X-ray Diffraction
ESA	European Space Agency
ExoMars	Exobiology on Mars
HiRISE	High Resolution Imaging Science Experiment
ICDD	International Center for Diffraction Data
IR	Infrared
ISRO	Indian Space Research Organization
MAVEN	Mars Atmosphere and Volatile Evolution mission
MER	Mars Exploration Rover
MOLA	Mars Orbiter Laser Altimeter
MRO	Mars Reconnaissance Orbiter
MSL	Mars Science Laboratory
NASA	National Aeronautics and Space Administration
NIR	Near-Infrared
VNIR	Visible and Near-Infrared
XRD	X-ray Diffraction
XRF	X-ray Fluorescence

1. Introduction

1.1 Overview and Exploration of Mars

The fourth planet from the Sun, Mars (figure 1.1), has been the focus of increasing interest in the past 50 years, as an enhanced understanding of astronomy, physics, geology and engineering has enabled detailed orbital and in-situ study of the planet. At the time of writing this thesis, there are two working scientific rovers on the surface of Mars (NASA Curiosity and NASA Opportunity) and six orbiters in operation about Mars (ESA Mars Express, NASA Mars Reconnaissance Orbiter, NASA 2001 Mars Odyssey, NASA MAVEN, ISRO Mars Orbiter Mission and ESA ExoMars Trace Gas Orbiter). A current goal of Mars research is the identification of past habitable environments, which is enabled with remote sensing and in-situ technologies to characterise the surface mineralogy of Mars. The general characteristics of Mars are given in table 1.1.

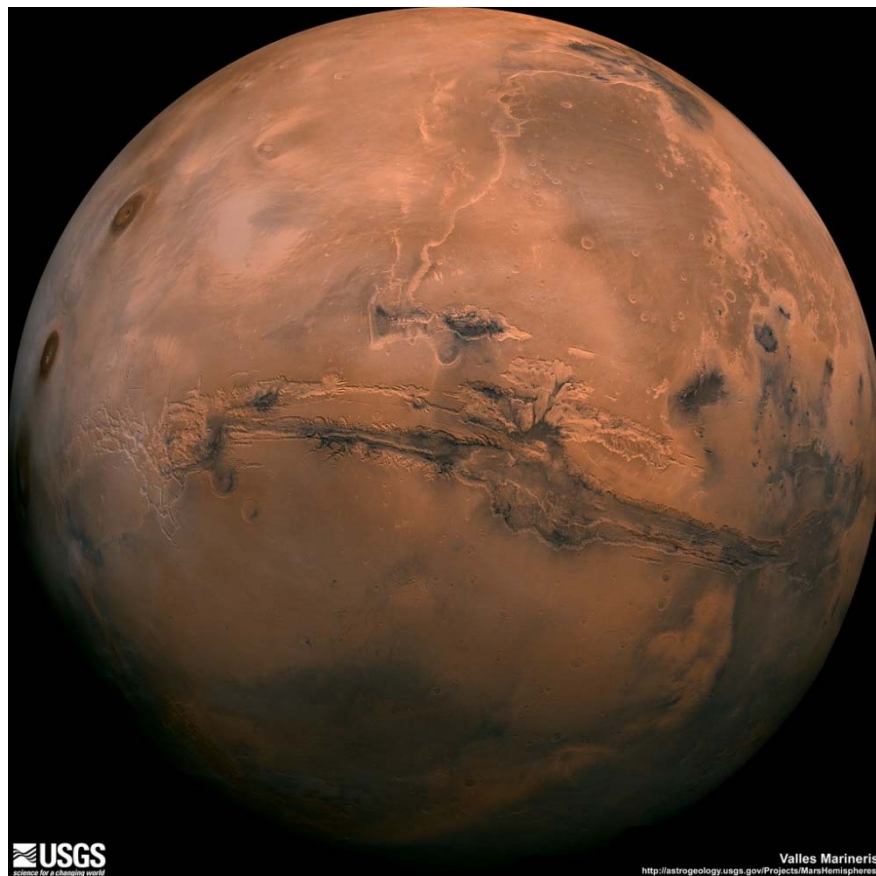


Figure 1.1. Viking image mosaic of Mars showing the Valles Marineris hemisphere, with a scale of 0.6 km/pixel (USGS, 2011).

Table 1.1. General characteristics of Mars (Carr, 2006; NASA, 2016).

Mass	6.42×10^{23} kg
Mean radius	3389.5 km
Gravity	3.71 ms^{-2}
Semi-major axis	227.92×10^6 km (1.52 A.U.)
Orbital period	669.6 sols
Sidereal rotation period (sol)	24 hours 39 minutes 35.2 seconds
Average surface pressure	0.636 kPa
Average surface temperature	~210 K
Major atmospheric constituents	95.32% CO ₂
	2.7% N ₂
	1.6% Ar
	0.13% O ₂
	0.08% CO

1.1.1 Mars from Orbit

Although astronomers had previously been able to discern some detail of the surface of Mars, it wasn't until the arrival of the NASA Mariner spacecraft that the first high-resolution observations were made. In the 1960s, the initial Mariner missions (4, 6 & 7) performed flybys of Mars and confirmed the presence of a CO₂ rich atmosphere, a small intrinsic magnetic field and a heavily cratered surface. Mariner 9 was the first spacecraft to orbit Mars, arriving at Mars in November 1971; however Mars was engulfed in a global dust storm at the time of arrival. After this had cleared, Mariner 9 was able to image the surface to reveal the largest volcanoes, canyons and channels in the solar system, in addition to the previously seen heavily cratered ancient terrain. This suggested Mars had a “warm and wet” history as opposed to its current “cold and dry” state (Hartmann and Raper, 1974; Carr, 1996). Viking 1 & 2 were the next spacecraft to arrive at Mars in 1976; the identical spacecraft both consisted of a lander and orbiter. As shown in figure 1.2, the Viking orbiters mapped the entire surface of Mars at 200 m/pixel with some areas as high as 9 m/pixel (Carr, 1996), and the Infrared Thermal Mapper (IRTM) instrument returned thermal inertia data providing information on surface particle sizes at up to 30 km/pixel resolution (Christensen and Moore, 1992). The Viking landers set down in Chryse Planitia (Viking 1) and Utopia Planitia (Viking 2), returning the first colour views of Mars that revealed a rocky and dusty surface. Soil analysis at both landing sites revealed Si and Fe abundance in the upper regolith, with weathered basalts at the

Viking 1 Lander site (Binder et al., 1977) and sulphates at the Viking 2 Lander site (Mutch et al., 1977; Carr, 2006).

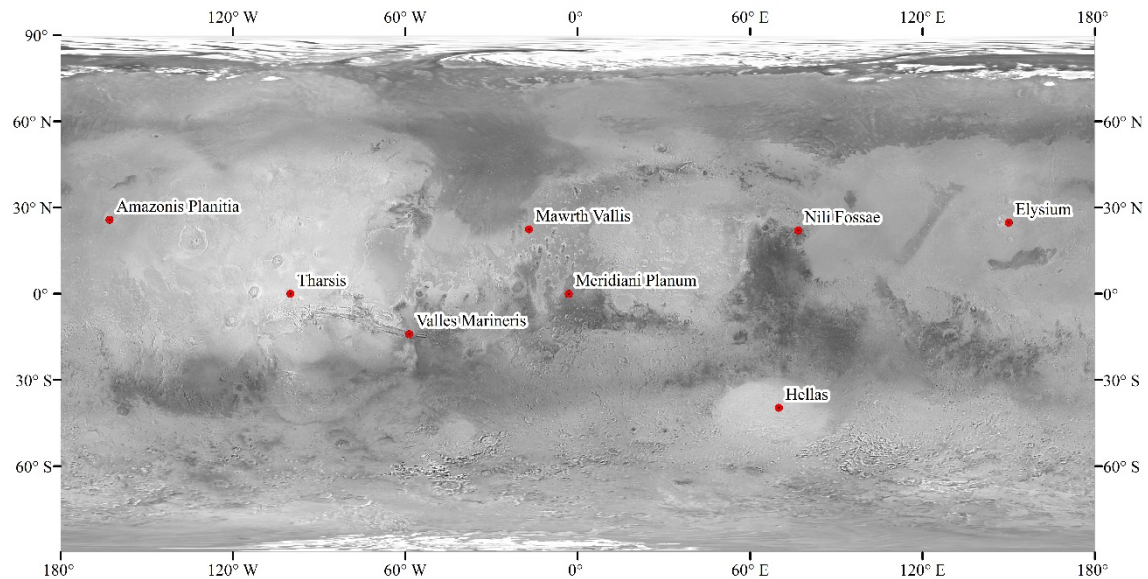


Figure 1.2. Global image map of Mars compiled from ~4600 Viking Orbiter images, with a resolution of 231 m/pixel (USGS, 1991).

The next advances in Mars science from orbital remote sensing and surface exploration came in the 1990s, when Mars Global Surveyor (MGS) entered orbit about Mars in September 1997. MGS carried three instruments to study the surface of Mars: the high-resolution Mars Orbiter Camera (MOC), the Thermal Emission Spectrometer (TES) and the Mars Orbiter Laser Altimeter (MOLA) (Albee et al., 1998). These instruments enabled the global characterisation of the Martian surface, where MOC showed gully-forming fluid action (Malin and Edgett, 2001) and MOLA provided elevation data of the surface, enabling accurate topographical models of the surface to be produced, as shown in figure 1.3 (Smith et al., 2001).

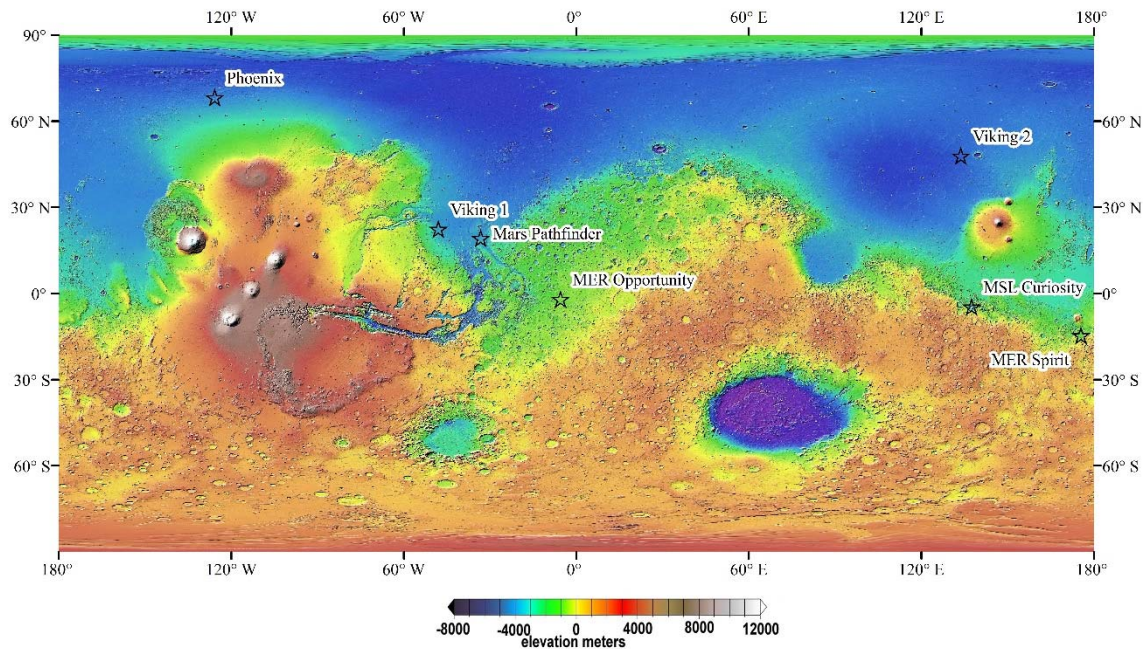


Figure 1.3. Colourised and shaded MOLA map of Mars (USGS, 2003), with locations of successful landers and rovers marked (USGS, 2012).

Mars Odyssey (MO), inserted into Mars orbit in October 2001, carries two instruments for the study of the Martian surface: the Thermal Emission Imaging System (THEMIS) and the Gamma Ray Spectrometer (GRS). THEMIS furthered the mineralogical view of the Martian surface provided by TES, with a spatial resolution of 100 m (Christensen et al., 2003; Carr, 2006), but it wasn't until the arrival of the European Space Agency's Mars Express (MEX) in 2004 that mineralogical evidence for the surface interaction of water was identified. Two of the instruments on board Mars Express, which is still in operation at the time of writing this thesis, furthered the understanding of the surface of Mars: the High Resolution Stereo Camera (HRSC) and the Observatoire pour la Minéralogie, l'Eau les Glaces et l'Activité (OMEGA). The OMEGA visible-shortwave infrared imaging spectrometer mapped hydrated mineral exposures at a spatial resolution of 1.8 km, resulting in the identification of three types of hydrated minerals (Fe/Mg phyllosilicates, Al phyllosilicates and hydrated sulphates) at five locations on Mars: Terra Meridiani, Mawrth Vallis, Nili Fossae, Aram Chaos and Valles Marineris along with scattered other highland locations (Bibring et al., 2006; Poulet et al., 2007). Poulet et al. (2005) suggested that the formation of phyllosilicates occurred predominantly during the early Noachian, followed by a more acidic environment in which sulphate formation was prevalent, with a subsequent study (Bibring et al., 2006) proposing three distinct eras of

alteration based on OMEGA observations — “Phyllosian”, “Theiikian” and “Siderikian” — characterised by phyllosilicates, sulphates and ferric oxides, respectively. These three eras can be loosely linked to the Noachian, Hesperian and Amazonian epochs (Bibring et al., 2006), which are defined by impact-cratering rates as illustrated in figure 1.4, with localities illustrated in figure 1.5. The lack of strong mafic and hydrated minerals in OMEGA data of the northern plains of Mars could be the result of surface coatings masking spectral signatures (Mustard et al., 2005).

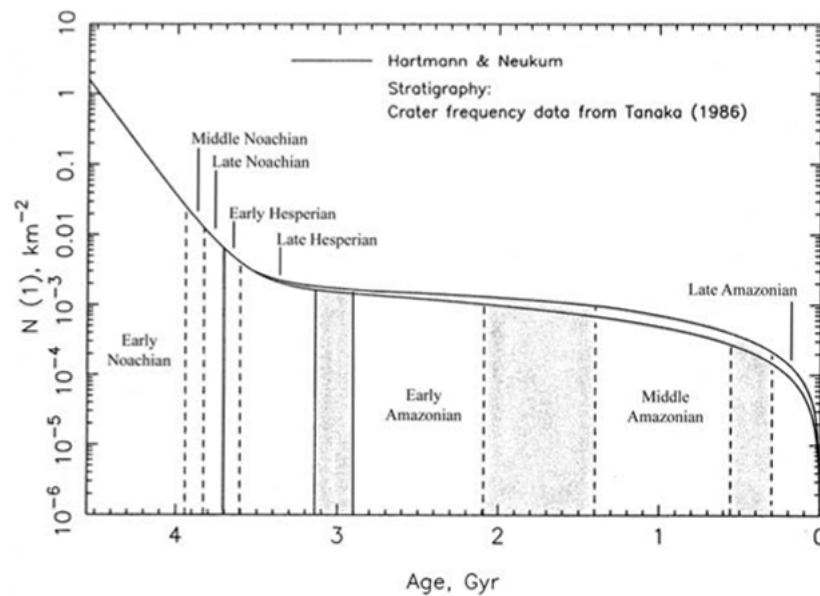


Figure 1.4. The Hartmann and Neukum Martian Chronology Model (Hartman and Neukum, 2001). Defined by cratering statistics, the localities of these three epochs (Noachian, Hesperian and Amazonian) are spatially mapped in figure 1.5.

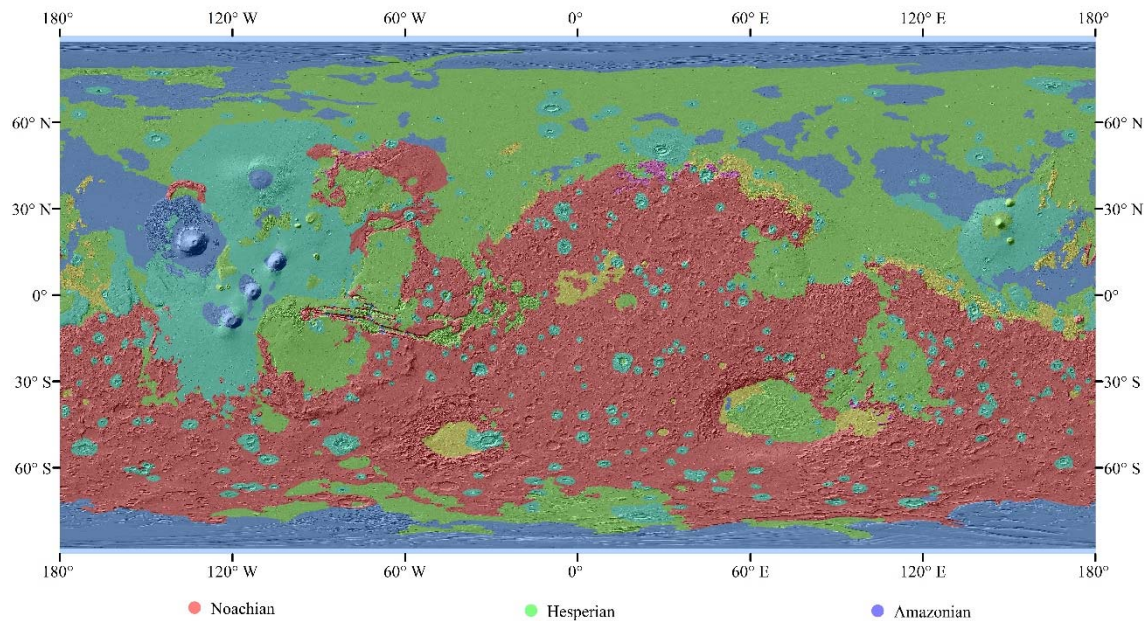


Figure 1.5. Map of the Mars stratigraphic epochs (figure 1.4), where RGB colours are merged for transitional units. Data is taken from Tanaka et al. (2014) and superimposed on a greyscale MOLA elevation map (USGS, 2003).

The most detailed view of the surface of Mars has and is currently being provided by NASA's Mars Reconnaissance Orbiter (MRO), which provides high-resolution imagery acquired with the Context Camera (CTX) and the High Resolution Imaging Science Experiment (HiRISE). MRO also carries the Compact Reconnaissance Imaging Spectrometer for Mars (CRISM) instrument, which provides higher-resolution hyperspectral imagery at a spatial resolution 18-40 m/pixel (Murchie et al., 2007, 2009a, 2009b). Providing the greatest spatial resolution spectral data of the surface of Mars to date, CRISM has enabled the identification of numerous hydrated mineral exposures coupled with deposit morphology, thus enabling a more detailed understanding of Mars' surface mineralogy and providing insights about past environmental conditions. Phyllosilicates have been identified in numerous environments such as layered sediments and within impact craters, which have indicated hydrothermal formation as well as excavation of older surfaces (Mustard et al., 2008; Murchie et al., 2009a; Ehlmann et al., 2009, 2011b; Carter et al., 2010, 2013). Hydrated sulphate mineral and carbonate deposits have also been detected (Ehlmann et al., 2008, 2009; Murchie et al., 2009a; Carter and Poulet, 2012). Figure 1.6 shows the global distribution of aqueous mineral detections on Mars compiled using OMEGA and CRISM data (Ehlmann and Edwards, 2014).

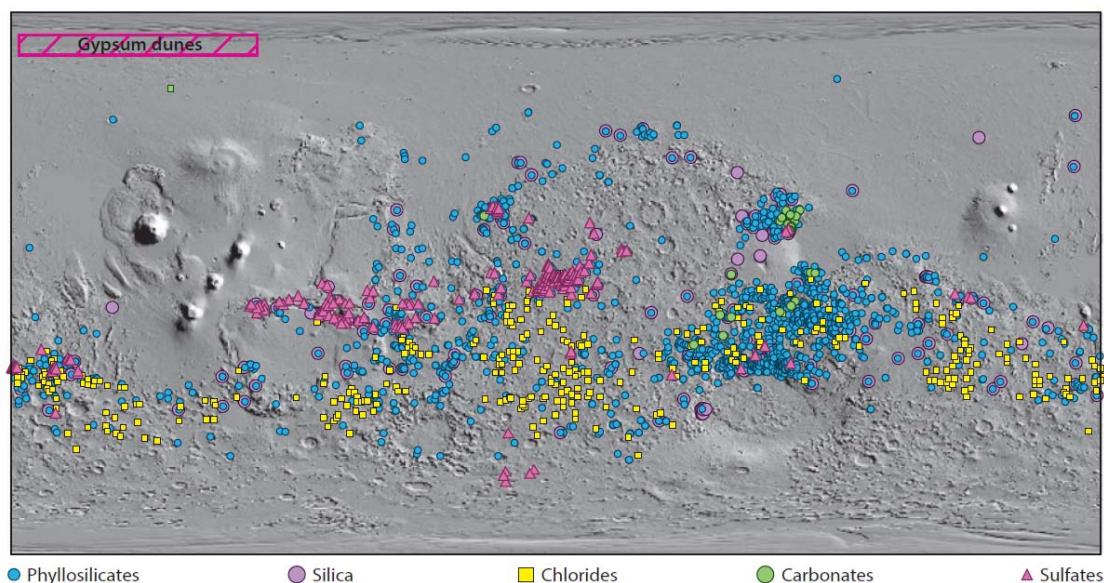


Figure 1.6. Global distribution of aqueous minerals on Mars (Ehlmann and Edwards, 2014).

1.1.2 Mars from the Surface

The view of Mars provided from orbit has enabled and guided surface missions such as Mars Pathfinder, the Mars Exploration Rovers (MER) and Mars Science Laboratory (MSL) rover, which landed on Mars in 1997, 2004 and 2012, respectively.

The in-situ measurements of carbonate minerals made by MER Spirit at Gusev crater suggest a volcanic hydrothermal formation during the Noachian, and are consistent with CRISM observations (Morris et al., 2010; Carter and Poulet, 2012). MER Opportunity, deployed at Meridiani Planum, discovered layered sedimentary rocks and sulphate minerals including Mg-, Ca-sulphates and jarosite, along with hematite-rich spherical concretions that formed from the interaction of groundwater (Squyres et al., 2006). MER Opportunity also discovered gypsum veins at Endeavour crater (Squyres et al., 2012), where phyllosilicates and sulphates have also been identified in orbital datasets (Wray et al., 2009).

Furthermore, the remote detection of clay deposits in Gale crater (Milliken et al., 2010; Thomson et al., 2011), were subsequently confirmed in-situ with X-ray diffraction measurements taken on-board Curiosity (Vaniman et al., 2014; Bish et al., 2014).

1.1.3 Martian Meteorites

Rocks that have been ejected from Mars by impacts and have subsequently fallen to Earth as meteorites are known as the Martian meteorites. Currently there are 174 entries

(including paired stones) for Martian meteorites in the Meteoritical Bulletin Database (2016), of which 142 are basaltic to lherzolitic igneous rocks classified as shergottites, 18 are olivine-clinopyroxene cumulates classified as nakhlites (Treiman, 2005) and 3 are dunitic cumulates classified as chassignites, leaving 11 meteorites classified as neither of these three main classes. The three main classifications each owe their name to a documented fall of one of the meteorites in that class; Shergotty, Nakhla and Chassigny (Nyquist et al., 2001). Known as the SNC meteorites, these samples of the Martian surface have been the subject of much study, with the nakhlites being of prime interest.

Studies have shown that the nakhlites are olivine-clinopyroxene rocks, which all represent the same lithologic unit with a common basaltic crystallisation age of 1.3 Ga (Nyquist et al., 2001). The presence of hydrated, secondary minerals have also been discovered within the nakhlites, indicating fluvial alteration on Mars (Gooding et al., 1991; Bridges and Grady, 2000; Changela and Bridges, 2010; Bridges and Schwenger, 2012; Hicks et al., 2014). This fluvial activity is recorded in veins within brittle fractures, which are truncated by the fusion crust suggesting a pre-terrestrial (Martian) origin. K-Ar dating of alteration products (smectite- and siderite-veined olivine grains) suggest that the nakhlites were altered ≤ 670 Myr (Shih et al., 1998; Swindle et al., 2000). Cosmogenic nuclides suggest a common ejection from Mars < 10 -12 Myr (Korochantseva et al., 2011). Subsequent modelling of the alteration fluid has shown how the nakhlite alteration minerals were formed as a result of interaction with a potentially habitable neutral to alkaline brine with temperatures 50-200 °C in a near-surface setting, such as an impact-induced hydrothermal environment (Bridges and Schwenger, 2012). This highlights the importance of mineralogical analysis as certain minerals can indicate possible habitable environments on a body such as Mars, which is explored further in Chapter 4 of this thesis with remote sensing data.

1.2 Future Exploration of Mars

NASA exploration of Mars is guided by four goals defined by the Mars Exploration Program Analysis Group (NASA MEPAG, 2016):

1. Determine if Mars ever supported life.
2. Understand the processes and history of climate on Mars.
3. Understand the origin and evolution of Mars as a geological system.
4. Prepare for human exploration.

These four goals guide NASA missions to Mars, and most currently the landing site selection for the NASA Mars 2020 rover. The rover, of a similar design to MSL Curiosity, will have instruments to characterise geological samples in-situ using X-ray fluorescence and Raman spectroscopy (Allwood et al., 2015; Beegle et al., 2015; Clegg et al., 2015).

The joint ESA and Roscosmos Exobiology on Mars (ExoMars) program, which consists of an orbiter, lander and rover, is tasked with: searching for signs of past and present life on Mars, investigating how the water and geochemical environment varies, and investigating atmospheric trace gases and their sources. The Trace Gas Orbiter was inserted into orbit about Mars on October 19th 2016, however the Schiaparelli lander crashed on the surface of Mars (ESA, 2016a, 2016b). The ExoMars rover is planned to arrive at Mars in 2020 (ESA, 2016c).

With landing sites yet to be finalised for the two rover missions mentioned above, data provided by HiRISE, CRISM and other instruments (MOLA, TES, etc.) is currently being heavily utilised to examine areas that meet both the science goals and the engineering requirements of the proposed missions (NASA JPL, 2016; ESA, 2015). Previous remote sensing studies of the surface of Mars have highlighted areas of possible exploration; however further analysis is required to ascertain the accessibility of a potential landing site with respect to engineering constraints of a mission. This thesis comprises a study of the surface of Mars (Chapter 4), highlighting areas for possible future exploration in-situ with a lander or rover.

1.3 Thesis Focus and Outline

The focus of this thesis is the analysis of the surface of Mars using remotely sensed near-infrared (NIR) data and high-resolution imagery, with the aim of highlighting areas of future exploration by studying post-Noachian impact induced hydrothermal systems. The link to future missions was further explored by lab-based development of a novel back-reflection X-ray diffraction technique that could, potentially, be deployed on the robotic arm of a planetary lander or rover. These techniques enable the remote and subsequent in-situ identification of minerals that, in some cases, can be a key indicator of potential past habitable environments on Mars.

Chapter 2 describes the theory of reflectance spectroscopy and associated analytical techniques used to identify the surface mineralogy, with a focus on the surface of Mars. NIR, elevation and high-resolution imaging datasets provided by Mars orbiters are described along with instrument descriptions and associated analytical techniques.

Chapter 3 gives a background to X-ray diffraction for mineral identification including different analytical techniques with a focus on the back-reflection method. Interpretation of X-ray diffraction data is described along with an outline of the experimental facilities used at the University of Leicester and the Diamond Light Source. The production of X-rays and X-ray fluorescence is also described.

Chapter 4 presents the study of post-Noachian impact induced hydrothermal activity using high-resolution imagery and NIR data provided by NASA instruments on-board Mars Reconnaissance Orbiter. Motivated by the study of Martian meteorites, where studies have suggested an impact-induced alteration environment (Changela and Bridges, 2010; Bridges and Schwenzer, 2012; Hicks et al., 2014), this study highlights areas of possible future exploration on Mars. The results of this study have been published (Turner et al., 2016).

Chapter 5 contains the data acquired during the laboratory-based testing of a novel back-reflection X-ray diffraction technique at the University of Leicester. A method of X-ray fluorescence suppression is described, with some results previously published in Hansford et al. (2014). Mineral samples studied using the technique include iron-oxides, carbonates, sulphates and phyllosilicates. The geometry of the technique allows for unprepared whole-rock analysis and so, for some samples, both whole-rock and prepared pressed powder pellet datasets were acquired for comparison. This study demonstrates the capability of the technique and highlights its potential for future deployment for planetary science missions.

Chapter 6 explores the back-reflection technique further with the application of high-resolution back-reflection X-ray diffraction at the Diamond Light Source, and shows how the experimental technique can be used to accurately determine the sample unit-cell. The results from this study have been submitted for publication (Hansford et al., 2017).

Chapter 7 summarises the thesis, and suggests avenues for future work.

2. Reflectance Spectroscopy for Remote Mineral Identification

The study of the surface of Mars to identify a geologic process of interest or area for future in-situ exploration requires the ability to characterise the surface mineralogy using remote sensing techniques, and thus a knowledge of the datasets available. In this chapter, the theory of reflectance spectroscopy, the spectral characteristics of mineral groups and their identification using CRISM data is described. Additional datasets that aid in the analysis of the Martian surface, such as high-resolution imagery and elevation data provided by HiRISE, CTX and MOLA, are also outlined along with analytical techniques.

2.1 Reflectance Spectroscopy

The definition of reflectance (I/F) is the wavelength-dependent reflected energy (F) relative to the irradiation (I). Upon interaction with the surface of a planetary body, some of the solar radiation is absorbed by processes such as crystal field transitions, charge transfers and vibrational effects. This absorption of energy is manifested as decreases in the reflectance spectra at the associated wavelength of the corresponding planetary surface mineralogy (figure 2.1).

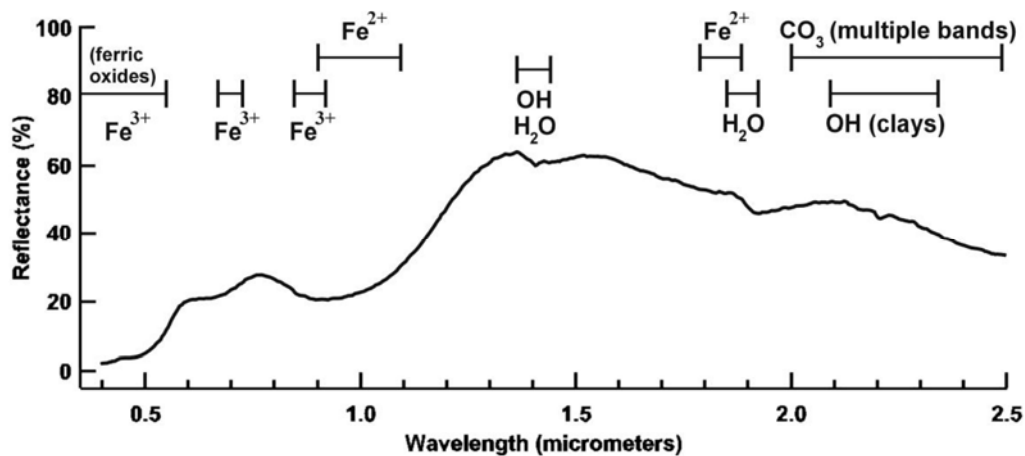


Figure 2.1. Common mineralogical spectral absorption features and their wavelength positions (Grebby, 2011).

The process of absorption and reflection of solar radiation by a change in medium can be mathematically described (Clark, 1999). Upon incident interaction with a different

medium some photons are reflected and some are refracted into the different medium; their absorption is determined by the Beer-Lambert Law:

$$I = I_0 e^{-kx} \quad (2.1)$$

where I is the observed intensity at a distance x through a medium of absorption coefficient k , with I_0 being the initial intensity. Absorption coefficient k is defined as

$$k = \frac{4\pi\kappa}{\lambda} \quad (2.2)$$

where κ is the extinction coefficient of the material and λ is the wavelength of the radiation. The extinction coefficient κ is the imaginary part of the complex index of refraction m

$$m = n - i\kappa \quad (2.3)$$

where n is the index of refraction. Conservation of energy states that the sum of reflected (R), transmitted (T) and absorbed (A) energy must equal the incident solar radiation (I).

$$I = R + T + A \quad (2.5)$$

As R , T and A are ratios of a given component (i.e. wavelength), this equation can be simplified to

$$1 = R_\lambda + T_\lambda + A_\lambda \quad (2.6)$$

and assuming that all radiation is either reflected or absorbed ($T_\lambda = 0$) it can be assumed that

$$1 = R_\lambda + A_\lambda \quad (2.7) \text{ (Clark, 1999).}$$

This section focuses on the indicative wavelength absorption (A_λ) processes of geologic minerals in reflectance spectra.

2.1.1 Electronic Transitions: Crystal Field Transitions and Charge Transfers

Crystal field transitions are caused by transition elements (Fe, Co, Ni, etc.) and their unfilled electron shells. The orbitals of all transition elements have identical energies; however, when such atoms are located in a crystal field the energy levels split, resulting in multiple orbital energy levels that enable an electron to be excited from a low energy level into a relatively higher energy level by absorption of a photon, provided the photon energy is sufficient (i.e. greater energy than the difference between states). The valence state of the atom and crystal symmetry determines the energy levels, which are influenced by the coordination and type of ligands formed (Burns, 1993). For example, Fe^{2+} produces an absorption feature near 0.90 – 1.00 μm when in six-fold coordination for the orthorhombic minerals olivine and orthopyroxenes. This absorption feature is shifted when in octahedral coordination to near 1.00 – 1.10 μm for monoclinic minerals such as clinopyroxenes (Rothery, 1987).

Incident photons can cause an electron to move between neighbouring ions (or between ligands and ions); these inter-element transitions are known as charge transfers and cause broad absorption bands in the ultraviolet to visible wavelength regions (Clark, 1999). For example, iron oxides, which are abundant on Mars, (e.g. goethite (FeOOH) and hematite (Fe_2O_3)) have an intense charge transfer absorption in the ultraviolet region ($< 4.0 \mu\text{m}$) that extends to visible wavelengths resulting in their red colour (Clark, 1999).

2.1.2 Vibrational Processes

Incident photons excite the inter-atomic bonds in a molecule or crystal structure, causing them to vibrate. A non-linear polyatomic molecule consisting of N atoms has $3N - 6$ normal modes of vibration known as fundamentals. A vibration can occur at approximate multiples of the fundamental frequency; these are known as overtones. A mixture of vibration modes can also occur; these are known as combinations. Notation of vibrational effects of a molecule follow: ν_1, ν_2, ν_3 for the fundamental modes; $2\nu_1, 3\nu_2, 4\nu_3$ for the overtone modes; and $\nu_1 + \nu_2, \nu_2 - \nu_3, \nu_1 + \nu_2 + \nu_3$ for combination modes (Clark, 1999). Similarly, a linear polyatomic molecule consisting of N atoms has $3N - 5$ normal modes of vibration. Diatomic molecules only have one possible vibration corresponding to the compression and stretching of the singular bond.

The three fundamentals of H_2O vapour occur at 2.738 μm , 6.270 μm and 2.663 μm for symmetric OH stretch (ν_1), H-O-H bend (ν_2) and asymmetric OH stretch (ν_3), respectively. Due to hydrogen bonding, these shift in liquid water to 3.106 μm (ν_1), 6.079

μm (ν_2) and $2.903 \mu\text{m}$ (ν_3). In the $1.0\text{--}2.6 \mu\text{m}$ range, features occurring near $1.4 \mu\text{m}$ and $1.9 \mu\text{m}$ correspond to the first overtones of the OH stretches and the combinations of the OH stretches with the H-O-H bend, respectively (Hunt, 1977; Clark, 1999). More specifically, the overtones and combinations that occur in the $1.0\text{--}2.0 \mu\text{m}$ range are: $1.135 \mu\text{m}$ ($\nu_1 + \nu_2 + \nu_3$), $1.38 \mu\text{m}$ ($\nu_1 + \nu_3$), $1.454 \mu\text{m}$ ($2\nu_1 + \nu_3$) and $1.875 \mu\text{m}$ ($\nu_2 + \nu_3$) (Hunt, 1977). Therefore, distinctions between H_2O and OH bearing minerals can be made. For metal-OH bearing minerals, a combination metal-OH bend with the OH stretch occurs close to $2.2\text{--}2.3 \mu\text{m}$. Section 2.3 provides a detailed explanation of absorption bands attributed to a wide range of minerals of interest in this thesis.

The linear triatomic molecule CO_2 has four fundamentals near $7.2 \mu\text{m}$ (ν_1), $4.3 \mu\text{m}$ (ν_2) and $15 \mu\text{m}$ (ν_3) (two fundamentals). These are due to the symmetric (ν_1) and antisymmetric (ν_2) CO stretches, along with symmetric and asymmetric O-C-O bends (ν_3). The symmetric stretch ν_1 is not infrared (IR) active as the dipole moment remains 0 during the vibration. The two symmetric and asymmetric O-C-O bends occur at the same frequency, therefore only one spectral absorption will be observed for these two degenerate modes. In the $1.0\text{--}2.6 \mu\text{m}$ range, features occur near $1.4 \mu\text{m}$, $1.6 \mu\text{m}$, $2.0 \mu\text{m}$, $2.3 \mu\text{m}$ and $2.5 \mu\text{m}$ due to overtones and combinations (Salby, 1995; Stuart, 2004).

Spectral absorptions caused by rotational transitions of a molecule, and the combination of these rotational transitions with vibrational (ro-vibrational) transitions, were not considered for this thesis because rotational transitions of a molecule are only possible for gaseous phases. This is because the intermolecular forces present in a solid prohibit molecular rotation, meaning rotational transitions are not applicable for identification of a mineral present on the surface of Mars.

2.1.3 Atmospheric Effects

The impact of an atmosphere on the measured spectral characteristic of surface materials must be considered. This is because the path of the ground-attenuated signal to the detector passes through the atmosphere. The interaction between solar radiation and the atmosphere is principally the same as with the surface: electronic transitions and vibrational effects occur.

The atmosphere of Mars contains over 95% CO_2 , which produces a triplet absorption feature around $2.0 \mu\text{m}$ (Salby, 1995; Stuart, 2004; McGuire et al., 2009). This absorption does not saturate the spectra, meaning the atmosphere is not opaque and minerals can be detected on the surface of Mars. This $2.0 \mu\text{m}$ CO_2 atmospheric

contribution is minimised in the spectra by applying the empirical ‘volcano-scan’ correction (McGuire et al., 2009), as outlined in section 2.3.1.1.

2.1.4 Grain Size

The grain size of a material can also affect the form of its reflectance spectrum. Fine-grained materials produce a strong scattering of light at the surface due to more grain interfaces per unit area resulting in a smaller fraction of solar radiation being refracted into the grain, where absorption occurs. The depth of spectral absorptions increases with grain size, with spectral saturation commonly occurring at grain sizes $>250 \mu\text{m}$ for most minerals, as larger grains are effectively opaque (Pieters, 1983). This is described by the Beer-Lambert Law (equation 2.1; Clark, 1999).

2.2 Spectral Absorptions in the 1.0 – 2.6 μm Region of Mineralogical Interest

In the context of Mars exploration, the analysis of the surface mineralogy has been increasingly of interest in order to determine the presence of past water-altered environments as these have implications for previous habitable environments (Murchie et al., 2007, 2009a; Ehlmann et al., 2009; Ehlmann and Edwards, 2014; Grotzinger et al., 2014). This current research approach requires the ability to discern between areas dominated by mafic, phyllosilicate, sulphate and carbonate minerals. This section details the characteristic absorption bands associated with these mineral types, along with their origin with regards to mineral structure, and formation mechanisms.

It is important to note that, aside from the above mineral groups, the spectra of both H_2O ice and CO_2 ice also exhibit prominent absorption features in the 1.0–2.6 μm region. Specifically, H_2O ice has diagnostic absorption bands at 1.25 μm , 1.5 μm and 2.0 μm , whereas CO_2 ice has 1.435 μm and 2.281 μm absorptions (Langevin et al., 2007).

2.2.1 Mafic Minerals

Formed by igneous processes and indicators of unaltered rocks, mafic minerals describe silicate minerals that are rich in iron and magnesium. The nesosilicate olivine $(\text{Fe,Mg})_2\text{SiO}_4$ is an important rock-forming mineral in mafic and ultramafic rocks. Olivine is identified by a characteristic absorption in its spectrum at $\sim 1.0 \mu\text{m}$, which is caused by crystal field transitions of Fe^{2+} (Mustard et al., 2005). In contrast, the spectrum of the pure forsterite endmember (Mg_2SiO_4) is featureless (Adams, 1975). Pyroxenes $(\text{Ca,Fe,Mg})_2\text{Si}_2\text{O}_6$, are chain silicate minerals present in igneous rocks. Generally,

pyroxenes have two characteristic bands that shift depending on Ca and Fe content – low Ca pyroxenes tend to have a strong absorption at 0.9 μm and a broad absorption 1.8 μm , which are shifted to 1.0 μm and 2.3 μm for high Ca pyroxenes with an increasing Fe content (Adams, 1975; Mustard et al., 2005). A selection of mafic mineral spectra taken from the CRISM RELAB spectral library – a database of spectra that has been acquired of Mars-analog materials – (NASA, 2012) is shown in figure 2.2.

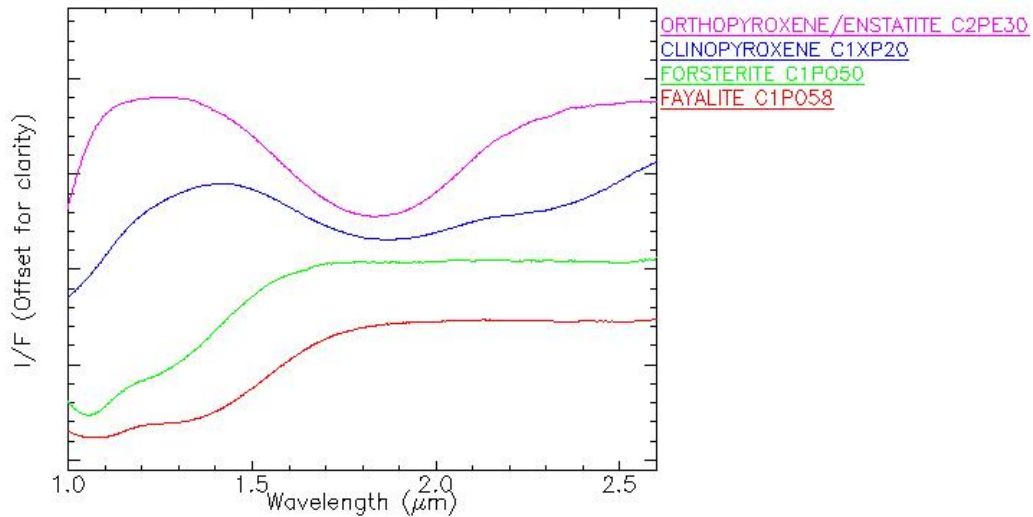


Figure 2.2. Selected CRISM RELAB spectra (NASA, 2012) of mafic minerals Fe-rich olivine endmember fayalite, Mg-rich olivine endmember forsterite, clinopyroxene and orthopyroxene.

2.2.2 Phyllosilicate Minerals

Phyllosilicates are silicate minerals comprised of one octahedral sheet and up to two tetrahedral sheets bonded together in parallel, and an interlayer. Octahedra comprise of OH^- anions and 2 to 3 cations (Mg, Al or Fe); octahedra with 3 divalent cations are trioctahedral phyllosilicates whereas octahedra with two trivalent cations and a vacancy are dioctahedral phyllosilicates. Tetrahedra are comprised of Al, Si or Fe^{3+} cations and O^{2-} anions. The interlayer may be either vacant, or containing a cation such as Na^+ , Ca^{2+} , K^+ or H_3O^+ , or an octahedral sheet (chlorites). Phyllosilicates are classified by: the ratio of tetrahedral to octahedral layers; the resultant charge at the interlayer site from the tetrahedral and octahedral cation occupancies; and the occupancy of the interlayer (Bishop et al., 2008).

Phyllosilicates form under a variety of environmental conditions, but all require prolonged exposure to an aqueous environment and are thus of particular significance for investigations of water-rock interaction on Mars. Under standard terrestrial pressures and temperatures, kaolinite forms in acidic conditions whereas neutral to alkali conditions

favour the clays, smectites and illite in the presence of Ca and K, respectively. Serpentine sheet silicates can form as the result of alteration of ultrabasic rocks and olivine in particular, by hydrothermal fluids $\leq 400^\circ\text{C}$. Prehnite, a sheet silicate is characteristic of hydrothermal processes at $200 - 400^\circ\text{C}$ (Deer et al., 1992).

The 2:1 (tetrahedral to octahedral ratio) phyllosilicate smectite group includes minerals such as montmorillonite (figure 2.3a) and nontronite, which are dioctahedral with Al^{3+} and Fe^{3+} . A slight negative charge in smectites is caused by cation substitutions, meaning a cation such as Na, Mg or Ca along with varying amounts of H_2O in the interlayer site is required to balance it out (Bishop et al., 2008).

The kaolinite-serpentine phyllosilicate group is classified by having a tetrahedral to octahedral ratio of 1:1. Kaolinite (figure 2.3b) and chrysotile have Al^{3+} and Mg octahedral cations, and are electrostatically neutral so do not contain interlayer cations (i.e. molecular water is not contained in the interlayer) (Bishop et al., 2008).

The 2:1 phyllosilicate mica group have $\sim 25\%$ Si tetrahedral sites replaced with Al, resulting in a charge deficit that is compensated in the interlayer region by Na, K or Ca. Micas have high layer charge, meaning they are non-expanding and do not contain interlayer H_2O (Bishop et al., 2008).

The 2:1 chlorite phyllosilicate group have edge-sharing octahedra in the interlayer occupied by a Mg/ Fe^{2+} and OH combination. The Mg- and Fe-rich trioctahedral species in this group are clinocllore (figure 2.3c) and chamosite, respectively. Chlorites contain little or no water with variable layer charge; they are non-expanding (Bishop et al., 2008).

A spectral absorption feature at $1.9 \mu\text{m}$ is attributed to combinations of bending and stretching vibrations of H_2O within a mineral structure and is a first indication of the presence of phyllosilicate minerals. Combination overtones of H_2O , along with OH overtones caused by structural stretching vibrations result in another absorption at $\sim 1.4 \mu\text{m}$. In phyllosilicates, the position of the OH overtone is influenced by the octahedral cation present, causing it to shift between $1.38 - 1.43 \mu\text{m}$ (Bishop et al., 2008). Absorptions between $2.0 - 2.6 \mu\text{m}$ are most indicative of a hydrated silicate phase. More specifically, Al-OH absorptions occur at $\sim 2.21 \mu\text{m}$, whereas Fe- and Mg-OH absorptions occur at $\sim 2.29 \mu\text{m}$ and $\sim 2.32 \mu\text{m}$, respectively (Bishop et al., 2002a, 2002b). A selection of phyllosilicate mineral spectra taken from the CRISM RELAB spectral library (NASA, 2012) is shown in figure 2.4.

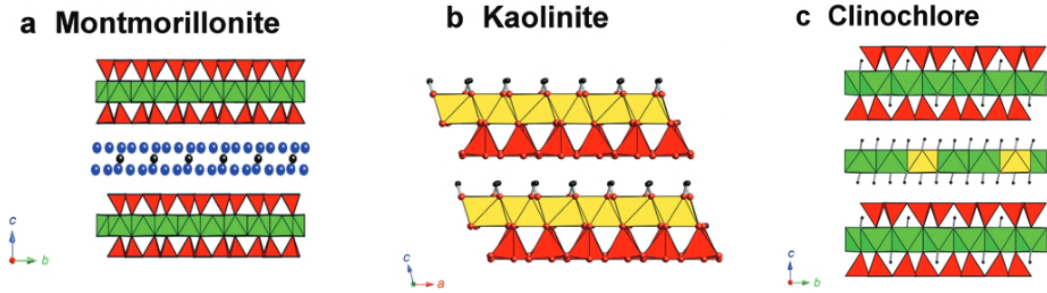


Figure 2.3. Mineral structures. A) Montmorillonite: 2:1 tetrahedra to octahedra with a H₂O dominated interlayer, B) Kaolinite: 1:1 tetrahedra to octahedral, and C) Clinocllore: 2:1 tetrahedra to octahedra with an octahedra interlayer. Red structures represent tetrahedra with green and yellow structures representing octohedra (Dyar et al., 2007).

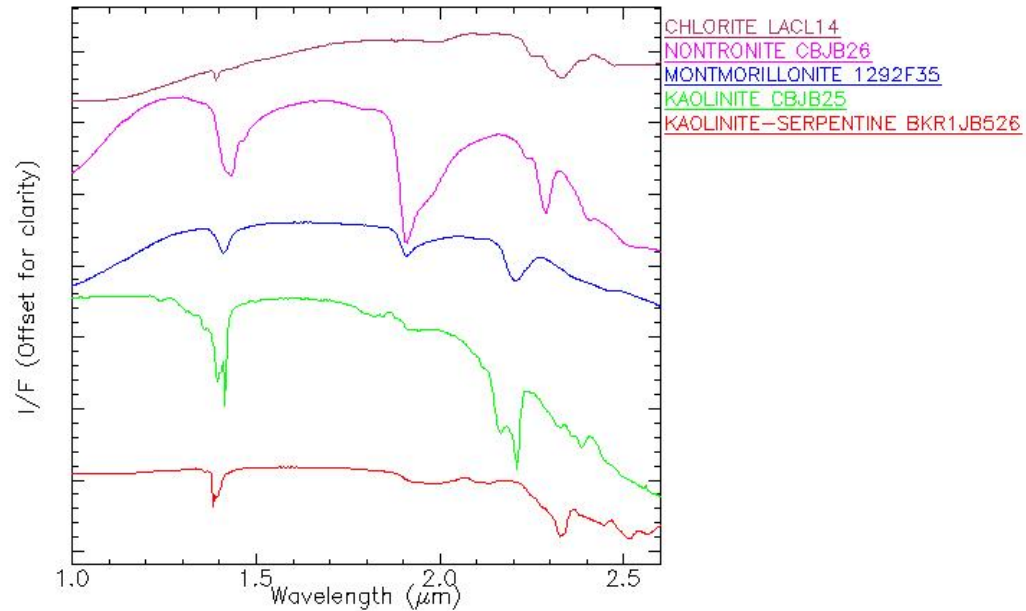


Figure 2.4. Selected CRISM RELAB spectra (NASA, 2012) of phyllosilicate minerals chlorite, nontronite, montmorillonite, kaolinite and kaolinite-serpentine.

2.2.3 Sulphate Minerals

Sulphates form through the evaporation of a body of standing water or groundwater, under acidic conditions. The structures of sulphates involve metal cations (M) in MO₆ or M(H₂O)₆ octahedra and SO₄ tetrahedra. Kieserite (MgSO₄·H₂O) is comprised of Mg(SO₄)O₃ chains corner linked by adjacent chains of octahedra and tetrahedra. Gypsum (CaSO₄·2H₂O) has a similar structure to anhydrite, but with an H₂O interlayer that is linked to the tetrahedral O atoms by hydrogen bonds. Anhydrite (CaSO₄) comprises of CaO₈ dodecahedra and SO₄ tetrahedra constructed in chains of alternating tetrahedra and dodecahedra, linked by edge sharing adjacent dodecahedra and corner

sharing dodecahedra and tetrahedra. Structures of jarosite ($\text{KFe}^{3+}(\text{OH})_6(\text{SO}_4)_2$) and alunite ($\text{KAl}_3(\text{SO}_4)_2(\text{OH})_6$) are based on infinite octahedral-tetrahedral sheets that are held together by hydrogen bonds and interstitial cations. Rozenite ($\text{Fe}^{2+}\text{SO}_4 \cdot 4\text{H}_2\text{O}$) comprises clusters of $\text{Fe}_2^{2+}(\text{SO}_4)_2\text{O}_8$ polyhedra with hydrogen bonds within and between adjacent clusters (Cloutis et al., 2006).

Fundamental S-O bending and stretching absorption bands occur at longer wavelengths (8–10 μm , 13–18 μm and 19–24 μm) than those studied in this thesis. However, S-O bending overtones occur in the 2.1–2.7 μm region (the exact position and depth is dependent on the associated cation), along with H₂O- and OH- combinations. Generally, monohydrated sulphates have a broad absorption band at ~ 2.0 μm with a diagnostic absorption band at 2.4 μm , whereas polyhydrated sulphates have absorption bands around 1.4 μm and 1.9 μm , consistent with H₂O and OH overtones, with a drop-off near 2.4 μm (Cloutis et al., 2006). Jarosite and alunite do not contain H₂O and therefore lack the associated absorption bands, but OH- related absorption bands are exhibited; including 2.27 μm and 2.18 μm for jarosite and alunite, respectively. A selection of sulphate mineral spectra taken from the CRISM RELAB spectral library (NASA, 2012) is shown in figure 2.5.

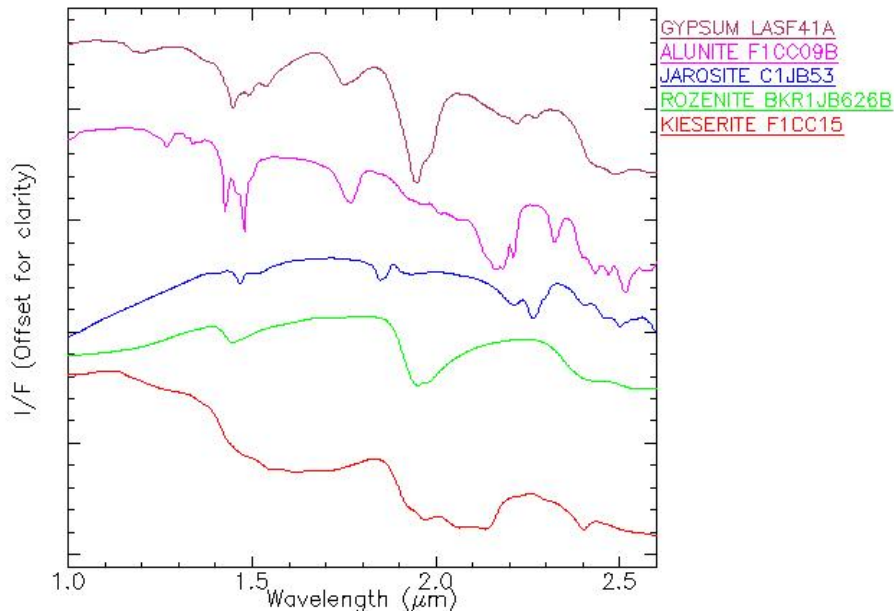


Figure 2.5. Selected CRISM RELAB spectra (NASA, 2012) of sulphate minerals gypsum, alunite, jarosite, rozenite and kieserite.

2.2.4 Carbonate Minerals

Formed as a weathering product of neutral-to-alkaline, HCO_3^- bearing water, carbonates have absorption bands around 2.3 μm and 2.5 μm due to C-O bending and stretching vibrational modes causing overtone and combination tones, but their exact position depends on the major cation. Mg-rich carbonates have absorption bands at 2.30 μm and 2.50 μm , Ca-rich carbonates have absorption bands at 2.34 μm and 2.54 μm , and Fe-rich carbonates have absorption bands at 2.33 μm and 2.53 μm (Gaffey, 1987). A selection of carbonate mineral spectra taken from the CRISM RELAB spectral library (NASA, 2012) is shown in figure 2.6.

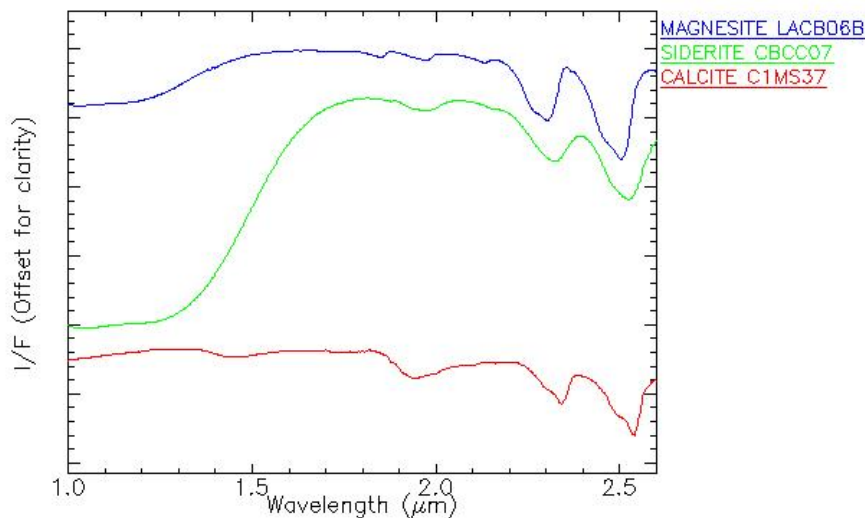


Figure 2.6. Selected CRISM RELAB spectra (NASA, 2012) of carbonate minerals magnesite, siderite and calcite.

2.3 Remote mineral identification using reflectance spectroscopy

The identification of the surface mineralogy of Mars using reflectance spectroscopy has, and is currently, being achieved by the Compact Reconnaissance Imaging Spectrometer for Mars (CRISM) on-board the Mars Reconnaissance Orbiter (MRO). CRISM is a hyperspectral imager, acquiring data in the range 362–3920 nm that enables the identification of mafic, phyllosilicate, sulphate and carbonate minerals (Murchie et al., 2007).

MRO was inserted into a sun-synchronous, near-circular 255 × 320 km, near-polar, 3 pm orbit about Mars in March 2006, and is still operational at the time of writing this thesis (Zurek and Smrekar, 2007). The MRO spacecraft carries six instruments: CRISM, the High Resolution Imaging Science Experiment (HiRISE), the Context

Camera (CTX), the Mars Color Imager (MARCI), the Mars Climate Sounder (MCS) and the Mars Shallow Radar sounder (SHARAD).

2.3.1 The CRISM Instrument

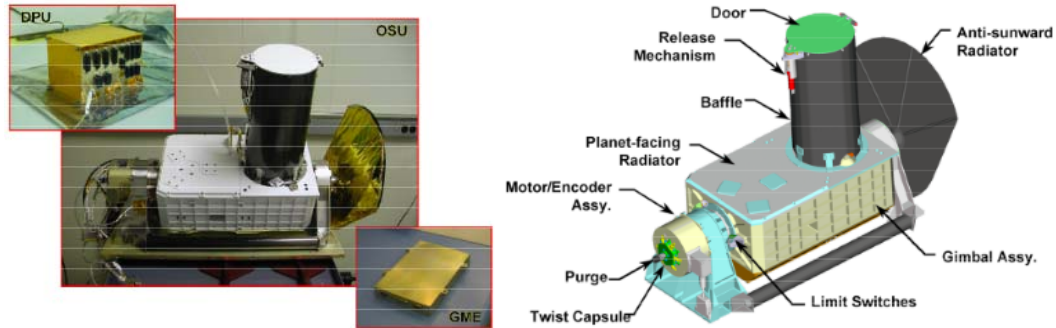


Figure 2.7. Left: Photographs of the CRISM Optical Sensor Unit (OSU), Digital Processing Unit (DPU) and Gimbal Motor Electronics (GME). Right: Configuration of the CRISM OSU (Murchie et al., 2012).

The CRISM instrument on-board MRO is a spectrometer that measures electromagnetic radiation in the visible to shortwave infrared wavelength region of the electromagnetic spectrum. Specifically, CRISM records radiation across 544 channels in the 362–3920 nm range, with a spectral resolution of 6.55 nm/channel. The instrument operates in a number of targeted imaging modes (table 2.1). In targeted mode, CRISM acquires images with a ground footprint of $\sim 10 \times 3\text{--}20$ km and a spatial resolution (i.e. pixel size) of 18–40 m. This is achieved using a gimballed Optical Sensor Unit (OSU) to compensate for the orbital motion of MRO, allowing for a long acquisition time (2–3 minutes) of a targeted area and acquisition of data with a high signal-to-noise ratio (>300 at 500–2500 nm, and >100 for all wavelengths) (Murchie et al., 2007). CRISM also images the Martian surface in a mapping mode, in which the instrument acquires 100–200 m/pixel nadir images of ~ 10 km in width and ≤ 550 km long (Murchie et al., 2007). Atmospheric scenes are also acquired to monitor seasonal variations and general atmospheric properties.

CRISM utilises a 100 mm aperture Ritchey-Chretien telescope with a focal length of 441 mm to focus an image of Mars towards the CRISM sensor optics, where the beam is split. The visible and near-infrared (VNIR) component of the beam is reflected towards the VNIR detector and the infrared (IR) component is transmitted towards the IR detector. To minimise thermal-generated electron contribution to background noise (dark current), the VNIR and IR detectors are operated at temperatures of 213 K and 104 – 108 K, respectively (Murchie et al., 2007).

Table 2.1. CRISM targeted imaging modes (Johns Hopkins University, 2013).

Mode	Description	Resolution (m/pixel)	Footprint size (km)	Dates Acquired (year_day)
FRT	Full Resolution Targeted	18	~10×10	2006_270 – 2012_146
HRL	Half Resolution Targeted	40	~10×20	2006_273 – 2012_146
HRS	Half Resolution Short	40	~10×8	2006_273 – 2012_144
FRS	Full Resolution Short	18	~10×3	2012_275 – present

2.3.1.1 Processing of CRISM data

Pre-processed CRISM TRDR (Targeted Reduced Data Record) v3 I/F observations (Murchie et al., 2009b) were obtained from the NASA Planetary Data System Geosciences Node and subsequently processed and analysed using the CRISM Analysis Toolkit (CAT) version 7.2.1; a software tool released by the CRISM team that is an extension to the Environment for Visualising Images (ENVI) software package. The first stage of processing involved a photometric correction by division of the cosine of the incidence angle of the observation to correct for non-normal solar incidence, followed by an atmospheric correction using the volcano scan method (McGuire et al., 2009) described below.

The CRISM volcano scan correction for atmospheric effects utilises a reference transmission spectrum of CO₂ that is obtained by scaling observations made of the base and summit of Olympus Mons. The transmission spectrum is then scaled to CRISM spectra so that by division the Lambert albedo is forced to be the same at two wavelengths: 1.980 μm (λ_1) and 2.007 μm (λ_2). λ_1 is outside the CO₂ absorption bands whereas λ_2 is deep inside the CO₂ absorption bands, both corresponding to CRISM spectral bands (McGuire et al., 2009). This method uses the following model for atmospheric transmission and surface reflection:

$$I/F(\lambda) = A_L(\lambda) \cos(\theta_i) (T(\lambda))^\beta \quad (2.8)$$

where the surface reflectance $I/F(\lambda)$ is defined as the product of the Lambertian albedo $A_L(\lambda)$ at wavelength λ , the cosine of the angle of incidence of solar radiation $\cos(\theta_i)$ and the Olympus Mons transmission spectrum of CO₂ $T(\lambda)$ to the power of β (McGuire et al., 2009). The exponent β is calculated on a pixel-by-pixel basis and is determined from

$$\beta = \frac{\ln\left(\frac{I/F(\lambda_1)}{I/F(\lambda_2)}\right)}{\ln\left(\frac{T(\lambda_1)}{T(\lambda_2)}\right)} \quad (2.9)$$

which is derived from

$$A_L(\lambda_1) = A_L(\lambda_2) \quad (2.10)$$

and by equation (2.8)

$$I/F(\lambda_1)/T(\lambda_1)^\beta = I/F(\lambda_2)/T(\lambda_2)^\beta \quad (2.11)$$

Applying natural log and rearranging equation 2.11 gives equation 2.9. This method of correction assumes no change in surface albedo between λ_1 and λ_2 . The use of an experimentally acquired transmission spectrum of CO₂ assumes that the aerosol and dust quantities at the base and summit of Olympus Mons are equal, and that the wavelength calibration since acquisition of the transmission spectrum is unchanged (McGuire et al., 2009).

2.3.1.2 Mineral Identification Using CRISM Data

The final step of processing CRISM spectral images involved the calculation of summary products (table 2.2) (Pelkey et al., 2007). The summary products were images computed by combining specific CRISM wavebands in a way that highlights minerals with specific spectral characteristics, which aid in identifying areas of mineralogical interest in the CRISM images, along with a corresponding spectrally bland (featureless) region. For example, the D2300 summary parameter in table 2.2 highlights areas with 2.3 μm absorptions, which indicate the presence of Fe/Mg-rich phyllosilicates. The average spectrum of a selected region of interest is subsequently ratioed to the average spectrum of the selected spectrally bland region. This approach aids in dividing out systematic artefacts along with residuals from instrument artefacts and the atmospheric correction in the spectrum of interest, therefore accentuating compositional differences between the regions. This conventional method of spectral information extraction from CRISM data has been used in several previous studies (e.g., Ehlmann et al., 2009; Milliken et al., 2010).

Table 2.2. Key CRISM summary parameters and their formulae (Murchie et al., 2009a).

Name	Parameter	Formulae
OLINDEX	Olivine index	$\frac{R1695}{0.1 \times (R1050 + R1210) + 0.4 \times (R1330 + R1470)} - 1$
LCPINDEX	Low-Ca Pyroxene index	$\frac{R1330 - R1050}{R1330 + R1050} \times \frac{R1330 - R1815}{R1330 + R1815}$
HCPINDEX	High-Ca Pyroxene index	$\frac{R1470 - R1050}{R1470 + R1050} \times \frac{R1470 - R2067}{R1470 + R2067}$
BD1900	1.9 μm band depth	$1 - \frac{0.5 \times (R1930 + R1985)}{a \times R1857 + b \times R2067}$
BD2100	2.1 μm band depth	$1 - \frac{0.5 \times (R2120 + R2140)}{a \times R1930 + b \times R2250}$
BD2210	2.21 μm band depth	$1 - \frac{R2210}{a \times R2140 + b \times R2250}$
BD2290	2.29 μm band depth	$1 - \frac{R2290}{a \times R2250 + b \times R2350}$
D2300	2.3 μm drop	$1 - \frac{R2290 + R2320 + R2330}{R2140 + R2170 + R2210}$
SINDEX	Sulphate index	$1 - \frac{R2100 + R2400}{2 \times R2290}$

^aFor the formulae, wavelength references are in nm and values a and b are determined by $a = 1 - b$ and $b = (\lambda_C - \lambda_S)/(\lambda_L - \lambda_S)$ where $BD_C = 1 - R_C/(a \times R_S + b \times R_L)$ (Pelkey et al., 2007).

Extracted spectra were then compared to the USGS spectral library for mineral identification, which was based on recognising similarities in spectral shape in addition to the presence of concurrent spectral absorption features. To rapidly reduce the number of possible minerals, the spectral feature fitting tool in ENVI was first used to narrow down the number of candidate minerals. Spectral feature fitting helps to automatically identify closely matching minerals based on a continuum-removed (background absorption-removed) least squares fitting of reference spectra to the spectrum of interest (Clark et al., 1990). Modelling and removing the continuum enhances the appearance of the often subtly expressed diagnostic absorption features. Subsequently, a manual visual comparison of the remaining spectra was undertaken in order to identify the most likely candidate mineral.

The ENVI CAT v7.2.1 tool for map-projecting CRISM spectral cubes was used to export processed CRISM images and CRISM summary parameter maps to ArcGIS for integration with other high-resolution imagery (e.g. CTX, HiRISE), to provide additional context.

2.4 Ancillary Data

High-resolution imagery and topographical data provides geological and geomorphological context for the mineral detections. Accordingly, data acquired by HiRISE, CTX and MOLA were utilised for this purpose; with comparisons made to mineral detections in CRISM data.

2.4.1 HiRISE and CTX

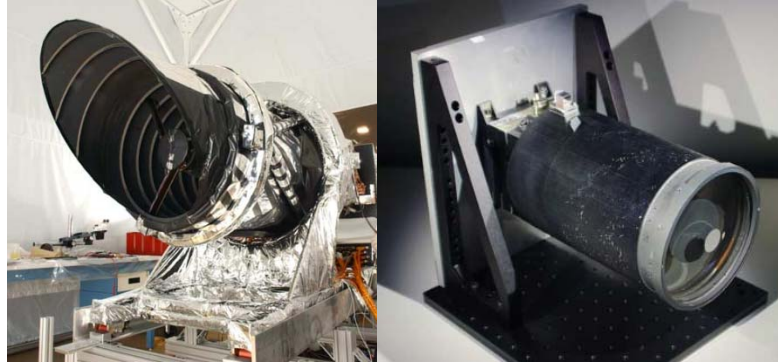


Figure 2.8. Left: HiRISE instrument inside clean room (McEwen et al., 2007). Right: CTX instrument on supporting bracket (Malin et al., 2007).

The HiRISE instrument is capable of acquiring 0.3 m/pixel images at 300 km altitude. It is of a mirror telescope design featuring a 0.5 m diameter primary mirror with an effective focal length of 12 m, focusing on to an array of 14 CCD detectors (McEwen et al., 2007).

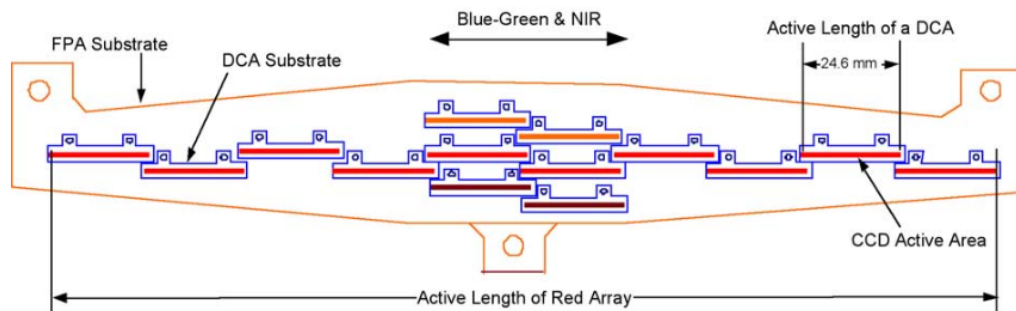


Figure 2.9. HiRISE CCD layout on the focal plane array (FPA), with each detector chip assembly (DCA) outlined (McEwen et al., 2007).

As shown in figure 2.9, 10 of these 14 detectors image in the red region (570–830 nm), 2 detectors image in the blue-green region (~400–580 nm) and 2 detectors image in the NIR region (~790–1100 nm). Each CCD detector is 2048×128 pixels. Configured for long-track integration, HiRISE provides swath widths of 6 km and 1.2 km with the RED and ‘colour’ CCDs. The signal-to-noise ratio (SNR) for the RED channel varies from 90:1 to

250:1, which is the result of time delay integration (TDI) (McEwen et al., 2007). TDI is the process of imaging the same piece of ground multiple times (up to 128 times with HiRISE) and summing the resultant signal to increase SNR (Bergstrom et al., 2004).

CTX uses a 350 mm Schmidt-type telescope with $f/3.25$ catadioptric optics to achieve a 5.7° field of view to acquire 6 m/pixel images, ~ 30 km wide and ≥ 40 km long, at 300 km altitude (Malin et al., 2007). A colour filter band pass of 500–700 nm is used to reduce the loss of detector modulation transfer function from diffusion at the red end of the visible spectrum and the effects of atmospheric scatter at the blue end of the visible spectrum. The detector is a Kodak 5000-element CCD that has 7 μm pixels and an average quantum efficiency (QE) of $>60\%$. This QE, combined with $f/3.25$ optics, provides a typical SNR of $>100:1$, with a worst case of 40:1 (Malin et al., 2007). CTX provides high-resolution imagery of the surface of Mars that can be used as geological and geomorphological context for other MRO observations (CRISM, HiRISE and SHARAD).

CTX and HiRISE imagery was obtained in JPEG2000 format and manipulated in the ArcGIS software. Tie-points were used, when needed, to correctly georeference lower-resolution datasets to equivalent- or higher-resolution datasets, and to mosaic HiRISE images, with a transparent background value set to clear null data in the frame. Occasionally, ENVI was used with HiRISE images to scale, crop and manipulate greyscale stretches.

Both CTX and HiRISE imagery is regularly used to create digital terrain models (DTMs). HiRISE Digital Terrain Models (DTMs) are available from the HiRISE website, when already produced, but when not available they can be produced from a HiRISE stereo image pair using BAE Systems SOCET SET and the Integrated Software for Imagers and Spectrometers (ISIS) program.

2.4.2 MOLA

Topographic data from the Mars Orbiter Laser Altimeter (MOLA) instrument, on-board Mars Global Surveyor, was acquired from September 1999 until June 2001, when the instrument failed (Smith et al., 2003). Launched in 1996, MGS achieved a sun-synchronous, near-polar orbit with a 378 km average altitude about Mars in 1997 and operated successfully until 2006 (Albee et al., 2001; NASA, 2007).

The MOLA instrument utilised 8 ns laser pulses at a rate of 10 Hz, directed nadir, and two-way pulse travel time between the instrument and the surface of Mars to deduce

altimeter data. MOLA operated successfully with a vertical accuracy of 1 m and along-track shot spacing of 300 m with spot size of 168 m with a range resolution of 37.5 cm, at 400 km orbital altitude. The resultant altimeter spot dataset covered the surface of Mars between $\pm 87^\circ$ latitude (Smith et al., 2001). The MOLA dataset has been interpolated to produce a topographic map (digital elevation model) of Mars with a spatial resolution of 128 pixels per degree (Smith et al., 2003). Due to high point spacing and size relative to surface geologic features (e.g., small craters, knobs and faults) smoothing and interpolation errors exist within the MOLA dataset.

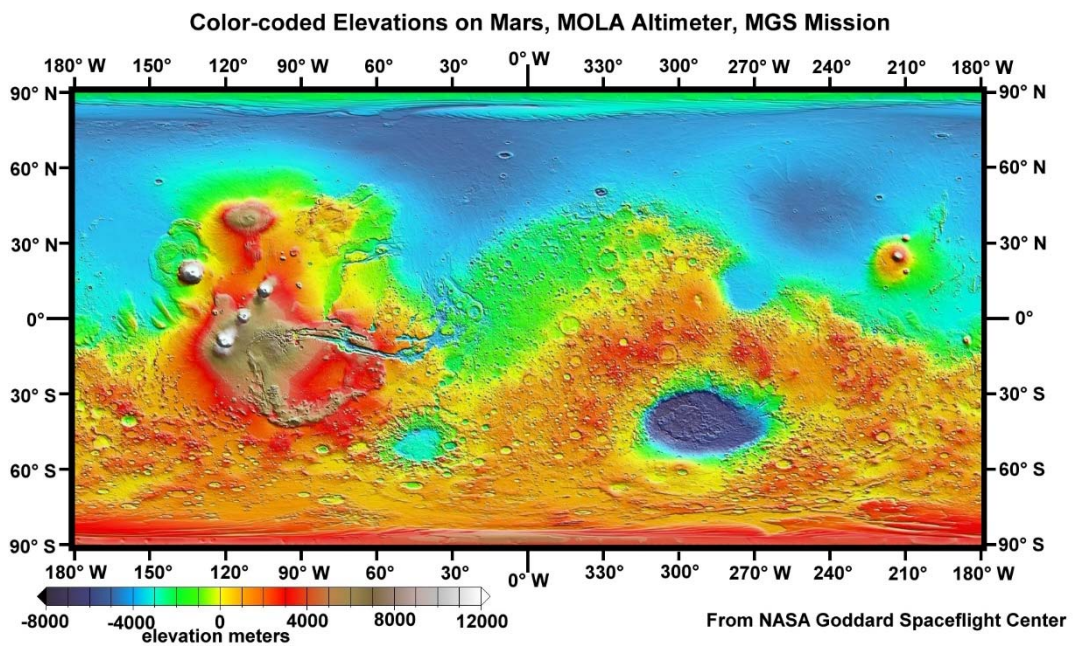


Figure 2.10. Colourised and shaded MOLA map of Mars (USGS, 2003).

MOLA measurements have resulted in the first global elevation model of Mars (figure 2.10), becoming the basis of countless studies of Mars. It has become a reference for other datasets, including higher resolution CTX and HiRISE digital terrain models. The MOLA elevation and point datasets were used to compute slope maps using the Slope tool within ArcGIS Spatial Analyst toolbox.

3. Theory and Application of X-ray Diffraction for Mineral Identification

The use of X-rays to study a crystal structure was first carried out in 1912 by German physicist Max von Laue, who reasoned that if crystals were composed of regularly spaced atoms, then electromagnetic waves with wavelengths approximately equal to the atomic spacing in a crystal would be diffracted by such crystals (Laue, 1952a, 1952b). Walter Friedrich and Paul Knipping tested this hypothesis experimentally under the supervision of von Laue; a copper sulphate crystal was placed in the path of a narrow polychromatic X-ray beam with a photographic plate arranged to record diffracted X-rays. Upon the second attempt, when the photographic plate was placed behind the copper sulphate crystal with respect to the incident X-ray beam, a pattern of spots was recorded on the photographic plate, proving that crystals diffract X-rays (Friedrich and Knipping, 1952). Not only did this transmission method prove the periodic arrangement of atoms within a crystal but it also proved the wave nature of X-rays (Eckert, 2012).

W. L. Bragg analysed the experimental works of von Laue, Friedrich and Knipping to deduce the mathematical relation required for X-ray diffraction (XRD), known as Bragg's Law:

$$n\lambda = 2d \sin \theta \quad (3.1)$$

where n denotes the order of diffraction, λ the wavelength of the electromagnetic radiation (the X-rays), d the interplanar spacing and θ the angle of the incident and diffracted electromagnetic radiation to the crystal planes (Bragg, 1913). The application of Bragg's Law enables the analysis and quantification of crystal structures, therefore enabling the identification of minerals.

The original Laue method is carried out in modern day XRD, along with an alternative method of XRD that tends to subject a powdered sample to a monochromatic X-ray source and record the diffracted X-rays in a 2θ range using a simple counting-based detector. This technique, known as the powder method, requires the exposed sample surface to be flat with sub-millimetre accuracy. For the majority of samples where this not the case (e.g. geologic samples), a process of sample preparation is adopted where the sample is reduced to a fine powder and then presented to the instrument with a uniformly flat surface with sub-millimetre accuracy (Cullity and Stock, 2001). These requirements have led XRD to be mainly adopted as a laboratory-based technique,

however despite sample preparation requirements, XRD instruments such as Lunar XRD (Blake, 2000), Mars-XRD (Hill et al., 2011; Marinangeli et al., 2007, 2011) and Chemistry and Mineralogy (CheMin) XRD instrument on the NASA Mars Science Laboratory (MSL) rover (Blake et al., 2012) have previously been developed for space missions. Although only the CheMin instrument on-board MSL has been flown. Measurements taken by CheMin help to provide a ground-truth to remote sensing observations with instruments like CRISM, as discussed in Chapter 2. Remote sensing data provided by CRISM also aids to guide surface exploration and subsequent measurements by CheMin (Milliken et al., 2010; Thomson et al., 2011; Vaniman et al., 2014).

In this chapter the theory of XRD is explained along with a novel back-reflection energy-dispersive X-ray diffraction method that has been utilised, explored and tested extensively in this thesis.

3.1 Derivation of Bragg's Law and Summary of Crystal Structures

Consider two X-ray waves incident at angle θ on two layers of atoms separated by a distance d , as shown in figure 3.1.

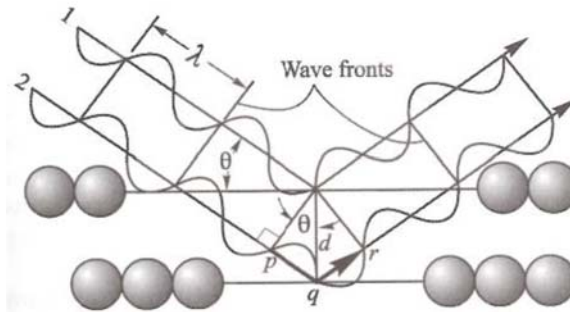


Figure 3.1. Illustration of Bragg's Law (Nesse, 2011).

As shown in figure 3.1, for constructive interference to occur the X-rays elastically scattered by the crystal atoms must be in-phase. Hence, for waves 1 and 2 to be in-phase post-scattering, the following criterion must be met:

$$\overline{pqr} = n\lambda \quad (3.2)$$

where n is an integer number of λ wavelengths and \overline{pqr} is the path of a scattered X-ray illustrated in figure 3.1. Using trigonometry the following relation can be deduced:

$$\overline{pq} = \overline{qr} = d \sin \theta \quad (3.3)$$

$$\overline{pqr} = 2\overline{pq} = 2d \sin \theta \quad (3.4)$$

Substituting for \overline{pqr} in equations 3.2 and 3.4, Bragg's Law can be deduced:

$$n\lambda = 2d \sin \theta \quad (3.5)$$

This can be re-written as

$$\lambda = 2 \frac{d}{n} \sin \theta \quad (3.6)$$

resulting in the interpretation that as the coefficient of λ is at unity, any reflection can be considered a first-order ($n = 1$) reflection with a revised plane spacing of d/n . This gives the simplified Bragg equation:

$$\lambda = 2d \sin \theta. \quad (3.7)$$

Considering that $\sin \theta$ cannot exceed unity, it can be concluded that the condition for diffraction at any angle 2θ is $\lambda < 2d$ (Cullity and Stock, 2001). Bragg's law mathematically illustrates how the known direction (θ) and wavelength (λ) of a radiation source can be used to probe a crystal structure, and hence the application of Bragg's Law enables the determination of the d -spacings of a crystal structure.

To understand the d -spacings of a crystal structure it is important to realise what a crystal is: a periodic distribution of atoms, molecules or ions. In a pure, well ordered, crystal, the external faces are representative of the internal symmetry and the physical properties are influenced by the symmetry. The crystal structure can be considered to comprise a lattice and a motif. The crystal lattice is an array of repeating points of identical environment, and the unit cell of a crystal lattice is defined as the smallest repeating parallelogram, drawn from lattice point to lattice point, which is representative of the symmetry of the lattice. The crystal motif (also known as the basis) is the assortment of atoms, molecules or ions that are found within the unit cell, and are translated to all the lattice points, hence representing the crystal (Tanner, 1995). Atoms comprise of a nucleus of protons and neutrons, with one or more electrons orbiting at defined energy levels. An electron hole (also commonly termed 'hole') is an electron vacancy that has a positive charge. By the nearly free electron model, when subjected to an electric field (i.e. a periodic lattice potential), electrons with a negative effective mass are accelerated in the opposite direction to the applied field and therefore appear

positively charged. These holes can move through the lattice by effectively interchanging their position with an electron (Tanner, 1995).

In the 19th century a French crystallographer, Bravais, investigated all possible lattice configurations and concluded that there are 7 possible crystal systems, and up to 14 possible lattice configurations. Representative geometric diagrams of these systems are shown in figure 3.2 and their properties are detailed in table 3.1 (Cullity and Stock, 2001).

The planes of the crystal are described by the Miller indices (hkl) which are based on the vectors of a 3D lattice: \mathbf{a} , \mathbf{b} and \mathbf{c} ; where \mathbf{a} is divided into h parts, \mathbf{b} is divided into k parts and \mathbf{c} is divided into l parts. The d -spacing between the crystal planes is related to the Miller indices by the equation:

$$\frac{1}{d^2} = \frac{\frac{h^2}{a^2} \sin^2 \alpha + \frac{k^2}{b^2} \sin^2 \beta + \frac{l^2}{c^2} \sin^2 \gamma + \frac{2hk}{ab} (\cos \alpha \cos \beta - \cos \gamma) + \frac{2kl}{bc} (\cos \beta \cos \gamma - \cos \alpha) + \frac{2hl}{ca} (\cos \gamma \cos \alpha - \cos \beta)}{1 - \cos^2 \alpha - \cos^2 \beta - \cos^2 \gamma + 2 \cos \alpha \cos \beta \cos \gamma} \quad (3.8)$$

which can be simplified for each crystal system outlined in table 3.1 (Girolami, 2016).

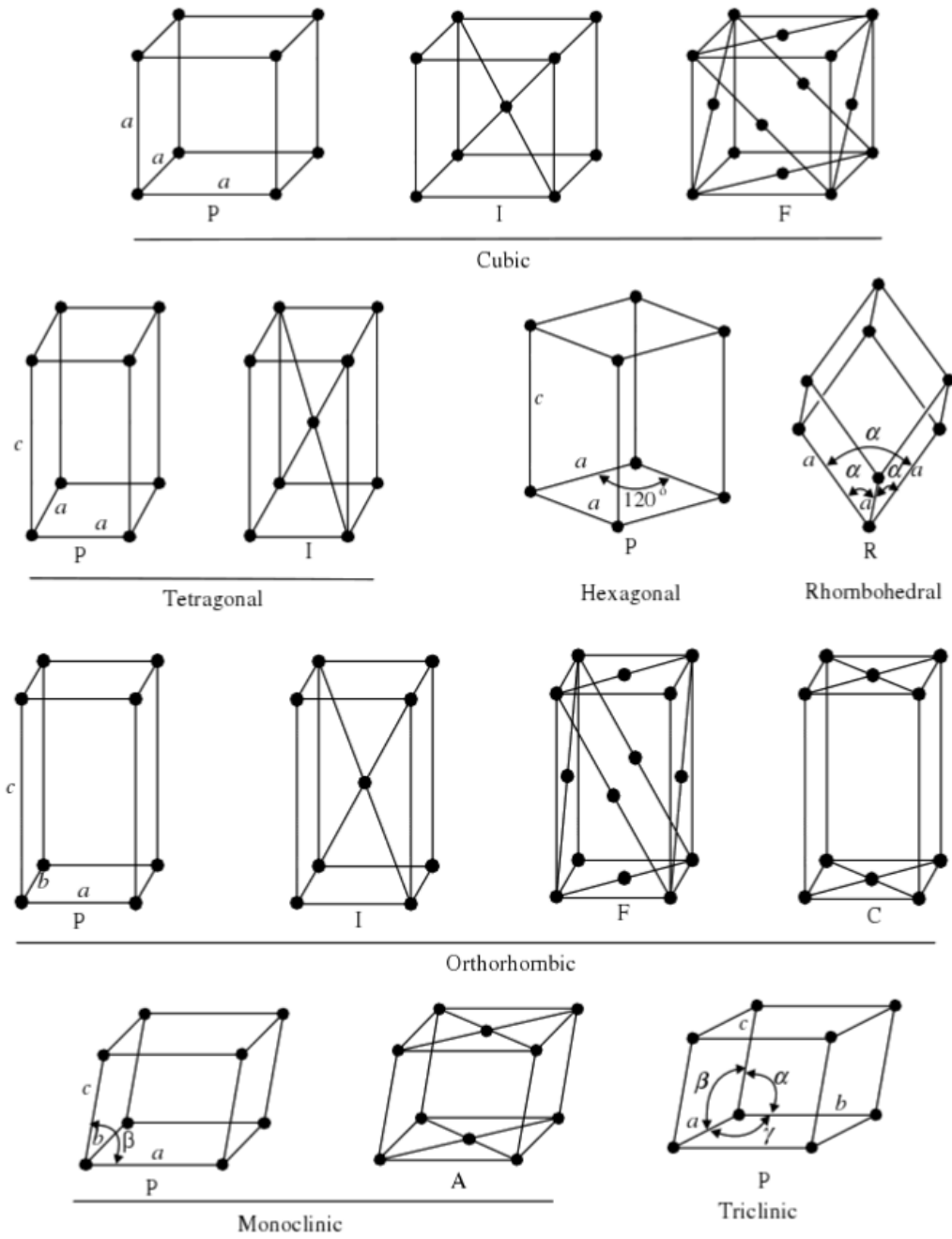


Figure 3.2. Geometric projections of the unit cells for each of the 14 possible Bravais lattices (Cullity and Stock, 2001).

Table 3.1. The 14 possible Bravais lattices and their geometric properties.

Crystal System	Unit Cell ^a	Bravais Lattice	Lattice Symbol ^b
Cubic	$\alpha = \beta = \gamma = 90^\circ$	Simple	P
	$a = b = c$	Body-centred	I
		Face-centred	F
Tetragonal	$\alpha = \beta = \gamma = 90^\circ$	Simple	P
	$a = b \neq c$	Body-centred	I
Hexagonal	$\alpha = \beta = 90^\circ$	Simple	P
	$\gamma = 120^\circ$		
	$a = b \neq c$		
Rhombohedral (trigonal)	$\alpha = \beta = \gamma \neq 90^\circ$	Simple	R
	$a = b = c$		
Orthorhombic	$\alpha = \beta = \gamma = 90^\circ$	Simple	P
	$a \neq b \neq c$	Body-centred	I
		Base-centred	C
		Face-centred	F
Monoclinic	$\alpha = \gamma = 90^\circ$	Simple	P
	$\beta \neq 90^\circ$	Base-centred	C
	$a \neq b \neq c$		
Triclinic	$\alpha \neq \beta \neq \gamma \neq 90^\circ$	Simple	P
	$a \neq b \neq c$		

^aThe unit cells are described by a , b and c dimensions along the 3-dimensional (x , y and z) crystal axes, and the angles between them are described by α , β and γ . ^bSimple, primitive unit cells are given P or R lattice symbols, whereas other, non-primitive unit cells are given other lattice symbols (Cullity and Stock, 2001). See figure 3.2 for geometric diagrams of each Bravais lattice.

3.2 Angle-Dispersive X-ray Diffraction

In angle-dispersive X-ray diffraction (ADXRD), a monochromatic X-ray source is used to probe a crystalline sample over a range of angles to determine the crystal structure. This can be undertaken using various methodologies including rotating-crystal, transmission, parallel-beam and powder methods (Cullity and Stock, 2001; He, 2011; Girolami, 2016).

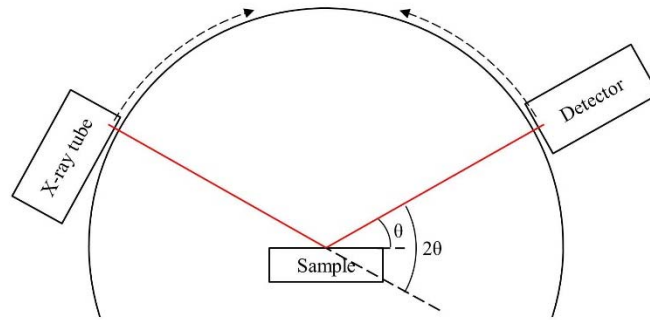


Figure 3.3. Angle-dispersive X-ray powder diffraction using a goniometer where the X-ray tube and detector move together, at equal rates, in the direction of increasing θ .

In powder ADXRD, a packed-powder sample is typically subjected to a monochromatic X-ray source through a range of 2θ angles (e.g. $2\theta = 5 - 90^\circ$) with a counting-based detector, as illustrated in figure 3.3. This is often undertaken using a Bragg-Brentano diffractometer, where the sample and detector are rotated together by θ and 2θ respectively, with respect to a static monochromatic X-ray source. The divergence of the sample-incident X-ray beam is controlled by use of divergence and Soller slits, which consequently carve the incident X-ray beam into a series of triangles that illuminate the sample in the plane of diffraction. The diffracted beam is also divergence controlled, with receiving and Soller slits being positioned prior to detector incidence (Cullity and Stock, 2001). The use of these slits results in greater peak resolution, but lower diffraction peak intensity; however, this can be mitigated by increasing X-ray exposure time. This technique produces a plot (e.g. figure 3.4) of the diffracted X-ray intensity against the 2θ angle for a crystalline sample.

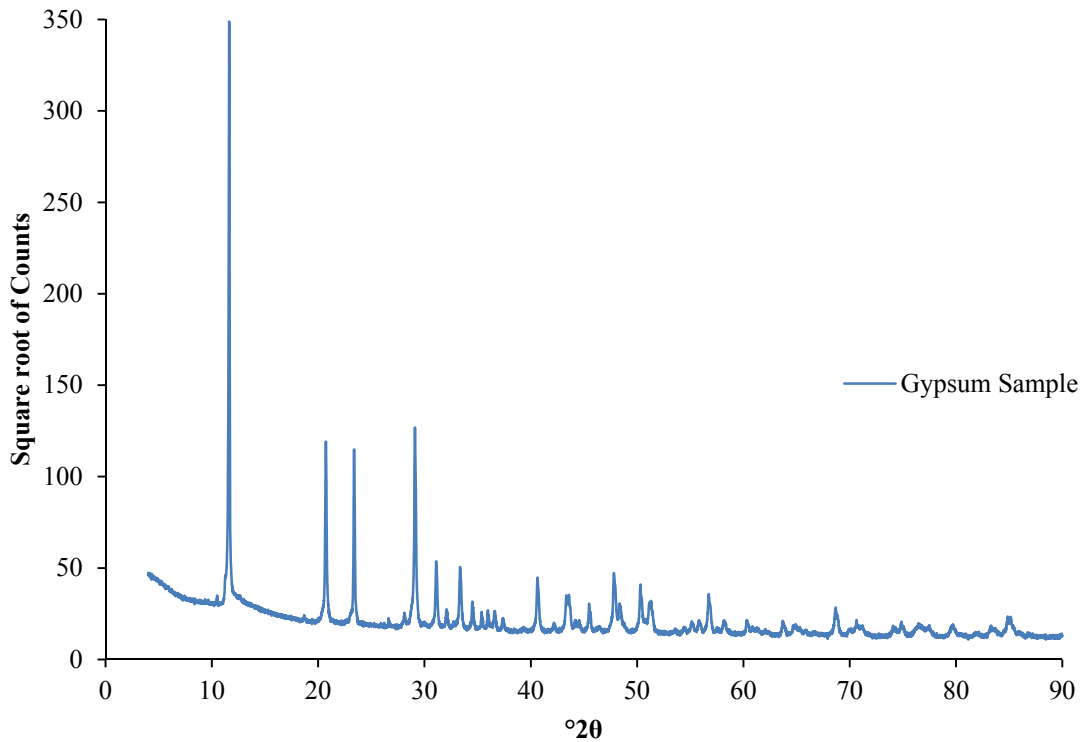


Figure 3.4. Example powder diffraction plot of square root of detector counts against 2θ for a gypsum sample. Data was acquired using a Bruker D8 Advance laboratory instrument in the Geology Department at the University of Leicester. This is discussed in Chapter 5.

For the powder method, the sample is crushed into a fine powder and packed into a sample holder with a uniformly flat surface, with the aim to ensure sufficiently small crystallite (fine-powder particle) sizes and to randomly orientate each particle of the powder. For highly crystalline samples, the large number of randomly orientated crystallites exposed to the incident X-ray beam produces a continuous ‘cone’ of diffraction from the sample (known as the Debye-Scherrer cone), and therefore results in accurate representative peak intensities (Girolami, 2016). Poor-powder averaging, caused primarily by large crystallite sizes, produce incomplete “spotty” Debye-Scherrer cones because of the lack of crystallites in the correct orientations to diffract into all points around the Debye-Scherrer cone (Cullity and Stock, 2001).

The constituents of a sample are identified by comparing the diffraction peak position and intensity in the 2θ plot (e.g. figure 3.4) with known crystalline materials from a powder XRD database. This process of peak identification is completed once all (or the majority) of the diffraction peaks are identified. Issues arise with peak identification when multiple minerals could explain a single peak. This suggests peak overlap is present, whereby a single peak in the diffraction data is masking one or more

diffraction peaks that occur at the same position. Ideally, diffraction peak intensity can give information about abundances of crystalline material, but this can be obscured due to preferred orientation and grain size (Girolami, 2016).

Preferred orientation of crystallites occurs in the powder-packed samples where crystallites fit-together in a non-random fashion. This is especially prevalent with plate and needle shaped crystals, and results in the preferential exposure of certain lattice planes causing enhancement of the respective diffraction peaks (Girolami, 2016). This enhancement is caused by non-uniform Debye-Scherrer cones caused by the orientation of the crystallites that alter the intensity distribution of diffraction around the cone. Analysis of the enhancement of diffraction peaks caused by preferred orientation can be undertaken to determine the degree of preferred orientation along the preferred (*hkl*) plane within the incident X-ray beam illuminated area of a sample (Cullity and Stock, 2001). It is important to realise that whilst preferred orientation will cause enhancement of the directly affected diffraction peaks, other diffraction peaks will be reduced in intensity.

In this thesis, preferred orientation of crystallites was accounted for in XRD sample analysis by use of the March-Dollase function. The March-Dollase function corrects all diffracted X-ray intensities for axially symmetric flat- or needle-like crystallites that are preferentially aligned along a specific (*hkl*) plane by use of the March coefficient, *r*, in the pole-figure profile formulation $(r^2 \cos^2 \alpha + r^{-1} \sin^2 \alpha)^{-3/2}$ where α is the angle between the diffracting plane and the specified (*hkl*) preferred orientation plane. A March coefficient, *r*, with a value of 1 indicates random orientation of crystallites, an *r* value of <1 indicates that the specified planes are preferentially orientated parallel to the sample surface and an *r* value of >1 indicates that the specified planes are preferentially orientated perpendicular to the sample surface (Dollase, 1986). In general, this translates to flat-like and needle-like crystallites depending on how the preferred orientation was formed.

Sample grain size needs to be considered when analysing resultant powder XRD spectra. Large sample grain sizes result in anomalously high or low diffraction peak intensities due to poor powder averaging; fewer crystallites contribute to each diffraction peak. Depending on instrument characteristics, larger crystallites may also contribute to narrower diffraction peaks. Nominal grain sizes in the micron range tend to give good powder averaging resulting in representative diffraction peak intensities. Increased diffraction peak broadening occurs with smaller grain size due to incomplete constructive interference, with the limit of zero grain size (i.e. a non-crystalline, amorphous material)

resulting in background “hump” in the resultant XRD plot. This relationship is mathematically illustrated by the Scherrer equation:

$$t = \frac{k\lambda}{B \cos \theta} \quad (3.9)$$

where

$$B^2 = W_{\text{sample}}^2 - W_{\text{standard}}^2 \quad (3.10)$$

In the Scherrer equation (3.9) t is the grain diameter, k the “shape factor” (between 0.8 and 1.2), λ the incident wavelength, θ the Bragg angle of the peak and B is the peak broadening, in radians. B is given by equation 3.10, where W_{sample} and W_{standard} are the full width half maximums of the diffraction peak in the sample and reference spectra, respectively (Girolami, 2016).

Other methods of ADXRD include the rotating-crystal and the parallel beam methods. The rotating-crystal XRD method uses a monochromatic X-ray source and a 3- or 4- circle goniometer to measure the diffraction of X-rays of a single-crystal sample 50–250 μm in size in four angles enabling a detailed analysis of a sample crystal structure (Cullity and Stock, 2001). Parallel beam XRD uses a goniometer-type setup, where the divergent X-ray beam is transformed into a parallel beam by use of a parabolic Göbel mirror prior to sample incidence. Soller slits covering an area equal to the effective area of the detector are positioned in front of the detector (in the path of the detector-incident X-rays) to control beam divergence. As a result this technique is largely insensitive to sample surface roughness, and is utilised as a powder XRD technique (Cullity and Stock, 2001; He, 2011). A detailed explanation of the Laue, rotating-crystal and parallel-beam XRD methods is beyond the scope of this thesis, as none of these techniques has been utilised.

3.3 Energy-Dispersive X-ray Diffraction

Following the invention of energy-resolving solid-state detectors in the 1960s, an energy-dispersive approach to XRD was developed (Giessen and Gordon, 1968; Buras et al., 1968). This approach uses a fixed geometry and a broadband X-ray source, thus by the Planck-Einstein relation

$$E = \frac{hc}{\lambda} \quad (3.11)$$

Bragg’s Law (equation 3.7) becomes

$$Ed \sin \theta = \frac{hc}{2}, \quad (3.12)$$

which can be simplified to

$$Ed \sin \theta = 6.199 \text{ keV } \text{Å}. \quad (3.13)$$

Solid-state detectors, such as a charge-coupled device (CCD) or silicon drift detector (SDD), record the diffracted X-rays at a fixed scattering angle, resulting in a plot of diffracted X-ray energy against counts.

Typically small scattering angles ($\theta < 10^\circ$) are used with high energy X-rays of 10–150 keV to detect d -spacings of the order 0.2–3.6 Å. Advantageously, this energy range results in minimal overlap of the diffraction and fluorescence peaks as well as sample penetration, resulting in applications such as drug identification and residual stress measurements (Cook et al., 2009; Kämpfe et al., 2005). Applications of energy-dispersive XRD (EDXRD) at larger scattering values include examination of cultural heritage artefacts (Mendoza Cuevas et al., 2015).

The three main advantages of EDXRD compared to ADXRD are: (1) the fixed geometry allows simple implementation; (2) the simultaneous collection of the entire diffraction pattern; (3) lower exposure times due to the simultaneous collection of the entire diffraction pattern. The main disadvantages of EDXRD with respect to ADXRD are: (1) the peak widths are typically an order of magnitude larger; (2) the overlap of X-ray fluorescence peaks can obscure diffraction peaks; (3) quantitative analysis is hindered by the non-uniformity of the source radiation (Cullity and Stock, 2001; Hansford, 2011a). Owing to these disadvantages, ADXRD is still the definitive XRD method, although in certain applications EDXRD is more suitable. For instance, the collection of the entire diffraction pattern resulting in lower exposure times enables rapid identification for on-stream applications in industrial mineral process streams (O'Dwyer and Tickner, 2008).

3.4 Detector Technology

The key to non-synchrotron based EDXRD is the invention of energy-resolving solid-state detectors. Two types of solid-state detectors are commonly used in XRD; the CCD and the SDD.

CCDs are used in both the ADXRD and EDXRD techniques. The solid-state detector design can be considered to be a 2-dimensional array of capacitors referred to as 'pixels', each measuring the energy of incoming photons by collection of charge. This imaging design is capable of measuring incoming photon intensity over an angular range

(ADXRD) such as in CheMin (Blake et al., 2012) and MarsXRD (Hill et al., 2011; Marinangeli et al., 2007, 2011), but is also capable of measuring photon energy over the same range (EDXRD and XRF) as utilised in part of this thesis. Cooling of CCDs during operation is required to minimise the thermo-generated electron contribution to background noise, known as dark current. Typically CCDs are cooled to temperatures in the region of $-90\text{ }^{\circ}\text{C}$ to reduce this effect (Smith et al., 2004).

SDDs are commonly used in EDXRD and X-ray fluorescence. Their design differs to that of CCDs in that instead of having an imaging type detector with multiple ‘pixels’, only one ‘pixel’ exists for the area carved out by the detector. The SDD working principle uses an initially charge-depleted high-resistive silicon layer that is subject to radiation, creating charge clouds of electron-hole pairs that are then separated by a parallel electric field, causing electrons to drift towards an anode and the holes being collected by the electrodes (Gatti and Rehak, 1984). The silicon layer, an n-type semiconductor, is depleted by applying a negative voltage to p^+ field rings (Lechner et al., 1996). Figure 3.5 illustrates the working principle of the SDD.

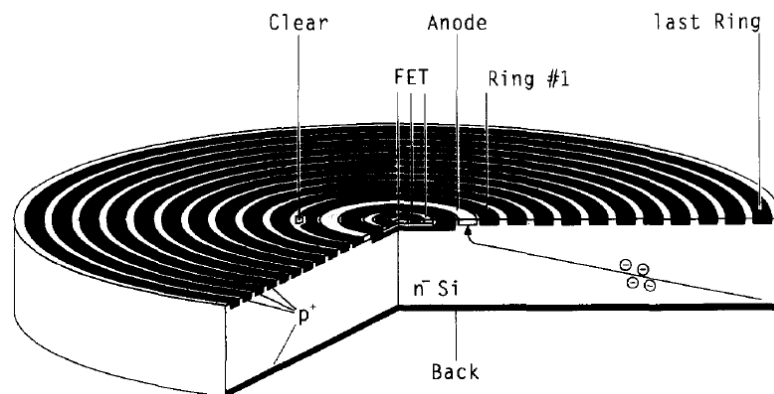


Figure 3.5. Cylindrical silicon drift detector cross section showing the drift of electrons to an anode ring by influence of the p^+ field rings. The annotated ‘Back’ is exposed to incoming radiation. The field-effect transistor (FET) is also labelled (Lechner et al., 1996).

In SDDs the anode capacitance is extremely small, resulting in a low equivalent noise level enabling higher count rates. Integrating part of the amplifying electronics, the front-end transistor (FET), onto the detector takes advantage of the low anode capacitance and minimises the stray capacitance of the interconnection detector-amplifier. In the case of the setup later outlined in section 3.5.2, signal electrons are discharged from the anode in voltage pulses resulting in detector dead-time. Due to the construction and low noise

characteristics of SDDs, only moderate Peltier cooling to approximately $-20\text{ }^{\circ}\text{C}$ is required to mitigate the effects of thermally generated electrons (Lechner et al., 1996).

In comparison to CCDs, SDDs are advantageous in returning a higher spectral resolution, higher count rate and having less demanding cooling requirements. Nevertheless, CCDs can be advantageous in terms of acquiring imaging XRD data over an angular range. This can be useful in distinguishing diffraction peaks from fluorescence peaks in EDXRD without having to alter the sample-detector geometry, but also enables ADXRD without a goniometer-type instrument design (e.g. CheMin on MSL (Blake et al., 2012)).

3.5 Generation of X-rays and X-ray Fluorescence

X-rays are often generated through use of an X-ray tube, in which electrons are produced by thermionic emission from a filament and are accelerated towards an anode by a high voltage potential between the cathode (the filament) and anode. Bremsstrahlung X-rays are then generated by rapid deceleration of the electrons caused by interaction with the nuclei of the anode material (Cullity and Stock, 2001). Figure 3.6 shows an example of Bremsstrahlung radiation produced by an X-ray tube with a molybdenum anode.

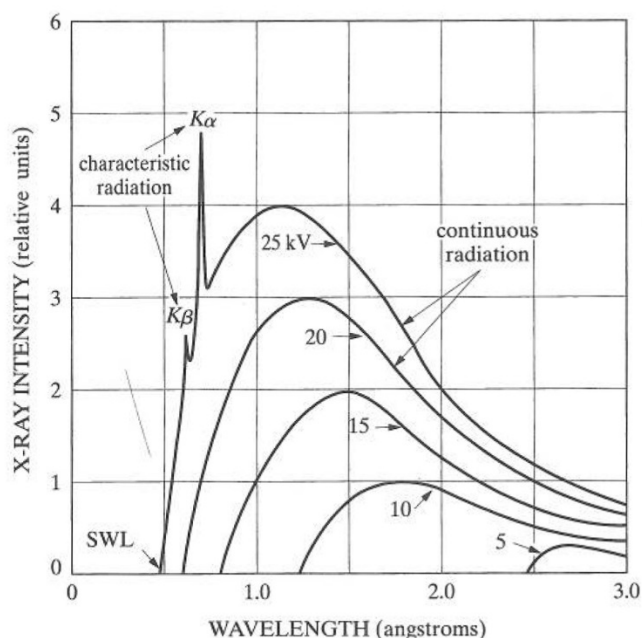


Figure 3.6. X-ray spectra of molybdenum as a function of applied X-ray tube voltages: 5, 10, 15, 20 and 25 keV (as annotated). Figure illustrates how featureless spectra, known as continuous radiation, change with the inclusion of molybdenum characteristic radiation at energies greater than the associated K-edge. Figure also illustrates the change in the short-wavelength limit (SWL) (Cullity and Stock, 2001).

As shown in figure 3.6, X-ray intensity is zero up to a wavelength known as the short-wavelength limit (SWL), after which the intensity rapidly increases to maximum and gradually decreases. Considering the electrons that transfer their energy in one collision (i.e. $eV = h\nu$), the minimum X-ray energy E_{min} is given by

$$E_{min} = eV \quad (3.14)$$

where e is the elementary charge and V is the X-ray tube voltage. Hence, the short-wavelength limit can be determined using the Planck-Einstein relation:

$$\lambda_{SWL} = \frac{hc}{eV} = \frac{1.24 \times 10^4}{V} \text{ \AA}. \quad (3.15)$$

The produced featureless X-ray spectrum is known as the continuous spectrum up until the electrons have sufficient energy to cause X-ray fluorescence of the anode. This is known as characteristic emission as the fluorescence exhibited is characteristic of the anode material, as shown in figure 3.6.

X-ray fluorescence (XRF) occurs when an incoming highly energetic charged particle (such as an X-ray photon or electron) is of sufficient energy to eject an electron from the orbital shells of an atom. This results in a higher energy electron being transferred to the lower energy level and a photon being emitted at an energy equivalent to the transition. For example, an atom is considered to consist of a nucleus surrounded by K, L and M shells of electrons so a vacancy in the K shell may be filled from either the L or M shell (figure 3.7).

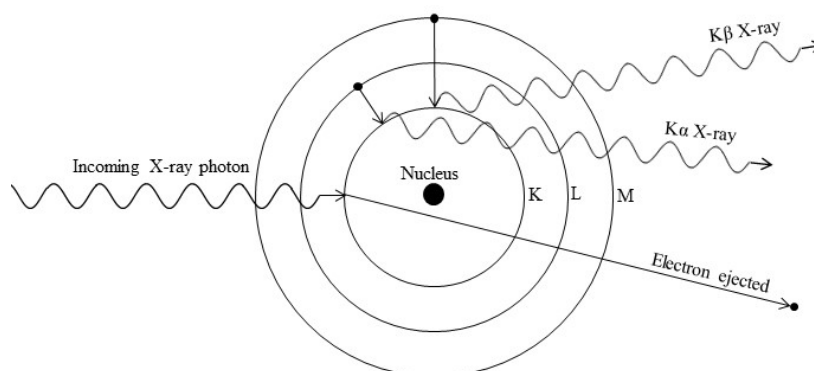


Figure 3.7. X-ray fluorescence diagram of $K\alpha$ and $K\beta$ fluorescence.

In figure 3.7, an incoming X-ray photon exceeds the binding energy of a K shell electron, causing it to be ejected. The K shell vacancy is filled by either an L or M shell

electron transition that produces respective $K\alpha$ or $K\beta$ X-ray fluorescence. Similarly, an electron ejected from the L shell and its vacancy being filled from the M or the N shell causes respective $L\alpha$ or $L\beta$ emission. Shells K, L, M and N correspond to principle quantum numbers ($n =$) 1, 2, 3, 4 etc. Each shell has multiple sub-shells defined by the angular (l), magnetic (m) and spin (s) quantum numbers, with values 0 to $n - 1$, $\pm l$ and $\pm \frac{1}{2}$, respectively. The total moment J is the vector sum $l + s$. By the Pauli Exclusion Principle, no two electrons within an atom can have the same set of quantum numbers, hence the shell/energy level structure. X-ray emission (and hence energy transitions) are governed by the selection rules: $\Delta n \geq 1$, $\Delta l = \pm 1$ and $\Delta J = 0, \pm 1$ (not $0 \leftrightarrow 0$) (Jenkins, 1999). Included here for completeness, the emitted X-ray photon energy is given by

$$\Delta E = Rhc(Z - \varepsilon)^2 \left(\frac{1}{n_1^2} - \frac{1}{n_2^2} \right) \quad (3.16)$$

where R is the Rydberg constant, Z is the atomic number of the element, ε is the shielding charge parameter and n_1 and n_2 are the principal quantum numbers of the shells.

3.6 Back-Reflection Energy-Dispersive X-ray Diffraction

A novel EDXRD technique was proposed and proved by Hansford (2011a; 2013). This technique utilises a back-reflection geometry that is largely insensitive to sample morphology, therefore extensive sample preparation like that used in the powder method is not required. The concept of this technique is described below.

Using the modified form of Bragg's Law, equation 3.13, at $2\theta = 180^\circ$ leads to the equation (Hansford, 2011a):

$$Ed = 6.199 \text{ keV } \text{\AA}. \quad (3.17)$$

An ADXRD instrument commonly scans through the range $2\theta = 5 - 90^\circ$ using $\text{Cu-}K\alpha$ radiation, corresponding to the d -spacing range 17.67–1.09 \AA , which in the back-reflection geometry corresponds to 0.35–5.7 keV. This energy range has a significant overlap with the K-shell fluorescence of common rock-forming elements: O, Na, Mg, Al, Si, K, Ca and Ti (Hansford, 2011a). Fluorescence peaks aid the identification of minerals present in a sample, but their overlap can mask the presence of diffraction peaks, hindering mineral identification. An experimental method of varying the X-ray source energy to suppress fluorescence of elements can reveal the underlying diffraction data,

hence this back-reflection geometry can be utilised to return the diffraction and fluorescence data of a sample for mineralogical analysis, as demonstrated in Chapter 5 and Hansford et al. (2014). Further characteristics of the back-reflection technique are highlighted here.

The density of reflections in the back-reflection geometry needs to be considered, due to the low resolution of EDXRD. As shown by equation 4 of Hansford (2011a) — which is based on equation 1 of Buchsteiner and Stüsser (2009) — the density of diffraction peaks per unit energy can be calculated using the equation:

$$D \simeq \frac{32\pi V}{h^3 c^3 M} E^2 \sin^3 \theta \quad (3.18)$$

where D is the density of reflections, V unit-cell volume and M is the number of lattice points per unit cell multiplied by the average multiplicity. In equation 3.18, h and c are Planck's constant and the speed of light, respectively. Equation 3.18 shows that the density of reflections is directly proportional to the square of the energy and peaks at the back-reflection geometry ($2\theta = 180^\circ$).

The resolution of the diffraction peaks in the back-reflection geometry also needs to be considered. This was done by Hansford (2011a), who related the energy resolution of a typical solid-state detector to the equivalent angular resolution in ADXRD by the equation:

$$\delta(2\theta) = \frac{2\delta E}{E_a \cos \theta} \quad (3.19)$$

In equation 3.19 $\delta(2\theta)$ is the angular peak width, E_a is the ADXRD X-ray energy at incidence angle θ . The energy peak width, δE , is given by

$$\delta E = 2.36W \sqrt{\frac{FE}{W} + r^2} \quad (3.20)$$

where W is the energy per electron-hole pair, r is the root-mean-square readout noise in electrons and F is the Fano factor. The Fano Factor is a material-dependant statistical adjustment factor required to relate the X-ray energy to the energy per electron-hole pair. Hansford (2011a) applied equations 3.19 and 3.20 to show how, in the back-reflection geometry, the peak resolution is not as competitive as laboratory ADXRD diffractometers that achieve a resolution of $0.1^\circ 2\theta$ or better in comparison (figure 3.8).

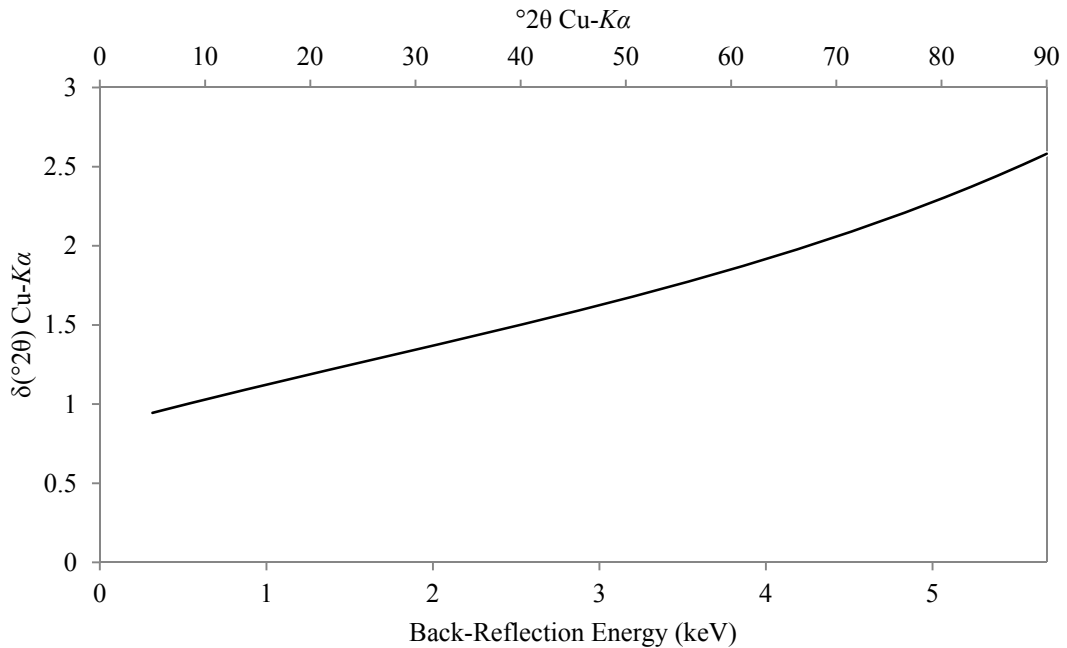


Figure 3.8. Resolution of the back-reflection method in terms of angular peak widths. A Fano factor of 0.11, energy per electron-hole pairing of 3.68 eV and root-mean-square readout noise of 6.9 electrons is assumed (Hansford, 2011a).

The back-reflection geometry enables almost the entirety of the power of the diffraction cones to be captured by the detector. This reduces the number of crystallites requiring illumination for representative diffraction peak intensities. When considering sample morphology (i.e. different parts of the sample being at different distances from the detector) it is important to realise that an incident X-ray beam is illuminating an area on the sample, and therefore a significant departure from planarity would affect resultant XRD spectra. However, the technique can be largely considered to be insensitive to sample morphology by ensuring a small X-ray spot size and illuminating a relatively flat area of a sample that results in only minor diffraction peak shifts (Hansford, 2011a). This technique is therefore favourable for the analysis of select unprepared samples (Hansford, 2013).

The energy of each diffraction peak has a weak dependence on 2θ at angles close to 180° and so primary beam angular divergence constraints can be relaxed for the back-reflection geometry (Hansford, 2011a). Due to detector resolution constraints resulting in relatively broad diffraction peaks, this statement largely holds true for EDXRD in general.

The use of low-energy X-rays with respect to their very weak penetrating power was discussed by Hansford (2011a), who highlighted that in the Earth's atmosphere the

transmission of 1 keV X-rays through 40 mm of air is negligible, this rising to 7.9 % for 2 keV X-rays (Henke et al., 1993). Therefore, measures need to be taken if an instrument based on the back-reflection technique is to be developed for terrestrial applications. One option being to flush the volume between the sample and detector with helium, which would give a 96% transmission of 1 keV X-rays for a path length of 40 mm. Under a Martian atmosphere, a path length of 40 mm for 1 keV X-rays gives 82% transmission. However, in both Earth and Mars applications the instrument would require windows to keep the X-ray tube and detector under vacuum because in an X-ray tube electrons are produced by thermionic emission: a process of heating a high voltage cathode under vacuum, giving electrons sufficient thermal energy to “evaporate” from the surface and escape. Hansford (2011a) suggested the use of 8 μm DuraBeryllium windows for this purpose, which give ~32% transmission at 1 keV rising to ~87% at 2 keV. For Mars based applications the use of two such windows and an X-ray path length of 40 mm resulted in a transmission of 8.4% at 1 keV, which increases rapidly towards higher energies. For application of the back-reflection technique on an air-less body, such as the Moon or an asteroid, no windows need to be incorporated into an instrument design and the full energy range can be accessed.

The back-reflection EDXRD technique was tested in two laboratory setups for this thesis: a pre-existing CCD facility and a bespoke SDD facility. These are outlined below.

3.6.1 Pre-existing CCD Facility

Initial experiments to demonstrate the back-reflection geometry were conducted using a pre-existing non-optimised setup (Hansford, 2013). The pre-existing CCD facility, pictured in figure 3.9, comprised of a vacuum chamber equipped with an X-ray tube source, sample holder and CCD.



Figure 3.9. Photographs of the pre-existing CCD facility showing where the X-ray beam enters the vacuum chamber, position of the CCD and the pellet sample holder with the ^{55}Fe source secured on the side.

Equipped with a Cu anode, the X-ray tube source had an electron incidence angle of 75° relative to the anode surface, along with a 15° X-ray take-off angle. A light baffle was placed between the X-ray tube and the main chamber to prevent light from the filament reaching the light-sensitive CCD within the vacuum chamber. To restrict the size of the X-ray spot size incident on the sample, a collimator of diameter 5 mm was used. As a result, the X-ray spot incident on the sample had a diameter of ~ 10 mm. An optical filter comprising of a $2\ \mu\text{m}$ polyamide film with $1\ \mu\text{m}$ Al coating was used. A diagram illustrating the setup is shown in figure 3.10. The distance between the sample and CCD was not as small as outlined by Hansford (2011a) (20mm), which, together with large source-sample distances, resulted in larger integration times of 3 hours.

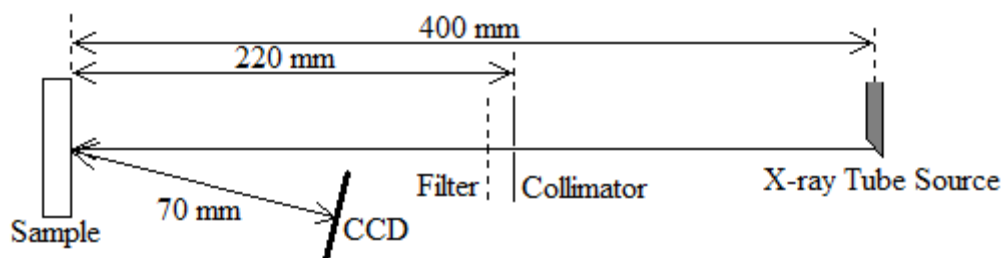


Figure 3.10. Diagram illustrating the pre-existing CCD setup of the X-ray Tube, Collimator, Filter, Sample and CCD. Diagram not to scale.

The CCD used was a CCD-22 manufactured by e2v, which has an imaging area of 600×600 pixels where each pixel is $40\ \mu\text{m} \times 40\ \mu\text{m}$ in size (Smith et al., 2004). The CCD itself was operated in frame-transfer mode. Both the CCD and sample were mounted on rotating arms within the vacuum chamber; this allowed not only various X-ray incident angles on the sample to be achieved but also various 2θ angles to be accessed. The exact back-reflection geometry could not be achieved because the CCD blocked the incident X-ray beam when $2\theta = 180^\circ$. Therefore the CCD was rotated so that it covered the 2θ range $148\text{--}168^\circ$. Only data taken from the top third of the CCD ($161\text{--}168^\circ$) was used for mineralogical analysis, this portion of the acquisition is sufficiently close to $2\theta = 180^\circ$ ensuring insensitivity to sample morphology (Hansford, 2013). Data processing was carried out using in-house developed software, and mineral identification was undertaken by the comparison of models produced by PoDFluX (Hansford, 2009).

3.6.2 Bespoke SDD Facility

The pre-existing CCD facility was not fully optimised for the back-reflection technique, so a bespoke back-reflection EDXRD setup was devised to explore the technique under conditions that may mirror the design characteristics of a back-reflection instrument, which may be deployed on a future planetary mission (i.e. shorter source-sample and sample-detector distances). This optimised setup consisted of a vacuum chamber, X-ray tube source, motorised sample stages, detector (collision) guard and SDD (figure 3.11). This setup differs to the non-optimised setup in that sample-detector distances are much smaller resulting in shorter acquisition times, and the back-reflection geometry was more closely achieved by use of an approximately annular Rocco2 SDD manufactured by PNSensor. The use of a SDD instead of a CCD is necessary to cope with the much higher count rates, but also offers enhanced energy resolution and only requires cooling to approximately -23 °C by use of a Peltier cooling system (as opposed to liquid nitrogen). The X-ray tube source was equipped with a Cu anode and mounted vertically, directing X-ray photons into the chamber. Although a collimator is mounted on the X-ray tube source, the sample-incident X-ray beam is limited by an additional 1.8 mm diameter collimator that was mounted into the central aperture of the SDD. A 2.5 µm filter of aluminised Lexan (approximately 0.5 µm Al and 2.0 µm polycarbonate (Lexan)) was positioned at the end of the X-ray tube. A light baffle was positioned between the X-ray tube and main chamber to prevent light from the filament from reaching the SDD within the vacuum chamber.

The motorised sample stages, manufactured by Zaber, enabled the sample to be remotely moved horizontally (i.e. in the x and y planes) and vertically (in the z plane) using control software on the laboratory PC, whilst the chamber was under vacuum. Vertically, the closest the sample-stage could be positioned was 18 mm below the SDD, and the furthest was 118 mm. Horizontally, the sample-stage could also be manoeuvred within a 50 mm range in both x and y planes. The manoeuvrable sample stages enable close sample-detector distances (~20 mm nominally) and, consequently, shorter acquisition times of the order of 20 minutes, as opposed to 3 hours with the non-optimised facility. An additional metal plate consisting of four pellet holders was constructed to enable the analysis of multiple samples during one session. The pellet recess for both the sample stage and metal plate was 3 mm, with each recess ~33 mm diameter. A detector (collision) guard was designed and deployed to prevent sample-detector collisions. Positioned below the SDD, between the detector and sample stage, the detector guard was

designed to cut power to the sample stage motors should it come into contact with a sample. The SDD comprised of four detector channels each operating within a software window, facilitating individual calibration and use of each detector channel. The use of 4 detector channels was useful in determining crystallite information of a sample: differences in peak intensities across the 4 channels would suggest incomplete Debye-Scherrer cones (i.e. spotty rings) due to large crystallite sizes.

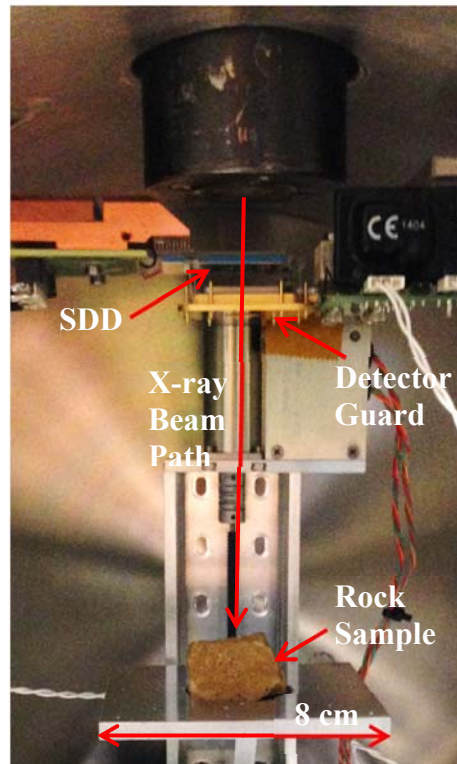


Figure 3.11. Photograph of the bespoke SDD back-reflection facility showing the direction of the X-ray beam, location of the sample stages with rock sample, detector (collision) guard and SDD. In the photograph the stages are set to the maximum distance from the detector. During data acquisition the sample was much closer to the detector.

3.7 High-Resolution Back-Reflection XRD at the Diamond Light Source

The Diamond Beamline B18 was used in this thesis for testing the back-reflection XRD technique in a high-resolution configuration. The Diamond Light Source located at the Harwell Science and Innovation Campus in Oxfordshire is the UK's national synchrotron science facility, funded by the Science and Technology Facilities Council and the Wellcome Trust. Supported by ~500 staff, over 7000 academic and industry researchers from a wide variety of disciplines use the 3 GeV Diamond synchrotron. To produce the 3 GeV electrons at Diamond, electrons are initially produced by thermionic emission. These electrons are then accelerated to 90 keV in a continuous stream by

earthed anodes, and further accelerated to 100 MeV by a linear accelerator. These 100 MeV electrons are subsequently injected into a booster synchrotron, where the electrons are accelerated by 36 dipole bending magnets and a radio frequency voltage source up to an extraction energy of 3 GeV. The 3 GeV electrons are then injected into the storage ring. The storage ring at Diamond consists of 24 straight sections linked together by 48 dipole magnets to bend the electron beam through 360° with a 561.6 m circumference, completing a single circumference orbit in $\sim 2 \times 10^{-6}$ s with a lifetime of >10 hours. Maintained under vacuum, the storage beam is topped-up by the booster synchrotron to replace lost electrons, and energy losses are compensated for by a cavity of electromagnetic fields oscillating at radio frequencies to provide an energy boost, enabling uninterrupted experiments. A set of 2 m long undulating magnets that have magnetic period of 27 mm are located around the storage ring to provide additional acceleration to the electrons (Diamond, 2016). Electrons are extracted from the storage beam at tangents into beamlines that are each tailored for a specific use. Diamond has the capacity for 40 beamlines, with 27 beamlines currently operational and 3 under construction at the time of writing. Each beamline consists of a front end, an optics hutch, an experimental hutch and a control cabin. Electrons are extracted from the storage ring at the front end and directed into the optics hutch where a series of optics (i.e. collimators, monochromators and diffraction gratings) filter and focus the beam to a desired wavelength for an experiment located within the experimental hutch; this is all controlled from the control cabin (Diamond, 2016).

The Diamond Beamline B18 is tailored for general purpose X-ray absorption spectroscopy in the energy range 2.05–35 keV. The optics hutch of B18 contains: a water cooled collimating Si mirror to focus the beam 20 m from the source; a water cooled double crystal monochromator with pairs of Si(111) and Si(311) crystals; and a double toroidal mirror located 25 m from the source to focus the beam both horizontally and vertically (Diamond, 2016). This facilitates a highly monochromatic X-ray source enabling the back-reflection XRD technique to be investigated in a high resolution configuration, with respect to energy.

Within the B18 experimental hutch a chamber was configured with a SDD and a sample holder which could be rotated about a vertical axis, as shown in figure 3.12.

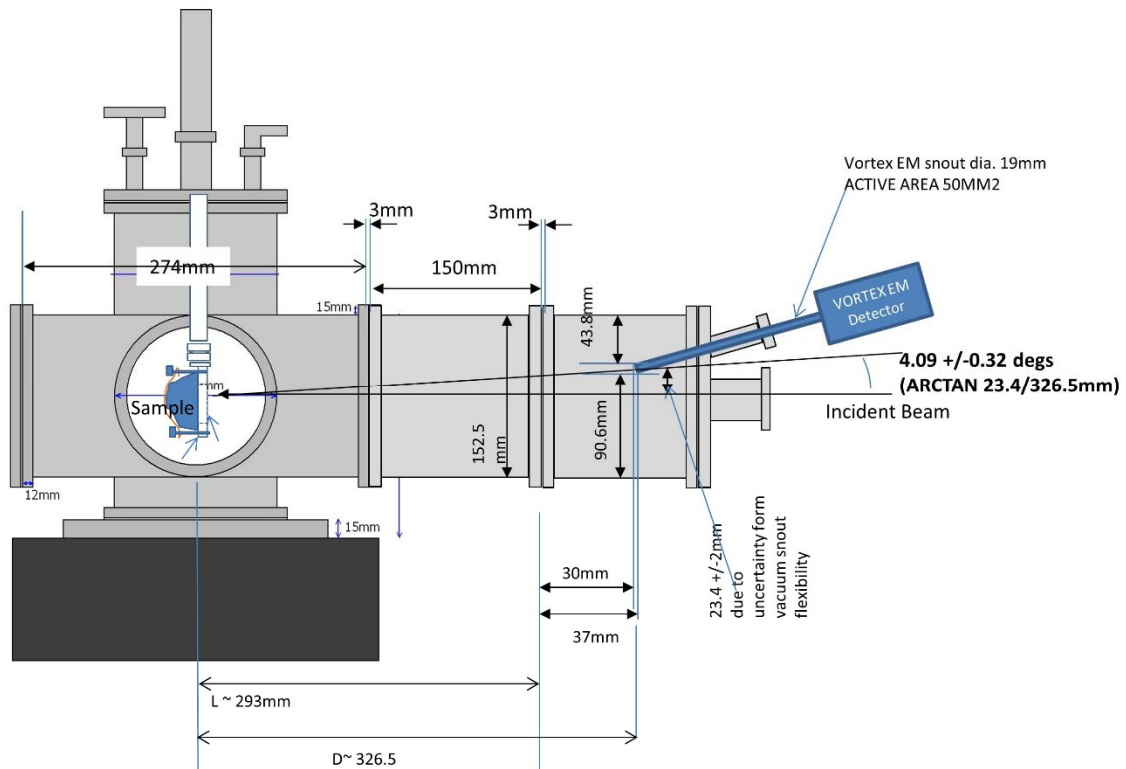


Figure 3.12. Experimental configuration for testing the back-reflection geometry in a high-resolution configuration at the Diamond Light Source. A Vortex EM SDD is positioned 326.5 mm from the sample, which can be individually rotated $\pm 45^\circ$ about a vertical axis (Cibin, 2014).

As shown in figure 3.12, an angle of $2\theta = 175.91 \pm 0.32^\circ$ was achieved. The beamline energy was stepped through the energy range 2.1–5.0 keV, which was achieved by the monochromator in the optics hutch. This energy range and geometry corresponds to d -spacings of 2.95–1.24 Å. A full experimental run took 28 minutes with the monochromator stepping through at 13 milli-degrees per second resulting in an approximate step size of 1 eV. The sample was mounted on a sample holder as shown in figure 3.12. To prepare the chamber for the experiment the sample was positioned and the chamber sealed, after which the chamber was pumped down to a vacuum. Once under vacuum the chamber was brought back up to pressure with He and then pumped down to vacuum again, before being brought back up to pressure with He. This process of flushing the chamber with He was to minimise fluorescence from atmospheric constituents, particularly Ar. The area of the sample exposed to the beam was approximately $1 \times 2 \text{ mm}^2$.

An EDXRD spectrum was recorded per approximate 1 eV step between 2.1–5.0 keV, resulting in a vast dataset per sample. An IDL program was developed to extract the scattered diffraction peak per \sim eV step by windowing, and to remove the background

baseline from the dataset caused by Rayleigh scattering. Diffraction peaks were then indexed for mineral identification using a reference library from the International Centre for Diffraction Data.

3.8 X-ray Diffraction Instruments on Space Missions

XRD instruments have been previously proposed for in-situ mineral identification on missions to the Moon and Mars, but only deployed on Mars. In-situ mineral identification aids in the geologic characterisation of an environment, and provides a ground-truth to orbital measurements like those outlined in Chapters 1, 2 and 4. The first proposal for using an XRD instrument dates from the 1960s, when NASA was heavily involved with lunar exploration. The lunar XRD instrument prototypes constructed at NASA JPL used a Bragg-Brentano geometry with Cu X-ray tube, Soller slits and Xe gas proportional detectors. Weighing 20 kg and suffering from unreliable power-supplies, the program ran from 1960–1968 without instrument deployment (Blake, 2000). Another instrument that was extensively developed but not deployed was the MarsXRD instrument intended for the then ESA/NASA ExoMars rover (Marinangeli et al., 2007). Designed for both XRD and XRF measurements, Mars-XRD prototype instruments utilised an ^{55}Fe X-ray source to probe a powder sample in a reflection geometry with three CCDs covering the range $2\theta = 6 - 65^\circ$ arranged at an 8 cm radius from the sample (Hill et al., 2011; Marinangeli et al., 2007, 2011).

The Chemistry and Mineralogy X-ray Diffraction (CheMin) instrument on Mars Science Laboratory (MSL) is the only XRD instrument to be deployed on a space mission at the time of writing this thesis. CheMin has been operating on Mars since August 2012. CheMin utilises a Co X-ray source, 32-sample wheel and a CCD-224 frame transfer imager manufactured by e2v (the modern version of a CCD-22) configured in a transmission geometry (figure 3.13). The Co X-ray source operates at a nominal 28 keV with a filament current of 1.5 A, producing continuum and characteristic X-radiation directed at the sample with an approximate 70 μm sample spot size with the aid of a pinhole collimator. The 600×1182 frame-transfer CCD-224 has an active area of 600×582 pixels with an energy range of 1–15 keV and an energy resolution of ≤ 250 eV at 6.93 keV. During operation the CCD is cryocooled to between -48°C and -22°C to reduce the effect of dark current. Primarily designed to capture XRD events in the 2θ angular range of $5-50^\circ$ with a resolution of $\leq 0.35^\circ 2\theta$, CheMin can also capture XRF events. CheMin has sample cells spaced around the circumference. Geological standards

permanently occupy 5 of the 32 sample cells, with the other 27 cells reusable that can each hold 400 mm³ of drill powder. However, only ≤ 76 mm³ of drill powder is delivered to the instrument, which is pre-sieved to < 150 μm by the sample delivery system and vibrated during operation by piezoelectric actuators to ensure the random orientation of crystallites (Blake et al., 2012). So far, CheMin has identified a range of primary minerals (e.g. olivine, pyroxene, feldspars) and secondary minerals formed by water-rock reaction (e.g. smectite, sulphates, magnetite) (Vaniman et al., 2014).

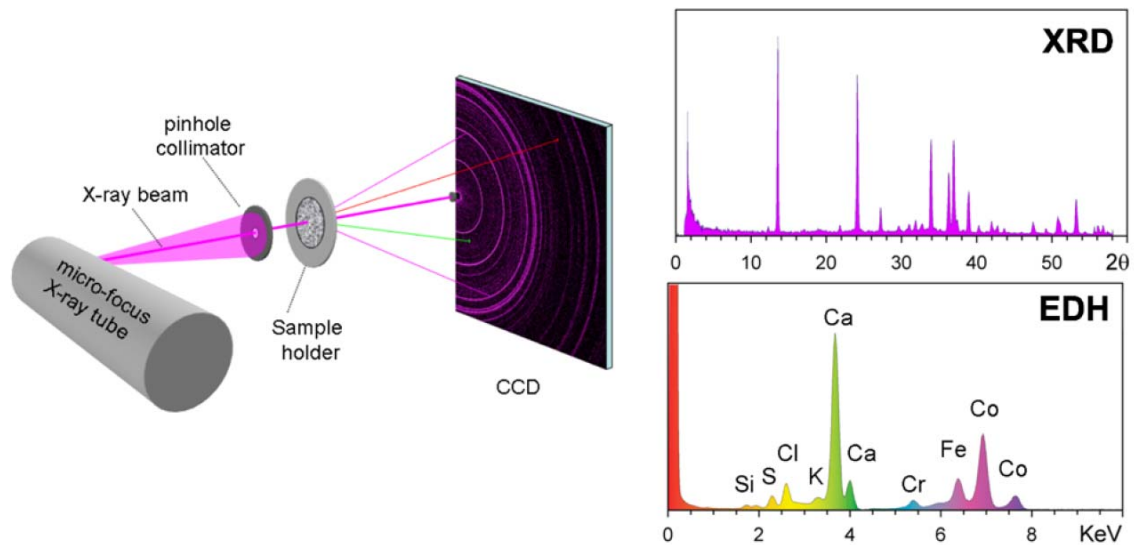


Figure 3.13. CheMin instrument geometry (left) with an exemplar XRD 2θ spectrum (top right) and X-ray energy-dispersive histogram (EDH) (bottom right), however CheMin is not calibrated to acquire EDH datasets (Blake et al., 2012).

The need for sample preparation for planetary XRD can be a hindrance, as strict mass and power budgets may not allow the tools required. The back-reflection XRD concept introduced in this chapter lends itself to a compact, lightweight instrument design that can be put on a robotic arm of a planetary lander or rover, and that would not require samples to be crushed to a fine powder. In Chapter 5, this technique is tested on a variety of pellet and whole rock samples using the pre-existing CCD and bespoke SDD facilities outlined in 3.6.1 and 3.6.2.

4. Hydrothermal Activity Recorded in Post Noachian-aged Impact Craters on Mars

Published in Journal of Geophysical Research: Planets, 121(4), pp.608-625, 2016.

DOI: 10.1002/2015JE004989

Co-authors: J.C. Bridges, S. Grebby and B.L. Ehlmann.

Hydrothermal systems have previously been reported in ancient Noachian and Hesperian-aged craters on Mars using CRISM but not in Amazonian-aged impact craters. However, the nakhlite meteorites do provide evidence of Amazonian hydrothermal activity. This study uses CRISM data of 144 impact craters of ≥ 7 km diameter and 14 smaller craters (3-7 km diameter) within terrain mapped as Amazonian to search for minerals that may have formed as a result of impact-induced hydrothermal alteration or show excavation of ancient altered crust. No evidence indicating the presence of hydrated minerals was found in the 3-7 km impact craters. Hydrated minerals were identified in 3 complex impact craters, located at 52.42°N, 39.86°E in the Ismenius Lacus quadrangle, at 8.93°N, 141.28°E in Elysium, and within the previously studied Stokes Crater. These 3 craters have diameters of 20 km, 62 km and 51 km, respectively. The locations of the hydrated mineral outcrops and their associated morphology indicate that two of these three impact craters — the unnamed Ismenius Lacus Crater and Stokes Crater — possibly hosted impact-induced hydrothermal systems, as they contain alteration assemblages on their central uplifts that are not apparent in their ejecta. Chlorite and Fe-serpentine are identified within alluvial fans in the central uplift and rim of the Ismenius Lacus crater, whereas Stokes Crater contains a host of Fe/Mg/Al phyllosilicates; however, excavation origin cannot be precluded. Our work suggests that impact-induced hydrothermalism was rare in the Amazonian and/or that impact-induced hydrothermal alteration was not sufficiently pervasive or spatially widespread for detection by CRISM.

4.1 Introduction

Understanding the history, nature and occurrence of hydrated minerals in the Martian crust is key to identifying potential past habitable environments. Recent investigations carried out using the Mars Exploration Rovers (MER), Mars Express (MEX), Mars Reconnaissance Orbiter (MRO) and Mars Science Laboratory (MSL) have revealed hydrated minerals in a diverse range of environments (e.g. Squyres et al., 2004;

Bibring et al., 2006; Poulet et al., 2007; Ehlmann et al., 2009; Murchie et al., 2009a; Grotzinger et al., 2014; Ehlmann and Edwards, 2014). Furthermore, remote sensing studies using the OMEGA (Observatoire pour la Minéralogie, l'Eau, les Glaces et l'Activité) and CRISM (Compact Reconnaissance Imaging Spectrometer for Mars) visible to infrared spectrometers on MEX and MRO, respectively, have identified phyllosilicates predominantly in ancient Noachian era terrains of Mars (Poulet et al., 2005; Mustard et al., 2008; Ehlmann et al., 2011a; Carter et al., 2013). These studies, along with others (e.g. Marzo et al., 2010; Mangold et al., 2012; Osinski et al., 2013), have reported evidence of hydrothermal minerals associated with numerous craters formed in the Noachian and Hesperian terrains, mostly via excavation of older altered material, but with impact-induced hydrothermalism occurring in a small number of craters.

Here we investigate nominally Amazonian terrains to determine how widespread impact-associated secondary mineral assemblages within post-Noachian craters are and to compare the mineralogy and geologic setting of these assemblages with those in more ancient cratered terrains. The goal is to assess the timing and frequency of occurrence of hydrothermal activity in the Amazonian.

4.1.1 Remote Sensing of Mars with OMEGA and CRISM

In early studies, the OMEGA visible-shortwave infrared imaging spectrometer was utilised to map hydrated mineral exposures at a spatial resolution (pixel size) of 1.8 km, resulting in the identification of three types of hydrated minerals — Fe/Mg phyllosilicates, Al phyllosilicates and hydrated sulphates — at five locations on Mars: Terra Meridiani, Mawrth Vallis, Nili Fossae, Aram Chaos and Valles Marineris along with scattered other highlands locations (Bibring et al., 2006; Poulet et al., 2007). Interpreting OMEGA observations in the context of the geological history of Mars, Poulet et al. (2005) suggested that formation of phyllosilicates occurred predominantly during the early Noachian, followed by a more acidic environment in which sulphate formation was prevalent. In a subsequent study, Bibring et al. (2006) proposed three distinct eras of alteration based on OMEGA observations — “Phyllosian”, “Theiikian” and “Siderikian” — characterised by phyllosilicates, sulphates and ferric oxides, respectively. These three eras can be loosely linked to the Noachian, Hesperian and Amazonian epochs (Bibring et al., 2006). Mustard et al. (2005) reported that OMEGA data in the northern plains of Mars

lack strong mafic absorptions as well as absorptions due to hydrated minerals but suggested that surface coatings could mask such signatures.

More recently, higher-resolution hyperspectral imagery of Mars has been acquired by the CRISM instrument at 18-40 m/pixel (Murchie et al., 2007, 2009a, 2009b). The higher spatial resolution of CRISM in comparison to OMEGA has resulted in the identification of numerous hydrated mineral exposures coupled with deposit morphology, thus enabling a more detailed understanding of Mars' surface mineralogy and providing insights about past environmental conditions. Phyllosilicates, predominantly Fe/Mg smectites, have been detected in layered sediments (Al smectite is also present), intracrater fans, plains sediments and basement/exhumed deposits (also known as “deep phyllosilicates”) (Mustard et al., 2008; Murchie et al., 2009a). Many of these deposits contain minerals formed in hydrothermal environments such as chlorite ((Mg,Fe)₅Al(AlSi₃)O₁₀(OH)₈), prehnite (Ca₂Al₂Si₃O₁₀(OH)₂), serpentine ((Mg, Fe)₃Si₂O₅(OH)₄), and zeolites (Mustard et al., 2008; Ehlmann et al., 2009, 2011b). Hydrated sulphate mineral deposits have been detected in intracrater clay-sulphate deposits, Meridiani-type layered deposits, valles-type layered deposits, siliceous layered deposits and gypsum plains (Murchie et al., 2009a). Carbonate deposits have also been detected, more rarely, with CRISM data in Noachian terrains (Ehlmann et al., 2008, 2009; Murchie et al., 2009a; Carter and Poulet, 2012; Bultel et al., 2015). Analysis of CRISM data has also helped guide landing site selection and rover-based investigations on MER and MSL. Moreover, CRISM analyses of Gale Crater indicated clay deposits (Milliken et al., 2010; Thomson et al., 2011) consistent with X-ray diffraction measurements taken on-board MSL to date (Bish et al., 2014; Vaniman et al., 2014). These deposits formed largely through burial diagenesis of basaltic sediments rather than impact-induced alteration (McLennan et al., 2014; Bridges et al., 2015).

In-situ investigations carried out by the MER program have also uncovered evidence of aqueous alteration. Specifically, the MER Opportunity rover has identified the presence of acid groundwater-fed sabkha-type deposits rich in sulphates, along with veins of various phyllosilicate minerals and Ca-sulphate within Noachian materials exposed in Endeavour crater (Arvidson et al., 2014). The MER Spirit rover has revealed evidence for hydrothermal activity in the Gusev Crater floor (Ming et al., 2006; Squyres et al., 2008; Morris et al., 2010; Filiberto and Schwenzer, 2013), although there is no clear link to heat released from the Gusev impact. The in-situ measurements made by MER Spirit at Gusev crater are consistent with CRISM observations (Carter and Poulet, 2012).

4.1.2 Theory of Impact-Induced Hydrothermal Activity

A hypervelocity impact into a planetary crust produces a shock wave that compresses and transfers a large amount of energy to the crust. This shock event is not thermodynamically reversible: upon decompression of the planetary crust by rarefaction waves, waste heat is produced which raises the temperature of the planetary crust (Melosh, 1989). On Mars, a central uplift is more likely to form for impact craters above 7 km diameter, caused by the rise of deep-seated rocks located beneath the crater as it returns to a state of gravitational equilibrium during the later stages of impact crater formation. The existence of this central structure classifies the crater as complex (Melosh, 1989; Abramov and Kring, 2005). The uplift of warm, deep-seated material can, if the crust is water- or ice-rich, establish subsurface convection cells of water that alter the surrounding rock to produce phyllosilicate-rich alteration phases (Schwenzer and Kring, 2009). The longevity of such impact-induced hydrothermal systems depends on the physical and kinetic properties of the impactor, permeability of the planetary crust, and the subsequent size and type of the resultant impact crater (Abramov and Kring, 2005; Barnhart et al., 2010; Rathbun and Squyres, 2002). In simple craters (<~ 7 km on Mars), shock-emplaced heat dominates due to the lack of a central uplift and a negligible amount of impact melt; thus, convection cells cannot be easily established.

Research has suggested that subsurface impact-induced hydrothermal activity in the volatile-bearing crust of Mars has the potential to last for 67,000 years for a 30 km diameter crater, 290,000 years for a 100 km diameter crater, and up to ~10 Myr for craters the size of the Hellas basin (~2000 km diameter) (Abramov and Kring, 2005). The prolonged period of time that the host rock is subjected to heat and water suggests that an impact-induced hydrothermal system can produce and sustain a habitable environment for microbial life (Rathbun and Squyres, 2002; Abramov and Kring, 2005; Cockell et al., 2012).

4.1.3 Evidence for Impact-Induced Hydrothermal Activity on Mars

Spectral evidence for impact-induced hydrothermal systems on Mars is scarce, with the oldest of the possible examples being the ~153 km diameter Noachian-aged Holden impact crater (-26.04°N, 325.98°E) located in the Margaritina Sinus quadrangle, within which extensive erosion of the ejecta and southwest rim/terraces of the crater has exposed megabreccias, interpreted as pre-Holden materials excavated by impact (Grant et al., 2008). Tornabene et al. (2009) and Osinski et al. (2013) utilised HiRISE and

CRISM data to show that light-toned fractures within the megabreccia exhibit absorptions at $\sim 1.9 \mu\text{m}$ and $\sim 2.3 \mu\text{m}$, indicating the presence of Fe/Mg clays. Osinski et al. (2013) suggested that these secondary mineral-bearing fractures are indicative of impact-induced hydrothermal alteration.

More recent impact-induced hydrothermal activity has been suggested for the ~ 40 km diameter Hesperian-aged Toro complex impact crater (17.04°N , 71.83°E) in the Syrtis Major quadrangle, with prehnite, chlorite, smectites and opaline materials detected in impact-melt bearing crater-fill deposits along, in and around the central uplift as well as in the ejecta (Ehlmann et al., 2009; Marzo et al., 2010; Osinski et al., 2013a). Marzo et al. (2010) proposed a model of impact excavation and impact-induced hydrothermal activity for Toro crater, given morphologic features within the central peak consistent with hydrothermal systems and hydrated minerals within the crater central peak and floor. However, Ehlmann et al. (2009, 2011b) mapped the same minerals both inside and outside the crater peak and argued for their origin by excavation of hydrothermally altered materials that pre-dated the crater.

Majuro crater (-33.26°N , 84.35°E), on the north-eastern Hellas basin rim, represents another example of potential impact-induced hydrothermal alteration during the Hesperian, and perhaps provides the strongest evidence for such a system to date. Available MRO and MEX coverage of this ~ 45 km diameter late-Hesperian-aged complex impact crater reveals Fe/Mg phyllosilicates and opaline silica in the crater rims, floor and central peak (Mangold et al., 2012). This crater also contains a 20 km long alluvial fan extending from the crater wall to the floor at the base of the central uplift that has an unaltered northern upper section and an altered lower section. Mangold et al. (2012) concluded that the altered minerals in the fan most likely formed following hydrothermal circulation initiated by the crater-forming impact and subsequent re-deposition by physical weathering in the alluvial fan.

An impact-induced hydrothermal alteration hypothesis has also been proposed for the ~ 50 km diameter Micoud complex impact crater (50.58°N , 16.35°E) located in the late-Hesperian-aged (Tanaka et al., 2014) Vastitas Borealis formation in the northern plains, where the presence of prehnite in and around the central uplift is shown with CRISM data (Gross et al., 2012). Hydrated silica deposits and Fe/Mg phyllosilicates in the central uplift of 78 km diameter Ritchey crater (-28.5°N , 309°E), which formed in the Hesperian, have been shown to post-date the impact and may result from impact-induced aqueous alteration (Sun and Milliken, 2014).

Collectively, the CRISM data indicate that subsurface hydrothermal processes were widespread: found in excavated Noachian crust from hundreds of craters (Mustard et al., 2008; Ehlmann et al., 2011a, 2011b). Definitely impact-induced hydrothermal processes — arguably harder to uniquely identify from orbit — are restricted to a few candidate locations, the most outstanding of which is a late Hesperian crater.

4.1.3.1 *The Nakhlite Martian Meteorites*

Evidence for hydrated, secondary minerals is also found in the Martian Shergottite, Nakhlite, and Chassigny (SNC) meteorites, most notably in the nakhlite group (Gooding et al., 1991; Bridges and Grady, 2000; Changela and Bridges, 2010; Bridges and Schwenzer, 2012; Hicks et al., 2014). Formed on Mars in the Amazonian, ~1.3 Ga, in a basic-ultrabasic lava flow or shallow intrusion (~100 m), these basaltic cumulate clinopyroxenite rocks have veins within brittle impact-induced fractures that contain the alteration minerals: ferric saponite ($\text{Ca}_{0.25}(\text{Mg,Fe})_3((\text{Si,Al})_4\text{O}_{10})(\text{OH})_2 \cdot n(\text{H}_2\text{O}))$), ferric serpentine, siderite (FeCO_3), a gel/poorly crystalline saponite, and salts (Gooding et al., 1991; Bridges and Grady, 2000; Changela and Bridges, 2010; Hicks et al., 2014). Truncation of these veins by the fusion crust indicates a pre-terrestrial (Martian) origin (Gooding et al., 1991). Poorly crystalline materials located within fractured olivine ($(\text{Mg, Fe})_2\text{SiO}_4$) and mesostasis indicates that the nakhrites underwent rapid cooling. Together with the veining within the brittle fractures — which suggest the presence of shock effects (though of lesser magnitude than seen in the shergottites (Nyquist et al., 2001)) — this suggests that the nakhlite parent body may have been at the margins of a short-lived Amazonian-era impact-induced hydrothermal system (Changela and Bridges, 2010). Computer modelling with the program CHILLER showed that the nakhlite alteration assemblage formed from a potentially habitable neutral to alkaline brine with a peak temperature $\leq 150\text{-}200$ °C in a near-surface setting, with Ca-rich siderite precipitating at these high temperatures and saponite and serpentine precipitating once the fluid had cooled to ~50 °C (Bridges and Schwenzer, 2012). K-Ar dating of alteration products (i.e. smectite- and siderite-veined olivine grains) suggests this fluid activity occurred ≤ 670 Myr (Shih et al., 1998; Swindle et al., 2000).

4.1.4 This Study

In this study we use CRISM data acquired for impact craters emplaced within Amazonian terrains to assess the extent to which evidence of hydrothermal alteration of post-Noachian aged materials is present. Using the latest USGS Geologic Map of Mars (Tanaka et al., 2014) as a guide, we have analysed 282 CRISM images covering 158 craters in the northern hemisphere of Mars. As a result, 3 craters have been found to exhibit compelling spectral features that indicate the presence of hydrated minerals, two of which may have evidence for post-impact hydrothermal systems.

4.2 Methods

4.2.1 The CRISM, HiRISE, CTX and MOLA Instruments

The CRISM instrument on-board MRO is a visible/shortwave-infrared imaging spectrometer, which in targeted mode acquires 18-40 m/pixel images of $\sim 10 \times 3\text{-}20$ km areas from 362 nm to 3920 nm over 544 channels, with a spectral sampling of 6.55 nm/channel. This is achieved using a gimbaled optical sensor unit to compensate for the orbital motion of MRO, allowing for a long acquisition time (2-3 minutes) of a targeted area and acquisition of data with a high signal-to-noise ratio (Murchie et al., 2007). CRISM also images the Martian surface in a mapping mode, where the instrument acquires 100-200 m/pixel nadir images of ~ 10 km in width and ≤ 550 km long (Murchie et al., 2007).

High-resolution imagery provides geological context for the mineral detections. Accordingly, imagery acquired by the High Resolution Imaging Science Experiment (HiRISE) and Context Camera (CTX) — both also on-board MRO — were utilised for this purpose. The HiRISE instrument is capable of acquiring 0.3 m/pixel images at 300 km altitude (McEwen et al., 2007), whereas CTX can acquire 6 m/pixel images at 300 km altitude (Malin et al., 2007).

Topographic data from the Mars Orbiter Laser Altimeter (MOLA), on-board the Mars Global Surveyor, was obtained and used to provide profiles of impact craters and to help ascertain the depth of the mineral signatures of interest. MOLA successfully mapped the topography of Mars with a vertical accuracy of 1 m and along-track shot spacing of 300 m with spot size of 168 m at 400 km elevation mapping orbit (Smith et al., 2001). The resultant topographic map of Mars has a resolution of 128 pixels per degree, and we use profiles extracted from this global map.

4.2.2 Identification of Candidate Craters

The impact craters were identified using a combination of the geologic map of Mars (Tanaka et al., 2014), the Robbins and Hynek (2012) crater database, MOLA topographic data, and CTX imagery. The analysis approach taken involved cropping the Robbins and Hynek (2012) crater database to units mapped as Amazonian in the USGS Mars quadrangles, and then systematically searching each quadrangle for applicable impact craters with high resolution CRISM scenes: FRS, FRT, HRL and HRS (Full Resolution Short, Full Resolution Targeted, Half Resolution Long and Half Resolution Short, respectively). Applicable candidate craters were defined as those that had distinct and complete crater walls and floors/central uplifts. Filled-in craters were excluded from this study because of the difficulty in identifying potential impact-induced hydrothermal alteration beneath the infill material using CRISM data.

Initially, impact craters with diameters ≥ 7 km were selected for analysis as this represents the transition diameter from simple to complex impact craters, where impact-induced hydrothermal systems are more likely to occur (Daubar and Kring, 2001; Abramov and Kring, 2005). Impact crater diameters were extracted from the Robbins and Hynek (2012) crater database.

A secondary survey of smaller impact craters was carried out on impact craters ≥ 3 km and < 7 km. This extends the selection to include simple craters, for which the shock-emplaced heat would be the dominant heat source (Schwenzer and Kring, 2013), and impacts large enough to eject material from the surface of Mars (Head et al., 2002). Large outcrops of post-impact generated hydrated minerals would be unlikely for simple craters as shock-emplaced heat would dominate, resulting in smaller hydrous mineral deposits within outcrops, as opposed to widespread alteration driven by a hydrothermal cell. Smaller outcrops with hydrous minerals are more likely to be restricted to rocky interiors or masked by later fill or dust, and so additional selection criteria based on Thermal Emission Spectrometer (TES) dust coverage was introduced. Only craters with TES dust coverage index ($1350\text{-}1400\text{ cm}^{-1}$ average emissivity) > 0.94 (Ruff and Christensen, 2002), indicating minimum dust coverage, were studied.

4.2.3 CRISM Data Processing and Spectral Identification of Minerals

Raw CRISM data was converted to I/F (Murchie et al., 2009b) and obtained from the NASA Planetary Data System Geosciences Node. The data was subsequently processed and analysed using the CRISM Analysis Toolkit (CAT) version 7.2.1, a

software tool released by the CRISM team that is an extension to the Environment for Visualizing Images (ENVI) software package. Photometric effects were corrected by division of the cosine of the incidence angle of the observation, and atmospheric effects were corrected using the volcano scan method (McGuire et al., 2009). Summary products (Pelkey et al., 2007) were then calculated and used to identify regions with spectral properties of interest, along with a corresponding spectrally bland region. The region of interest was ratioed to a bland patch within the same image columns to divide out the systematic instrument artefacts and residuals from the atmospheric correction in the spectrum of interest, accentuating compositional differences between the regions. This conventional method of spectral extraction from CRISM data has been used in several previous studies (e.g. Ehlmann et al., 2009; Milliken et al., 2010).

Mafic, non-hydrated minerals were highlighted by deriving olivine and high- and low-calcium pyroxene (OLINDEX, LCPINDEX and HCPINDEX) summary parameters from the CRISM imagery. Olivine, $(\text{Fe,Mg})_2\text{SiO}_4$, was identified by characteristic absorptions in its spectrum at $\sim 1.0 \mu\text{m}$, which are caused by crystal field transitions of Fe^{2+} (Burns, 1970). In contrast, the spectrum of the pure forsterite endmember (Mg_2SiO_4) is featureless (Adams, 1975). Pyroxenes, $(\text{Ca,Fe,Mg})_2\text{Si}_2\text{O}_6$, generally have two characteristic bands that shift depending on Ca and Fe content — low Ca pyroxenes tend to have a strong absorption at $0.9 \mu\text{m}$ and a broad absorption at $1.8 \mu\text{m}$, which are shifted to $1.0 \mu\text{m}$ and $2.3 \mu\text{m}$ for high Ca pyroxenes with an increasing Fe content (Adams, 1975; Mustard et al., 2005).

Hydrated minerals were initially identified by a diagnostic spectral feature at $1.9 \mu\text{m}$, which is attributed to combinations of bending and stretching vibrations of H_2O within the mineral structure. Combination overtones of H_2O , along with OH overtones caused by structural stretching vibrations result in an absorption at $\sim 1.4 \mu\text{m}$. In phyllosilicates, the position of the OH overtone is influenced by the octahedral cation present causing it to shift between $1.38\text{-}1.43 \mu\text{m}$ (Bishop et al., 2008). Absorptions between $2.0\text{-}2.6 \mu\text{m}$ are most indicative of the hydrated silicate phase present. More specifically, Al-OH and Si-OH absorptions occur at $\sim 2.21 \mu\text{m}$, whereas Fe- and Mg-OH absorptions occur at $\sim 2.29 \mu\text{m}$ and $\sim 2.32 \mu\text{m}$, respectively (Bishop et al., 2002a, 2002b). Monohydrated sulphates have a broad absorption band at $\sim 2.0 \mu\text{m}$ with a diagnostic absorption band at $2.4 \mu\text{m}$, whereas polyhydrated sulphates have absorption bands around $1.4 \mu\text{m}$ and $1.9 \mu\text{m}$, consistent with H_2O and OH overtones, with a drop-off near $2.4 \mu\text{m}$ (Cloutis et al., 2006). Carbonates have absorption bands around $2.3 \mu\text{m}$ and $2.5 \mu\text{m}$, but

their exact position depends on the major cation. Mg-rich carbonates have absorption bands at 2.30 μm and 2.50 μm , Ca-rich carbonates have absorption bands at 2.34 μm and 2.54 μm and Fe-rich carbonates have absorption bands at 2.33 μm and 2.53 μm (Gaffey, 1987). H₂O ice has diagnostic absorption bands at 1.25 μm , 1.5 μm and 2.0 μm , whereas CO₂ ice has 1.435 μm and 2.281 μm absorptions (Langevin et al., 2007).

4.2.4 Definition of a “Null” Result

A “Null” result in this study is defined as an impact crater that meets the criteria previously outlined but CRISM analysis did not reveal the presence of hydrated minerals. For clarification, this does not definitively rule out the presence of hydrated minerals, but rather simply indicates the inability to identify them using the CRISM data at 18-40 m/pixel scale and with the possibility of dust cover.

4.3 Results

Following analyses of 267 CRISM images covering 144 craters ≥ 7 km diameter in the northern hemisphere of Mars, just 3 craters were found to show compelling spectral features suggesting the presence of hydrated silicate minerals (figure 4.1). No sulphate minerals were found in this study. The locations and associated diameters of these 3 impact craters are detailed in table 4.1. An additional 15 CRISM images covering 14 impact craters of diameters ≥ 3 km and < 7 km in relatively dust-free Amazonian mapped terrain units in the Northern Plains were also analysed, but no evidence for the presence of hydrated minerals was found. There was no CRISM coverage for candidate impact craters found in Amazonian terrains in west Hellas Basin. Appendix A of this thesis shows the full list of impact craters and associated CRISM images analysed in this study.

Table 4.1. Amazonian impact craters with phyllosilicates found in this study (*Crater ID refers to the crater identification tag in Robins and Hynek (2012)).

Name	Quadrangle	Crater ID*	Diameter (km)	Lat (°N)	Lon (°E)
Unnamed	Ismenius	05-000375	20.0	52.42	39.86
	Lacus				
Unnamed	Elysium	15-000018	50.8	8.93	141.28
Stokes	Cebrenia	07-000008	62.5	55.62	171.23

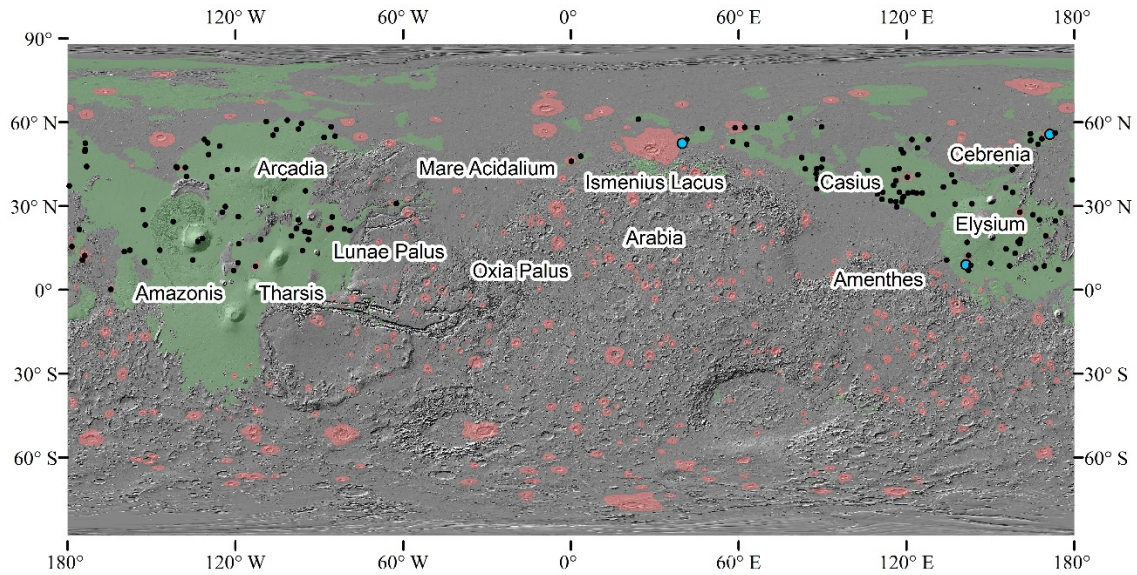


Figure 4.1. Greyscale MOLA map showing the impact craters analysed in this study. Amazonian-Hesperian terrains are highlighted in green, with Amazonian-Hesperian Impact (AHi) units highlighted in red. Only AHi units overlying Amazonian-Hesperian terrains were considered in this study; map units from Tanaka et al. (2014). CRISM data from 158 impact craters were studied, with 3 craters showing evidence of hydrated minerals. Black dots indicate impact craters that did not show hydrated minerals; blue dots indicate impact craters that contain hydrated minerals.

4.3.1 Unnamed Ismenius Lacus Impact Crater

This unnamed, ~20 km diameter impact crater, listed as 05-000375 in the Robbins and Hynek (2012) crater database, is a complex impact crater located at 52.42°N, 39.86°E in the Ismenius lacus quadrangle of Mars (figure 4.2). The terrain impacted is mapped as an Amazonian-Hesperian-aged unit (Tanaka et al., 2014) and a recent study used crater counts to date this crater as 0.3 Ga (Sun and Milliken, 2015). The impact crater has a pronounced central uplift with a maximum diameter of 4.9 km and radial, multi-layered, fluidised ejecta previously noted as hummocky with broad lobes (Robbins and Hynek, 2012). The crater floor has a minimum MOLA elevation of -4.49 km with an overall crater depth of 1.2 km with respect to the crater rim. Inspection of HiRISE PSP_009561_2325 and ESP_040958_2325 showed evidence for 4 alluvial fans in the wall and central peak (figures 4.2B-D).

Four CRISM scenes cover the impact crater: FRT0000BFA6, FRT0001B619, HRL000194F4 and HRL0001B89D. Summary products derived from FRT0000BFA6 indicated absorptions at ~1.9 μm and ~2.3 μm in materials in the central structure, both in rocky materials and in alluvial fans on the central uplift of the impact crater (figures 4.2C, 4.2D and 4.3). Further analysis of continuum-removed CRISM spectra (figure 4.3)

revealed a 1.92-1.94 μm absorption, indicating the presence of molecular H_2O , in addition to an absorption centred at 2.35 μm and a shoulder at ~ 2.2 -2.3 μm for spectra of fan #1 and megabreccia material. The spectra for the fan #1 material also has an absorption at ~ 1.48 μm that together with the other absorptions present in this spectra suggest the possibility of prehnite. For all spectra present in figure 4.3, the absorptions indicate the presence of Fe/Mg phyllosilicates, possibly Fe-serpentines or chlorites. A broad absorption centred near 1.25 μm indicates the presence of iron, either in an Fe-bearing igneous mineral or in the Fe/Mg phyllosilicate phase. The hydrous signatures are confined to the central structure, including probable megabreccia blocks, rocky alcoves at the head of each of the gullies, and alluvial fans (figure 4.3) but do not extend on to the crater floor. Sands within the crater are enriched in mafic minerals.

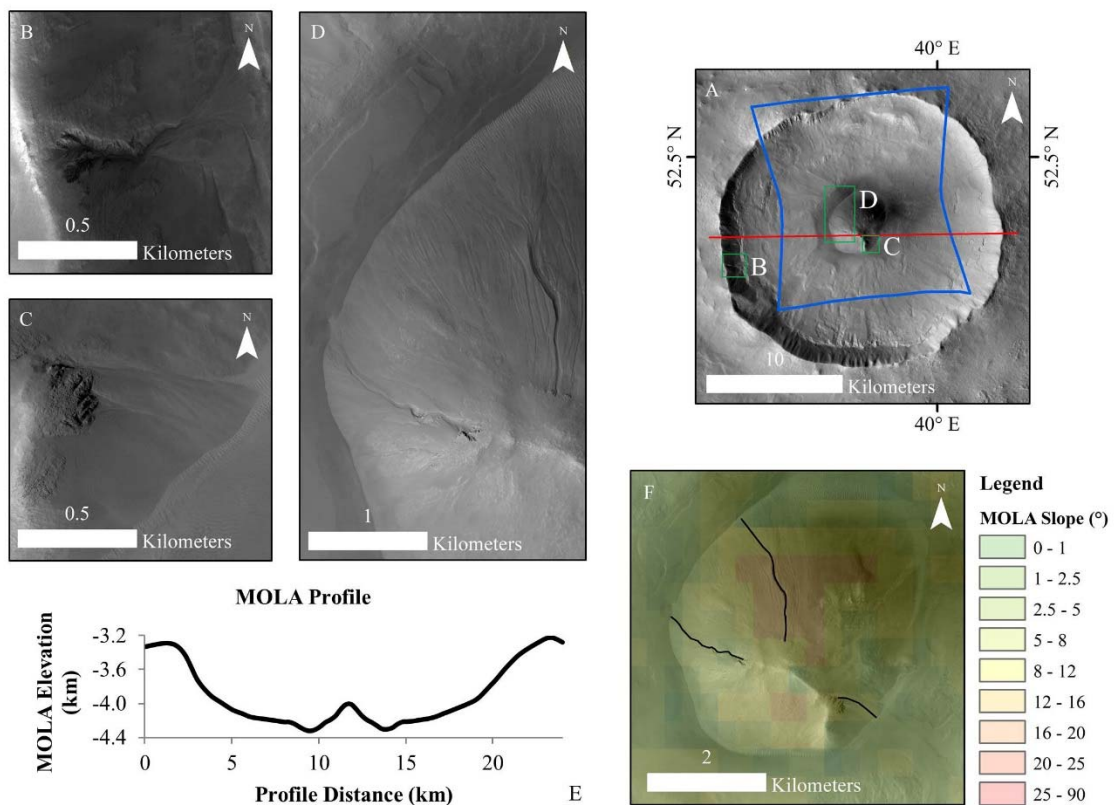


Figure 4.2. 20 km complex impact crater located 52.42°N 39.86°E in the Ismenius Lacus quadrangle of Mars. **A)** CTX B02_010260_2327 with CRISM FRT0000BFA6 outline (blue) and location of the MOLA profile (red) overlain. **B)** Alluvial fan located on western crater wall in HiRISE ESP_040958_2325. **C)** Alluvial fan located on the south-west region of the central uplift in HiRISE PSP_009561_2325. **D)** Alluvial fans located on northern and western regions of the central uplift in HiRISE PSP_009561_2325 showing dark toned material indicating possible recent movement of material within the gully. **E)** MOLA profile of the crater illustrated in A by the red line. **F)** MOLA-derived slope map of central uplift showing that the largest gully (gullies / fans tracked with black lines) on the northern region of the central uplift has formed where the slope is greatest.

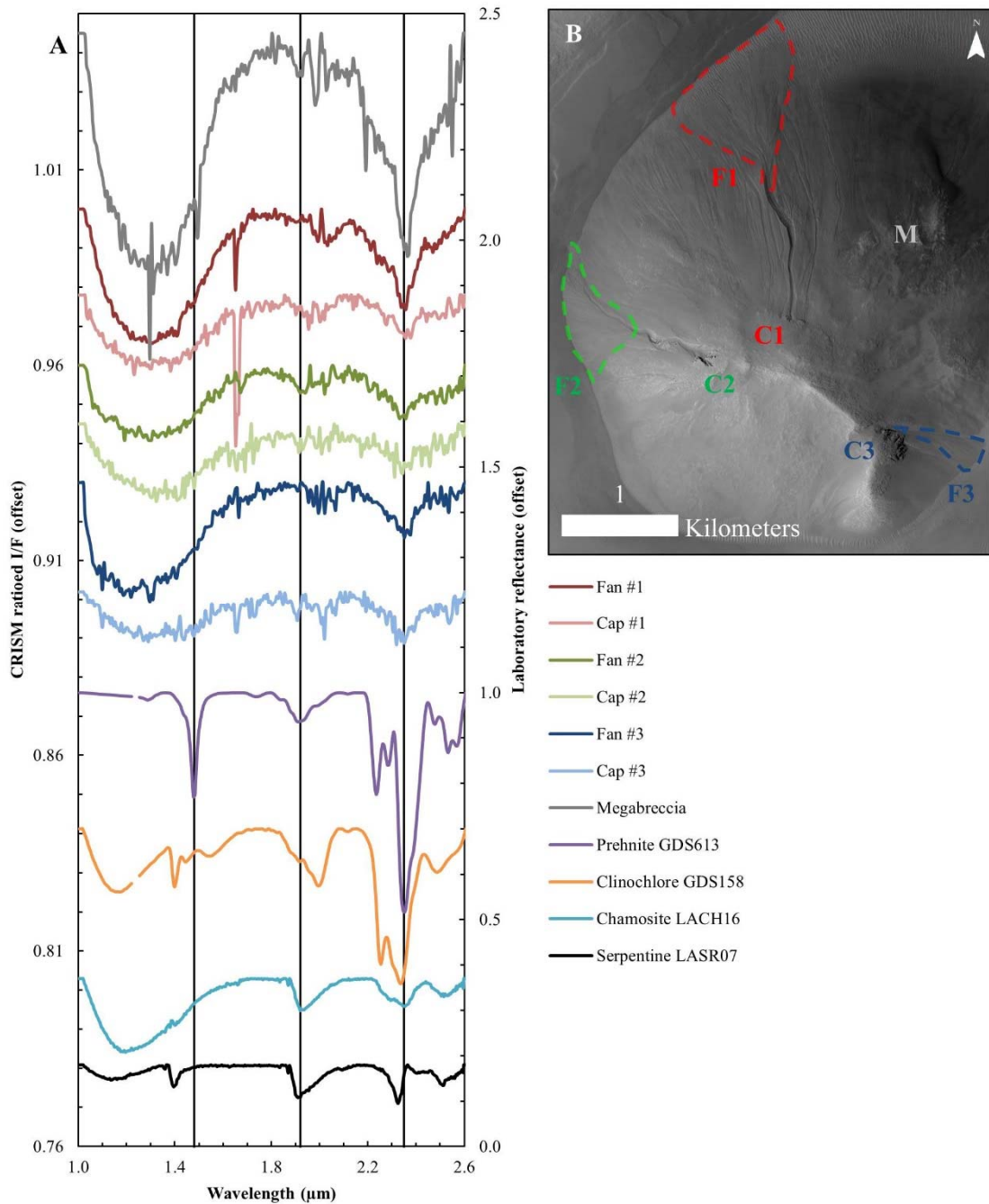


Figure 4.3. 20 km complex impact crater located $52.42^{\circ}\text{N } 39.86^{\circ}\text{E}$ in the Ismenius Lacus quadrangle of Mars. **A)** CRISM continuum-removed spectra extracted from FRT0000BFA6 of fans shown in B. The $1.92\text{-}1.94 \mu\text{m}$ and $2.351 \mu\text{m}$ absorptions indicate the presence of chlorite / Fe-serpentine /prehnite. Apparent absorptions at 1.65 and $2.0 \mu\text{m}$ are caused by a filter boundary and residual atmospheric absorptions, respectively. Laboratory spectra are from the USGS spectral library (Clark et al., 2007). **B)** HiRISE PSP_009561_2325_RED showing gullies and fans in the central uplift, with areas of CRISM spectral extraction outlined. Fan 1, Fan 2 and Fan 3 are sized 0.73 km^2 (1817 CRISM pixels), 0.28 km^2 (705 CRISM pixels) and 0.14 km^2 (358 CRISM pixels), respectively. Cap #1-3 and megabreccia spectra shown in A are sized 400, 55, 80 and 91 CRISM pixels, respectively.

A MOLA profile of the crater was extracted (figure 4.2E) and a slope map derived from the 128 pixels per degree MOLA topographic map of Mars, using the slope tool within the ArcGIS spatial analyst toolbox (figure 4.2F). The northern gully/alluvial fan has a slope maximum of 14.7° and a minimum of 4.5° , whereas the western gully/alluvial fan has a slope maximum of 6.4° and a minimum of 3.3° . The smaller fan shown in figure 4.2C has a slope maximum of 7.8° and a minimum of 4.0° . In this study gullies are observed on pole-, eastern- and western-facing slopes. In contrast, a study of the Northern Hemisphere showed that gullies at this latitude tend to form on equator-facing slopes (Heldmann et al., 2007). Slope length from the rocky cap on the central peak to the edge of the alluvial fans (as illustrated by the black lines in figure 4.2F) was found to be 2.3 km and 1.5 km for the northern and western gullies/fans, respectively, and 780 m for the southern fan.

The northern fan emanates from the bottom of the gully measuring 110 m across and expands out to 1.1 km across at the base of the fan over a distance of 900 m. The deposits from the excavated gully at the base of the northern fan also intersect a dune field, and multiple smaller gully and fan features are in close proximity to the northern gully/fan, with some cross-cutting others. This cross-cutting nature indicates a series of gully/fan formations transporting excavated material from the upper central uplift to the base in multiple, distinct episodes of activity. In comparison, the western fan emanates from the bottom of the western gully measuring 50 m across and expands out to 1 km across over a 600 m distance. Shown in figure 4.2C, a smaller channel/fan is noticeable to the south on the central uplift that has a spectral signature comparable to the previous two fans (figure 4.3). This smaller fan emanates directly from a rocky cap and fans out to 380 m over a 780 m distance.

An additional fan located on the western crater wall was identified (figure 4.2B). Analysis of CRISM HRL000194F4 covering this fan suggests that the area lacks a clear hydrous mineral signature. CRISM images FRT00018405 and HRL0001B89D covering the crater ejecta did not show the presence of hydrous minerals.

4.3.2 Unnamed Elysium Impact Crater

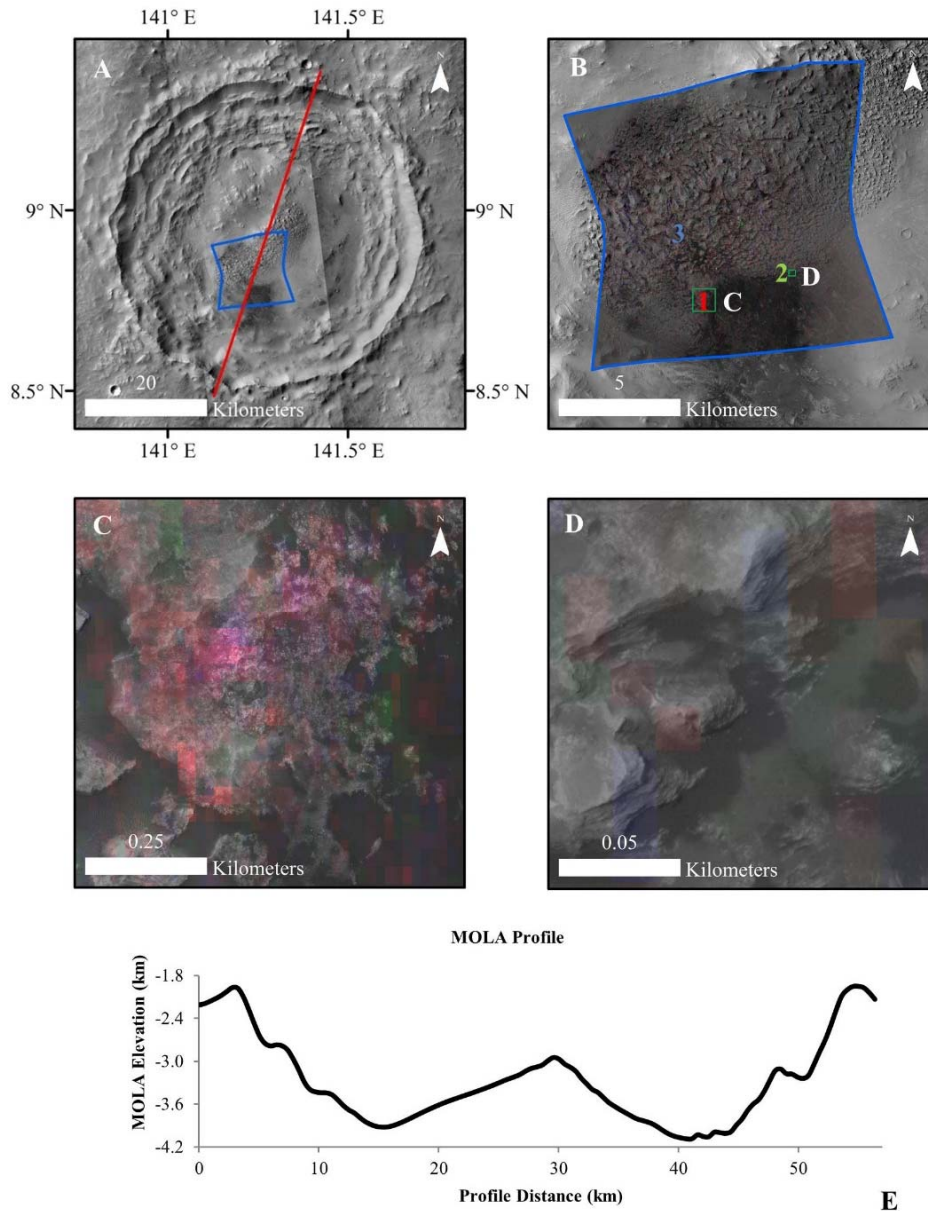


Figure 4.4. ~51 km diameter unnamed complex impact crater located 8.93°N, 141.28°E in the Elysium quadrangle of Mars. **A)** CTX mosaic showing the impact crater with CRISM FRT0000619D outline (blue) and location of the MOLA profile (red) overlain. **B)** CTX mosaic with CRISM FRT0000619D RGB parameter map (Table 2.2; Pelkey et al., 2007) composite D2300 (red), BD2210 (green) and BD1900 (blue). Context locations for zoomed views in C and D are indicated by the green boxes. Context locations for spectra in figure 4.5 are shown by 1, 2 (from within green boxes) and 3. **C)** HiRISE ESP_043051_1890_RED overlain with CRISM RGB parameter map (shown in B) reveals areas of mixed absorptions (1.9 μm and 2.3 μm highlighted by purple). **D)** Close-up of central uplift in a portion of HiRISE PSP_008305_1890_RED (overlain with CRISM RGB parameter map shown in B), showing the morphology of the central uplift, proposed to be eroded crater fill. **E)** MOLA profile of the crater illustrated in A by the red line.

Shown in figure 4.4, the ~51 km diameter impact crater, listed as 15-000018 in the Robbins and Hynes (2012) crater database, is a complex impact crater in Amazonian-Hesperian volcanic terrain (Tanaka et al., 2014) located at 8.93°N, 141.28°E in the Elysium quadrangle of Mars. A recent study (Sun and Milliken, 2015) used crater counts to date this crater as 3.46 Ga, and thus, it is early Amazonian- or late Hesperian-aged (Werner and Tanaka, 2011). The crater has slumped, terraced walls, a central uplift with an approximate diameter of 25 km and crater floor with dunes and sedimentary materials, interpreted to be later fill (figure 4.4A). The ejecta is single-layered, fluidised and hummocky with broad lobes (Robbins and Hynes, 2012). The crater floor has a minimum MOLA elevation of -4.05 km with an overall crater depth of 2.05 km with respect to the height of the crater rim. High-resolution imagery CTX P19_008305_1890 and HiRISE PSP_008305_1890 (shown in figures 4.4B-D) reveals that the floor of the crater to the south of the central uplift contains ~130 km² of eroded layered sedimentary deposits and dark dunes.

Five CRISM scenes cover the impact crater: FRT0000619D, FRT0000B0BE, FRT00017788, HRL000166A4 and HRS0000AB65. Summary parameters derived from FRT0000619D suggest the presence of Fe/Mg-rich phyllosilicates in the eroded relict sedimentary layers on the central uplift of the impact crater (figures 4.4C-D). This is further corroborated through spectral analysis of the CRISM data, which reveals 1.92-1.93 μm H₂O absorptions along with 2.29-2.31 μm Fe, Mg-OH absorptions (figure 4.5).

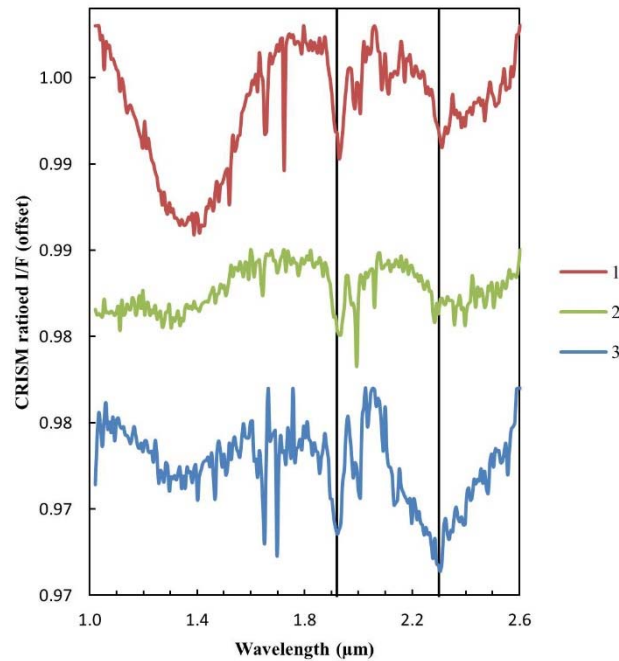


Figure 4.5. CRISM continuum-removed spectra extracted from FRT0000619D of eroded crater fill in Elysium impact crater, shown in figures 4.4B-C. The spectra show 1.92-1.93 μm and 2.29-2.31 μm absorptions, which are consistent with Fe/Mg phyllosilicates.

4.3.3 Stokes Impact Crater

The ~62 km diameter Stokes complex impact crater (07-000008 in the Robbins and Hynek (2012) crater database) is a complex impact crater located at 55.62N, 171.23E within the Cebrenia quadrangle of Mars. The terrain impacted is mapped as an Amazonian-Hesperian aged unit (Tanaka et al., 2014) and a recent study used crater counts place an upper bound on this crater age 3.75 Ga (Sun and Milliken, 2015). As seen in figures 4.6A and 4.6B, the central uplift of Stokes Crater is highly fractured, the crater floor has slump deposits derived from the crater walls, and the ejecta is radial, double-layered and hummocky with broad lobes, as previously stated by Robbins and Hynek (2012).

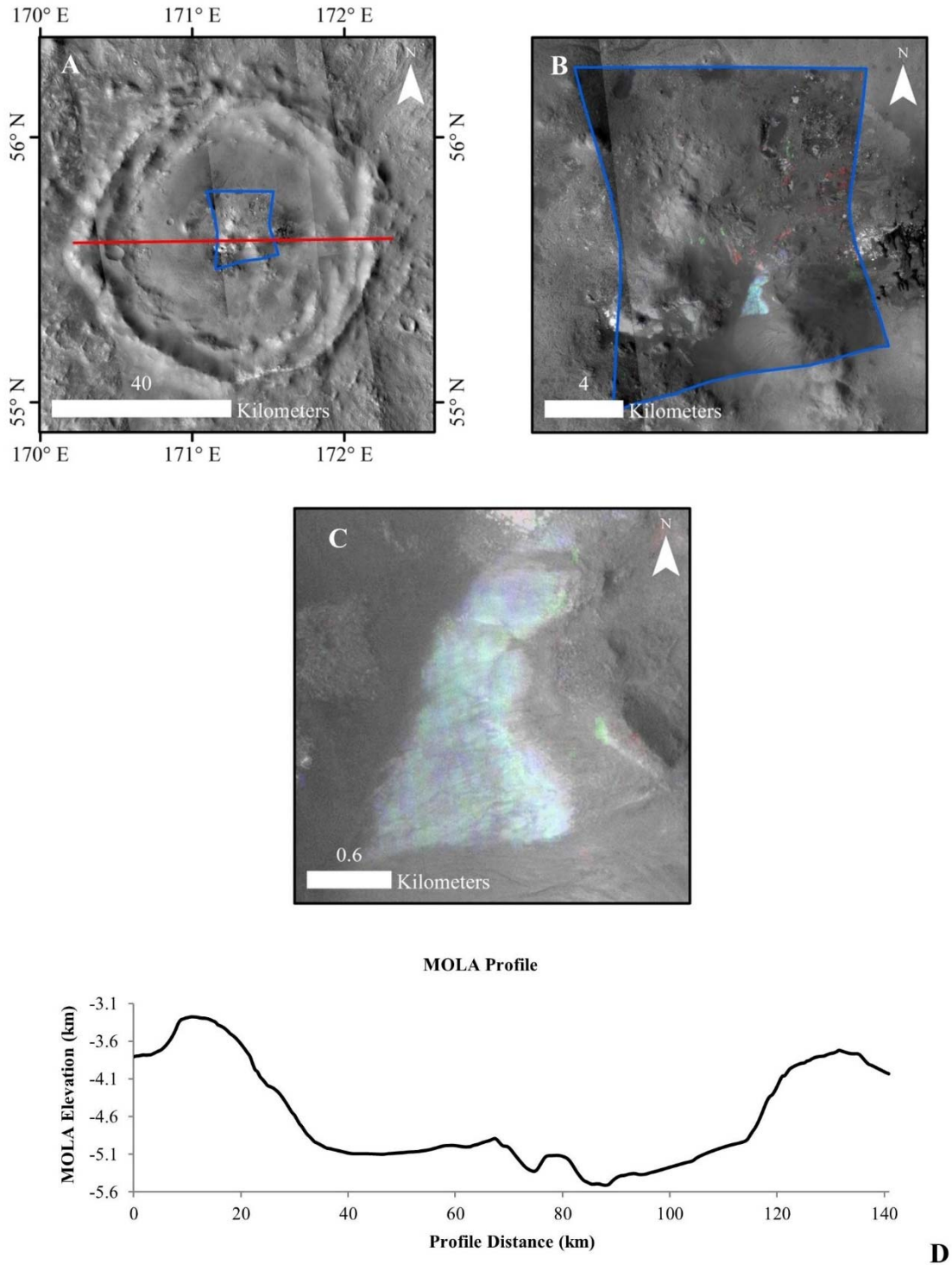


Figure 4.6. Complex impact crater Stokes located 55.62°N, 171.29°E of diameter 62 km. **A)** CTX mosaic showing the impact crater with CRISM FRT0000ADA4 outline (blue) and location of the MOLA profile (red) overlain. **B)** CTX mosaic with CRISM FRT0000ADA4 RGB parameter map (Pelkey et al., 2007) composite D2300 (red), BD2210 (green) and BD1900 (blue) overlain and colour-merged. **C)** Image extracted from B showing areas of mixed absorptions by RGB parameter maps (1.9 μm and 2.21 μm highlighted by cyan). **D)** MOLA profile of impact crater shown in A.

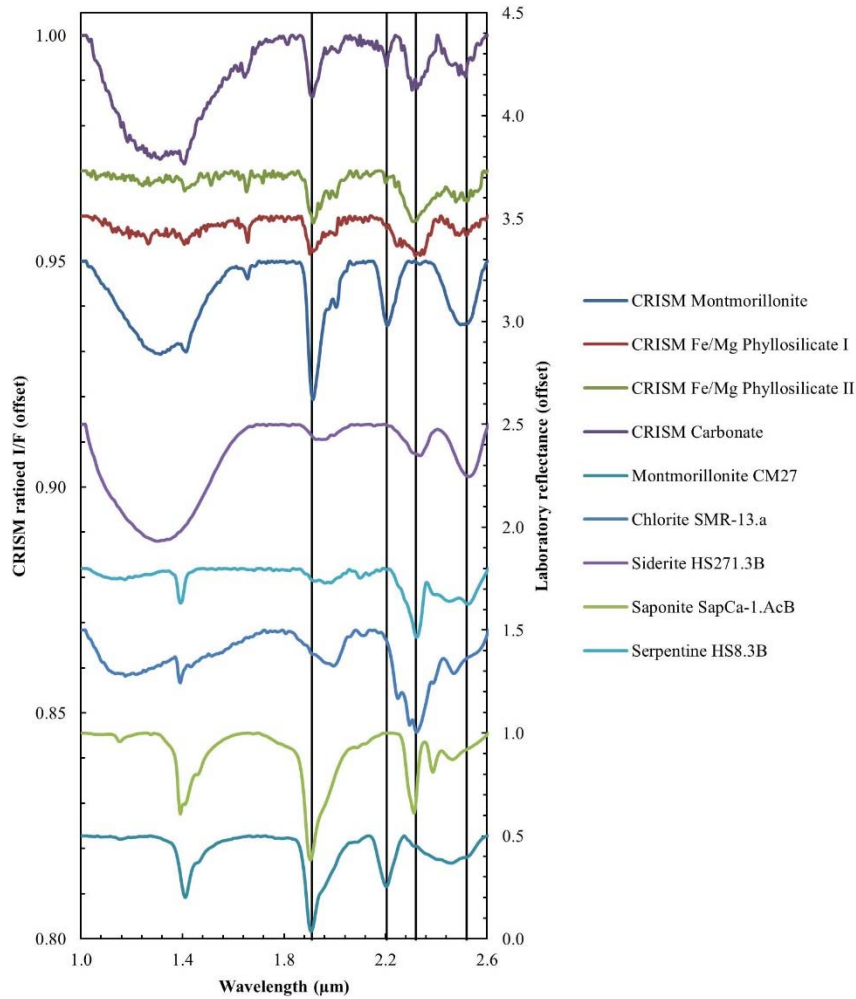


Figure 4.7. Comparisons of extracted spectra from FRT0000ADA4 covering Stokes impact crater shown in figure 4.6 and spectra from the USGS Spectral Library (Clark et al., 2007). All extracted CRISM spectra have an absorption at $\sim 1.91 \mu\text{m}$. Additional absorptions are found for CRISM Montmorillonite at $2.2054 \mu\text{m}$, CRISM Fe/Mg phyllosilicate I at 2.25 and $2.33 \mu\text{m}$, CRISM Fe/Mg phyllosilicate II at $2.31 \mu\text{m}$, and CRISM carbonate at 2.33 and $2.52 \mu\text{m}$. All extracted spectra have an absorption at $2.5 \mu\text{m}$, indicating an intermixed phase. USGS Spectra for Montmorillonite CM27, Chlorite SMR-13.a, Saponite SapCa-1.AcB, Serpentine HS8.3B and Siderite HS271.3B.

A previous CRISM investigation of this crater (scene FRT0000ADA4) detected Fe-Mg phyllosilicate, chlorite, and the Al phyllosilicates montmorillonite $((\text{Na,Ca})_{0.33}(\text{Al,Mg})_2(\text{Si}_4\text{O}_{10})(\text{OH})_2 \cdot n\text{H}_2\text{O})$ and kaolinite $(\text{Al}_2\text{Si}_2\text{O}_5(\text{OH})_4)$, along with pyroxene and olivine in and around the fractured central uplift (Carter et al., 2010). Similar observations have been made in this study, although additional minerals have also been detected. Figure 4.7 compares four spectra extracted from CRISM FRT0000ADA4 with spectra from the USGS Spectral Library. All CRISM extracted spectra have an

absorption at $\sim 1.91 \mu\text{m}$. Montmorillonite has been identified with an Al-OH absorption extending 2.15-2.28 μm centred at 2.2054 μm , as previously identified by Carter et al. (2010), although terrains we sampled also have a strong $\sim 2.5 \mu\text{m}$ absorption not typical of montmorillonite and indicating an intermixed hydrated phase, possibly a hydrated salt or zeolite. Fe/Mg-rich phyllosilicate, comparable to chlorite, has been identified by an absorption at 2.33 μm with a shoulder at 2.25 μm , as previously identified by Carter et al. (2010). Another Fe/Mg-rich phyllosilicate is identified by a 2.31 μm absorption. Finally, a spectrum comparable to the carbonate siderite was identified by absorptions at 2.33 μm and 2.52 μm . CRISM coverage of the crater ejecta (FRT00008A1E, HRL000183FB, HRL000194A3 and HRS0001B728) proved inconclusive for the identification of hydrous minerals. Both the present study and that of Carter et al. (2010) suggest the presence of alteration minerals within the central uplift of the crater, but absence in the ejecta surrounding the crater.

4.4 Discussion

A previous investigation of hydrated deposits detected in 9 impact craters located in the northern lowlands concluded that the bulk of large diameter impact craters in the northern plains expose the pre-altered Noachian basement (Carter et al., 2010, 2013). The distinction between excavation and impact-induced alteration is dependent on the location of the hydrated minerals within the impact crater. Occurrences of impact-induced, hydrated mineralization are expected in and around the central uplift and lower crater walls, whereas excavated hydrated minerals would lead to deposits of hydrated minerals in the central uplift, walls, but also in the crater ejecta (Abramov and Kring, 2005; Ehlmann et al., 2011b). In the case of this study, each impact crater was carefully considered for the arguments of pre- versus post-impact induced hydrothermal alteration.

4.4.1 Unnamed Ismenius Lacus Impact Crater

For the unnamed impact crater in the Ismenius Lacus quadrangle shown in section 4.3.1, it is possible that the observed Fe/Mg phyllosilicates formed within the central uplift and were subsequently excavated, transported and deposited by the processes that led to the formation of the gullies and alluvial fans — by a process of physical weathering. The source of the gullies can also clearly be tracked to rocky alcoves on the central peak that have spectral signatures consistent with Fe/Mg phyllosilicates (figure 4.3). Megabreccia blocks on the central uplift also have spectral signatures suggestive of

Fe/Mg phyllosilicates. As shown in the results these Fe/Mg phyllosilicate minerals are likely to be Fe-serpentine or chlorite, possibly with prehnite.

The relatively juvenile nature of the alluvial fan with no surface impact craters means that chemical weathering on the surface is unlikely to be the origin of the secondary minerals. The two alluvial fans differ from previous findings in that they emanate from gullies that do not appear on equator-facing slopes as suggested by previous studies for gullies at this latitude (Heldman et al., 2007). In this study, gullies have been observed on pole-facing, eastern and western slopes with slopes ranging from 3.3°-14.7°. In comparison, a previous study showed that gully formation in the 30°-45°S latitude region typically requires steep slopes as 87% of detected gullies have formed on slopes >21° (Dickson et al., 2007). As detailed above, the network of channels comprising the northern- and western-facing gullies can be tracked back to a rocky cap on the central peak (figure 4.2D). This suggests a prolonged, perhaps episodic, period of gully and fan formation, implying that such fans are not the result of one event alone, which is consistent with other studies of gully systems in impact craters (Schon et al., 2009). At the northern base of the central uplift, the fan deposits are obscured by an overlying dune field. A fan angle of repose of >26° (Heldmann and Mellon, 2004) and gully and alluvial morphology indicate that formation by a dry mass-wasting process is unlikely. The intact state of the gully and fan differ from others found in the northern hemisphere where the majority tend to be eroded (Heldmann et al., 2007), indicating that the gullies found in figure 4.3 are young in comparison.

The location of the phyllosilicate minerals — within alluvial fans, gullies and megabreccia blocks on the central uplift — suggests a post-impact alteration process, although pre-impact formation and subsequent excavation cannot be ruled out with 18 m-scale orbital reflectance data alone. The lack of hydrous minerals in the crater walls and, more importantly, ejecta further suggests the possibility of an impact-induced hydrothermal system. The Fe/Mg phyllosilicates — likely Fe-serpentine or chlorite — detected in the alluvial fans and gullies may have formed in the subsurface of the central uplift where the circulation of hydrothermal fluids might have been present post-impact. Then, these altered deposits were since excavated, eroded, and transported by the gully system to the alluvial fans at the base of the central uplift. We favor this model of recent redistribution of hydrated minerals, but alternatively, the central peak may have discharged waters through the central peak to form the channels and alluvial fans. If

prehnite is present then it would indicate alteration at elevated temperatures of 200-350 °C (Robinson and Bevins, 1999).

4.4.2 Unnamed Elysium Impact Crater

The unnamed Elysium impact crater in section 4.3.2 exhibits hydrated minerals in heavily eroded sediments around the southwest region of the central uplift. No hydrated minerals are found around the crater rim or in the ejecta. The interior sediments appear to postdate the formation of the crater with no obvious link to the crater's formation or potential impact hydrothermal history. They may be analogous to interior layered deposits frequently found in large craters, notably within Arabia Terra. The clay minerals may have formed in place through diagenesis, similar to that in Gale Crater (Bridges et al., 2015), or have formed outside the crater and been deposited. The hydrated minerals found here are unlikely to be the result of impact-induced hydrothermal alteration.

4.4.3 Stokes Impact Crater

In section 4.3.3, the spectra of Stokes impact crater show no clear evidence of absorptions due to hydrous minerals in the crater ejecta. Nevertheless, previous work concluded that all hydrated minerals formed pre-impact due to the proximity of a suite of alteration minerals (serpentine, chlorite, nontronite and kaolinite) to unaltered olivine and pyroxene within the central structure of the crater (Carter et al., 2010). The analysis of Stokes crater was part of a study that showed nine craters in the northern plains host hydrated silicates, and the conclusion of excavation applied to the group of craters as a whole because only the largest of the craters, which had the capacity to excavate beneath post-Noachian units, had signatures of hydrated minerals (Carter et al., 2010). Studies have shown that Al-phyllsilicates might form as a result of impact-induced hydrothermal alteration (Schwenzer and Kring, 2009). Al-phyllsilicates have been found by MER Opportunity at Endeavour crater, along with Fe-smectites (Arvidson et al., 2014). Previous studies of Majuro and Toro impact craters have demonstrated how the link between hydrated minerals and the central uplift can help in identifying impact-induced hydrothermal systems (Marzo et al., 2010; Mangold et al., 2012). The Al-phyllsilicate, possibly montmorillonite, is detected on a large outcrop within the fractured central uplift of Stokes crater (figure 4.6C). Either formation post impact or excavation are permitted; orbital reflectance data at 18 m per pixel resolution cannot distinguish.

4.4.4 Comparisons with previous studies

Fe/Mg phyllosilicates in the central peak but not the upper walls and ejecta are consistent with impact-induced hydrothermal models for complex impact craters in which serpentine, chlorite and nontronite ($\text{Na}_{0.3}\text{Fe}^{3+}_2(\text{Si},\text{Al})_4\text{O}_{10}(\text{OH})_2 \cdot n\text{H}_2\text{O}$) are predicted to occur on central uplifts (Schwenzer and Kring, 2009, 2013). Clearly, impact excavation from depth could also produce hydrated minerals in the central peak. In the absence of a mechanism for masking the spectral signature of excavated materials in the walls and ejecta but not in the central uplift, the most logical explanation is post-impact formation of the hydrated minerals. However, one mechanism for masking signatures could be higher topographic relief in the central peak resulting in more active erosion leaving the minerals exposed and free of dust cover compared to the crater walls and ejecta.

Previous studies reported that 19 impact craters out of a sample of 100 show hydrated minerals in the northern plains, and concluded that these hydrated minerals were excavated from pre-existing underlying layers dating from the Noachian, based on depth-to-diameter relations (Carter et al., 2010, 2013). However, on the basis of our results, it is evident that each crater must be individually analysed in detail in order to determine the exact origin of hydrated minerals. We conclude that 1-2 of the 158 post-Noachian craters may host hydrated minerals formed by impact-induced hydrothermal activity. Another recent study of clays on crater central peaks found that ten Amazonian-aged impact craters showed evidence for hydrated minerals, and four craters had clays solely in impact melt units (Sun and Milliken, 2015). The study by Sun and Milliken (2015) differs from this one by studying a global population of 633 impact craters on Mars and then using crater counts to determine the age of each crater, rather than using superposition relationships with terrains mapped and craters counted for the latest USGS geologic map of Mars, as in this study.

Our results suggest impact-induced hydrothermal alteration may be associated with the central uplifts of the unnamed Ismenius Lacus impact crater and Stokes impact crater, implying post-Noachian impact hydrothermalism. Previous studies have found evidence for impact-induced hydrothermal alteration in the Hesperian-aged Majuro (Mangold et al., 2012) crater, and suggested for the Noachian-aged Holden crater (Grant et al., 2008; Tornabene et al., 2009; Osinski et al., 2013) and the Hesperian-aged Toro crater (Marzo et al., 2010). Moreover, meteorite data from the Amazonian-aged SNCs suggest that minor amounts of post-impact alteration occurred (Changela and Bridges, 2010; Bridges and Schwenzer, 2012; Hicks et al., 2014).

4.4.5 Low abundance of Impact-Induced Hydrothermal Systems

Multiple causes are possible for the apparent rarity of impact-induced hydrothermal systems within complex post-Noachian, and in particular Amazonian, impact craters (diameter >7 km). First, such systems may in fact have rarely occurred, limited by the availability of liquid water. Second, the paucity of identified systems could be the result of the lack of surface exposure of alteration minerals, since impact-induced hydrothermal systems are predominantly subsurface processes and, moreover, underlying lithology is frequently obscured from remote sensing by dust cover. In some regions on Mars (e.g. Tharsis) dust coverage is extensive, particularly in younger Amazonian-aged terrains, therefore limiting the use of reflectance spectroscopy. Extensive crater in-filling by sediments after impact-induced hydrothermal systems ceased would also obscure impact-associated hydrothermalism. Third, the abundance of alteration minerals could be relatively small in typical Amazonian hydrothermal systems, as exemplified by the abundance of alteration phases in the nakhlite meteorites (e.g. Changela and Bridges, 2011). The presence of hydrated phases at a few weight-percent abundance or less is not readily discernible in infrared remote sensing datasets. These hydrothermal systems causing little or spatially confined alteration would be impossible to detect with current remote sensing capabilities. Finally, the proportion of craters with high-resolution CRISM coverage is relatively small, which means the proportion of Amazonian craters that have experienced hydrothermal activity as a result of an impact could be underestimated.

The dominant heat source for a complex impact crater depends on crater size. For impact craters ≥ 7 km and <130 km this is the central uplift, whereas in larger diameter impact craters ($>\sim 130$ km) the dominant heat source is the impact melt rather than the central uplift. Nevertheless, the central uplift is still important as it raises the underlying geothermal gradient (Daubar and Kring, 2001). In contrast, for smaller, simple craters (diameter <7 km) the dominant heat source is shock-emplaced heat that may result in short-lived alteration of the Martian crust (Schwenzer and Kring, 2013). The smaller crater survey was included in this study in an attempt to identify alteration minerals in such impact craters; however, no hydrated minerals were identified. This lack of hydrated signatures could be due to a number of reasons: a) no alteration took place; b) alteration was restricted to the unexposed subsurface; c) dust coverage may be masking spectral signatures; d) the mineral outcrops are not sizable enough for CRISM to resolve; or, e) the alteration minerals are of low abundance.

4.4.6 Technical limitations of this study

This study highlights the current limitations in identifying impact-induced hydrothermal systems on Mars and analogues (or source regions) for the Martian meteorites. Current remote sensing technologies to determine surface composition (i.e., OMEGA and CRISM) use reflectance spectroscopy, and are unable to probe more than a millimeter beneath the surface, relying on erosion to expose bedrock and materials of interest for sensing. As previously stated, another limitation to consider is the ~ 20 m/pixel resolution of CRISM as some mineral outcrops may not be sizable enough to resolve at that scale. Nevertheless, CRISM has been able to provide a detailed surface mineralogy of Mars (e.g. Murchie et al., 2009a; Carter et al., 2013); however, analysis of the CRISM dataset is hampered by spectral artefacts such as spurious pixels caused by detector temperature (Murchie et al., 2009b). The standard approach of analysing CRISM data using spectral ratios (as used in this study) works well to divide out most spectral artefacts, although some still do persist (Murchie et al., 2009b). More complex statistics-based analysis using principal components analysis and minimum noise transformation was explored during this study but these techniques were found to be inapplicable to the dataset due to the systematic column-to-column differences and the presence of random noise.

4.4.7 Relevance to the Nakhrites

Previous work linking the nakhlite alteration assemblages to impact-induced hydrothermal systems has suggested that the size and age of craters examined in this study are those where such a mineral assemblage could have been produced (Changela and Bridges, 2010; Bridges and Schwenzer, 2012). Links between the laboratory-based studies on Earth of the nakhlites (Changela and Bridges, 2010; Hicks et al., 2014) and remote sensing studies of Mars have limitations as the nakhlites were excavated from the subsurface. Small amounts of alteration like those seen in the nakhlites e.g. $\sim \leq 1$ wt% may very well be undetectable in orbital infrared data, based on laboratory study of nakhlite bulk rock spectra (Hamilton et al., 1997; Schade and Wasch, 1999); however, the secondary minerals identified here (i.e., Fe/Mg phyllosilicates) are similar to those of the nakhlites and may have a similar impact-associated origin.

4.5 Conclusions

1. This study conducted CRISM analysis of 144 craters of ≥ 7 km diameter in terrains mapped as Amazonian or Amazonian-Hesperian on Mars. This search was mainly performed in the Northern lowlands with a further search around Hellas Basin however; no CRISM coverage was available for the Hellas region. Hydrated minerals in these impact craters appear scarce, with only 3 out of 144 craters in this study showing spectral signs of such minerals.
2. Gullies, alluvial fans, and uplifted breccia in the central uplift of an unnamed 20 km diameter impact crater (located at 52.42°N, 39.86°E in the Ismenius Lacus quadrangle) show spectral evidence for a chlorite or Fe-serpentine that may have formed through erosion and redeposition of impact-induced hydrothermal mineral assemblages during the Amazonian epoch.
3. Fe/Mg/Al phyllosilicates, chlorite and carbonate in the 62 km diameter Stokes impact crater may be the result of impact-induced hydrothermal alteration.
4. Excavation of older, pre-impact altered, Noachian terrains cannot be ruled out as a potential origin for the hydrated minerals found in this study.
5. A small crater survey concluded that 14 simple impact craters of diameters ≥ 3 km and < 7 km in relatively dust-free Amazonian terrains in the Northern plains lack hydrated minerals in available CRISM data.
6. Our work suggests that hydrothermalism was rare in the Amazonian or not extensive enough to be detectable at CRISM spatial scale.

5. Back-Reflection Energy-Dispersive X-ray Diffraction: Application and Analysis

In this chapter, the back-reflection energy-dispersive X-ray diffraction technique outlined in Chapter 3 is demonstrated and tested using a pre-existing CCD and bespoke SDD laboratory facilities by analysing a variety of pellet and whole rock samples. The sample morphology insensitivity of the back-reflection technique is demonstrated, along with a method of investigating preferred orientation of crystallites. The samples were selected on the basis of what would aid in the geologic characterisation of an area on a foreign body such as Mars. This study demonstrates the capability of the back-reflection method and showcases its suitability for potential deployment on a future planetary science mission. Future avenues of investigation for the back-reflection technique are also discussed.

5.1 Samples for Analysis

Samples selected for this analysis were chosen on the basis of demonstrating the suitability of the back-reflection technique for geologic characterisation of the mineralogy on a planetary body, such as Mars.

5.1.1 Oxide and Feldspar Minerals

Oxide and feldspar minerals selected for analysis were: quartz (SiO_2), goethite ($\alpha\text{-FeO(OH)}$), hematite (Fe_2O_3), plagioclase feldspar ($\text{NaAlSi}_3\text{O}_8 - \text{CaAl}_2\text{Si}_2\text{O}_8$), orthoclase feldspar (KAlSi_3O_8) and magnetite (Fe_3O_4). Feldspar minerals, outlined in figure 5.1, can indicate a variety of past geological environments due to temperature and pressure formation constraints, meaning the ability to detect and differentiate feldspars is an important aid in the characterisation of a geologic environment. Feldspars are one of the most abundant minerals present in igneous rocks and are also present in metamorphic and sedimentary rocks. The alteration and weathering of feldspars can result in clay minerals (Deer et al., 1992). Quartz can crystallise from molten magma or as a secondary mineral in hydrothermal veins, and is a major constituent of igneous, metamorphic and sedimentary rocks (Deer et al., 1992). Goethite is commonly produced as a weathering product from Fe-rich minerals and can precipitate from groundwater. It can also form as a result of hydrothermal alteration (Deer et al., 1992). Hematite is largely found as a weathering product of Fe-rich minerals, but can also occur in igneous rocks, where source

magma was poor in Fe^{2+} , and in metamorphic rocks due to the metamorphism of magnetite, siderite and hydrated Fe-oxides (Deer et al., 1992). Magnetite forms when mafic magma cools at a slow rate (Deer et al., 1992). Feldspars, quartz, hematite and magnetite have been discovered on Mars using XRD data returned by the CheMin instrument (Bish et al., 2013). Goethite has not been detected with CheMin at the time of writing, however it has previously been detected at Eagle crater, Meridiani Planum crater by MER Opportunity (Klingelhöfer et al., 2004) and at Gusev crater by MER Spirit (Klingelhöfer et al., 2006).

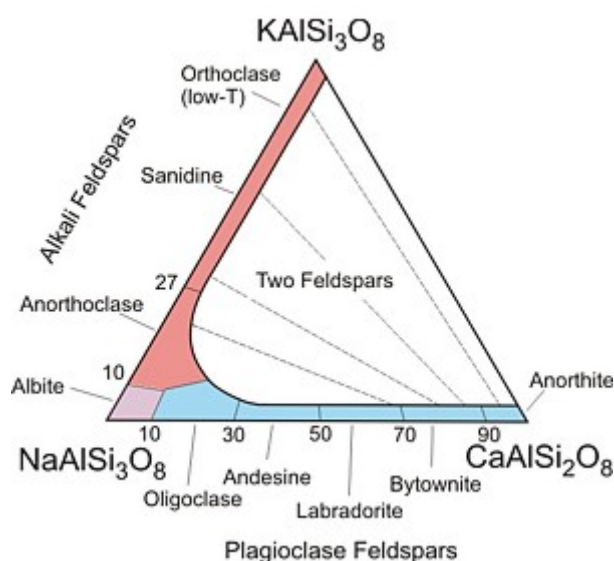


Figure 5.1. Feldspar solution series (Imperial College London, 2016).

5.1.2 Carbonate minerals

Carbonates such as calcite (CaCO_3) and dolomite ($\text{CaMg}(\text{CO}_3)_2$) were selected for analysis in this chapter. These sedimentary rocks are formed by the accumulation of sediments in a marine environment. Both calcite and dolomite form in hydrothermal environments, and Mg/Fe/Ca carbonates have previously been detected on Mars by MER Spirit in Columbia Hills, Gusev crater (Morris et al., 2010).

5.1.3 Sulphate Minerals

Sulphates such as gypsum ($\text{CaSO}_4 \cdot 2\text{H}_2\text{O}$), bassanite ($\text{CaSO}_4 \cdot 0.5\text{H}_2\text{O}$), anhydrite (CaSO_4) and jarosite ($\text{KFe}^{3+}_3(\text{OH})_6(\text{SO}_4)_2$) were analysed with the back-reflection technique. These minerals are of particular interest in planetary science as they can form from the evaporation of a body of standing water or groundwater. Sulphates have been detected with CheMin on-board MSL at Gale crater (Bish et al., 2013; Vaniman et al.,

2014) and by MER Opportunity at Meridiani Planum (Klingelhöfer et al., 2004; Clark et al., 2005; Squyres et al., 2012).

5.1.4 Phyllosilicate Minerals

Phyllosilicates such as prehnite ($\text{Ca}_2\text{Al}_2\text{Si}_3\text{O}_{10}(\text{OH})_2$), mica (muscovite ($\text{KAl}_2(\text{AlSi}_3\text{O}_{10})(\text{OH})_2$)), talc ($\text{Mg}_3\text{Si}_4\text{O}_{10}(\text{OH})_2$) and kaolinite ($\text{Al}_2(\text{Si}_2\text{O}_5)(\text{OH})_4$) were also analysed. Kaolinite deposits occur as alteration products of feldspars and muscovite type minerals by weathering or low-temperature hydrothermal alteration. Prehnite and talc occur as secondary minerals in igneous rocks as the result of hydrothermal alteration (Schwenzer and Kring, 2009), as discussed in Chapter 4. Prehnite, muscovite and kaolinite have been detected on Mars with remote sensing datasets (Ehlmann et al., 2009, 2011a, 2011b; Turner et al., 2016), with additional evidence for kaolinite identified by MER Spirit at Columbia Hills, Gusev crater (Wang et al., 2006).

5.2 Experimental Summary

Each of the samples outlined in section 5.1 were analysed with either the pre-existing CCD or bespoke SDD back-reflection facilities outlined in Chapter 3, which are briefly summarised here, along with data analysis techniques.

The pre-existing CCD laboratory facility consisted of a vacuum chamber equipped with an X-ray tube source, sample holder and a charge-coupled device (CCD) that was connected to a liquid nitrogen fed cold finger (figure 3.9). The sample holder and the CCD were manoeuvrable to allow for different 2θ configurations. Two different sample holders were available for the CCD laboratory facility: a pellet sample holder and a rock sample holder. For the experiments conducted in this chapter the facility was configured to meet a 2θ angular range of $161 - 168^\circ$, which is sufficiently close to 180° to meet the back-reflection criteria outlined in Chapter 3 and by Hansford (2011a). CCD energy-calibration was undertaken using an ^{55}Fe source in initial experiments where 50 frames were acquired, with a polyhalite ($\text{K}_2\text{Ca}_2\text{Mg}(\text{SO}_4)_2 \cdot 2\text{H}_2\text{O}$) calibration target later secured to the sample holders for a secondary wider-range energy calibration when subjected to 8 keV X-rays for 100 CCD frames. This was the experimental setup used by Hansford (2013) for the proof-of-principle experiments for the back-reflection technique.

The optimised, bespoke SDD facility consisted of a vacuum chamber equipped with an X-ray tube source, a sample platform mounted on translation stages and an annular silicon-drift detector (SDD) (figure 3.11). Source-sample and sample-detector

distances were variable and much shorter compared to the pre-existing CCD facility resulting in faster data acquisition times, and the back-reflection geometry is more closely achieved by use of an approximately annular SDD. SDD energy calibration was achieved by using sample fluorescence produced by subjecting the sample for analysis to an incident beam of X-rays, which was produced by an X-ray tube of excitation voltage of 8 kV with an emission current of 1.8 mA. Generally, fluorescence peaks were more dominant than diffraction peaks but when there was identification doubt comparisons were made between two 8 kV datasets acquired at different sample-detector distances (diffraction peaks would shift position as opposed to fluorescence peaks).

In both the pre-existing CCD and bespoke SDD laboratory facilities, for each sample an initial 8 kV spectrum was acquired to assess the extent of fluorescence peak overlap on the diffraction peaks. An initial 8 kV spectrum also ensured sufficient Bremsstrahlung intensity at 5 keV (1.24 Å in the back-reflection geometry). For spectra where fluorescence occurred at >2 keV, a method of fluorescence suppression was adopted where the X-ray tube voltage was tuned to just below the absorption edge energy. Due to the differences between absorption edge energy and the energy of fluorescence lines, any underlying diffraction peaks will be exposed in the resultant spectrum. For example, in a spectrum where Ca $K\alpha$ and $K\beta$ fluorescence is present at respective energies 3.691 and 4.013 keV the X-ray tube voltage can be tuned to just below the Ca K absorption edge at 4.034 keV to 4.03 keV, thus suppressing Ca fluorescence and exposing any underlying diffraction peak. This approach is shown in Hansford et al. (2014), demonstrating its effectiveness at exposing underlying diffraction peaks.

5.3 Data Analysis Approach

Data taken with the CCD back-reflection facility was processed using CCD analysis software developed in-house at the University of Leicester. Isolated and corner-connected single-pixel events were processed and interpreted by comparisons to model diffraction and fluorescence data produced by PoDFluX (Hansford, 2009). Diffraction and fluorescence peaks were discernable in the data returned by the pre-existing CCD facility, as the data could be split into regions where events were incident on the CCD. Spectra acquired at the top and bottom thirds of the CCD were compared to identify diffraction peaks, as their position would shift. PoDFluX models X-ray diffraction and fluorescence of a sample on to an imaging or energy-resolving detector by use of Monte Carlo ray-tracing simulations, and was previously used to investigate different XRD

geometries (Hansford, 2011b, 2012) including the back-reflection geometry (Hansford, 2011a, 2013; Hansford et al., 2014). For a PoDFluX simulation the instrument geometries, X-ray tube voltage and filament current need to be specified, along with the crystal structure of the mineral(s) to be modelled. Crystal structure files were obtained from the American Mineralogist Crystal Structure Database (AMCSD) (2016). Specified preferred orientation of crystallites along any given (*hkl*) plane can be accounted for in PoDFluX models, as it incorporates the March-Dollase function (Dollase, 1986; Hansford et al., 2014).

A modified version of PoDFluX, PoDFast, produces X-ray diffraction and fluorescence models without using Monte-Carlo ray tracing simulations (Hansford, 2015), and thus producing models at a much faster rate. PoDFast was incorporated into a mineral-fitting routine, whereby an experimentally acquired dataset can be plotted against a model produced by PoDFast and a chi-squared goodness of fit calculation is performed. The mineral-fitting routine iterates the PoDFast simulations, altering the energy calibration of the experimentally acquired spectrum, along with simulation run time and mineral/element quantities per iteration to enhance the model and give a closer fit to the experimental data. The mineral-fit routine can also estimate Rayleigh scattering contributions using PoDFast (Hansford, 2015), although this introduces a Cu- $L\alpha$ peak at ~ 0.9 keV that isn't present in the experimental data due to an aluminised Lexan filter positioned between the X-ray tube and the vacuum chamber. This filter is estimated to be 0.5 μm Al and 2.0 μm polycarbonate (Lexan) (Hansford, 2015). The mineral-fitting routine was used primarily for analysing datasets taken by the bespoke SDD laboratory facility.

5.4 Sample Results and Analysis

The back-reflection XRD results of a variety of anhydrous, carbonate, sulphate and phyllosilicate minerals are presented here, with key plots for each sample presented and additional plots located in Appendix B. Table 5.1 summarises the samples analysed in this chapter.

Table 5.1. Table of samples analysed in this chapter using the back-reflection technique.

Sample	Notes	Sample Form	Facility Utilised	Datasets Acquired ^a	Dataset location within this Thesis
<i>Sample Group A: Oxide and feldspar samples</i>					
Quartz	Quartz	Pellet	Pre-existing CCD	8 kV / 0.1 mA (1800 CCD frames / 3 hours)	Figure 5.2 & Appendix B.1
	pellet		Bespoke SDD	8 kV / 1.8 mA (20 minutes)	Figures 5.2 & 5.3
Goethite	Unknown	Pellet & Rock	Bespoke SDD	8 kV / 1.8 mA (10 minutes)	Appendix B.2
	origin			Fe-suppression 7.1 kV / 1.8 mA (10 minutes)	Figure 5.5 & 5.6
Hematite	Unknown	Pellet & Rock	Bespoke SDD	8 kV / 1.8 mA (10 minutes)	Appendix B.3
	origin			Fe-suppression 7.1 kV / 1.8 mA (10 minutes)	Figure 5.7 & 5.8
Evje	Orthoclase	Rock	Bespoke SDD	8 kV / 1.8 mA (10 minutes)	Appendix B.4
	feldspar			K-suppression 3.6 kV / 2.0 mA (30 minutes)	Figure 5.10
Iveland	Plagioclase	Rock	Bespoke SDD	8 kV / 1.8 mA (10 minutes)	Appendix B.5
	feldspar			Ca-suppression 4.03 kV / 2.6 mA (10 minutes)	Figures 5.12 – 5.14
Brastad	Magnetite	Rock	Bespoke SDD	8 kV / 1.8mA (10 minutes)	Appendix B.6
				Fe-suppression 7.1 kV / 1.8 mA (10 minutes)	Appendix B.6
				Ca-suppression 4.03 kV / 2.6 mA (20 minutes)	Figure 5.16
<i>Sample Group B: Carbonate samples</i>					
Hope	Limestone	Rock	Pre-existing CCD	8 kV / 0.1 mA (1800 CCD frames / 3 hours)	Appendix B.7
				Ca-suppression 3.95 kV / 1.0 mA (1800 CCD frames / 3 hours)	Figure 5.18 & Appendix B.7
BastilleA	Limestone	Rock	Pre-existing CCD	8 kV / 0.1 mA (1800 CCD frames / 3 hours)	Appendix B.8
				Ca-suppression 3.95 kV / 1.0 mA (1800 CCD frames / 3 hours)	Figure 5.18 & Appendix B.8
MindelA	Limstone	Rock	Pre-existing CCD	8 kV / 0.1 mA (1800 CCD frames / 3 hours)	Appendix B.9
				Ca-suppression 3.95 kV / 1.0 mA (1800 CCD frames / 3 hours)	Figure 5.19 & Appendix B.9

Back-Reflection Energy-Dispersive X-ray Diffraction: Application and Analysis

MindelB	Limestone	Rock	Pre-existing CCD	8 kV / 0.1 mA (1800 CCD frames / 3 hours)	Appendix B.10
				Ca-suppression 3.95 kV / 1.0 mA (1800 CCD frames / 3 hours)	Figure 5.19 & Appendix B.10
JDo-1	Japanese dolomite standard	Pellet	Pre-existing CCD	8 kV / 0.1 mA (1800 CCD frames / 3 hours)	Appendix B.11
			Bespoke SDD	Ca-suppression 3.95 kV / 1.0 mA (1800 CCD frames / 3 hours)	Figures 5.19 & 5.20 & Appendix B.11
				<i>Preferred Orientation Investigation</i>	Figure 5.21
				Ca-suppression 3.95 kV / 1.0 mA (1200 CCD frames / 2 hours)	
				Various angle offsets: 0°, 10°, 20°, 30° and 40°.	
<i>Sample Group C: Sulphate samples</i>					
WatchetB	Mars analogue	Pellet (×2) & Rock	Pre-existing CCD	8 kV / 0.1 mA (1800 CCD frames / 3 hours)	Appendix B.12
				Ca-suppression 3.95 kV / 1.0 mA (1800 CCD frames / 3 hours)	Appendix B.12
				S-suppression 2.4 kV / 1.6 mA (1800 CCD frames / 3 hours)	Figure 5.23 & Appendix B.12
				<i>Second pellet only</i>	
				S-suppression 2.4 kV / 1.6 mA (1800 CCD frames / 3 hours) ×2	Figures 5.24 – 5.25
		Rock	Bespoke SDD	8 kV / 1.8 mA (10 minutes)	Appendix B.12
				Ca-suppression 4.03 kV / 2.6 mA (10 minutes)	Appendix B.12
				S-suppression 2.4 kV / 2.6 mA (10 minutes)	Figure 5.28
WatchetC	Mars analogue	Pellet (×2) & Rock	Pre-existing CCD	8 kV / 0.1 mA (1800 CCD frames / 3 hours)	Appendix B.13
				Ca-suppression 3.95 kV / 1.0 mA (1800 CCD frames / 3 hours)	Appendix B.13
				S-suppression 2.4 kV / 1.6 mA (1800 CCD frames / 3 hours)	Figure 5.27 & 5.29 & Appendix B.13
				<i>Second pellet only</i>	Figure 5.28
				S-suppression 2.4 kV / 1.6 mA (1800 CCD frames / 3 hours)	Appendix B.13
		Rock	Bespoke SDD	8 kV / 1.8 mA (10 minutes)	Appendix B.13
				Ca-suppression 4.03 kV / 2.6 mA (10 minutes)	Figure 5.31

Back-Reflection Energy-Dispersive X-ray Diffraction: Application and Analysis

				S-Suppression 2.4 kV / 2.6 mA (10 minutes)	
Thackaringa	Jarosite	Rock	Bespoke SDD	8 kV / 1.8 mA (10 minutes)	Appendix B.14
				Fe-suppression 7.1 kV / 1.5 mA (10 minutes)	Appendix B.14
				K-suppression 3.4 kV / 2.8 mA (10 minutes)	Figure 5.33
<i>Sample Group D: Phyllosilicate samples</i>					
Wave Hill	Prehnite	Rock	Bespoke SDD	8 kV / 1.8 mA (10 minutes)	Appendix B.15
				Ca-suppression 4.03 kV / 2.6 mA (30 minutes)	Figure 5.35
Mica	Mica	Pellet	Bespoke SDD	8 kV / 1.8 mA (20 minutes)	Appendix B.16
				Fe-suppression 7.1 kV / 1.8 mA (20 minutes)	Appendix B.16
				Ti-suppression 4.9 kV / 2.0 mA (20 minutes)	Appendix B.16
				K-suppression 3.6 kV / 2.0 mA (20 minutes)	Figure 5.36
TPM26	Talc	Pellet	Bespoke SDD	8 kV / 1.8 mA (10 minutes)	Figure 5.37
				Fe-suppression 7.1 kV / 1.8 mA (20 minutes)	Figure 5.37
				Ca-suppression 4.03 kV / 2.6 mA (20 minutes)	Figure 5.37
ECC China	Kaolinite	Pellet	Bespoke SDD	8 kV / 1.8 mA (20 minutes)	Figure 5.38
Clay				K-suppression 3.6 kV / 2.0 mA (20 minutes)	Figure 5.38
Kaolin	Kaolinite	Pellet	Bespoke SDD	8 kV / 1.8 mA (20 minutes)	Figure 5.39
				K-suppression 3.6 kV / 2.0 mA (20 minutes)	Figure 5.39

^aExperimental X-ray tube voltage and filament current with type of element suppression specified, with experimental duration given in brackets with number of CCD frames detailed where applicable.

5.4.1 Group A: Oxide and feldspar Samples

Sample group A comprised of a variety of oxide and feldspar samples, which are detailed in table 5.1.

5.4.1.1 Quartz

A highly-crystalline quartz pellet obtained from the Department of Geology at the University of Leicester was obtained and selected for analysis. Data was acquired using the pre-existing CCD and bespoke SDD facilities as detailed in table 5.1. X-ray diffraction and X-ray fluorescence modelling for quartz in the back-reflection geometry was undertaken using PoDFluX (Hansford, 2009) using data from Kihara (1990). The model was able to accurately reproduce the experimental data, as shown in figure 5.3. This demonstrates the accuracy of modelling experimental data acquired of a simple, mono-mineral sample and therefore improves confidence for the analysis of more complex, multi-mineral samples; however, inaccuracies at low energies (<1 keV) highlight model weaknesses.

Analysis of the 8 kV dataset acquired with the bespoke SDD laboratory facility was undertaken using the mineral-fit routine, which showed quartz to be the dominant mineral with trace amounts of fluorescence from Cr and K. Additional O was included in the fluorescence fit. Al was also included in the fluorescence fit but its origin could be a contribution from the vacuum chamber, not the sample. This model is shown in figure 5.2, and is separated into the diffraction and fluorescence model components for close comparison to the bespoke SDD dataset in figure 5.3.

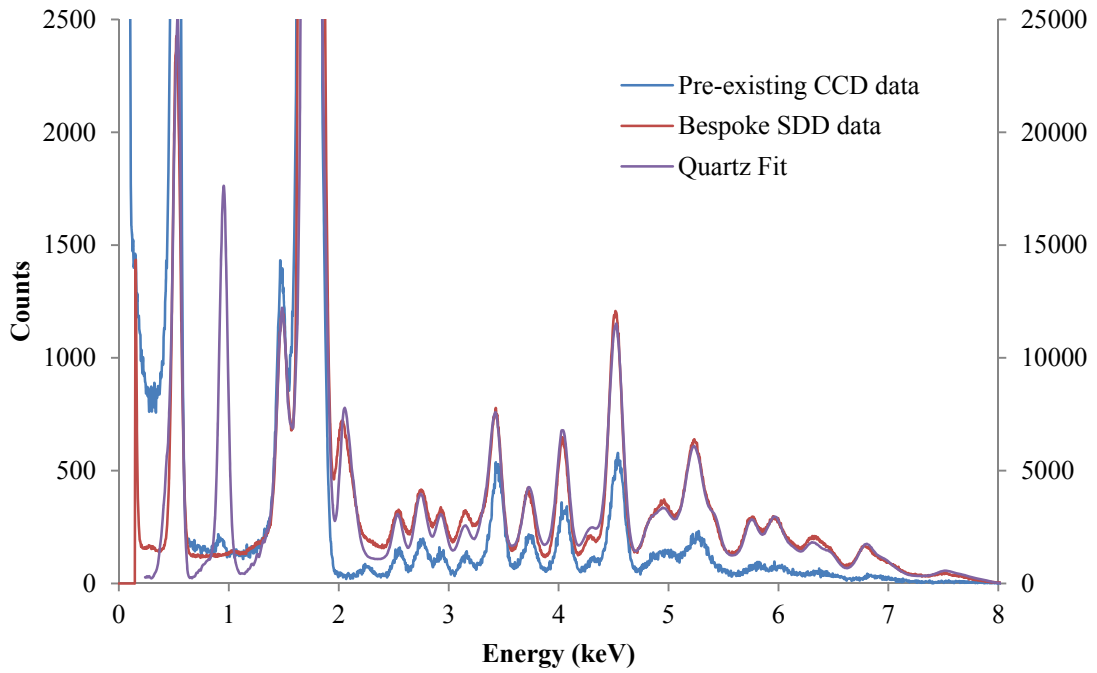


Figure 5.2. Datasets of a quartz pellet obtained with the pre-existing CCD and bespoke SDD back-reflection facilities. A Quartz fit produced by the mineral-fitting routine for the bespoke SDD dataset using data from Kihara (1990) is shown for comparative purposes.

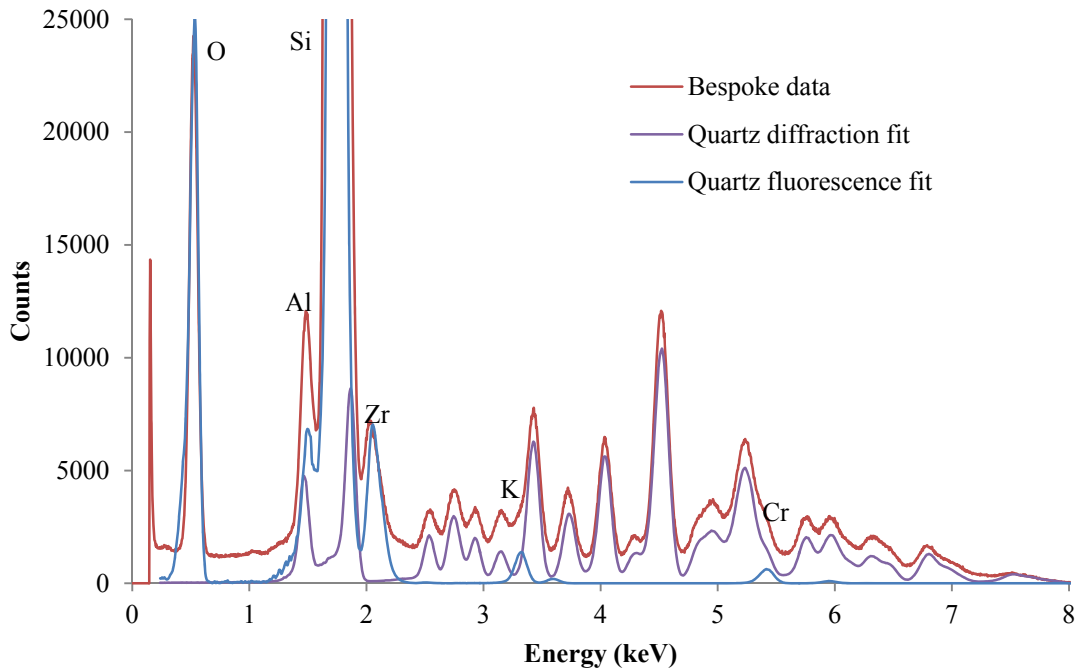


Figure 5.3. The bespoke SDD quartz pellet dataset compared to the diffraction and fluorescence components of the quartz fit shown in figure 5.2 created using the mineral-fitting routine with data from Kihara (1990). Rayleigh scattering is not included in diffraction or fluorescence fits in this figure.

5.4.1.2 Goethite

A goethite rock sample of unknown geological origin shown in figure 5.4 was obtained from the Department of Geology at the University of Leicester, and analysed using the bespoke SDD laboratory facility described in 5.2. Part of the whole rock sample was broken off, milled into a fine powder and pressed into a pellet with a boric acid backing. Datasets acquired of the goethite samples are outlined in table 5.1, with the Fe-suppression goethite pellet dataset shown in figure 5.5.



Figure 5.4. Goethite (left) and hematite (right) rock samples of unknown geological origin.

Figure 5.5 shows that the Fe-suppression dataset taken of the goethite pellet sample, obtained using the bespoke SDD facility, is best explained by a goethite fit produced using the mineral-fitting routine with data from Yang et al. (2006). A specified preferred-orientation effect along the (130) plane was determined through peak identification and is included in the goethite fit with a March coefficient of 0.613. Previous studies have shown (130) preferred-orientation effect in goethite, which is due to the orientation of needle-like crystallites along the (001) plane that enhances ($hk0$) peaks (Norrish and Taylor, 1962; Schulze and Schwertmann, 1984). The diffraction fit was marginally improved by the inclusion of 39% quartz, which explained a diffraction shoulder on the Si peak along with the Si fluorescence peak itself. Trace amounts of fluorescence from Cr was included in the fluorescence fit, along with additional O. Figure 5.6 shows the Fe-suppression dataset taken of the rock sample shown in figure 5.4 is explained well by goethite, as shown for the pellet sample in figure 5.5. The goethite fit also includes 22% quartz.

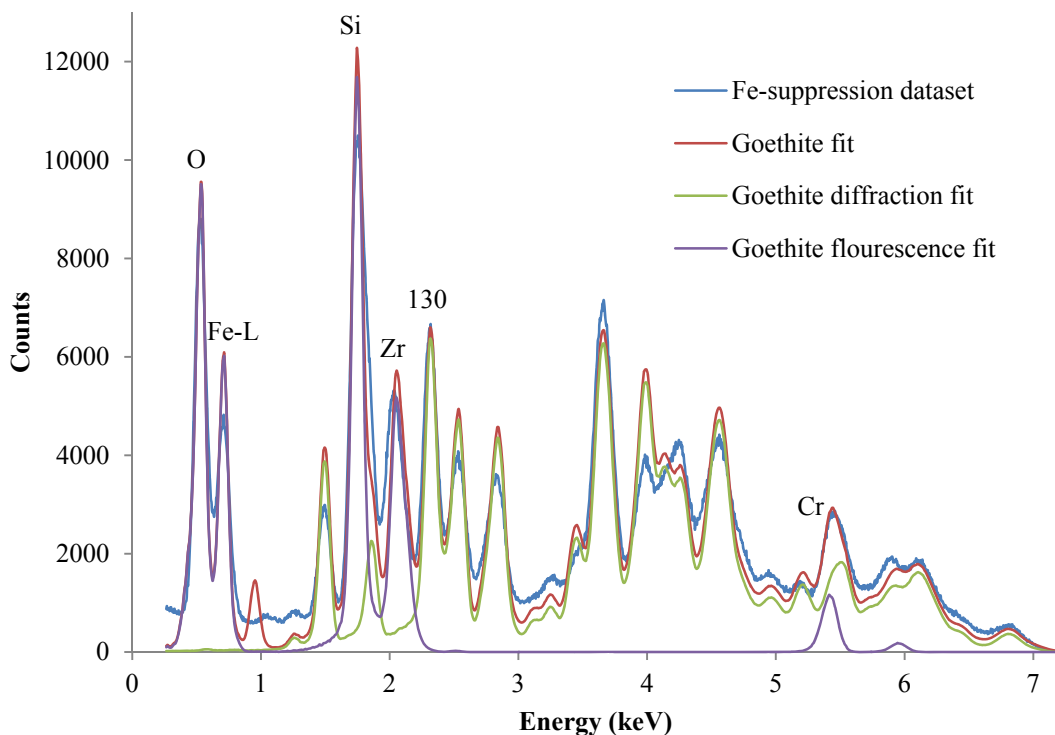


Figure 5.5. Fe-suppression dataset obtained using the bespoke SDD facility for goethite pellet sample compared to a goethite fit created using the mineral fitting routine with goethite data from Yang et al. (2006) and quartz data from Kihara (1990). The (130) reflection is marked along with fluorescence peaks. The diffraction and fluorescence constituents of the goethite fit are also plotted, neither of which account for Rayleigh scattering.

Differences between the goethite pellet and rock fits include an increase to the preferred orientation March coefficient along the (130) plane from 0.613 to 0.835. This change represents a decrease in preferred orientation of the crystallites along this plane for the rock sample, compared to the pellet, and therefore highlights a disadvantage of pellet sample preparation. It is important to note that the powder pellet is formed under pressure, and therefore the alignment of plate- or needle-type crystallites is to be expected (Girolami, 2016).

The 39% quartz component of the pellet as opposed to 22% quartz in the rock may be due to an inhomogeneous distribution of quartz, or this could be due to the difference in densities of goethite (4.274 g cm^{-3} (Yang et al., 2006)) and quartz (2.649 g cm^{-3} (Kihara, 1990)) that resulted in component separation during sample preparation. The difference in peak intensity between the model and the datasets could indicate that the model is underestimating peak-broadening effects or is incorrectly estimating Rayleigh scattering effects. Figures 5.5 and 5.6 demonstrate the ability of the back-

reflection technique combined with the mineral-fitting routine in identifying goethite (sample pictured in figure 5.4) with preferred orientation effects, along with varying amounts of quartz present.

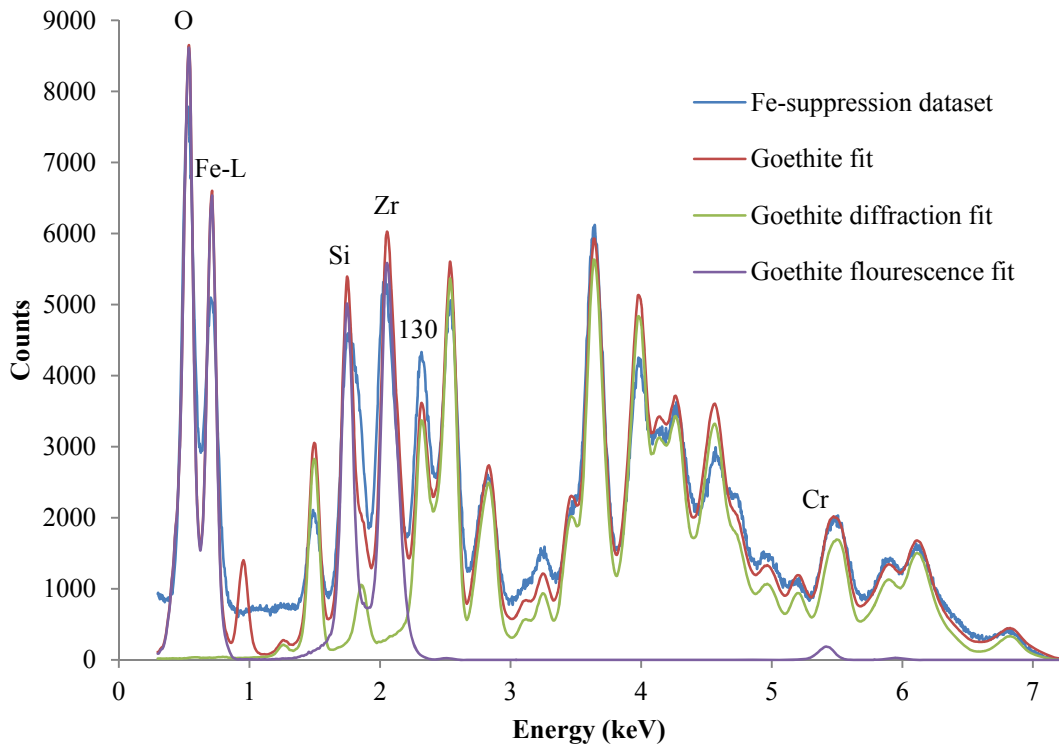


Figure 5.6. Fe-suppression dataset obtained using the bespoke SDD facility for the goethite rock sample shown in figure 5.4, compared to a goethite fit, which also included quartz, used goethite data from Yang et al. (2006) and quartz data from Kihara (1990). The (130) reflection is marked along with fluorescence peaks. The diffraction and fluorescence constituents of the goethite fit are also plotted, neither of which include Rayleigh scattering.

5.4.1.3 Hematite

A hematite rock sample of unknown origin shown in figure 5.4 was obtained from the Department of Geology at the University of Leicester, and analysed using the bespoke SDD laboratory facility described in 5.2. Part of the whole rock sample was broken off and milled into a fine powder to coat a resin pellet. Datasets were acquired using the bespoke SDD laboratory facility as outlined in figure 5.1, with the Fe-suppression hematite pellet dataset shown in figure 5.7.

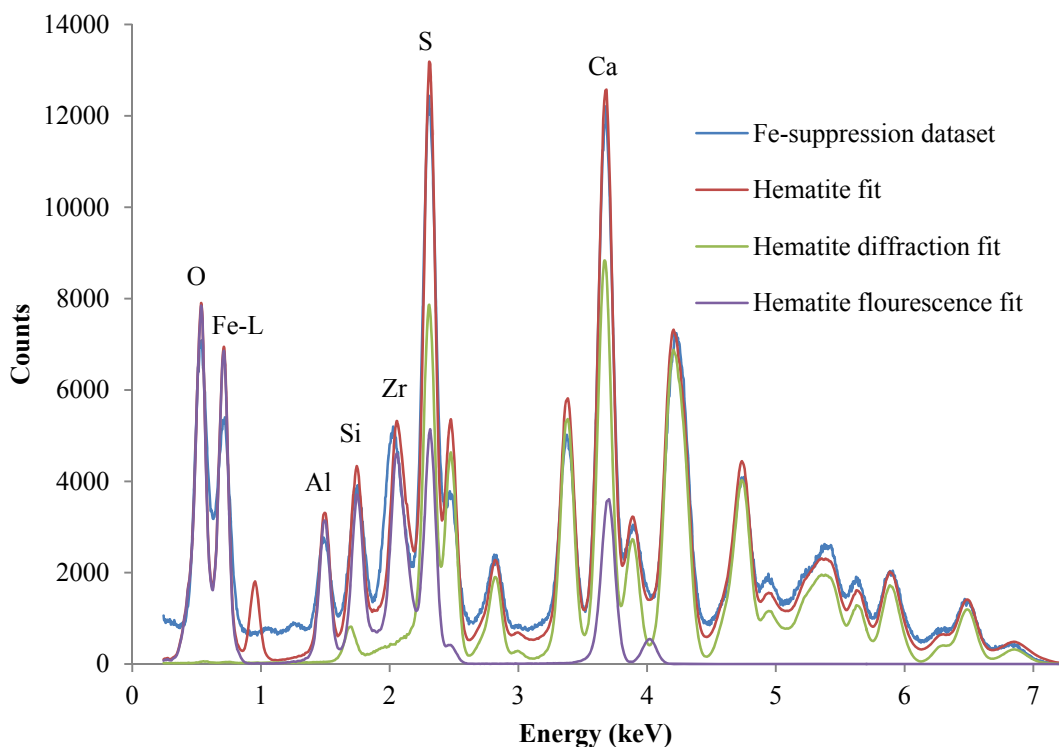


Figure 5.7. Fe-suppression dataset obtained using the bespoke SDD facility for the pellet made from the Hematite sample shown in figure 5.4, compared to a hematite fit that was created using the mineral-fitting routine with data from Blake et al (1966). The diffraction and fluorescence constituents of the hematite fit are also plotted, neither of which account for Rayleigh scattering.

Figure 5.7 shows that the Fe-suppression dataset taken of the pellet sample shown in figure 5.4 is best explained by a hematite fit produced by the mineral-fitting routine using data from Blake et al. (1966) with a preferred-orientation effect along the (001) plane with a March coefficient of 0.848 that was identified through peak identification. Trace amounts of fluorescence from Si, S and Ca were included, and additional O fluorescence was included in the fit, along with Al fluorescence that may be a contribution from the vacuum chamber. Figure 5.8 shows the Fe-suppression dataset taken of the rock sample shown in figure 5.4 is explained well by hematite, as shown by the pellet in figure 5.7.

Differences between the hematite pellet and rock fits include a marginal increase of the preferred orientation March coefficient along the (001) planes from 0.848 to 0.862. Peak positions and intensities of the hematite fits in figures 5.7 and 5.8 are comparable to the experimentally acquired data, and thus using the back-reflection technique the hematite sample in figure 5.4 can be assumed to be dominated by hematite.

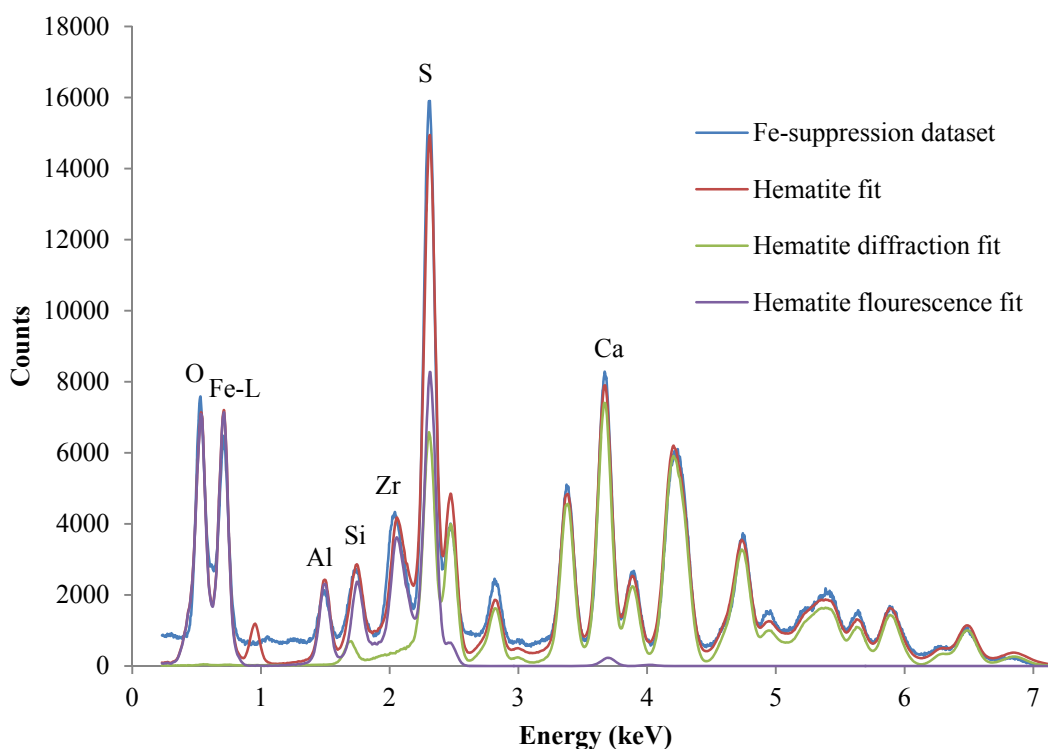


Figure 5.8. Fe-suppression dataset obtained using the bespoke SDD facility for the hematite rock sample shown in figure 5.4, compared to a hematite fit that was created using the mineral-fitting routine with data from Blake et al. (1966). The diffraction and fluorescence constituents of the hematite fit are also plotted, neither of which account for Rayleigh scattering.

5.4.1.4 Orthoclase Feldspar

Figure 5.9 shows an orthoclase feldspar rock sample from Evje, Norway obtained via UKGE Limited (<http://www.ukge.com>). The sample was analysed using the bespoke SDD facility outlined in section 5.2, with datasets acquired detailed in table 5.1. Figure 5.10 shows the results of the K-suppression data acquisition for the sample shown in figure 5.9, compared to orthoclase and sanidine fits calculated using the mineral-fitting routine with data from Tseng et al. (1995) and Keefer and Brown (1978). Rayleigh scattering is also estimated by the fits.

The fits shown in figure 5.10 suggest the sample shown in figure 5.9 is consistent with orthoclase/sanidine, which are both endmembers of the same solid solution series (Deer et al., 1992), meaning a definitive identification cannot be made. The quality of the mineral-fits are questionable, with inaccurate peak intensity shown most prominently at 2.44 keV for the (050) peak. A shoulder to the Si fluorescence peak at ~1.9 keV suggests the presence of quartz. As outlined in section 5.1, both orthoclase and sanidine are members of the same solid solution series. This data shows that the discrimination of

different members of alkali feldspar is difficult based solely on the diffraction data returned by the back-reflection technique.



Figure 5.9. Orthoclase feldspar rock sample from Evje, Norway. Sample obtained from UKGE Limited (<http://www.ukge.com>).

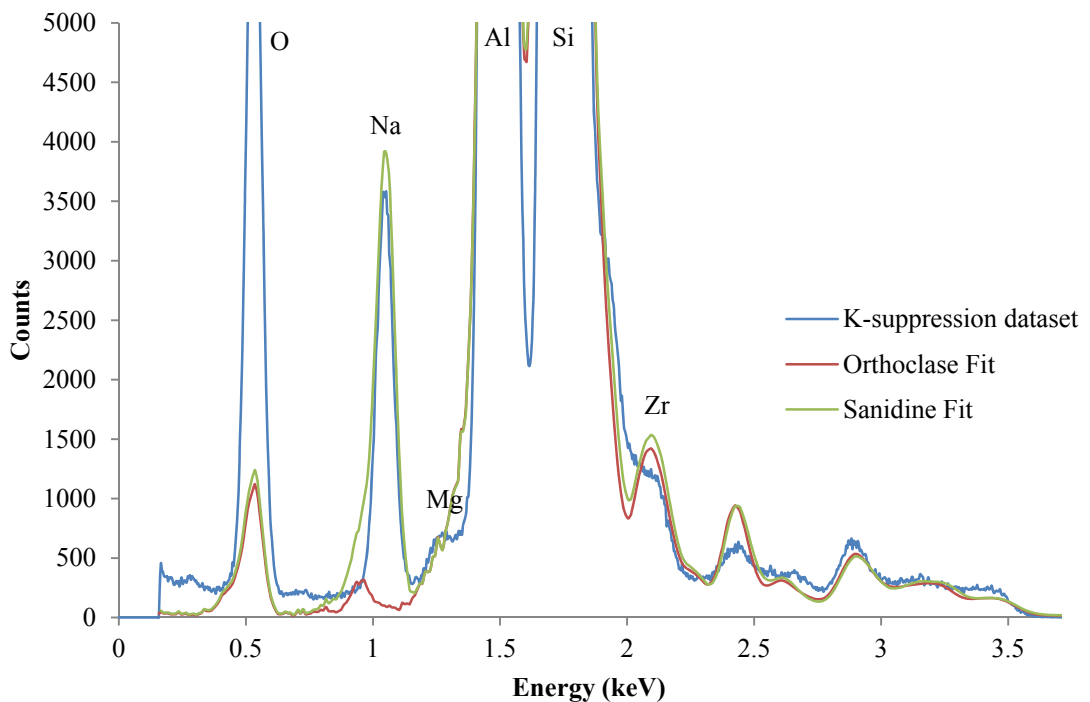


Figure 5.10. K-suppression dataset of the pellet made from the sample shown in figure 5.9 taken with the bespoke SDD setup, compared to orthoclase and sandine fits produced by the mineral-fitting routine with data from Tseng et al. (1995) and Keefer and Brown (1978).

5.4.1.5 Plagioclase Feldspar



Figure 5.11. Plagioclase feldspar rock sample from Iveland, Norway. Sample obtained from UKGE Limited (<http://www.ukge.com>).

Figure 5.11 shows a plagioclase feldspar rock sample from Iveland, Norway obtained via UKGE Limited (<http://www.ukge.com>). The sample was analysed using the bespoke SDD facility outlined in section 5.2, with datasets acquired detailed in table 5.1. The Ca-suppression dataset is shown in figure 5.12.

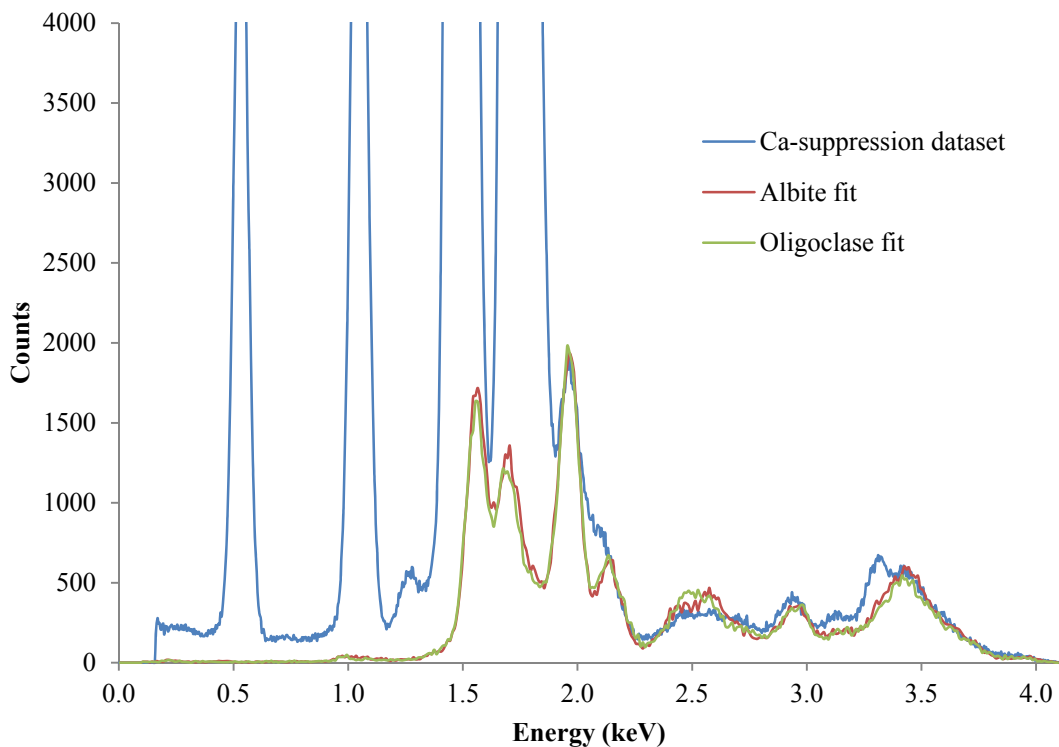


Figure 5.12. Ca-suppression dataset of the pellet made from the sample shown in figure 5.11 taken with the bespoke SDD facility, compared to albite and oligoclase fits produced by the mineral fitting routine with data from Armbruster et al. (1990) and Philips (1971).

Figure 5.12 shows the results of the Ca-suppression data acquisition for the sample shown in figure 5.10 compared to albite and orthoclase fits calculated using the mineral-fitting routine with data from Armbruster et al. (1990) and Philips (1971). The fits shown in figure 5.12 suggest the sample shown in figure 5.11 can be explained by either albite or oligoclase, or both. Figure 5.13 shows the Ca-suppression dataset compared to other plagioclase feldspar samples.

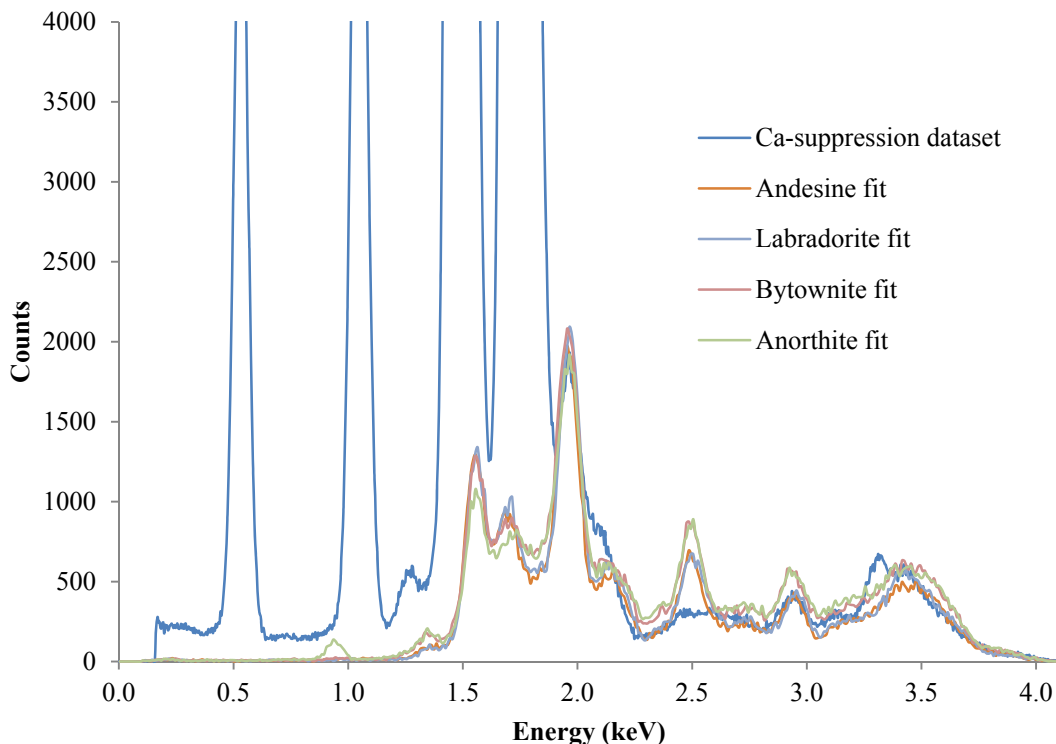


Figure 5.13. Ca-suppression dataset of the pellet made from the sample shown in figure 5.11 taken with the bespoke SDD facility compared to diffraction fits of the other plagioclase feldspars in the solid solution series that are not previously shown in figure 5.12. Andesine data was taken from FitzGerald et al. (1986), labradorite data was taken from Wenk et al. (1980), bytownite data was taken from Facchinelli et al. (1979) and anorthite data was taken from Angel et al. (1990).

All of the plagioclase feldspar mineral fits in figure 5.13 have a diffraction peak at ~ 2.5 keV that is not present in the Ca-suppression dataset. Figures 5.12 and 5.13 illustrate that the distinction between plagioclase feldspar minerals in the back-reflection geometry is difficult due to similarities in resultant diffraction spectra. Despite the similarities, further clarification as to the type of plagioclase feldspar sample shown in figure 5.11 was attempted, with the result shown in figure 5.14.

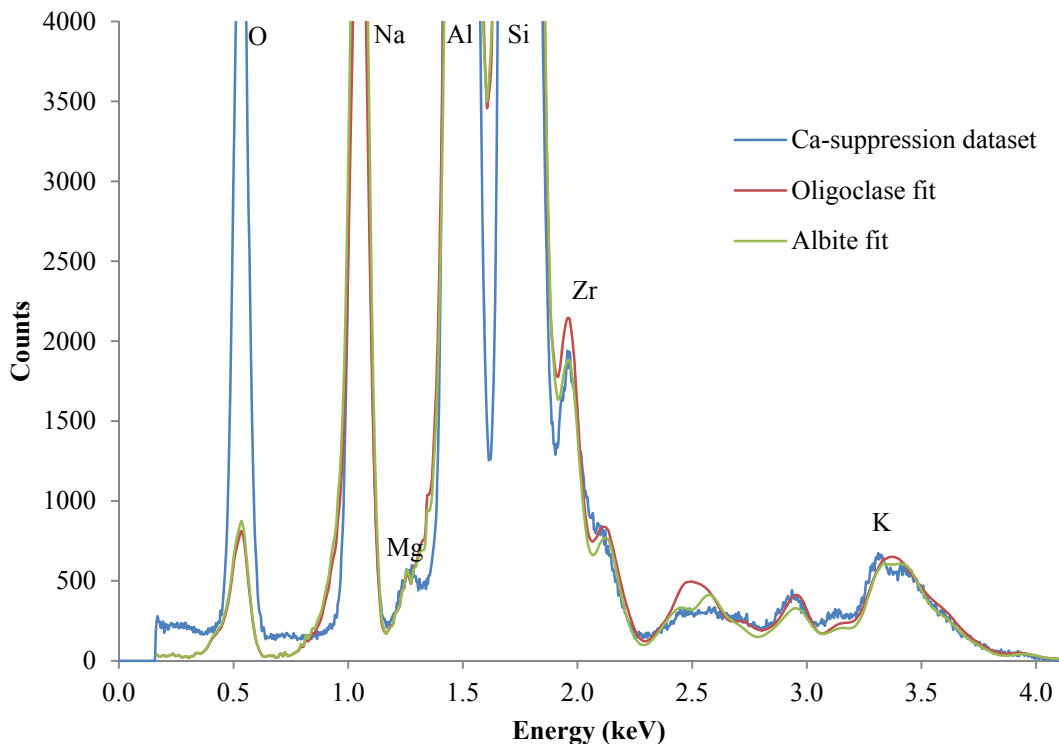


Figure 5.14. Ca-suppression dataset of the pellet made from the sample shown in figure 5.11 taken with the bespoke SDD facility, compared to refined oligoclase and albite fits using data from Armbruster et al. (1990) and Philips (1971).

Figure 5.14 shows that both oligoclase and albite fits refined using the mineral-fitting routine explain the Ca-suppression dataset sufficiently well. Although the oligoclase peak at 2.5 keV is not present in the Ca-suppression dataset, the peak itself is modelled to be broader and less intense than those shown in figure 5.13. Both fits in figure 5.14 include Mg and K fluorescence. Rayleigh scattering is also estimated.

5.4.1.6 Magnetite

Figure 5.15 shows a magnetite rock sample from Bråstad Mine, Arendal, southern Norway obtained via UKGE Limited (<http://www.ukge.com>). The whole rock sample was analysed with the bespoke SDD facility outlined in section 5.2. The details of the datasets acquired are shown in table 5.1, with the result of the Ca-suppression dataset for the sample shown in figure 5.16. Figure 5.16 shows a magnetite fit refined using the mineral-fitting routine with data from Wechsler et al. (1984). The magnetite fit explains the diffraction peaks Ca-suppression dataset with regards to the peak position, however there are some discrepancies in peak intensities that could be due to the large crystallites

of the rock sample (as shown in figure 5.15) contributing to overall poor-powder averaging.



Figure 5.15. Magnetite rock sample from Bråstad Mine, Arendal, Southern Norway. Sample obtained from UKGE Limited (<http://www.ukge.com>).

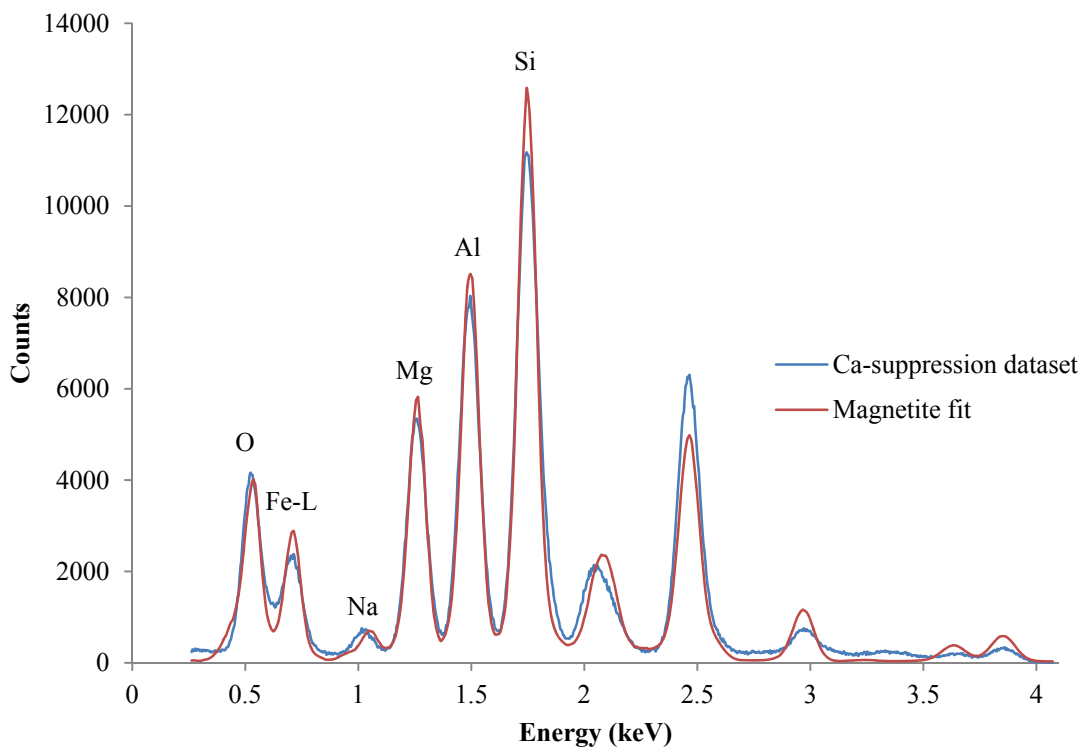


Figure 5.16. Ca-suppression dataset of the rock sample shown in figure 5.15, compared to a magnetite fit produced by the mineral-fitting routine using data from Wechsler et al. (1984).

5.4.2 Group B: Carbonate Samples

Sample group B contained carbonate rock and pellet samples, which are detailed in table 5.1, and pictured in figure 5.17.



Figure 5.17. Photograph of carbonate samples detailed in table 5.2. A: Hope collected from Hope Valley, Peak District, UK. B: BastilleA collected from Mt Rachais, Grenoble, France. C: MindelA collected from Mindelheimer Klettersteig, Allgäu Alps, Austro-German border. D. MindelB collected from same location as MindelA (C).

Limestone samples dominated by calcite are shown in figure 5.18, where a calcite diffraction model created by PoDFluX (Hansford, 2009) is compared to Ca-suppression datasets for the whole rock samples Hope and BastilleA. The Ca-suppression datasets were acquired using the pre-existing CCD setup as detailed in table 5.1.

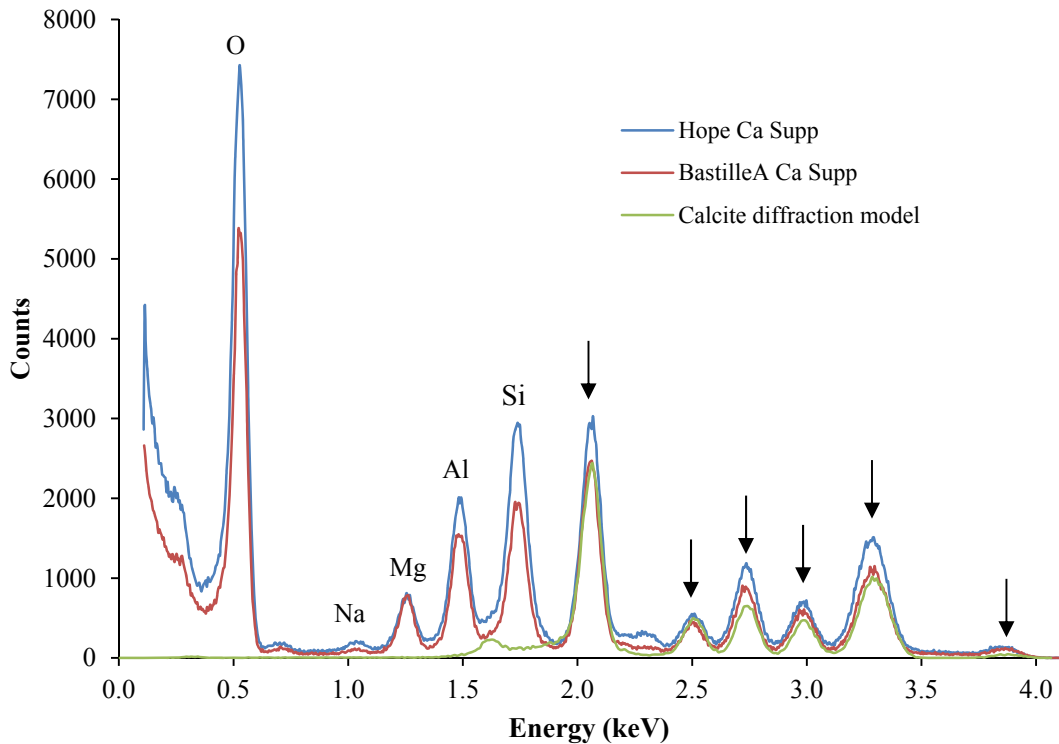


Figure 5.18. Ca-suppression datasets acquired of whole rock limestone samples Hope and BastilleA shown in figure 5.17 compared to a PoDFluX (Hansford, 2009) calcite diffraction model using data from Sitepu (2009). Fluorescence peaks are labelled and arrows indicate diffraction peaks.

Figure 5.18 shows that calcite explains 6 diffraction peaks in the sample spectra, with fluorescence of elements O, Na, Mg, Al and Si. The PoDFluX (Hansford, 2009) diffraction model explains the Hope and BastilleA samples well, indicating that the dominant mineral within the area illuminated by the incident X-ray beam is calcite.

Limestone samples dominated by dolomite are shown in figure 5.19, where a dolomite diffraction model created by PoDFluX (Hansford, 2009) is compared to Ca-suppression datasets for whole rock samples MindelA and MindelB, along with Japanese dolomite pellet JDo-1. As shown in figure 5.19, and Hansford et al. (2014), dolomite explains 5 diffraction peaks in the sample spectra, with fluorescence of elements O, Mg, Al and Si being considered. The PoDFluX (Hansford, 2009) diffraction model explains the data well with an exception being the diffraction peak at 2.17 keV, which is the (104) peak for dolomite.

There is a clear difference in diffraction peak occurrences, positions and intensities in calcite and dolomite samples due to the different unit cells in figures 5.18 and 5.19, demonstrating the capability of the back-reflection technique in distinguishing between these two carbonate minerals.

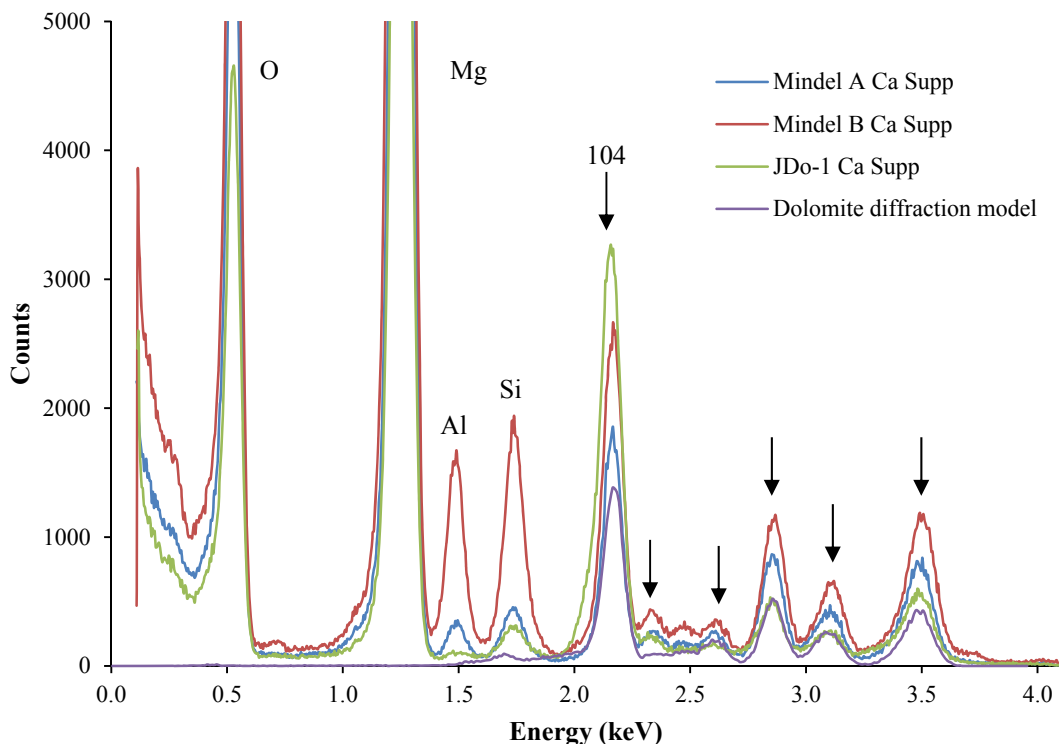


Figure 5.19. Ca-suppression datasets acquired of whole rock samples MindelA and MindelB along with the pellet sample JDo-1 shown in figure 5.17, compared to a PoDFluX (Hansford, 2009) dolomite diffraction model using data from Ross and Reeder (1992). Fluorescence peaks are labelled and arrows indicate diffraction peaks.

Figure 5.19 shows an enhanced peak intensity along the (104) plane for the Japanese geological standard JDo-1, suggesting the presence of preferred orientation. Upon analysis of this sample it was found not to be entirely dolomite; a model of 90% dolomite and 10% calcite (shown in figure 5.20) accounts for the small shoulder on the diffraction feature at 2.17 keV (the (104) peak) and the increased intensity at 3.29 keV due to the strong calcite diffraction peak. As shown and discussed in Hansford et al. (2014), the only previous mineralogical analysis of JDo-1 was found on the Geological Survey of Japan's website (<https://gbank.gsj.jp/geostandards/gsj1maine.html>) where calcite peaks in addition to dolomite peaks are shown in a JDo-1 X-ray diffraction pattern. This sample was also analysed using the back-reflection technique at the Diamond Light Source as shown in Chapter 6, which showed both dolomite and calcite diffraction peaks to be present.

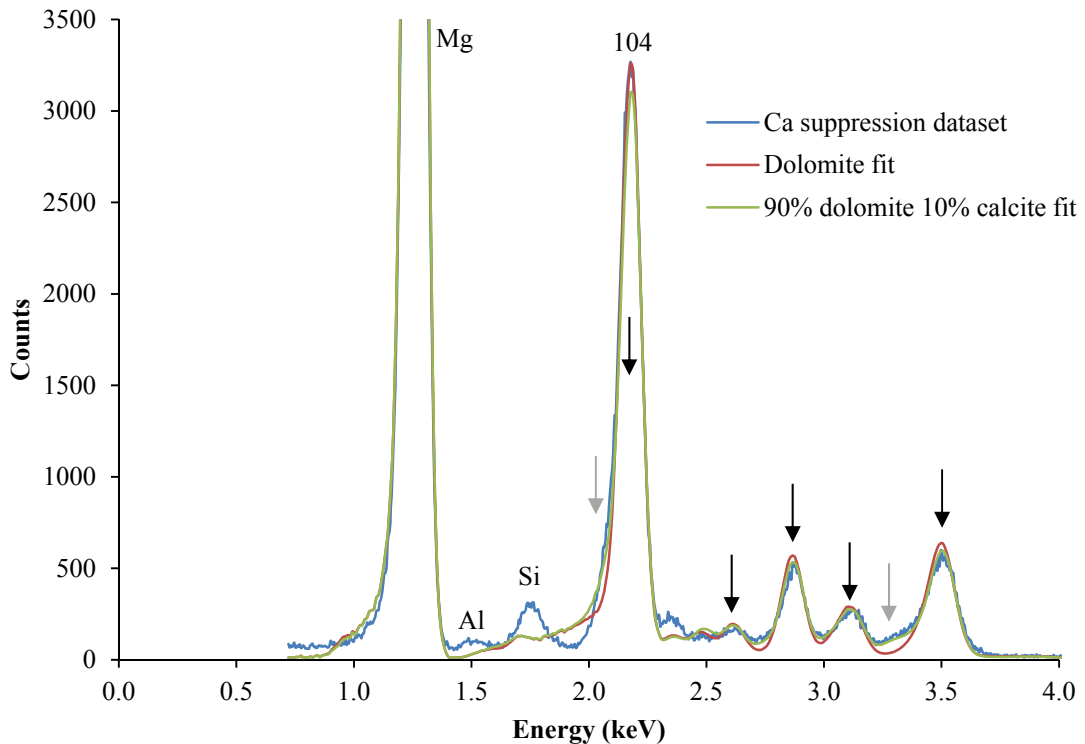


Figure 5.20. Ca-suppression dataset for the Japanese dolomite standard JDo-1 compared to 90% dolomite and 10% calcite diffraction and fluorescence models produced by the mineral-fitting routine using data from Ross and Reeder (1992) and Sitepu (2009). The dolomite peaks in the spectrum are indicated by the black arrows, whereas the identified calcite features are indicated by the grey arrows. The fluorescence peaks Mg, Al and Si are labelled. Data below 0.75 keV was not included in the fit, and is therefore not shown.

Figure 5.20 illustrates the 90% dolomite and 10% calcite fit for JDo-1, and shows the large discrepancy in peak intensity for the (104) dolomite peak can be explained by preferred orientation along this plane with a March coefficient of 0.604. To investigate the enhanced intensity of the (104) peak, experiments were undertaken whereby the JDo-1 sample was tilted about an axis perpendicular to the incident X-ray beam with datasets taken at 10° intervals.

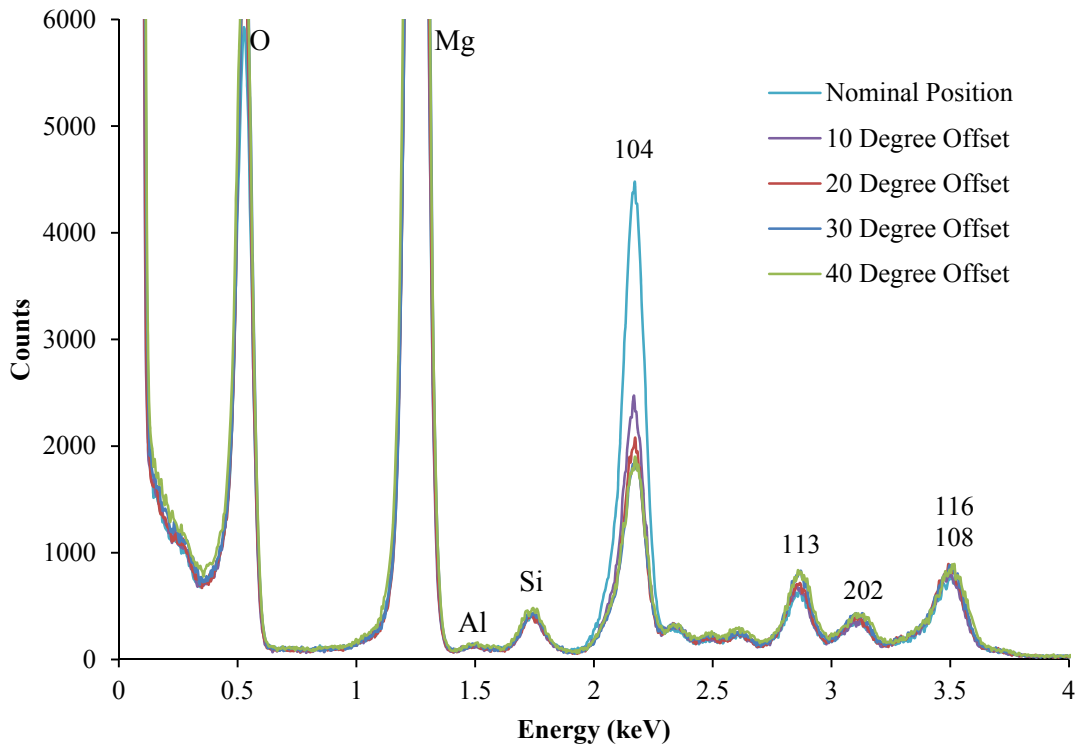


Figure 5.21. JDo-1 Ca-suppression spectra acquired at various sample angles. Fluorescence and diffraction peaks present are annotated. The variation in the (104) diffraction peak at 2.17 keV experimentally illustrates a preferred orientation effect of this sample.

Figure 5.21 clearly shows how the intensity of the diffraction feature at 2.17 keV can be attributed to preferred orientation at that d-spacing, representative of the preferential alignment of the crystallites with the (104) plane parallel to the sample surface, which was described by Larsson and Christy (2008). Calcite and dolomite exhibit perfect cleavage along the (104) plane with previous reports describing the preferred orientation of this plane parallel to the powder surface that is most prevalent in pressed samples (Perdikatsis, 2000; Suzuki et al., 1998). The variations of the intensities of the other five diffraction peaks can be considered negligible, in comparison.

5.4.3 Group C: Sulphates

Sample group C contained sulphate rock and pellet samples, which are detailed in table 5.1.

5.4.3.1 Gypsum samples from Watchet Bay

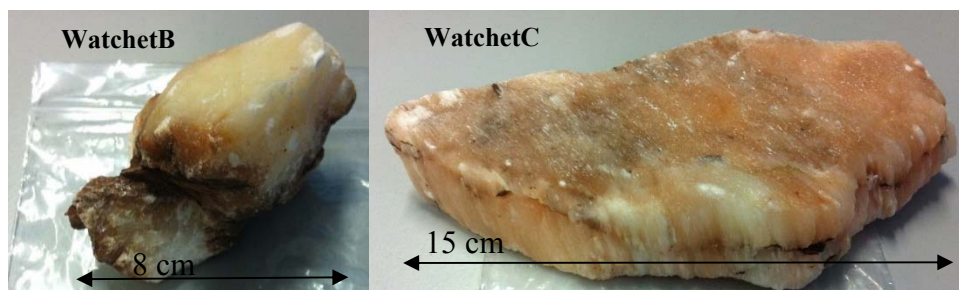


Figure 5.22. Photographs of sulphate samples: WatchetB and WatchetC.

Geological analogues of Yellowknife Bay in Gale Crater on Mars were collected by John Bridges from the Triassic Coast at Watchet Bay in Somerset UK, with the intention to analyse them to aid the investigations of vein formation on Mars. WatchetB and WatchetC samples shown in figure 5.22 were visually suspected to be gypsum. Crystal data was obtained for the minerals: gypsum ($\text{CaSO}_4 \cdot 2\text{H}_2\text{O}$) (Boeyens and Ichharam, 2002), bassanite ($2\text{CaSO}_4 \cdot \text{H}_2\text{O}$) (Ballirano et al., 2001) and anhydrite (CaSO_4) (Hawthorne and Ferguson, 1975). These minerals are of particular interest in planetary science as they can, for instance, form from the evaporation of a body of standing water or groundwater (Chevrier and Mathé, 2007) and are similar to sulphate veins identified at Yellowknife Bay by the Curiosity rover. The distinction between sulphate minerals such as gypsum ($\text{CaSO}_4 \cdot 2\text{H}_2\text{O}$) and anhydrite (CaSO_4), found in rock veins, is important in order to characterise fluid composition and temperature of ancient aqueous activity (Schwenzer et al., 2016).

Figure 5.23 shows a S-suppression dataset acquired using the pre-existing CCD facility for a pellet sample made from WatchetB, with experimental parameters outlined in table 5.1.

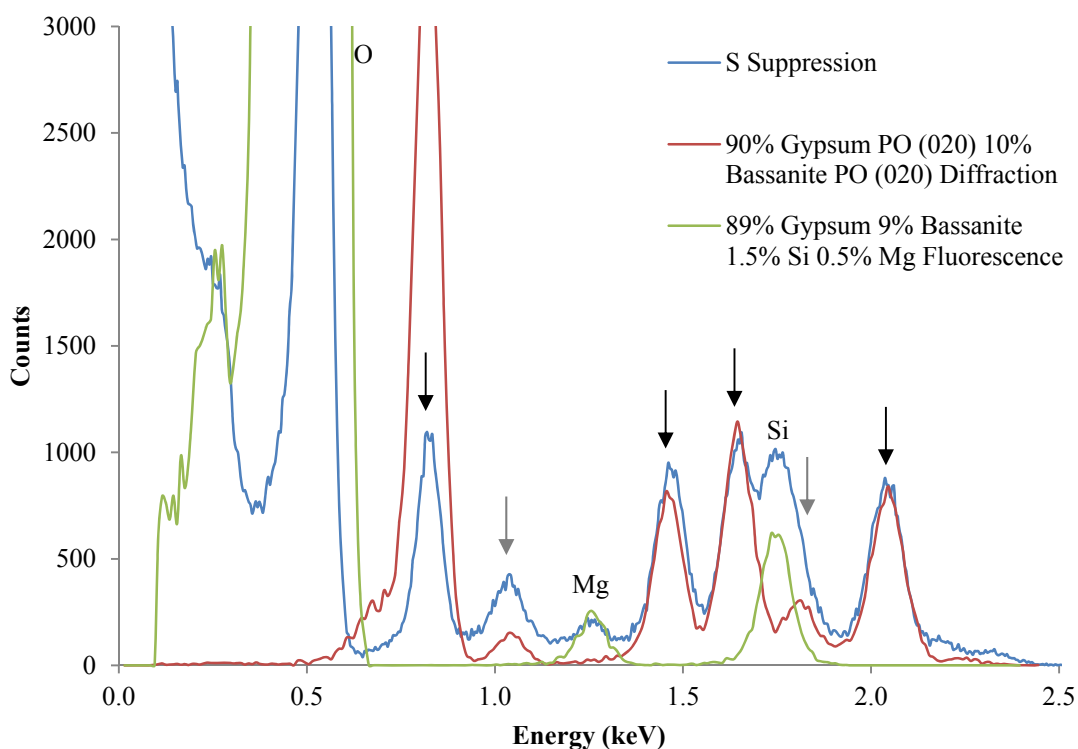


Figure 5.23. S-suppression dataset acquired of WatchetB compared to a PoDFluX models for gypsum (black arrows) and bassanite (grey arrows) diffraction and fluorescence using information from Boeyens and Ichharam (2002) and Ballirano et al. (2001). The diffraction model incorporated a preferred orientation effect along the (020) plane with a March coefficient of 0.4. The model explains the five diffraction peaks and a diffraction shoulder on the Si fluorescence peak, which suggests an overlap of Si fluorescence on a bassanite diffraction peak with good agreement with the experimental data.

Figure 5.23 shows that the WatchetB pressed powder pellet is explained by a mixture of 90% gypsum and 10% bassanite, with preferred orientation along the (020) plane. WatchetB was also analysed by the Department of Geology at the University of Leicester with a Bruker D8 Advance diffractometer, where gypsum was found to be the dominant mineral (Haidon, 2013). Given that bassanite was identified in figure 5.23, and that the sample is under vacuum during data acquisition, an additional pressed pellet was made from the same powder as the first pellet to ascertain if the occurrence of bassanite was a dehydration product of the X-ray diffraction experiment. A previous EDXRD study examined the dehydration of gypsum at 100 Pa pressure and found a one-step dehydration process to γ -anhydrite without the occurrence of bassanite (Carbone et al., 2008), as opposed to the two-step process described here.

Figure 5.24 shows a S-suppression dataset for the second pressed powder pellet made from the WatchetB. Data acquisition was initiated immediately after the chamber

had pumped down to 10^{-5} mbar. Gypsum, with a preferred orientation effect along the (020) plane with a March coefficient of 0.5, is shown to fit the data well in figure 5.24.

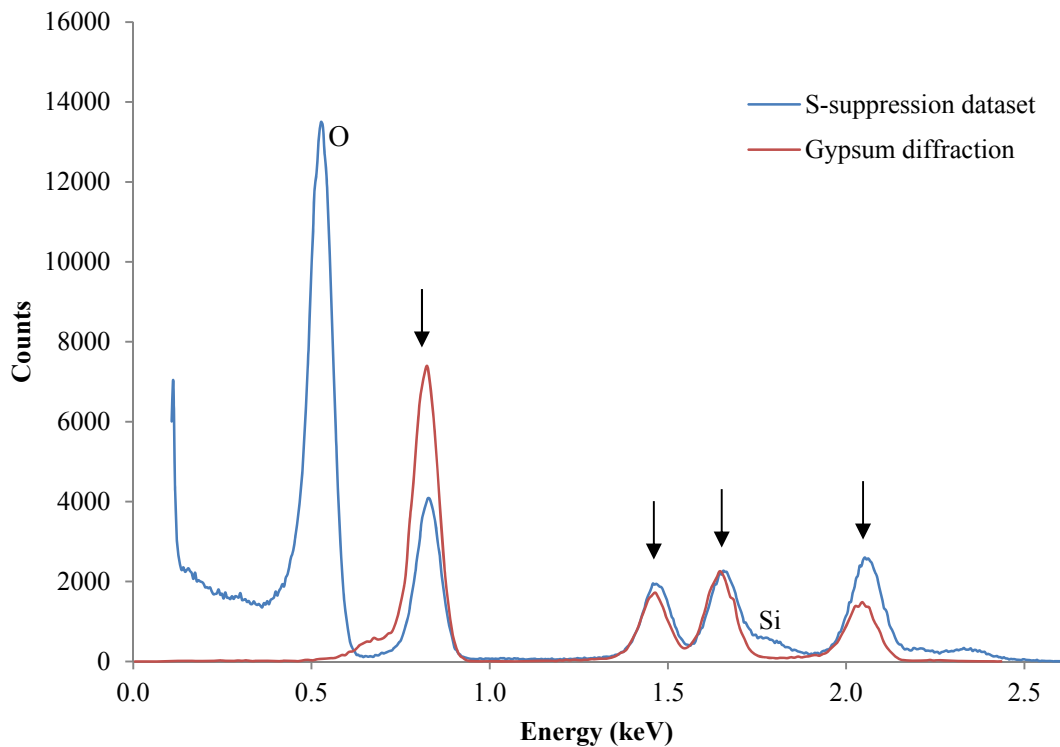


Figure 5.24. S-suppression dataset acquired of the second WatchetB pellet compared to a PoDFluX diffraction model for gypsum, using information from Boeyens and Ichharam (2002). The diffraction model incorporated a preferred orientation effect along the (020) plane with a March coefficient of 0.5.

The secondary pellet was left under vacuum, with another S-suppression dataset taken after two days showing that the sample had dehydrated under vacuum to anhydrite-III (figure 5.25). This demonstrates the difficulty in the analysis of hydrated samples that are exposed to a vacuum environment for an extended period of time, but also highlights the capability of the back-reflection technique in distinguishing between gypsum and bassanite.

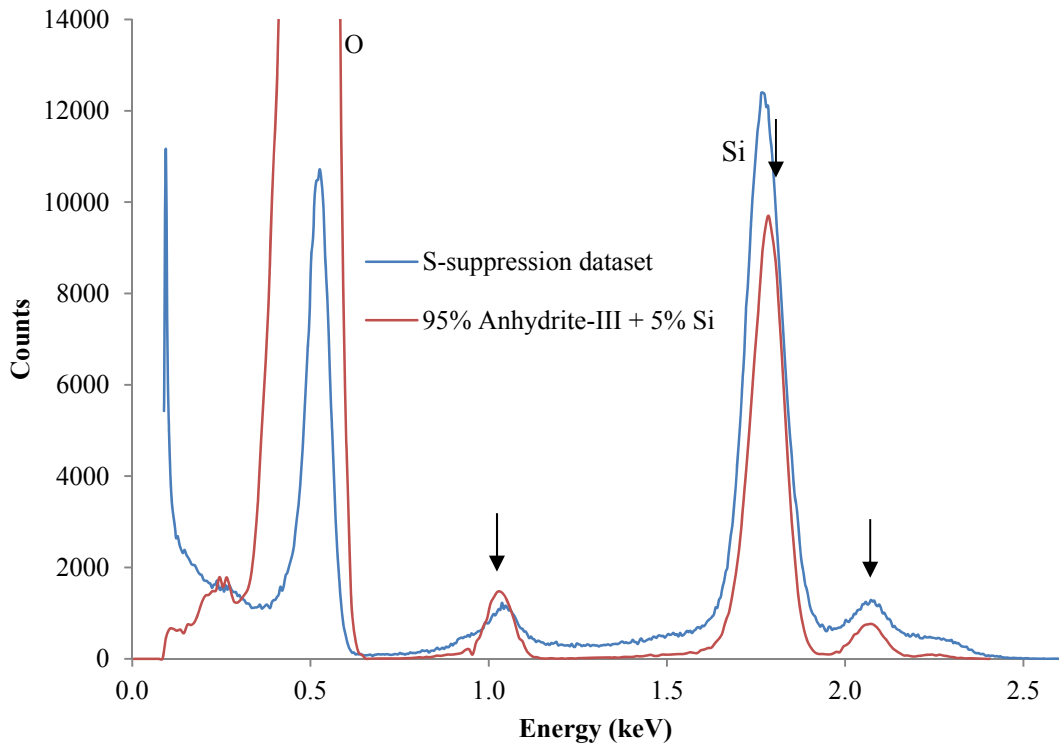


Figure 5.25. S-suppression dataset acquired of the second WatchetB pellet after two days of being subjected to a vacuum environment compared to a PoDFluX model for Anhydrite-III, using information from Bezou et al. (1995). The diffraction model incorporated a preferred orientation effect along the (020) plane with a March coefficient of 0.1.

Figure 5.26 shows a S-suppression dataset taken of WatchetB in its whole-rock form taken using the pre-existing CCD laboratory facility as detailed in table 5.1.

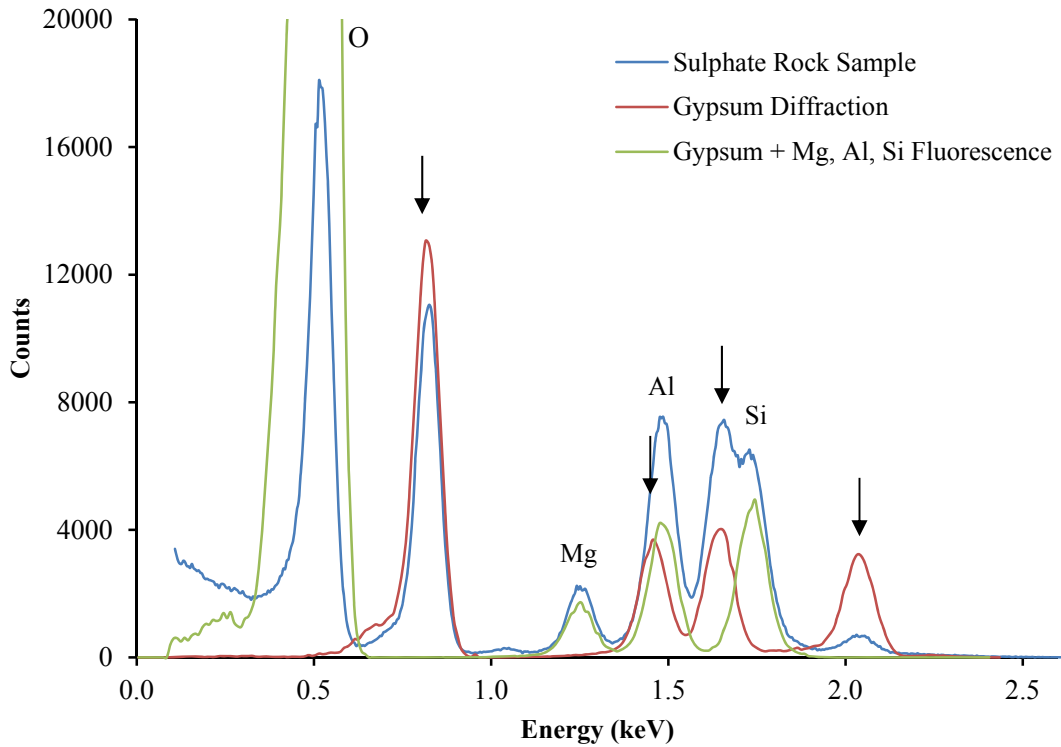


Figure 5.26. S-suppression dataset acquired of WatchetB compared to PoDFluX models for gypsum, using information from Boeyens and Ichharam (2002). The diffraction model incorporated a preferred orientation effect along the (020) plane with a March coefficient of 0.5.

The PoDFluX (Hansford, 2009) models in figure 5.26 show that the sample is explained by gypsum, using data from Boeyens and Ichharam (2002) with a preferred orientation effect along the (020) plane with a March coefficient of 0.5.

WatchetC shown in figure 5.27 was analysed using the pre-existing CCD and bespoke SDD facilities. Part of WatchetC was broken off and milled into a fine powder, from which a pressed powder pellet was made. 8 kV, Ca-suppression and S-suppression datasets were taken of the powder pellet. The S-suppression dataset is shown in figure 5.27, where it is compared to diffraction and fluorescence models produced by PoDFluX.

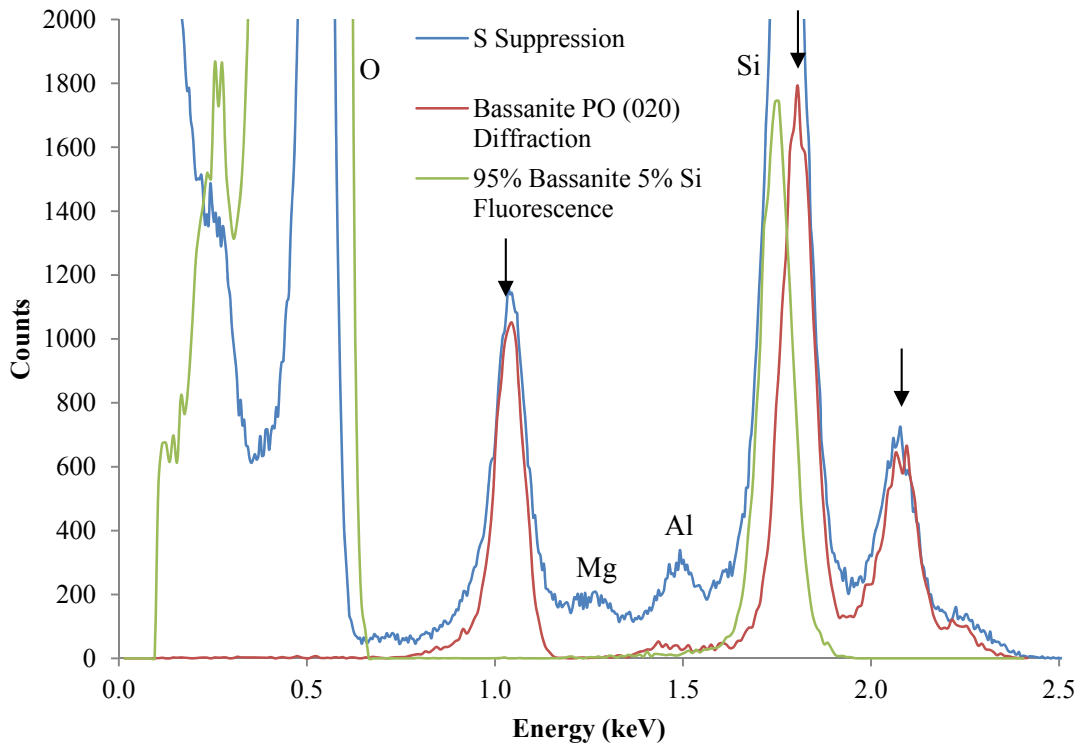


Figure 5.27. WatchetC pellet S-suppression dataset compared to a PoDFluX bassanite diffraction model incorporating a preferred orientation effect along the (020) plane. The PoDFluX fluorescence model of 95% bassanite with 5% Si shows how the diffraction peak at 1.75 keV is being obscured by Si, and the presence of this diffraction peak is confirmed in S-suppression CCD comparative plot in Appendix B.13.

Figure 5.27 shows that the WatchetC pressed powder pellet is explained by bassanite, with preferred orientation along the (020) planes. The inclusion of Si in the fluorescence model explains the broad peak at 1.75 keV. WatchetC was also analysed by the Department of Geology at the University of Leicester with a Bruker D8 Advance diffractometer, where it was found to be dominated by gypsum (Haidon, 2013). Given that bassanite was the only mineral identified in figure 5.27 and that the sample was under vacuum during data acquisition, it was hypothesised that dehydration occurred with WatchetC. An additional pressed pellet was made from the same powder as the first pellet to ascertain if the occurrence of bassanite was a dehydration product of the laboratory facility. The S-suppression dataset for this sample is shown in figure 5.28.

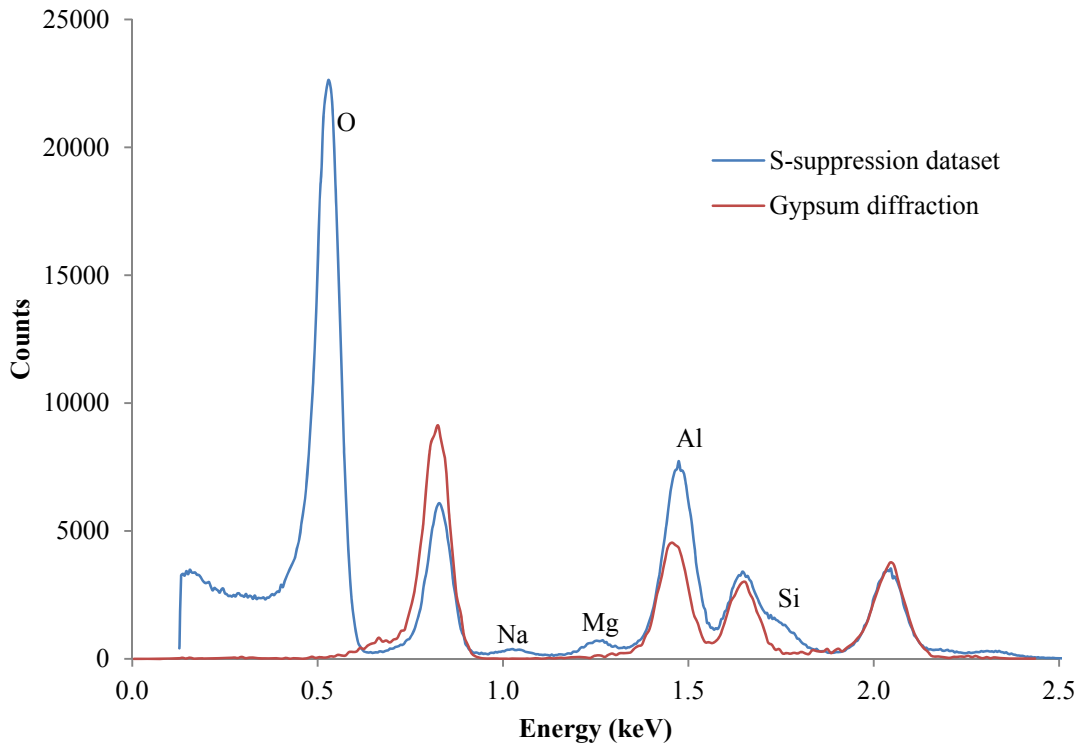


Figure 5.28. WatchetC pellet S-suppression dataset compared to a PoDFluX (Hansford, 2009) gypsum model with a preferred orientation effect along the (020) plane with a March coefficient of 0.6.

Figure 5.28 shows that the second pressed powder pellet sample from WatchetC is explained by a PoDFluX (Hansford, 2009) diffraction model for gypsum that includes a preferred orientation effect along the (020) plane with a March coefficient of 0.6. Fluorescence from O is present in the dataset along with trace amounts of Na, Mg, Al and Si. Figures 5.27 and 5.28, together with figures 5.23 - 5.25, shows that dehydration occurred with the first WatchetC pressed powder pellet due to prolonged exposure to vacuum.

A whole rock sample of WatchetC was analysed using the pre-existing CCD laboratory facility; a S-suppression dataset was acquired over the course of three hours (1800 CCD frames) where the X-ray tube voltage was set to 2.4 kV with a filament current of 1.6 mA. This dataset is shown in figure 5.29.

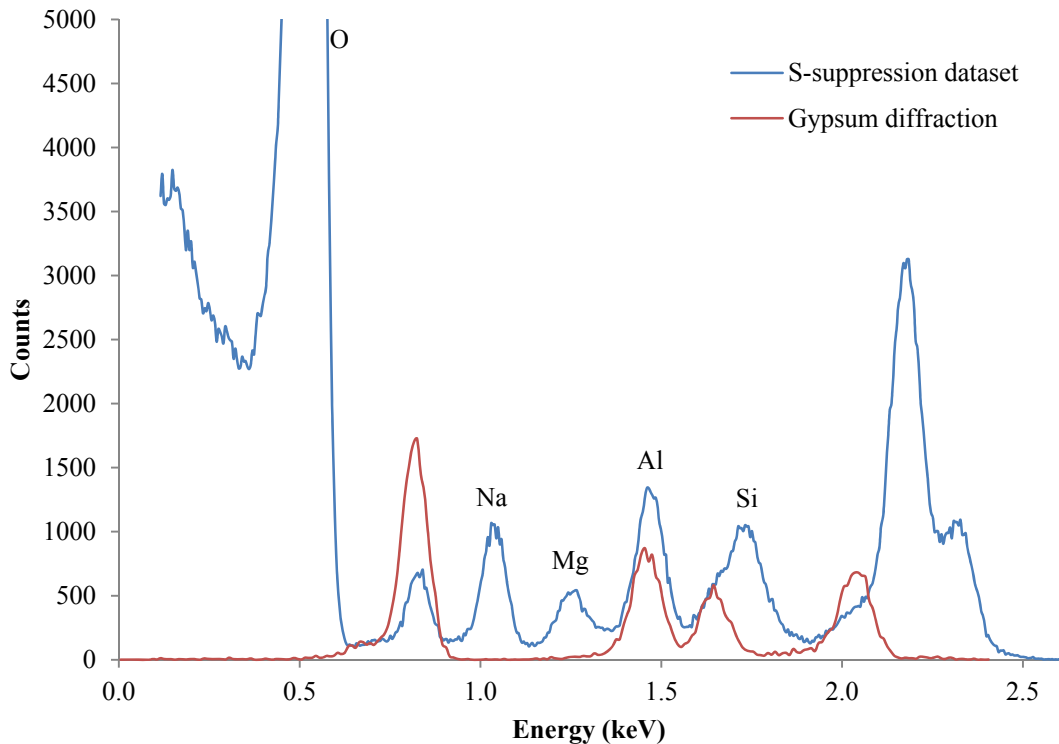


Figure 5.29. S-suppression dataset acquired of WatchetC compared to PoDFluX models for gypsum, using information from Boeyens and Ichharam (2002). The diffraction model incorporated a preferred orientation effect along the (020) plane with a March coefficient of 0.6. X-ray fluorescence peaks that are not predicted by the model are labelled.

Figure 5.29 shows the diffraction peaks in the S-suppression spectrum of the WatchetC whole rock sample compared to gypsum. The discrepancy in diffraction peak intensity at ~ 0.82 keV can be attributed to the use of the filter on the incident X-ray beam that reduces the X-ray intensity < 1 keV. The diffraction peak at ~ 2.05 keV is more intense than the diffraction shoulder in the experimental dataset and requires further investigation. The strong peak at ~ 2.2 keV is identified as a diffraction peak by its shift between the top and bottom regions of the CCD, as shown in Appendix B.13, however its origin is uncertain.

WatchetB and WatchetC whole rock samples were also analysed using the bespoke SDD facility outlined in section 5.2. Datasets were acquired for both samples where the X-ray tube was set to 8 kV with a filament current of 1.8 mA for the initial acquisitions, then 4.03 kV and 2.0 mA for a Ca-suppression acquisition and 2.4 kV and 2.6 mA for a S-suppression acquisition. Each dataset was acquired over a detector integration time of 10 minutes. Figures 5.30 and 5.31 show the S-suppression datasets compared to gypsum fits.

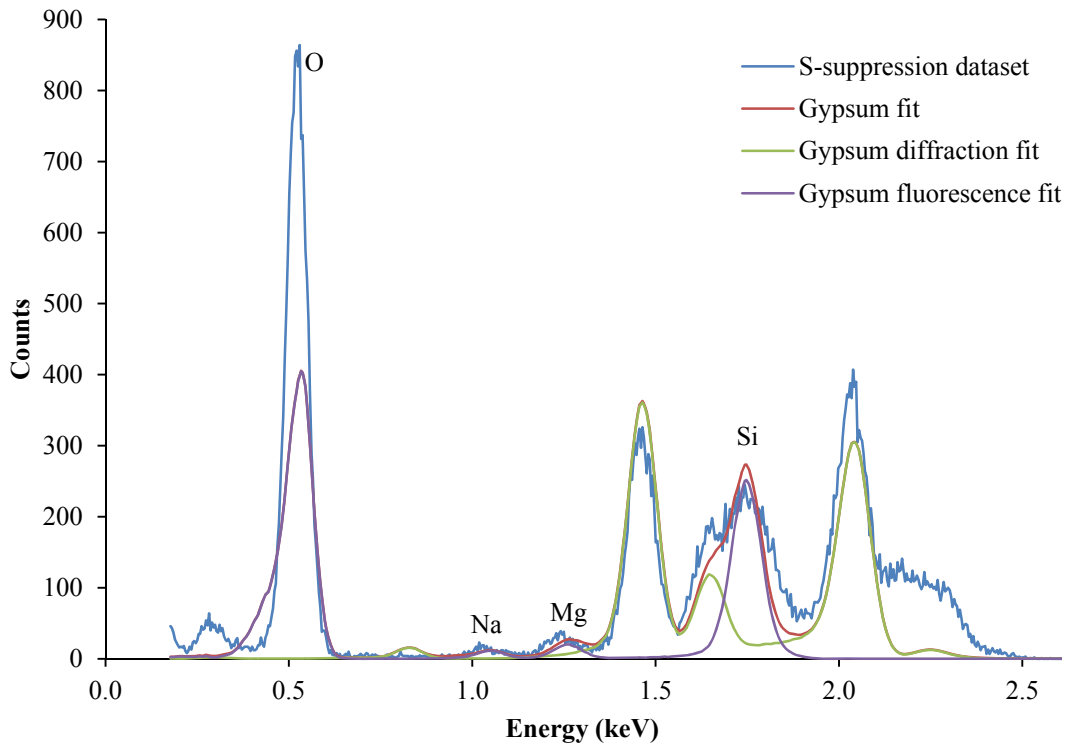


Figure 5.30. S-suppression dataset of WatchetB whole rock sample obtained using the bespoke SDD back-reflection laboratory facility compared to a gypsum fit produced by the mineral-fitting routine with data from Boeyens and Icharam (2002). A preferred orientation effect along the (020) plane with a March coefficient of 0.712 was included in the diffraction fit. The diffraction and fluorescence constituents of the gypsum fit are also plotted, neither of which account for Rayleigh scattering.

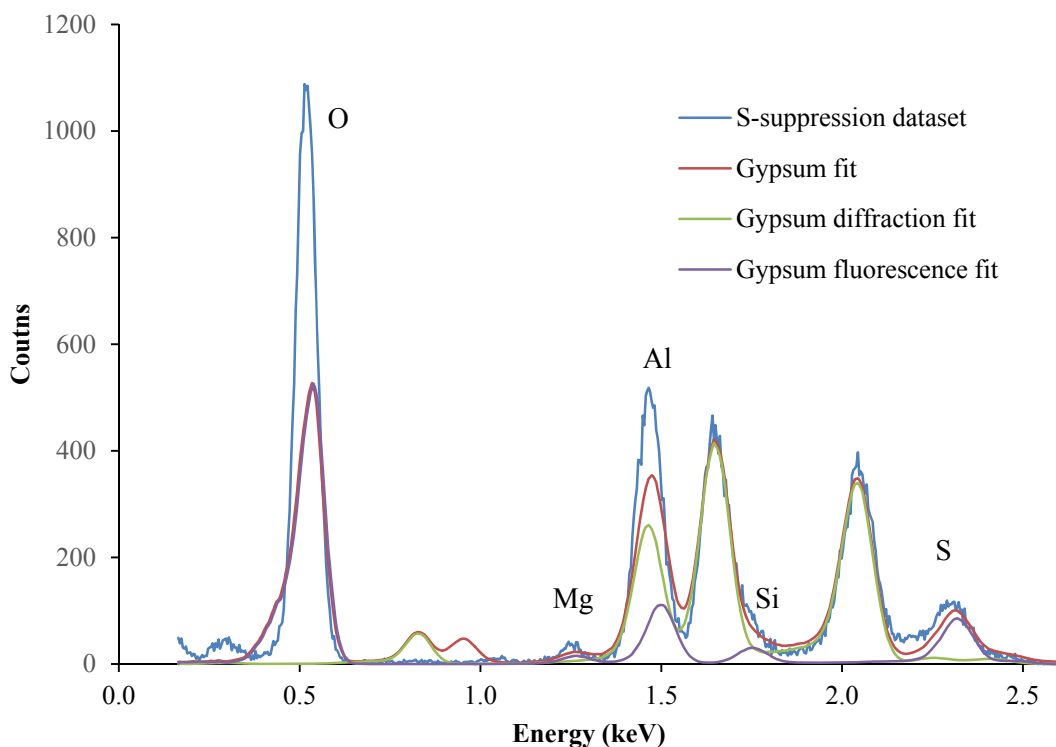


Figure 5.31. S-suppression dataset of WatchetC whole rock sample obtained using the bespoke SDD back-reflection laboratory facility compared to a gypsum fit produced by the mineral-fitting routine with data from Boeyens and Icharam (2002), with a preferred orientation effect along the (020) plane with a March coefficient of 0.469. The diffraction and fluorescence constituents of the gypsum fit are also plotted, neither of which account for Rayleigh scattering.

Figure 5.30 and 5.31 show the WatchetB and WatchetC rock samples to be of gypsum mineralogy, with different amounts of preferred orientation along the (020) planes. Trace amounts of fluorescence from Na, Mg, Al and Si are also present. The S fluorescence peak in figure 5.31 suggests that the X-ray tube voltage was set a little too high, resulting in a minor amount of S fluorescence. Peaks present below 1 keV were affected by the Al/Lexan filter on the X-ray tube apparatus and inaccurate estimation of Rayleigh scattering at low energies.

5.4.3.2 Jarosite

A jarosite whole rock sample (shown in figure 5.32) named Thackaringa was analysed using the bespoke SDD back-reflection laboratory facility outlined in section 5.2. The sample was acquired from a private collector (www.richardtaylor.co.uk) who collected the sample from Thackaringa, New South Wales, Australia. Datasets were acquired using the bespoke SDD laboratory facility, as outlined in table 5.1. Figure 5.33

shows the K-suppression dataset compared to a jarosite fit produced by the mineral-fitting routine. Figure 5.33 shows the Thackaringa rock sample to be of a jarosite mineralogy; however, there exists significant overlap of fluorescence peaks upon diffraction peaks. Also, the diffraction peak modelled at ~ 2.7 keV is much broader in the experimental dataset. The model does account for three prominent diffraction peaks at ~ 2.0 , ~ 2.7 and 3.2 keV. Additional elemental information was added to the model to account for Na, Al, Si and Zr fluorescence. The Zr fluorescence is attributed to the detector assembly within the bespoke SDD chamber, as previously noted, which slightly broadens the peak at ~ 2.0 keV that is otherwise dominated by jarosite diffraction.



Figure 5.32. Photograph of jarosite rock sample named Thackaringa. Sourced from a private collector who collected the sample from Thackaringa, New South Wales, Australia.

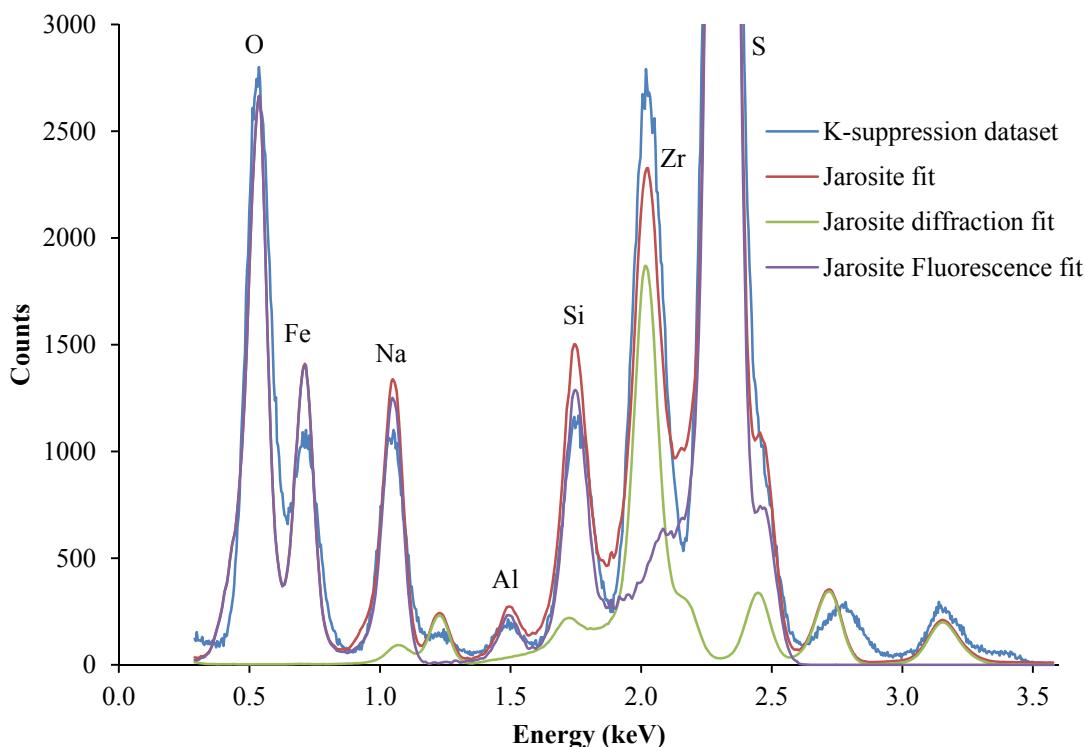


Figure 5.33. K-suppression dataset acquired of jarosite whole rock sample Thackaringa using the bespoke SDD laboratory facility outlined in section 5.2. A jarosite fit created using the mineral-fitting routine using data from Menchetti and Sabelli (1976), which includes the effects of Rayleigh scattering. The diffraction and fluorescence constituents of the jarosite fit are also plotted separately, neither of which account for Rayleigh scattering.

5.4.4 Group D: Phyllosilicates

Sample group D contained phyllosilicate rock and pellet samples that are detailed in table 5.1. The only rock sample of the group, Wave Hill, is imaged in figure 5.34.

5.4.4.1 Prehnite

Shown in figure 5.34, a prehnite whole rock sample named Wave Hill was analysed using the bespoke SDD back-reflection laboratory facility outlined in section 5.2. The sample was acquired from a private collector (www.richardtaylor.co.uk) who collected the sample from Wave Hill, Northern Territory, Australia. Datasets were acquired using the bespoke SDD laboratory facility as outlined in table 5.1. Figure 5.35 shows the experimentally acquired X-ray diffraction and fluorescence data to be comparable to a prehnite fit produced by the mineral-fitting routine using data from Detrie et al. (2009). Additional O, Na, and Fe was included in the fluorescence model, along with Ca, as a small quantity had been fluoresced during data acquisition. Rayleigh

scattering was also included in the prehnite fit. The position of the diffraction peaks in the 2.0 – 3.6 keV region are comparable although there are discrepancies in peak intensity. This is most apparent for the diffraction peak at 3.57 keV. The peak at ~0.9 keV is due to inaccurate estimation of Rayleigh scattering at low energies.



Figure 5.34. Photograph of prehnite rock sample named Wave Hill. Sourced from a private collector who collected the sample from Wave Hill, Northern Territory, Australia.

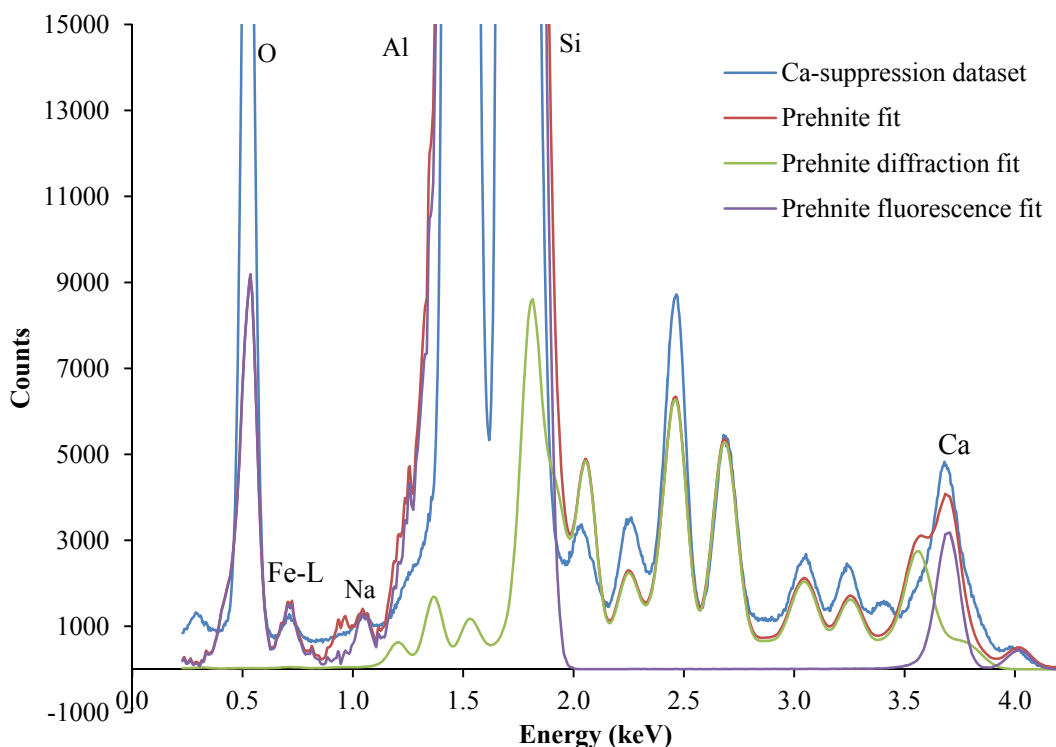


Figure 5.35. Ca-suppression dataset of Wave Hill whole rock sample obtained using the bespoke SDD back-reflection laboratory facility compared to a prehnite fit produced by the mineral-fitting routine with data from Detrie et al. (2009). The diffraction and fluorescence constituents of the prehnite fit are also plotted, neither of which account for Rayleigh scattering.

5.4.4.2 Mica

A mica pressed powder-pellet was made using mica powder supplied by Hopkins and Williams Ltd and obtained from the Department of Geology at the University of Leicester. Datasets were acquired using the bespoke SDD back-reflection laboratory facility as outlined in table 5.1. Figure 5.36 shows the K-suppression dataset compared to a muscovite (mica) fit produced by the mineral-fitting routine. Figure 5.36 shows that the mineral fit, using data from Rothbauer (1971), explains five diffraction features at ~ 1.9 keV, ~ 2.2 keV, ~ 2.5 keV, ~ 2.9 keV and ~ 3.1 keV, and therefore that the mica pellet is of a muscovite (mica) mineralogy. The fit also includes Zr fluorescence, which was noted previously to be a contribution of the detector assembly in the bespoke chamber. The peak at ~ 0.9 keV is due to inaccuracies with Rayleigh scattering at low energies.

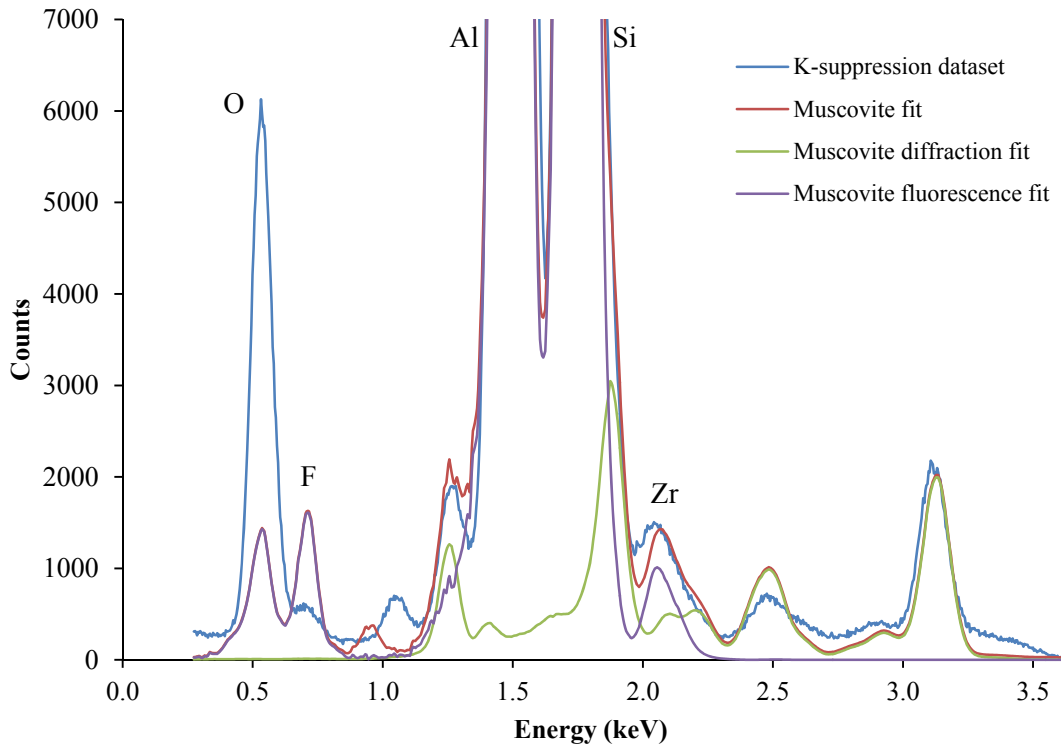


Figure 5.36. K-suppression dataset of the mica pellet obtained using the bespoke SDD laboratory facility outlined in section 5.2 compared to a muscovite (mica) fit produced by the mineral-fitting routine using data from Rothbauer (1971). The diffraction fit included a preferred orientation effect along the (001) plane with a March coefficient of 0.558. The mineral fit also accounts for Rayleigh scattering effects. The diffraction and fluorescence constituents of the muscovite (mica) fit are also plotted, neither of which account for Rayleigh scattering.

5.4.4.3 Talc and Kaolinites

Figures 5.37 – 5.39 show X-ray diffraction and fluorescence data acquired for samples of talc, china clay and kaolin. These samples were made using clay powders in the Department of Geology at the University of Leicester. Despite using data for talc and kaolinite from the AMCSD database, the mineral-fitting routine was unable to accurately reproduce the experimental datasets; however, a diffraction simulation of the expected phyllosilicate is included for comparative purposes.

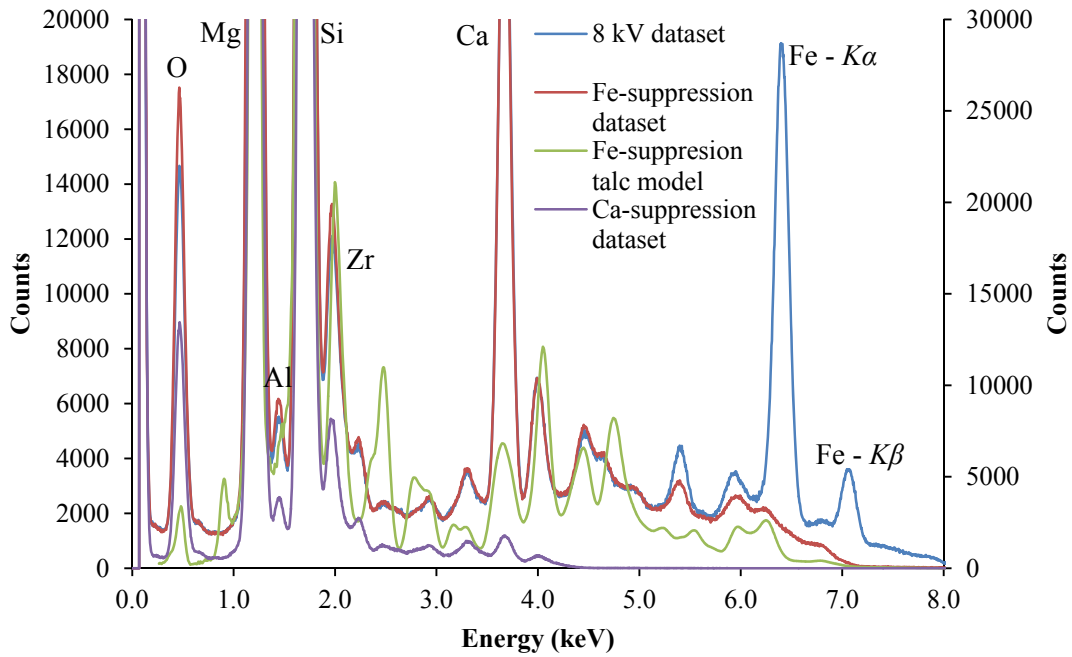


Figure 5.37. X-ray diffraction and X-ray fluorescence spectra of a pressed powder pellet of M26 Norwegian Talc. X-ray tube voltages and filament for the datasets are detailed in table 5.1. A Fe-suppression fluorescence and diffraction talc model created using the mineral-fitting routine using data from Perdikatsis and Burzlaff (1981) is included for comparison.

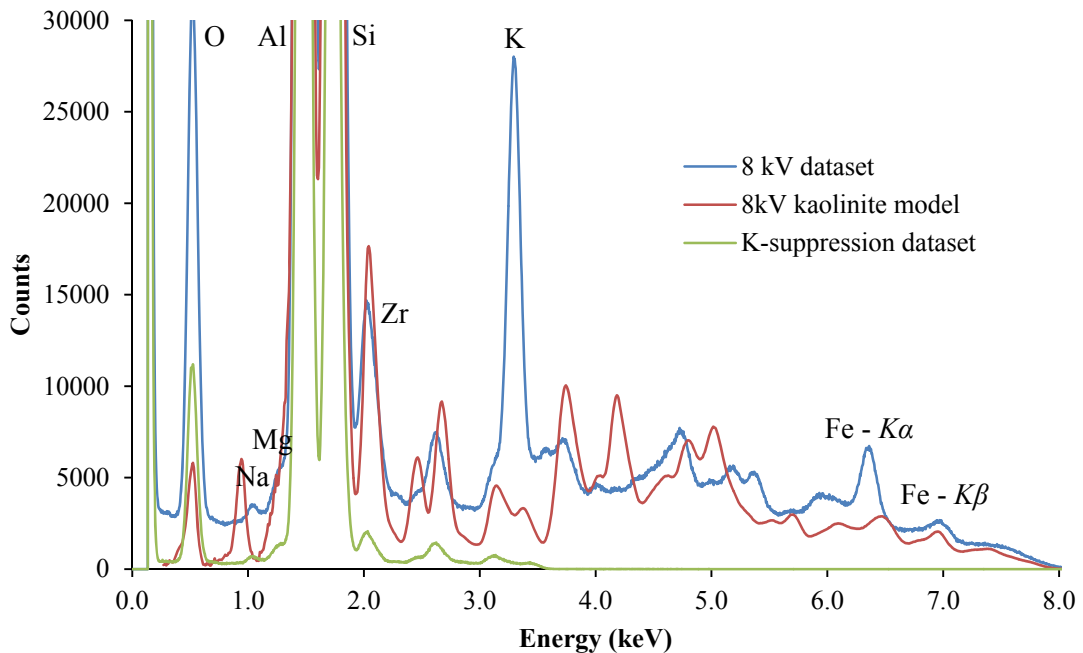


Figure 5.38. X-ray diffraction and X-ray fluorescence spectra of a pressed powder pellet of Fisons Kaolin. X-ray tube voltages and filament currents are detailed in table 5.1. An 8 kV kaolinite model created by the mineral-fitting routine with data from Bish and Von Dreele (1989) is included for comparison.

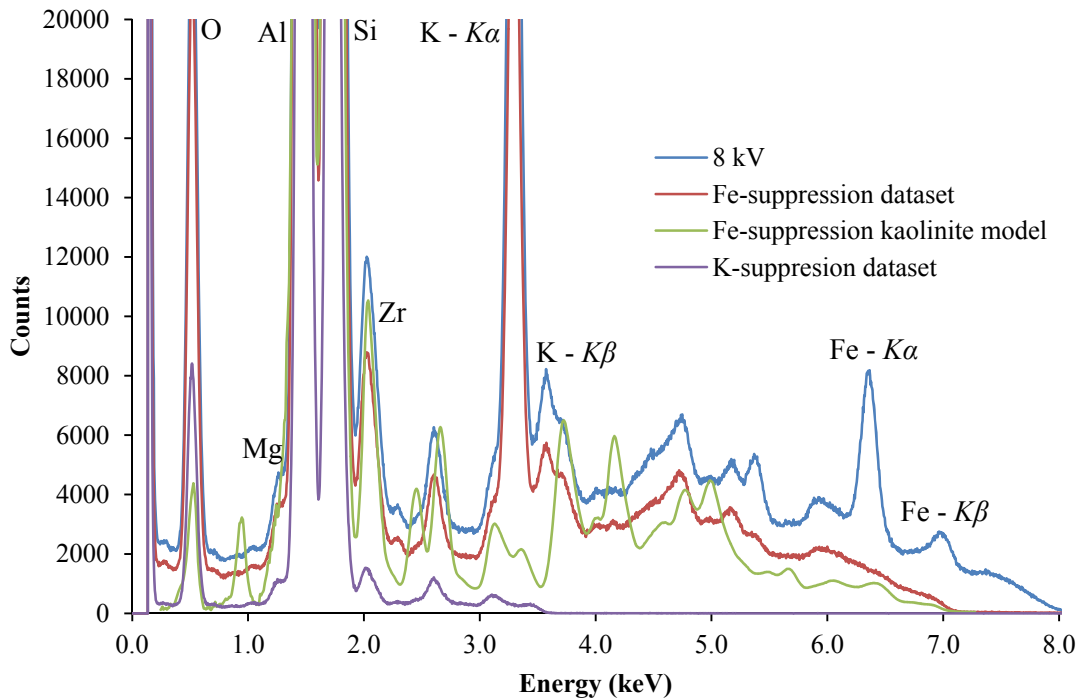


Figure 5.39. X-ray diffraction and X-ray fluorescence spectra of a pressed powder pellet of ECC China Clay (kaolin). X-ray tube voltages and filament currents are detailed in table 5.1. An Fe-suppression kaolinite model created by the mineral-fitting routine with data from Bish and Von Dreele (1989) is included for comparison.

5.5 Discussion

As shown in section 5.4, the back-reflection technique has been extensively tested on a variety of pellet and whole rock samples to demonstrate its capability in mineralogical analysis.

5.5.1 Oxides and Feldspars

The results and analysis in section 5.4.1 demonstrate the capability and constraints of the back-reflection X-ray diffraction technique in determining the presence of oxide and feldspar minerals in geological samples. Quartz (figure 5.3), goethite (figure 5.6), hematite (figure 5.8), orthoclase (figure 5.10) and plagioclase (figure 5.12) feldspar were detected in prepared pellet samples, whereas hematite (figure 5.8), magnetite (figure 5.15), goethite and quartz (figure 5.6) minerals were detected in whole rock samples. Figures 5.40 & 5.41 shows a comparison between the whole rock and pellet samples for goethite and hematite. The figures show the change in peak intensity due to preferred orientation effects, and also demonstrates the insensitivity of sample morphology for the back-reflection technique.

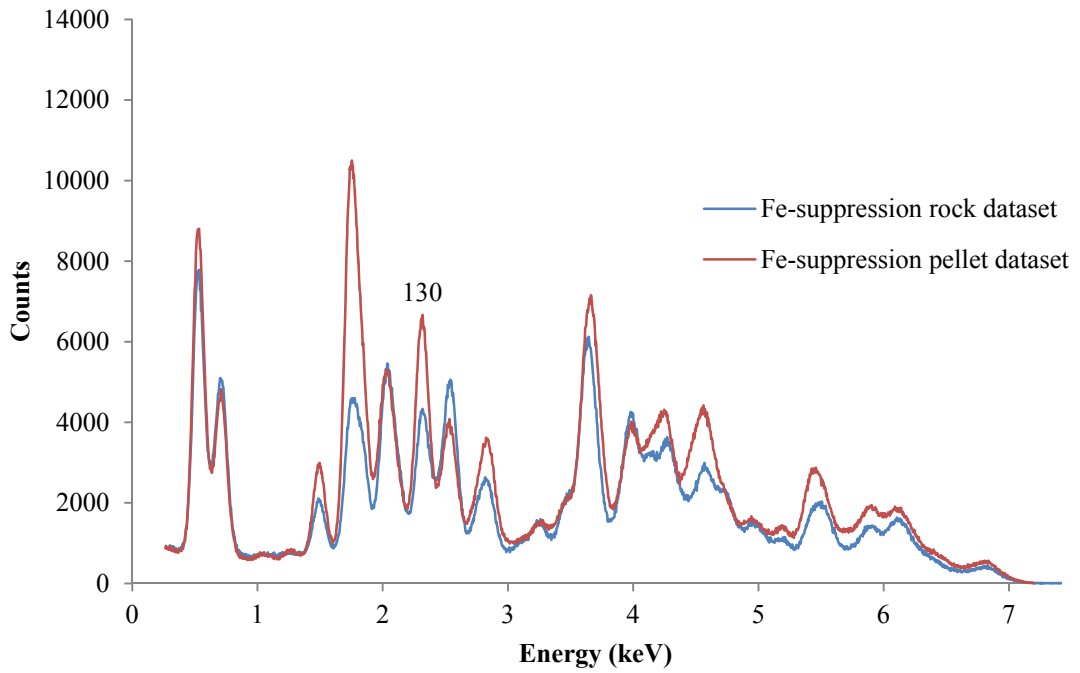


Figure 5.40. Goethite Fe-suppression datasets for the whole rock and pellet samples imaged in figure 5.4, with the goethite 130 peak marked highlighting the change in preferred orientation. Datasets are compared to goethite fits in figures 5.5 and 5.6.

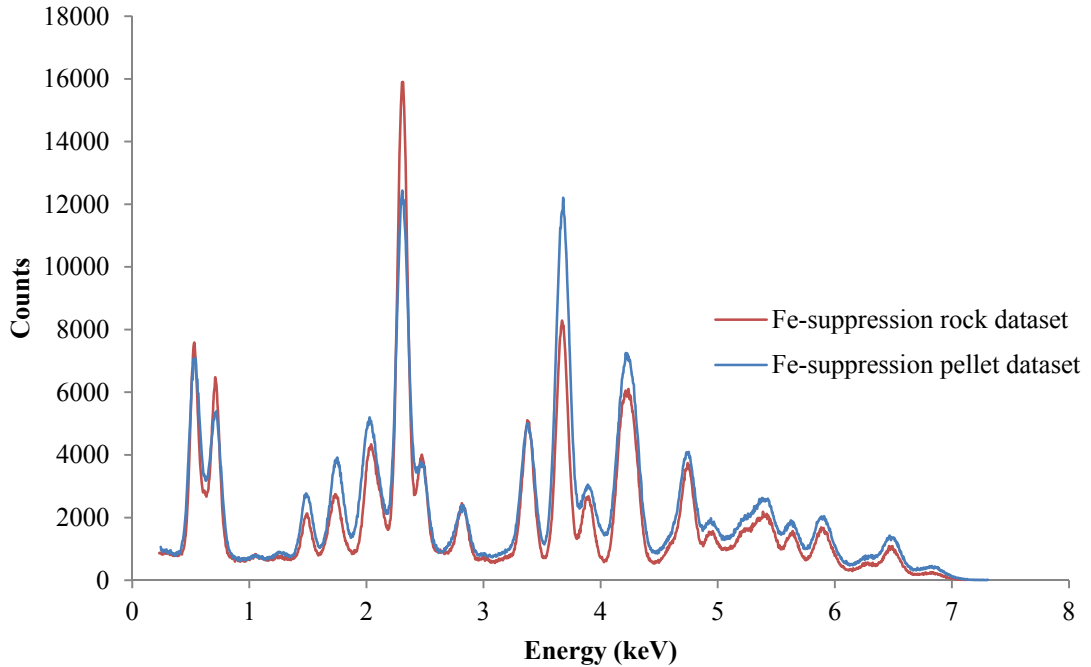


Figure 5.41. Hematite Fe-suppression datasets for the whole rock and pellet samples imaged in figure 5.4. Datasets are compared to hematite fits in figures 5.7 and 5.8.

The identification of quartz, goethite, hematite and magnetite was straightforward, whereas the analysis and identification of the feldspar samples imaged in figures 5.9 and 5.11 was not.

Figure 5.10 shows diffraction information of a sample orthoclase feldspar, which was characterised to be either orthoclase or sanidine, both of which are classified as alkali feldspars. The X-ray fluorescence information returned by the back-reflection technique showed the presence of both Na and K in the sample, meaning that orthoclase (KAlSi_3O_8) is either present with an additional Na bearing mineral or sanidine ($\text{K,Na(AlSi}_3\text{O}_8)$) is present, or perhaps a mixture of the two. The ambiguity and similarity between the minerals suggest that the sample can only simply be characterised as a K-rich alkali feldspar.

Figures 5.12 – 5.14 show how the back-reflection X-ray diffraction technique has difficulties in determining the type of plagioclase feldspar present in the rock sample imaged in figure 5.11, due to the similarities in their diffraction patterns. However, the back-reflection technique returns useful elemental information of the sample via X-ray fluorescence that can help guide analysis to approximate the type of plagioclase present. The different types of plagioclase feldspars have varying amounts of Na and Ca, where the Na endmember of the plagioclase is albite ($\text{NaAlSi}_3\text{O}_8$) and the Ca endmember of the series is anorthite ($\text{CaAlSi}_3\text{O}_8$). The minerals in-between these endmembers (oligoclase, andesine, labradorite and bytownite) can be classed in varying amounts of albite and anorthite. Figure 5.14 shows that albite and oligoclase are close fits for the X-ray diffraction features in the spectrum returned by a Ca-suppression acquisition; however it is unlikely that the sample can be classified as pure albite, as both Na and Ca fluorescence was present during sample analysis. Enough information was returned to classify the sample as plagioclase feldspar.

The difference in data quality between the pre-existing CCD and bespoke SDD laboratory facilities is illustrated in figure 5.2, where much faster integration times and higher signal-to-noise across the spectrum is shown to lead to clearer resolution of diffraction peaks at energies >5.5 keV. This is due to the shorter sample-detector distances in the bespoke SDD laboratory facility. Comparisons between the pre-existing CCD and bespoke SDD laboratory facilities are discussed in section 5.5.5.

5.5.2 Carbonates

The results and analysis in section 5.4.2 show that the back-reflection technique can accurately discriminate between carbonate minerals (calcite and dolomite) in whole rock samples, as illustrated in figures 5.18 and 5.19. The pellet of Japanese standard dolomite, JDo-1, was also analysed as shown in figure 5.20. The results in figures 5.18 – 5.20 are consistent with models, making mineral identification clear-cut. However, the issue of preferred orientation became apparent in the dolomite pellet JDo-1 and not for the whole rock sample; potentially indicating the advantage of unprepared whole rock samples over prepared pellet samples for analysis with the back-reflection XRD technique, although this may not be true in other cases. Preferred orientation effects are prevalent in processed samples when needle- or plate-like crystallites orientate themselves in a specific manner under pressure (i.e. when a powder pellet is pressed). This preferred orientation of a processed sample may not be present in unprepared samples (whole rocks) where crystallites may have formed in a random nature; however, natural preferred orientation can and does occur.

There were also some contaminants in the samples (Al, Mg and Si fluorescence) that indicated that there were minor amounts of additional minerals present but the contaminant content was low compared to calcite/dolomite content resulting in minimal interference of diffraction peaks.

5.5.3 Sulphates

The use of the back-reflection XRD technique to analyse Mars analogues from Watchet Bay in Somerset UK proved to be rather challenging. The analysis using the pre-existing CCD laboratory facility resulted in 90% gypsum 10% bassanite being identified in the first WatchetB pellet (figure 5.23) and bassanite being identified as the dominant mineral in the first WatchetC pellet (figure 5.24). The samples were also analysed using a Bruker D8 Advance diffractometer in the Department of Geology at the University of Leicester utilising powder samples of WatchetB and WatchetC, which revealed gypsum to be dominant in both samples, with no indications that bassanite or anhydrite were present (Haidon, 2013). The difference in the environmental conditions during different XRD techniques was thought most likely to be the cause of the different conclusions. In the pre-existing CCD laboratory setup the samples were placed under vacuum conditions whereas the ADXRD technique did not place them under vacuum. Given that the penetration depth of the back-reflection technique is the top few microns of a sample

(Hansford, 2011a), it is possible the sulphate samples were dehydrating under vacuum to this depth. Further analysis with additional pellet samples was carried out as shown in figures 5.24, 5.25 and 5.28. Datasets were taken as soon as possible after exposure to vacuum conditions, and the XRD analysis showed that both WatchetB and WatchetC were dominated by gypsum. As shown in figure 5.25, the second WatchetB pellet was left under vacuum and after two days the XRD spectrum changed to Anhydrite-III, showing that the samples were dehydrating under vacuum. Whole rock samples of WatchetB and WatchetC were also analysed using the pre-existing CCD (figures 5.26 and 5.29) and bespoke SDD (figures 5.30 and 5.31) laboratory facilities, from which gypsum was shown to be the dominant mineral. This study of gypsum samples from Watchet Bay highlights the capability of the back-reflection technique in distinguishing between gypsum and its dehydrated products (bassanite and anhydrite).

Section 5.4.3.2 shows that an XRD spectrum of a whole rock sample of jarosite analysed using the bespoke SDD laboratory facility, as shown in figure 5.33, can be identified as jarosite using the mineral-fitting routine.

5.5.4 Phyllosilicates

The whole rock analysis in section 5.4.4.1 demonstrates that the back-reflection technique has the ability to determine the presence of prehnite in a whole rock sample. This is particularly relevant for the detection of impact-induced hydrothermal systems, as outlined and studied in Chapter 4. Unfortunately the analysis in figure 5.35 is obscured by Ca fluorescence in a Ca-suppression acquisition. The presence of this fluorescence is due to the high-voltage power supply unit for the X-ray tube being set a little too high. The modelled diffraction peak intensities are also not fully comparable with the experimental acquisition; however, there is an agreement with diffraction feature positions. This could be due to a naturally occurring preferred-orientation effect in the whole rock sample.

In section 5.4.4.2, the analysis of a pressed powder pellet of mica shown in figure 5.36 demonstrates the capability of the back-reflection technique of identifying the presence of phyllosilicate minerals. The data acquired using the bespoke SDD back-reflection facility was analysed using the mineral-fitting routine to identify the presence of muscovite, a dioctahedral mica.

The analysis of talc and kaolinite samples, shown in section 5.4.4.3 (figures 5.37 – 5.39), proved unsuccessful. It is possible that preferred-orientation effects are the cause

for the difficulty in analysis, especially as the clay samples are pressed-powder pellets. Further work is required to fully ascertain whether this is the case, and to assess the capabilities of the back-reflection technique in a low-resolution, laboratory configuration to determine the presence of these clays in a sample.

5.5.5 Comparison of the two facilities

The two laboratory facilities used to demonstrate the capabilities of the back-reflection technique in this chapter each have different capabilities.

At the start of this study only the pre-existing CCD laboratory facility was available. This facility had large sample-detector distances resulting in the need for experimental acquisition times of the order of 3 hours to achieve reasonable signal-to-noise ratios. The CCD also required cooling via a liquid nitrogen fed cold finger, as outlined in section 5.2. This led to a significant amount of time required to capture a single dataset; however, the use of a CCD to capture a 2θ range of diffracted X-rays aided in distinguishing between diffraction and fluorescence peaks without the need to take additional datasets (as with the later bespoke SDD laboratory facility). The pre-existing CCD facility also enabled the perpendicular rotation of a sample with respect to the incident X-ray beam whilst under vacuum, which enabled the experimental determination of preferred orientation effects as identified with the (104) plane parallel to the surface of the JDo-1 pellet (figure 5.21). The rotating sample holder also enabled calibration targets to be secured on the sample holder and be rotated out of the incident X-ray beam and CCD field of view for sample data acquisition. The use of a CCD also added the imaging capability of a 2θ range that was useful in analysing samples with large crystallites. The pre-existing CCD facility also had a flexible geometry.

The purpose built bespoke SDD back-reflection laboratory facility more closely reflects the potential design of a compact instrument based on the back-reflection technique. The use of a SDD as opposed to a CCD was advantageous in minimal cooling requirements and greater count-rates due to shorter sample-detector distances. Evaluating the Ca- $K\alpha$ fluorescence peak in the WatchetB 8 kV datasets gave equivalent count rates of 18.2 and 647.8 counts per second for the pre-existing CCD and bespoke SDD laboratory facilities, respectively. The energy resolution of the SDD was also better than CCD resolution at high energies as shown in figure 5.2 and table 5.2. The annular SDD was also split into four channels, each covering an approximate 90° region. Comparisons of the four channels enabled the inspection of X-ray diffraction peak intensity, and

effectively the completeness of the Debye-Scherrer cone. Variations in peak intensity over these four channels indicated the presence of large crystallites. The translation stages used in the back-reflection facility enabled the analysis of multiple samples, as different samples could be manoeuvred in and out of the incident X-ray beam.

Table 5.2. Table comparing full width at half maximum values (FWHM) for specific XRF peaks for both the pre-existing CCD and bespoke SDD laboratory facilities. Values were extracted by fitting Gaussian peaks to the experimental data.

XRF Peak	FWHM (eV)	
	Pre-existing CCD Facility	Bespoke SDD Facility
Mg- $K\alpha$	85.3 ± 0.5	86.7 ± 0.5
S- $K\alpha$	100.6 ± 0.3	99.2 ± 0.2
K- $K\alpha$	110.0 ± 1.3	116.8 ± 0.4
Ca- $K\alpha$	126.2 ± 0.4	123.5 ± 0.1
Fe- $K\alpha$	174.5 ± 1.2	161.4 ± 0.2

The back-reflection technique, in comparison to more typical XRD techniques outlined in chapter 3, is beneficial for non-destructive, large-scale characterisation and preferred orientation analysis as highlighted by the work in this chapter (for example see figures 5.2, 5.40 and 5.41). Typical XRD techniques outlined in chapter 3, such as ADXRD instruments used in a laboratory or those deployed on Mars (CheMin), require sample preparation to ensure the small crystallite size as well as random orientation of crystallites to minimise preferred orientation effects.

5.5.6 Avenues of future work and applications

Future avenues of investigation of the back-reflection technique should focus on monochromating the sample-incident X-ray beam to enable greater diffraction peak resolution, like that explored in Chapter 6 at the Diamond Light Source. The diffraction and fluorescence modelling using PoDFluX and the mineral-fitting routine has proved to be useful in identifying sample constituents; however, greater resolution would enable more certainty in mineral identification, particularly of trace minerals.

PoDFluX and the mineral-fitting routine has been shown to be useful in identifying mineral constituents of samples in this chapter. The analysis of XRD data is initially problematic when the preferred-orientation of crystallites enhances specific peaks; however, once identified its effects can be modelled. As shown in figure 5.21,

experimental tilting of a sample with respect to the incident X-ray beam can reveal the presence of preferred-orientation. Change of preferred-orientation effects on specific (*hkl*) peaks can be modelled in PoDFluX and the mineral-fitting routine to aid in understanding its effect (e.g. figure 5.21). Only when a mineral fit can accurately reproduce all diffraction peak intensities, including the enhanced preferred orientation peak, can it be considered representative of the sample.

The mineral-fitting routine proved useful in estimating Rayleigh scattering contributions to the resultant model datasets; however, it was inaccurate at energies < 1 keV. On both the pre-existing CCD and bespoke SDD laboratory facilities filters were used on the X-ray tubes which significantly reduced the intensity of X-rays below 1 keV that, together with the difficulty in estimation of X-ray diffraction, fluorescence and Rayleigh scattering at these low energies. PoDFluX and mineral-fitting results do not accurately reproduce the attenuated spectra at low energies, and further investigation is suggested.

Sample-incident X-ray spot size was estimated to be ~10 mm diameter in the pre-existing CCD facility and ~7 mm in the bespoke SDD facility. A method of altering the spot size could be considered to make XRD measurements but this would depend on sample crystallite size. Fine-scale measurements, and subsequent fine-scale mapping, could be undertaken with a small spot size if powder averaging was sufficient. However, if greater powder averaging was required then a larger spot size would be required and possibly sample movement during acquisition.

5.6 Conclusions

1. Results show that the back-reflection technique has the ability to, in some cases, identify oxides, feldspars, carbonate, sulphates and phyllosilicates. Identification of these minerals in the context of planetary science is important as they aid in the characterisation of environments, such as an impact-induced hydrothermal environment as studied in Chapter 4.
2. The effects of sample morphology have been consistently shown to have negligible effects of mineral identification using diffraction data returned using the back-reflection technique.
3. The effects of preferred-orientation of crystallites can be experimentally determined using the back-reflection technique, and its effect on resultant X-ray

diffraction spectra can be accounted for using PoDFluX and the mineral-fitting routine.

4. The geometry of the back-reflection technique lends itself to a compact instrument design that could be deployed on the arm of a planetary lander.
5. Given the current low-resolution of the technique, further work would be required to make the instrument technique more competitive with similar non-destructive, rival techniques such as NIR reflectance and Raman spectroscopy techniques. However, measurements with the current low-resolution configuration could be complementary to measurements made using other techniques.

6. High-Resolution Back-Reflection Energy-Dispersive X-ray Diffraction

In this chapter, the back-reflection energy-dispersive X-ray diffraction technique is tested using the Diamond Light Source synchrotron facility, which is outlined in section 3.6 of this thesis. The back-reflection technique (Hansford, 2011a) described in Chapter 3 and demonstrated in Chapter 5 has been shown to be successful at identifying the mineral constituents of powder pellet and rock samples, which demonstrates the capability of the technique. The results in this chapter were obtained using a highly monochromatic beam at the Diamond Light Source that facilitated the capture of high-resolution X-ray diffraction data, as opposed to the comparatively lower-resolution laboratory facilities at the University of Leicester used in Chapter 5.

Using Beamline B18 at the Diamond Light Source, a monochromatic beam of X-rays was directed at a sample with an incident spot size of approximately $1.7 \times 0.9 \text{ mm}^2$ and swept through 2.1 – 5.0 keV with X-ray fluorescence, X-ray diffraction and Rayleigh scattering being recorded at regular intervals by a silicon drift detector (SDD) of 50 mm^2 area at $2\theta = 175.91 \pm 0.32^\circ$. The results shown here demonstrate the capability of a high-resolution, non-destructive, energy-dispersive back-reflection X-ray diffraction method that is uniquely insensitive to sample morphology. The high-resolution technique was applied to a variety of samples, with a selection of results analysed and explained in this chapter. This technique has a variety of geological and heritage applications where a high-resolution non-destructive method of analysis is required.

6.1 Analytical Procedure

Data was taken using the procedure outlined in section 3.6 and analysed using a series of purpose-written IDL (Interactive Data Language) computer programs. During data acquisition a Si(111) double-crystal monochromator swept through the X-ray energy range from 2.1 keV to 5.0 keV in 1376 seconds, with a SDD recording an energy spectrum at 16.2 milli-degree intervals of the monochromator. This resulted in a large dataset of SDD X-ray spectra containing diffraction, fluorescence and Rayleigh scattering against monochromator energy. The monochromator step size can be loosely described as $\sim 1 \text{ eV}$ across the dataset, but in reality the step size varied across the dataset as shown in figure 6.1. Figure 6.1 shows the amount of data points taken at low energies is greater compared

to high energies and therefore weak peaks may not be as easily identifiable at high energies compared to those at low energies as there are too few points per peak.

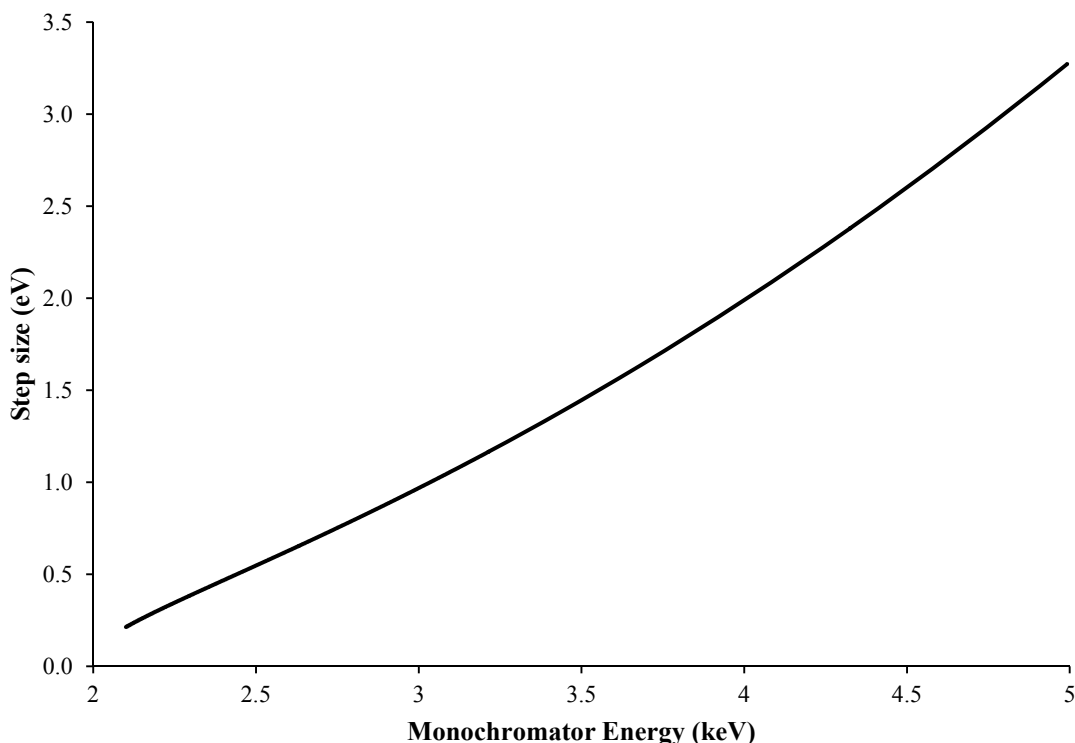


Figure 6.1. Plot of monochromator step size against monochromator energy to show the step size variation over the dataset.

An initial IDL program used a process of “windowing” to extract the diffraction information from the dataset and remove a baseline bias. The effect of this processing is illustrated in figure 6.2.

The first stage of the IDL program was written to extract the diffracted peak from each SDD spectrum. This process of “windowing” extracted a 30 eV region centred on the energy of the monochromated beam (the location of the diffracted peak) for each SDD spectrum. Application of this windowing program to extract the scattered peak aids in removing fluorescence contributions in the dataset. For example, in the sum SDD counts data in figure 6.2 there is a *K* edge at 3.691 keV that is significantly minimised in the window counts dataset.

The second stage of the IDL program was to remove the remaining baseline bias caused by Rayleigh scattering. This was excluded from the data by a recursive polynomial trend-line fitting and removal routine between specified absorption edges to best

approximate the dataset baseline. For each iteration, intensity values greater than the polynomial trend-line fit were removed. This fitting and removal process iterated until the chi-squared value for the fit converged (when a baseline fit was obtained). The dataset baseline corresponding to the fitted baseline was then removed, with a 0.01 bias added to the final spectrum to aid plotting. An additional 14 eV region centred on present absorption edges was masked to reduce the effect of the absorption edge on the baseline fitting process.

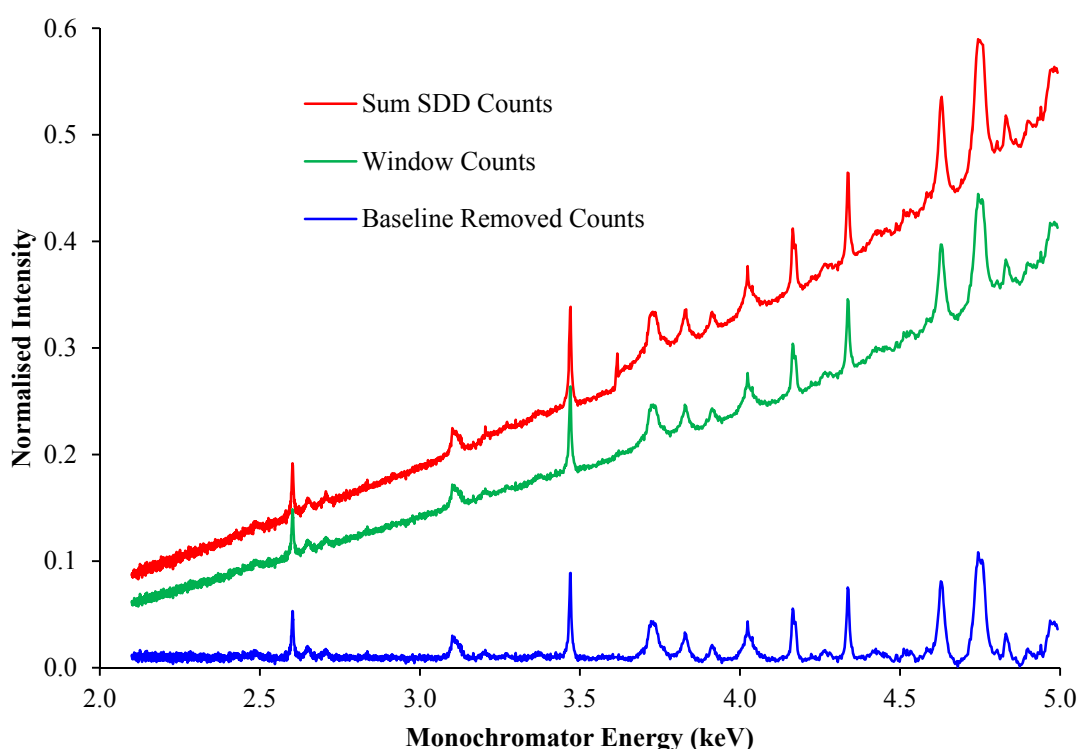


Figure 6.2. Plot of a kaolinite powder pellet dataset at various stages of IDL processing.

The peak positions were determined using a choice of four different lineshapes to enable the accurate extraction of centre line energy, and therefore the accurate determination of sample d-spacings. For this process, four different lineshapes were used: Gaussian, Lorentzian, Pseudo-Voigt and Pearson VII (Hansford, 2016a). The Pseudo-Voigt and Pearson VII lineshapes accurately reproduced the well-resolved experimental peaks that had good signal-to-noise, with Pearson VII lineshapes being marginally more accurate in some cases. Gaussian and Lorentzian lineshapes were used to reproduce the broadest peaks that had low signal-to-noise, which may have been the result of overlapping peaks. Generally, highly-crystalline materials produce sharp peaks whereas

minerals of lower crystallinity, such as clays, produce broad peaks as outlined in Chapter 2. This difference in peak breadth can enable a visual assignment of clays in a multi-mineral diffraction pattern (Moore and Reynolds, 1997).

The conversion of energy to d -spacing was achieved using a two-step calibration approach, as outlined by (Hansford et al., 2017). The first step was to use an acquired dataset of Si powder from the National Institute of Standards & Technology (NIST SRM 640c) that has four diffraction lines in the 2.1 – 5.0 keV energy range, to derive an average value for 2θ of 175.09° . This step in the calibration highlighted a discrepancy between nominal beam energy and true beam energy that was accounted for in the second step of the calibration. This second step used the model:

$$E' = pE + q \quad (6.1)$$

where E is the nominal beam energy, E' the true beam energy and p and q are parameters to be determined. The parameters p and q were determined using 32 diffraction peaks extracted from the NIST Si standard along with corundum and quartz powder pellets using a downhill simplex method of fitting to reduce the root-mean-square value of the difference between calculated d -spacings and fitted d -spacings. This gave $p = 0.999897 \pm 0.000012$ and $q = 0.51 \pm 0.04$ eV, demonstrating that the difference between nominal and true beam energy is minimal (Hansford et al., 2017). Conversion from energy to d -spacing was then calculated using the equation:

$$\frac{1}{d} = \frac{2 \sin \theta}{hc} (pE + q) = p'E + q' \quad (6.2)$$

where $p' = (1.61144 \pm 0.00002) \times 10^{-4} \text{ eV}^{-1} \text{ \AA}^{-1}$ and $q' = (8.2 \pm 0.6) \times 10^{-5} \text{ \AA}^{-1}$.

The International Center for Diffraction Data (ICDD) database 2015 release was used to identify the sample constituents by use of d -spacing searches to ultimately assign (hkl) Miller indices to each peak. Using the extracted d -spacing values, assigned Miller indices and assumed crystal system, the unit cell was determined for each mineral in a sample by use of an IDL least-squares fitting routine.

The identification of clay minerals in X-ray diffraction spectra based on all (hkl) peaks is not diagnostic due to the similarity of the **a** and **b** unit cell dimensions between different clay minerals however, the **c** unit cell dimension does differ between different

clay minerals. Consequently, the basal, (00 l), peaks are used as a primary method of clay identification, but the weak (060) peaks are also of importance in clay minerals as they enable the distinction between dioctahedral and trioctahedral types. This is because the **b** unit cell dimension is influenced by the cation size and site occupancy in the octahedral sheet, and is not influenced by the β monoclinic angle (Moore and Reynolds, 1997).

6.2 Results

The high-resolution back-reflection X-ray diffraction results of 7 powder pellet samples (quartz, dolomite, siderite, mica, talc and two kaolinites) are presented here. The samples were selected on the basis of previous investigations and their potential for demonstrating the back-reflection technique in a high-resolution configuration.

6.2.1 Quartz

Figure 6.3 shows the result for a quartz powder pellet sample, obtained from the Department of Geology at the University of Leicester, compared to the calculated quartz peak positions based on the determined unit cell. Quartz peaks were identified from baseline subtracted data using library diffraction data (Natl. Bur. Stand., 1981). The Miller indices and d -spacings of the identified peaks were used to calculate the mineral unit-cell dimensions, which is detailed in table 6.1.

Figure 6.3 shows that all 17 peaks were identified as quartz (which are detailed in Appendix C.1). During data processing a 30 eV break was introduced at 4.55 keV to aid in baseline estimation and subtraction. Table 6.1 details the calculated trigonal unit cell from the peaks identified, which is compared to a reference unit cell identified using the ICDD database.

Table 6.1. Calculated unit cell from identified peaks in figure 6.3 compared to a published unit cell for quartz.

Unit Cell Attribute	Sample quartz	Quartz, syn (Natl. Bur. Stand., 1981)
a (Å)	4.91388(6)	4.9134(2)
c (Å)	5.40498(9)	5.4053(4)
Volume (Å ³)	113.02	113.01

Error estimates are given in brackets and are quoted in units of the least significant digit.

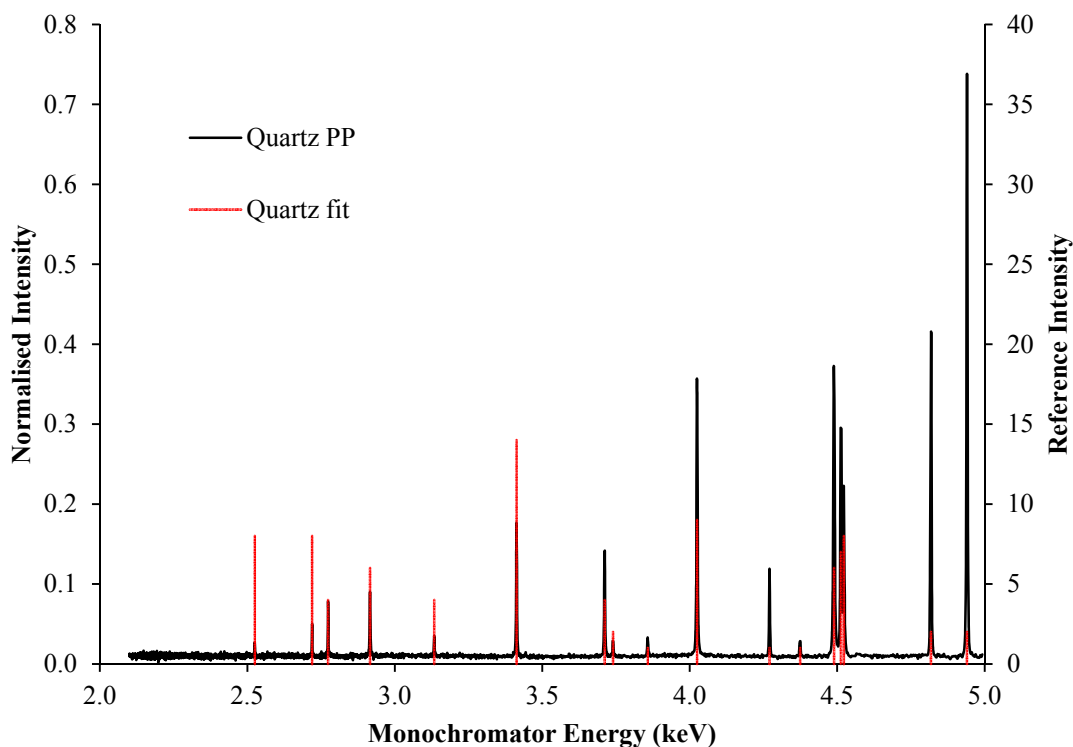


Figure 6.3. Quartz PP processed dataset compared to peak positions calculated using the fitted unit cell for quartz in table 6.1. Diffraction peak intensities are taken from Natl. Bur. Stand. (1981).

6.2.2 Dolomite

Figure 6.4 shows the identification of dolomite and calcite in a powder pellet by comparison to calculated dolomite and calcite peak positions based on the determined unit cells. The powder pellet is a Japanese dolomite standard known as JDo-1, and it was obtained from the Department of Geology at the University of Leicester. Dolomite peaks in the baseline subtracted data were identified using diffraction data from Keller and McCarthy (1985) and Ross and Reed (1992). Calcite peaks in the baseline subtracted data were identified using diffraction data from Swanson (1953) and Pilati et al. (1998). The Miller indices and d -spacings of the identified peaks were used to calculate the trigonal mineral unit-cell dimensions for dolomite and calcite, which are detailed in tables 6.2 and 6.3.

Figure 6.4 shows that 21 peaks were identified as dolomite and 8 peaks were identified as calcite (which are detailed in Appendix C.2). During data processing, additional 30 eV breaks were used at 4.43 keV and 4.7 keV to aid in baseline estimation and subtraction. Tables 6.2 and 6.3 detail the calculated unit cells for dolomite and calcite from the peaks identified, which are compared to reference unit cells identified using the ICDD database.

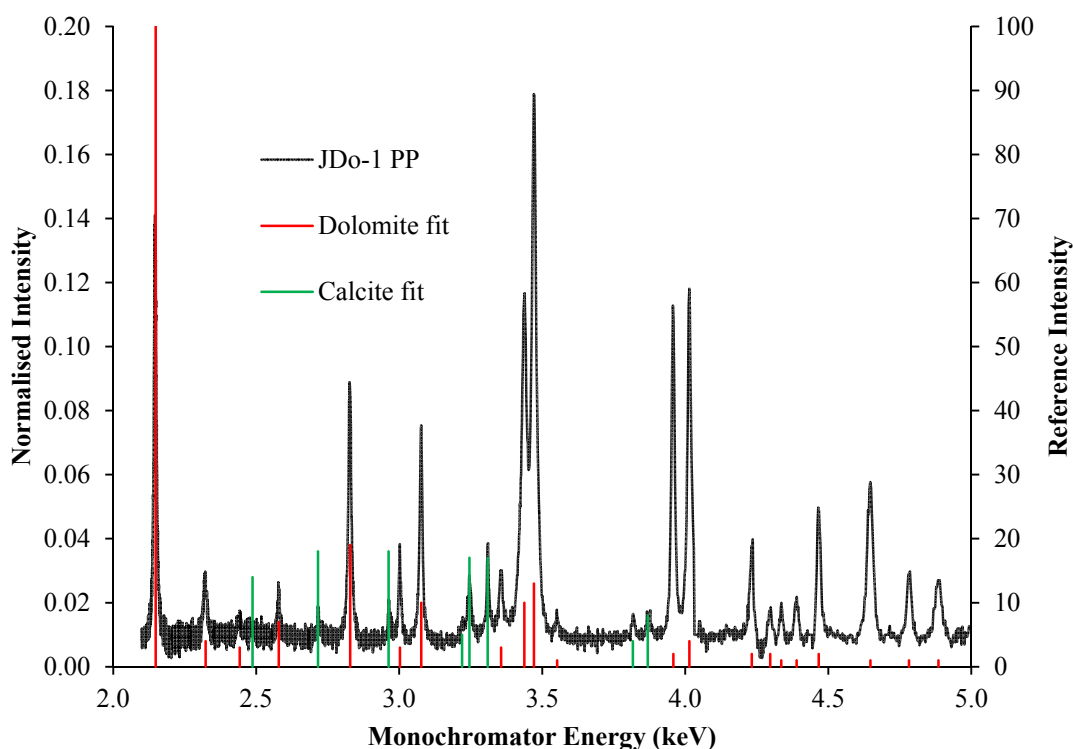


Figure 6.4. Dolomite (JDo-1) PP processed dataset compared to peak positions calculated using the fitted unit cells for dolomite and calcite in tables 6.2 and 6.3, respectively. Diffraction peak intensities for dolomite and calcite are taken from Killer and McCarthy (1985) and Swanson (1953).

Table 6.2. Calculated unit cell from identified peaks in figure 6.4 compared to published unit cells for dolomite.

Unit Cell Attribute	Sample JDo-1 dolomite	Dolomite (Keller and McCarthy, 1985)	Dolomite (Ross and Reed, 1992)
a (Å)	4.8123 (4)	4.8092(2)	4.8064(5)
c (Å)	16.0223(19)	16.020(5)	16.006(2)
Volume (Å ³)	321.33	320.88	320.22

Error estimates are given in brackets and are quoted in units of the least significant digit.

Table 6.3. Calculated unit cell from identified peaks in figure 6.4 compared to published unit cells for calcite.

Unit Cell Attribute	Sample JDo-1 calcite	Calcite (Swanson, 1953)	Calcite, syn (Pilati et al., 1998)
a (Å)	4.9890(9)	4.989	4.991(2)
c (Å)	17.0569(8)	17.062	17.062(2)
Volume (Å ³)	367.66	367.78	368.07

Error estimates are given in brackets and are quoted in units of the least significant digit.

6.2.3 Siderite

Figure 6.5 shows the identification of siderite and hematite in a powder pellet, of unknown origin, by comparison to calculated siderite and hematite peak positions based on the determined unit cells. Siderite peaks in the baseline subtracted data were identified using diffraction data from Effenberger et al. (1981) and Hematite peaks were identified using diffraction data from Yu et al. (1999). The Miller indices and d -spacings of the identified peaks were used to calculate the mineral unit-cell dimensions for siderite and hematite, which are detailed in tables 6.4 and 6.5.

Figure 6.5 shows that 17 peaks were identified as siderite and 4 peaks were identified as hematite (which are detailed in Appendix C.3). Tables 6.4 and 6.5 detail the unit cells for siderite and hematite, which are calculated from the peaks identified. These are compared to reference unit cells identified using the ICDD database.

Table 6.4. Calculated unit cell from siderite identified peaks in figure 6.5 compared to a published unit cells for siderite.

Unit Cell Attribute	Sample siderite	Siderite (Effenberger et al., 1981)	Siderite, magnesian (Merlini and Hanfland, 2013)
a (Å)	4.6750(3)	4.6916(4)	4.6738
c (Å)	15.2764(12)	15.3796(16)	15.271
Volume (Å ³)	289.14	293.17	288.89

Error estimates are given in brackets and are quoted in units of the least significant digit.

Table 6.5. Calculated unit cell from hematite identified peaks in figure 6.5 compared to a published unit cell for hematite.

Unit Cell Attribute	Sample hematite	Hematite (Yu et al., 1999)
a (Å)	5.0445(31)	5.0206(24)
c (Å)	13.7926(65)	13.7196(13)
Volume (Å ³)	303.96	299.49

Error estimates are given in brackets and are quoted in units of the least significant digit.

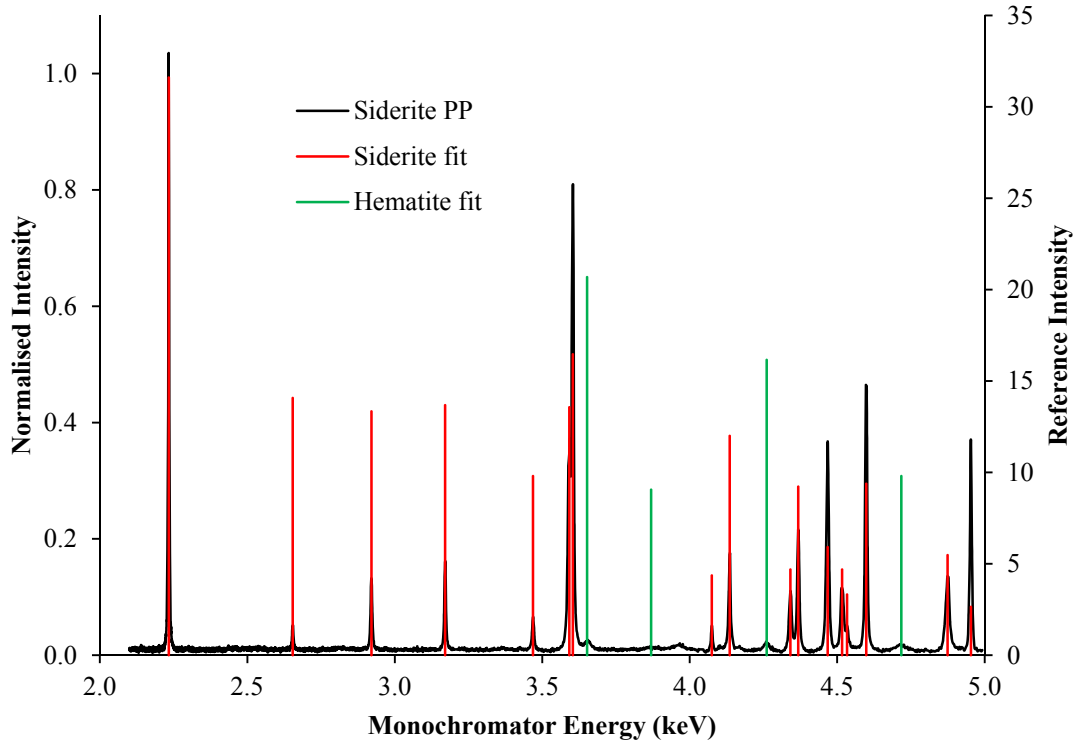


Figure 6.5. Siderite PP processed data compared to peak positions calculated using the fitted unit cells for siderite and hematite detailed in table 6.4 and 6.5, respectively. Diffraction peak intensities for siderite and hematite were taken from Effenberger et al. (1981) and Yu et al. (1999), respectively.

6.2.4 Kaolinite

Figure 6.6 shows the identification of kaolinite in two powder pellets by comparison to the calculated kaolinite peak positions. Both clay pellets were made in the Department of Geology at the University of Leicester from two powders: Kaolin and China Clay supplied by Hopkins & Williams Ltd and English China Clay PLC, respectively. Kaolinite peaks in the baseline subtracted data were identified using diffraction data from Young and Hewat (1988) and Collins and Catloe (1991). The Miller indices and d -spacings of the identified peaks were used to calculate the mineral unit-cell dimensions, which are detailed in table 6.7.

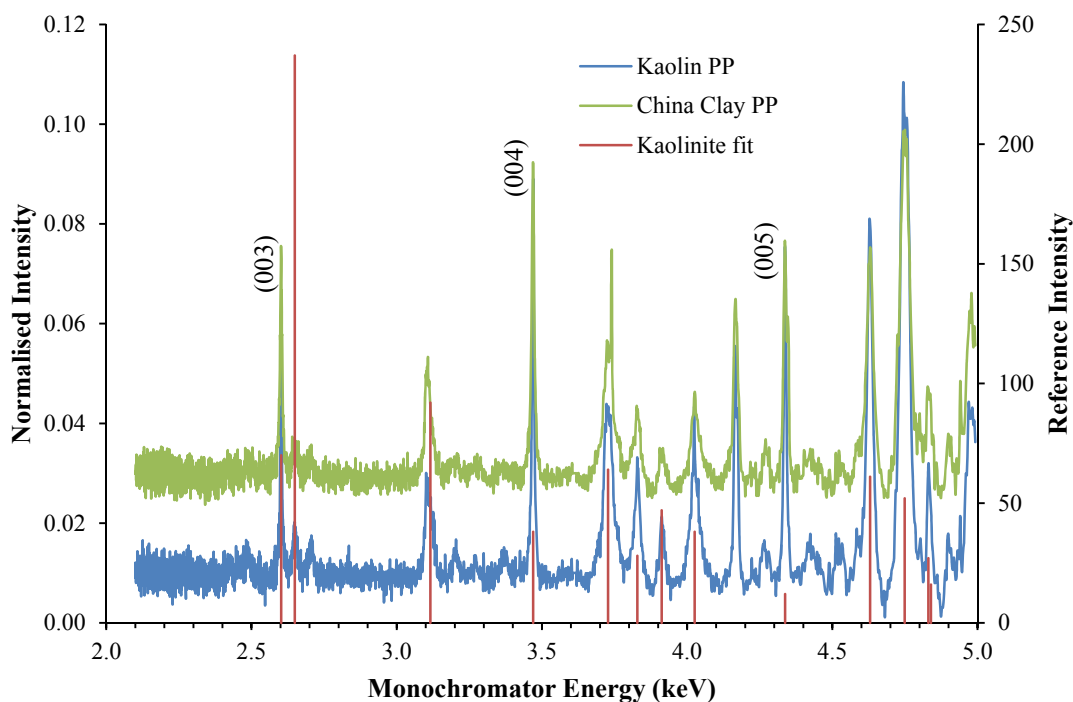


Figure 6.6. Kaolin PP and China Clay PP processed datasets compared to calculated peak positions using the fitted unit cell for kaolinite detailed in table 6.7. The basal peaks are labelled and the diffraction peak intensities for kaolinite are taken from Young and Hewat (1988).

Figure 6.6 shows that 13 Kaolin PP peaks were identified as kaolinite (which are detailed in Appendix C.4). The basal peaks were identified and are outlined in table 6.6, along with their d -spacings. Table 6.7 details the calculated unit cell from the peaks identified, and this is used in table 6.6 to calculate the d -spacing for comparison to the measured d -spacing. The calculated unit cell in table 6.7 is compared to two reference unit cells identified using the ICDD database. Unidentified peaks present in figure 6.6 were not accurately attributed to kaolinite, and consequently were not included in the unit cell fits.

Table 6.6. Extracted basal peak positions with calculated and fitted d -spacings for the kaolin powder pellet dataset shown in figure 6.6.

Miller Indices (hkl)	Energy (eV)	d -spacing (\AA)	d -spacing fit (\AA)	d diff (\AA)
0 0 3	2602.09	2.38440	2.38419	0.00021
0 0 4	3469.75	1.78823	1.78814	0.00009
0 0 5	4337.54	1.43051	1.43052	-0.00001

Table 6.7. Calculated unit cell from identified peaks in figure 6.6 compared to two published unit cells for kaolinite.

Unit Cell Attribute	Sample kaolinite	Kaolinite (Young and Hewat, 1988)	Kaolinite (Collins and Catlow, 1991)
a (Å)	5.1659(5)	5.14971(4)	5.1554
b (Å)	8.9578(14)	8.93507(7)	8.9448
c (Å)	7.3893(5)	7.38549(5)	7.4048
α (°)	91.824(7)	91.9283(4)	91.7
β (°)	104.444(16)	105.0439(4)	104.862
γ (°)	89.308(23)	89.7921(5)	89.822
Volume (Å³)	330.96	327.99	329.89

Error estimates are given in brackets and are quoted in units of the least significant digit.

6.2.5 Mica

Figure 6.7 shows the identification of mica and quartz in a powder pellet by comparison to calculated mica and quartz peak positions. Mica peaks in the baseline subtracted data were identified using diffraction data from Brigatti et al. (1998) and Birle et al. (1968), and quartz peaks were identified using library data (Natl. Bur. Stand., 1981). The Miller indices and *d*-spacings of the identified peaks were used to calculate the mineral unit-cell dimensions for mica and quartz, which are detailed in tables 6.9 and 6.10.

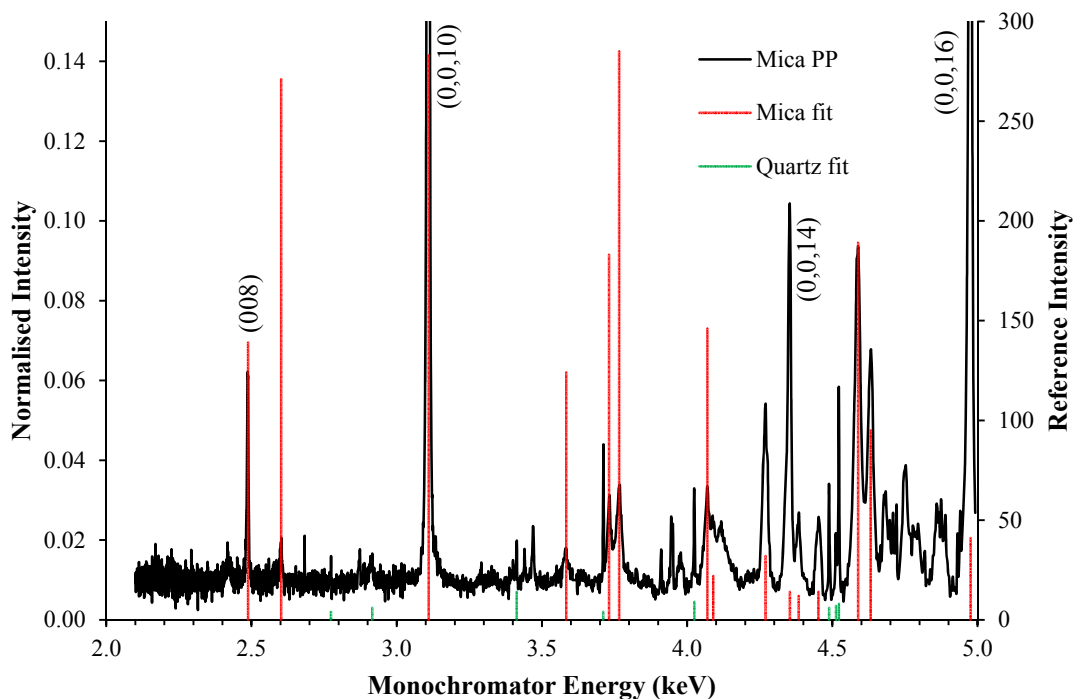


Figure 6.7. Mica PP processed dataset compared to peak positions calculated using the fitted unit cells for mica and quartz detailed in tables 6.9 and 6.10, respectively. The basal peaks are labelled and the diffraction peak intensities for mica (muscovite 2M1) and quartz are taken from Brigatti et al. (1998) and Natl. Bur. Stand. (1981).

Table 6.8. Extracted basal peak positions with calculated and fitted d -spacings for the mica powder pellet dataset shown in figure 6.7.

Miller Indices (hkl)	Energy (eV)	d -spacing (\AA)	d -spacing fit (\AA)	d diff (\AA)
0 0 8	2487.00	2.4947	2.4939	0.0008
0 0 10	3110.68	1.9946	1.9951	-0.0005
0 0 14	4353.28	1.4253	1.4251	0.0002
0 0 16	4977.61	1.2466	1.2470	-0.0004

Table 6.9. Calculated unit cell from mica identified peaks in figure 6.7 compared to two published unit cells for muscovite.

Unit Cell Attribute	Sample mica	Muscovite-2M1, ferrian (Brigatti et al., 1998)	Muscovite-2M1 (Birle et al., 1968)
a (\AA)	5.2065(14)	5.186(1)	5.194(4)
b (\AA)	9.0361(24)	8.991(3)	8.996(6)
c (\AA)	20.0518(10)	20.029(7)	20.096(2)
β ($^\circ$)	95.735(7)	95.77(3)	95.18
Volume (\AA^3)	938.65	929.17	935.16

Error estimates are given in brackets and are quoted in units of the least significant digit.

Table 6.10. Calculated unit cell from quartz identified peaks in figure 6.7 compared to a published unit cell for quartz.

Unit Cell Attribute	Sample quartz	Quartz, syn (Natl. Bur. Stand., 1981)	Quartz PP (figure 6.3, table 6.1)
a (Å)	4.9137(2)	4.9134(2)	4.91388(6)
c (Å)	5.4059(4)	5.4053(4)	5.40498(9)
Volume (Å ³)	113.04	113.01	113.02

Error estimates are given in brackets and are quoted in units of the least significant digit.

Figure 6.7 shows that 13 peaks were identified as mica (muscovite) and 8 peaks were identified as quartz (all of which are detailed in Appendix C.5). The basal peaks associated from mica (muscovite) were identified and are outlined in table 6.8, along with their d -spacings. Tables 6.9 and 6.10 detail the calculated unit cells from the peaks identified, and in the case of mica (muscovite) this is used in table 6.8 to calculate the d -spacing for comparison to the measured d -spacing. The calculated unit cells for mica (muscovite) and quartz in tables 6.9 and 6.10 are compared to references unit cells identified using the ICDD database. Unidentified peaks present in figure 6.7 were not accurately attributed to mica or quartz, and consequently were not included in the unit cell fits.

6.2.6 Talc

Figure 6.8 shows the identification of talc, magnesite and dolomite in a powder pellet by comparison to calculated talc, magnesite and dolomite peak positions. Talc peaks were identified using diffraction data from Gatta et al. (2013) and Perdikatsis and Burzlaff (1981), magnesite peaks were identified using data from Pilati et al. (1998) and dolomite peaks were identified using data from Keller and McCarthy (1985) and Ross and Reed (1992). To refine the fit further, the Miller indices and d -spacings were used to calculate the mineral unit-cell dimensions, which are detailed in tables 6.7, 6.8 and 6.9.

Figure 6.8 shows that 16 peaks were identified as talc, 6 magnesite and 10 dolomite (all of which are detailed in Appendix C.6). The (060) and basal peaks associated with talc were identified and are outlined in table 6.6, along with their d -spacings. Tables 6.7, 6.8 and 6.9 detail the calculated unit cells from the peaks identified, and in the case of talc this is used in table 6.6 to calculate the d -spacing for comparison to the measured d -spacing. The calculated unit cells for talc, magnesite and dolomite in tables 6.7, 6.8 and 6.9 are compared to reference unit cells identified using the ICDD

database. Unidentified peaks present in figure 6.8 were not accurately attributed to talc, magnesite or dolomite, and consequently were not included in the unit cell fits.

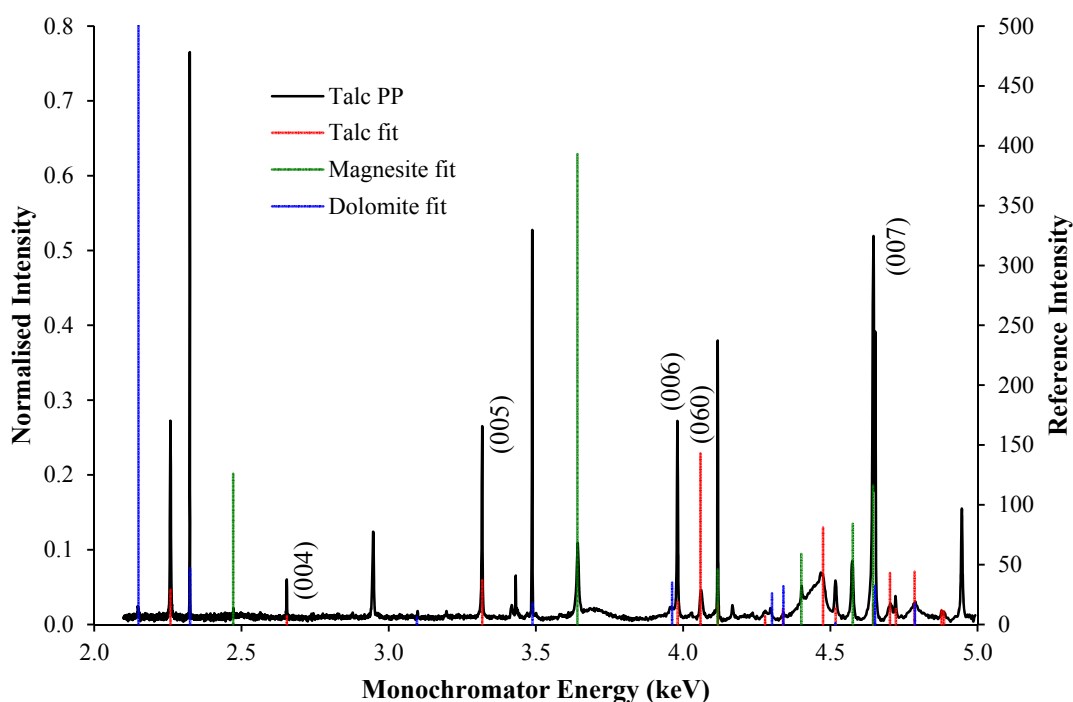


Figure 6.8. Talc processed dataset compared to calculated peak positions using the fitted unit peaks for talc and magnesite details in tables 6.12 and 6.13, respectively. The basal peaks are labelled, along with the (060) peak. The diffraction peak intensities of talc, magnesite and dolomite are taken from Perdikatsis and Burzlaff (1981), Pilati et al. (1998) and Ross and Reed (1992) for talc, magnesite and dolomite, respectively.

Table 6.11. Extracted basal and (060) peak positions with calculated and fitted d -spacings for the talc powder pellet dataset shown in figure 6.8.

Miller Indices (hkl)	Energy (eV)	d -spacing (\AA)	d -spacing fit (\AA)	d diff (\AA)
0 0 4	2653.79	2.3380	2.3378	0.0002
0 0 5	3317.38	1.8704	1.8701	0.0003
0 0 6	3980.70	1.5587	1.5584	0.0003
0 6 0	4059.90	1.5283	1.5289	-0.0006
0 0 7	4645.82	1.3356	1.3358	-0.0002

Table 6.12. Calculated unit cell from talc identified peaks in figure 6.8 compared to two published unit cells for talc.

Unit Cell Attribute	Sample talc	Talc 1A (Gatta et al., 2013)	Talc (Perdikatsis and Burzlaff, 1981)
a (Å)	5.2894(3)	5.2905(1)	5.290(3)
b (Å)	9.1759(5)	9.1739(1)	9.173(5)
c (Å)	9.4667(6)	9.4850(16)	9.460(5)
α (°)	91.353(12)	90.910(12)	90.46(3)
β (°)	99.618(8)	99.640(13)	98.68(5)
γ (°)	89.964(6)	90.101(11)	90.09(5)
Volume (Å ³)	453.84	453.79	453.77

Error estimates are given in brackets and are quoted in units of the least significant digit.

Table 6.13. Calculated unit cell from magnesite identified peaks in figure 6.8 compared to a published unit cell for magnesite.

Unit Cell Attribute	Sample magnesite	Magnesite (Pilati et al., 1998)
a (Å)	4.6272(12)	4.635(1)
c (Å)	15.0618(44)	15.023(2)
Volume (Å ³)	279.28	279.50

Error estimates are given in brackets and are quoted in units of the least significant digit.

Table 6.14. Calculated unit cell from dolomite identified peaks in figure 6.4 compared to a published unit cell for dolomite.

Unit Cell Attribute	Sample dolomite	Dolomite (Keller and McCarthy, 1985)	Dolomite (Ross and Reed, 1992)
a (Å)	4.8067(19)	4.8092(2)	4.8064(5)
c (Å)	16.0073(43)	16.020(5)	16.006(2)
Volume (Å ³)	320.29	320.88	320.22

Error estimates are given in brackets and are quoted in units of the least significant digit.

6.3 Discussion

The results shown in 6.2 demonstrate the capability of synchrotron-based high-resolution back-reflection X-ray diffraction. The energy range 2.1 – 5.0 keV, corresponding to the *d*-spacing range 2.953 – 1.243 Å, has been shown to be diagnostic in determining the presence and unit cells of quartz, dolomite, calcite, siderite and hematite.

6.3.1 Quartz, dolomite and siderite pellets

The sample shown in figure 6.3 is explained well by quartz, with all 17 recorded peaks attributed to quartz, with a unit cell calculated and compared to ICDD data in table 6.1.

The quartz pressed powder pellet analysed is made from highly-crystalline quartz obtained from the Department of Geology at the University of Leicester, and was analysed in Chapter 5. The small errors in the calculated quartz unit cell detailed in table 6.1 was due to the use of this sample to aid *d*-spacing calibration as outlined in section 6.1.

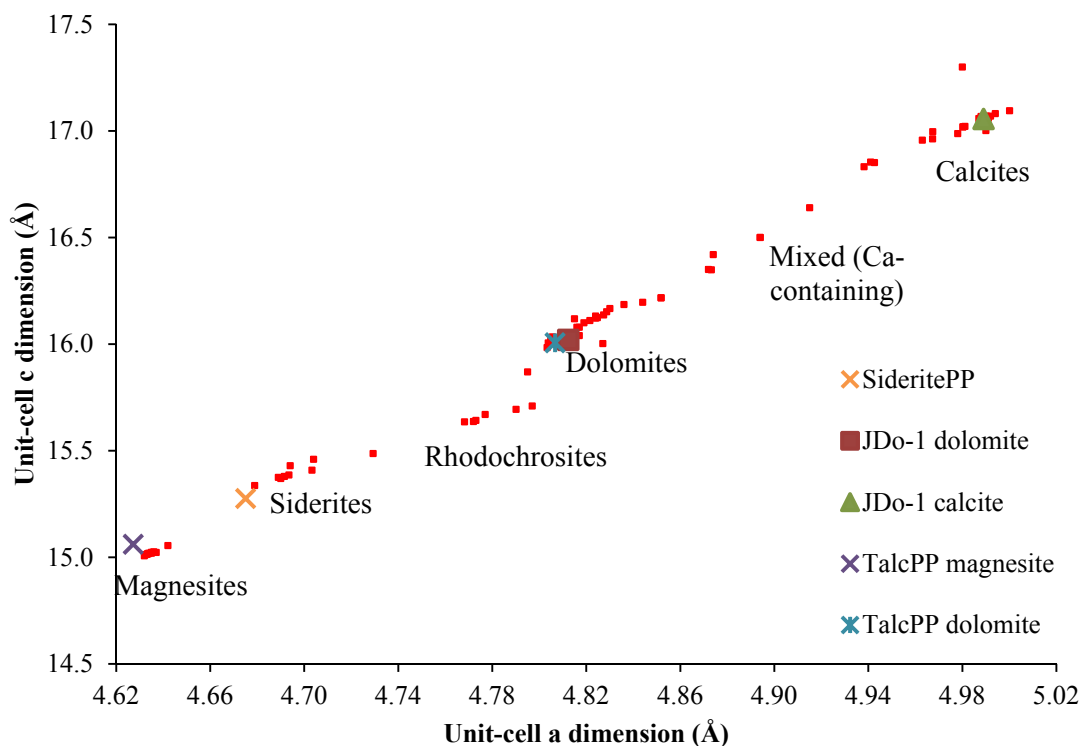


Figure 6.9. Unit-cell dimension distribution plot for carbonate minerals from the 2015 release of the ICDD powder diffraction database. The unit cells for carbonate minerals identified in JDo-1, Siderite PP and Talc PP from respective sections 6.2.2, 6.2.3 and 6.2.6 are shown for comparison.

The sample shown in figure 6.4 is explained well by dolomite and calcite, with 21 peaks identified as dolomite and 8 peaks identified as calcite. Calculated unit cells for the dolomite and calcite are shown and compared to ICDD data in tables 6.2 and 6.3. The unit cells are comparable to library datasets in figure 6.9 enabling the identification of dolomite and calcite. The sample pellet used is a dolomite standard known as JDo-1 obtained via the Department of Geology at the University of Leicester, and was also analysed in Chapter 5.

The sample shown in figure 6.5 is explained well by siderite and hematite, with 17 peaks identified as siderite, 4 peaks identified as hematite and 2 peaks were unidentified. Calculated unit cells for the siderite and hematite are shown and compared

to ICDD data in tables 6.4 and 6.5. Figure 6.9 shows a unit cell dimensional plot for comparison with carbonates in the ICDD database, and suggests that the type of siderite identified here is potentially a magnesian siderite, due to its outlier location towards the magnesite cluster. The comparison of a magnesian siderite unit cell in table 6.4 also suggests that the siderite identified here is a magnesian siderite.

The Quartz PP, JDo-1 and Siderite PP datasets and analysis have shown the back-reflection technique to be successful in a high-resolution configuration in identifying sample constituents. As shown by figures 6.3 - 6.5, the peak intensities imported from referenced datasets are not representative of the peak intensities in the experimental data. This is most likely due to the fixed geometry and the small ($1.7 \times 0.9 \text{ mm}^2$) area illuminated by the incident X-ray beam resulting in poor powder-averaging.

6.3.2 Clay pellets

The Kaolin PP and China Clay PP samples shown in figure 6.6 are comparable to kaolinite, where 13 peaks in the Kaolin PP dataset were determined to have a similar unit cell structure to kaolinite as shown in table 6.7. Basal peaks identified in table 6.6 indicate that kaolinite is likely to be present; however, as shown in Bailey (1988) one reflection can be explained by more than one (*hkl*) assignment. Clays already have broad diffraction peaks that can each mask multiple diffraction peaks; this peak overlap can make (*hkl*) peak assignments difficult as well as the significant range and number of unit cell parameters. Also, preferred orientation effects reduce the intensity of most non-basal peaks. For the Kaolin PP data presented here, the best fitting (*hkl*) assignment was included in the unit-cell fit, with other possible (*hkl*) assignments detailed in Appendix C.4. This sample was also analysed by the Department of Geology at the University of Leicester where, using a Bruker D8 Advance diffractometer, it was determined that the sample was of the kaolin group with mica present. The identification of kaolinite based on the results shown here can be tentatively concluded, which is highlighted by the large errors in the determined unit cell in table 6.7; although basal peaks have been identified, which is key in identifying the presence of clay (Moore and Reynolds, 1997). To determine the validity of the (*hkl*) assignments additional data analysis is required to refine the unit-cell fit. The origin of the unidentified peaks in the Kaolin PP dataset also needs to be ascertained.

The Mica PP sample shown in figure 6.7 is comparable to mica, where 13 peaks were calculated to have a similar unit-cell structure to mica (muscovite) as shown in table

6.9. 12 peaks have a similar unit-cell structure to quartz, as shown in table 6.10. Basal peaks were also identified in table 6.8, and indicate the presence of mica (muscovite). This sample was also analysed by the Department of Geology at the University of Leicester where, using a Bruker D8 Advance diffractometer, it was determined that the sample was of mica with kaolin group and K-feldspar present. The identification of mica based on the results shown here can be tentatively concluded; however, there are numerous peaks that are not attributed to either unit-cell fit presented here. Clearly additional data analysis is required to ascertain the origin of these unidentified peaks and refine the unit-cell fit, although basal peaks have been identified, which is key in identifying the presence of clay.

The Talc PP sample shown in figure 6.8 is comparable to talc, where 16 peaks were calculated to have similar unit-cell structure to talc as shown in table 6.12. 6 peaks have a comparable unit cell structure to magnesite, and 10 have a comparable unit-cell structure to dolomite, as detailed in respective tables 6.13 and 6.14. Basal peaks were also identified along with a (060) peak, detailed in table 6.11; these peaks indicate the presence of talc. Although this gives a clear indication to the presence of talc, there are 13 unidentified peaks in the dataset, which need to be assigned and their origin determined via additional data analysis. This sample was also analysed by the Department of Geology at the University of Leicester where, using a Bruker D8 Advance diffractometer, it was determined that the sample was of talc with magnesite, dolomite, quartz, mica, chlorite and serpentine also present.

The results presented and discussed here show that the identification of clays using synchrotron based high-resolution back-reflection XRD method is possible. For future work, it would be advantageous to analyse a single sample in multiple states to better determine the sample unit-cell structure. Other methods used in clay XRD analysis involve sample preparation to alter the unit cell structure and thus shift diffraction peaks by a known quantity, such as the use of ethylene glycol solvation and sample-heating to collapse expandable layers of the sample (Moore and Reynolds, 1997). Another technique that would be advantageous in future experimental work is to tilt the sample with respect to the incident X-ray beam in order to suppress basal peaks and enhance other peaks, enabling additional peak identification and assignment to derive unit-cells. This is possible because peak positions are unaffected by sample tilting in the back-reflection technique.

6.3.3 Experimental Method and Data Processing

The experimental method undertaken for this study was, although a first for the Diamond Light Source, not optimised. The sample-detector distances were too large resulting in comparatively low peak intensities and the point-detector was used in place of an annular detector centred on the incident X-ray beam meaning that the full intensity of the Debye-Scherrer cones was not captured. The latter is particularly important when dealing with low crystallinity materials that result in incomplete Debye-Scherrer cones (spottiness).

The windowing and baseline removal IDL program proved useful and successful, particularly at unveiling peaks at high energies; however, the choice of a polynomial trend-line fit also contributed to some baseline anomalies. In the JDo-1 dataset (figure 6.4) the region 3.2 – 3.6 keV has an elevated baseline feature that is due to the close proximity of several broad peaks with minor amounts of peak overlap resulting in a polynomial type fit. Whereas an interactive method of user identification of baseline type (linear or polynomial) is an alternative to baseline subtraction, future work should focus on modelling the Rayleigh scattering effects that cause the elevated baseline. This would enable better dataset characterisation and may reveal additional low-intensity peaks currently being masked.

In figures 6.3 – 6.8, background noise is greatest at 2.1 keV and decreases with increasing monochromator energy. Sample step size, and hence data point distribution, needs to be considered for interpreting the background noise as figure 6.1 clearly shows that the amount of data points taken at low energies is greater compared to high energies. Therefore with an increase in experimental acquisition time the background noise would decrease at low monochromator energy and aid in identification of weak peaks.

The selection of the lineshapes for peak centre energy extraction and d-spacing calculation proved useful during analysis, as not all peaks could be modelled by a single lineshape type. The Pearson VII lineshape was most commonly used as it could accurately replicate the experimentally obtained peaks, particularly narrow peaks with the Pseudo-Voigt lineshape being used where Pearson VII failed to accurately reproduce peaks. Gaussian and Lorentzian lineshapes were used for broad peaks.

6.3.4 Future application of High-Resolution Back-Reflection X-ray Diffraction

The results presented here illustrate the success of back-reflection X-ray diffraction in a high-resolution synchrotron facility. The ability to determine the unit-cell from the *d*-spacing range of 2.953 – 1.243 Å has been shown. Whole-rock analysis was

also undertaken using the experimental technique described in this chapter, with the results shown in Hansford et al. (2016).

The high-resolution synchrotron-based technique as it stands is clearly not practical for planetary lander deployment, as suggested for the laboratory-based back-reflection method in Chapter 5. However, depending on technology development it is not infeasible that this technique could be deployed in the future with use of compact monochromators but not at a resolution equivalent or better than that provided by a synchrotron facility. Applications in the planetary context are therefore currently restricted to Earth based samples, which include meteorites of planetary origin (lunar, Martian etc). Other applications where sample preparation is of paramount importance include cultural heritage studies of paintings and sculptures, along with archaeological studies of artefacts such as pottery where pigments and glazes can be identified. Cultural heritage and archaeological studies are undertaken to identify provenance and to ensure conservation of artefacts by monitoring material deterioration (Hansford et al., 2017).

6.4 Conclusions

1. The results shown here demonstrate the capability of synchrotron based high-resolution back-reflection X-ray diffraction in determining the presence of oxide, carbonate and clay minerals from the d -spacing range 2.953 – 1.243 Å; however, it would be very advantageous if this d -spacing range was extended to larger d -spacings for the analysis of clays in particular.
2. The experimental method needs optimisation with regards to minimising sample-detector distances to increase peak intensity and uncover additional low-intensity peaks. An annular detector instead of a point detector should also be utilised to capture the entire Debye-Scherrer cone.
3. More work is required to illustrate the capability of the technique in the analysis of clay minerals. A single sample in multiple states could be analysed, along with an optimised experimental facility and better characterisation of the baseline to reveal diffraction features.
4. High-resolution data would be complementary in the future analysis of samples using the lower-resolution back-reflection method, but not essential.

7. Synthesis and Conclusions

The aims of this thesis were to explore the novel back-reflection X-ray diffraction technique using a variety of laboratory facilities and geological samples to demonstrate its suitability for a surface-deployed planetary science mission, and to explore the possibility of impact-induced hydrothermal systems on Mars during the Amazonian epoch. These aims bring together two important aspects of Mars exploration; determination of an area of scientific interest using remote sensing data, and exploration of an instrument technique that would potentially be used in-situ to perform scientific analysis as well as providing a ground-truth to remote sensing data.

The possibility of and evidence for impact-induced hydrothermal systems on Mars was explored in Chapter 4, with appropriate background regarding interpretation and processing techniques of the Mars remote sensing data outlined in Chapter 2. The study has origins in Earth-based laboratory work of the nakhlite Martian meteorites. As outlined in section 4.1.3.1, alteration minerals in the nakhlites suggest that they were once altered in a sub-surface impact-induced hydrothermal environment within ≤ 670 Myr (Shih et al., 1998; Swindle et al., 2000; Changela and Bridges, 2010; Bridges and Schwenzer, 2012; Hicks et al; 2014). Orbital evidence for impact-induced hydrothermal systems during the Amazonian epoch was found and discussed.

A novel back-reflection X-ray diffraction technique that is insensitive to sample morphology, proposed and proved by Hansford (2011a, 2013) was explored using laboratory facilities at the Space Research Centre, University of Leicester. The two laboratory facilities that utilised a broadband X-ray source – the pre-existing CCD and bespoke SDD facilities – outlined in Chapter 3 and used extensively in Chapter 5, which together with PoDFluX, PoDFast and the mineral-fitting routine, were shown to be able to identify a variety of oxides, carbonates, sulphates and phyllosilicates in both whole-rock and pressed powder pellet form. The ability to experimentally verify the presence of preferred orientation of crystallites with the back-reflection technique and model the resultant effects in X-ray diffraction spectra were demonstrated with PoDFluX and the mineral-fitting routine. Appropriate knowledge for the interpretation of X-ray diffraction, and X-ray fluorescence, is outlined in Chapter 3. As shown in Chapter 6, the back-reflection technique was then further validated in a high-resolution configuration at the Diamond Light Source whereby a highly monochromatic X-ray beam was used to determine the presence of oxide, carbonate and clay minerals from the d-spacing range

2.953 – 1.243 Å (which corresponds to 2.1 – 5.0 keV). This work demonstrates the capability of the back-reflection technique primarily for the mineralogical analysis of unprepared whole rock samples with the possible application of planetary rover-based instrumentation, but also for other applications where the avoidance of sample preparation is of paramount importance. Such applications include cultural heritage and archaeological studies as outlined in chapter 6.

In this chapter, the research undertaken in Chapters 4 – 6 is summarised and discussed, with improvements and avenues of future work suggested.

7.1 Remote Sensing of Young Impact Craters on Mars

The study presented in Chapter 4 showcases how reflectance spectroscopy is used to remotely identify areas of interest on Mars, in this case possible impact-induced hydrothermal alteration. As summarised in sections 4.3 and 4.5, CRISM analysis of 144 impact craters in terrains mapped as Amazonian or Amazonian-Hesperian on Mars (Tanaka et al., 2014) revealed 3 impact craters showing hydrated spectral signatures, two of which could be the result of impact-induced hydrothermal alteration. This suggests that impact-induced hydrothermalism was rare during the Amazonian epoch, or is not detectable on the scale of the spatial resolution of CRISM (Turner et al., 2016).

The 20 km diameter complex impact crater (located at 52.42°N, 39.86°E in the Ismenius Lacus quadrangle) shown in section 4.3.2 and discussed in section 4.4.2 has CRISM spectral evidence for chlorite or Fe-serpentine with the possibility of prehnite in gullies, alluvial fans and uplift breccia in the central uplift. These deposits are proposed to have formed within the central uplift as a result of impact-induced hydrothermal alteration during the Amazonian epoch, then subsequently eroded and transported within the impact crater. The 62 km Stokes impact crater has CRISM spectral signatures of Fe/Mg/Al phyllosilicates, chlorite and carbonate, which may be the result of impact-induced hydrothermal alteration. This work highlights areas on the surface of Mars that may have provided a habitable environment for microbial life, and thus highlights these areas for possible future exploration.

The work in Chapter 4 shows that the identification of impact-induced hydrothermal systems in orbital data is non-trivial due to the process occurring predominantly in the sub-surface; however, the accurate mapping of surface morphology with mineralogical context can indicate where impact induced hydrothermal activity is more likely to have occurred. Whilst the techniques used with the CRISM dataset proved

adequate for identifying Fe/Mg/Al phyllosilicates in impact craters, future work should look to explore the possibility of impact induced hydrothermal activity by first developing tools to minimise the contribution of noise in the CRISM dataset and then explore the possibility of sub-pixel resolution from overlapping CRISM observations. Large (> 50 km diameter) Amazonian-aged complex impact craters in dust-free regions of Mars that currently have CRISM coverage could be analysed with OMEGA data; however, whilst the CRISM instrument is still operational coverage should be obtained of Amazonian-aged complex impacts of a range of diameters in dust-free locations.

This study highlighted the difficulty in identifying spectral signatures in young impact craters on Mars using CRISM data. The scarcity of hydrated spectra could be due to the limited spatial resolution of CRISM (20 m) or surface coatings (dust) masking spectral signatures however, it is important to note that impact-induced hydrothermal activity is predominantly a sub-surface process and may not be identifiable with reflectance spectroscopy and other orbital datasets. Typically, numerous CRISM pixels need to be spectrally averaged to obtain a significant signal-to-noise ratio, before a spectrally bland reference region is then used to ratio and emphasize spectral absorptions. This process typically results in a spectrum representative of numerous CRISM pixels and hence a large surface area. It is possible that mineral outcrops on the surface of Mars are too small to be accurately resolved in CRISM spectra, or are being obscured by surface dust coverage. The analysis of CRISM spectra is also non-trivial, as column-to-column differences and stochastic noise can lead to false-positive spectral absorptions. Due to these effects, a statistical approach to the analysis of CRISM data using principal components analysis and minimum-noise fraction transformations is not possible.

CRISM is a valuable tool for examining the surface mineralogy of Mars, and is used extensively in landing site investigations for future Mars missions (Carter et al., 2016; Golombek et al., 2016; Gross et al., 2016). The limitations of CRISM restrict the ability to accurately determine the surface mineralogy, and hence potential science targets may be overlooked. However, recent studies, including that in Chapter 4, have highlighted how the use of ancillary high-resolution imagery from instruments such as HiRISE can prove to be a powerful tool in providing morphological context to CRISM spectra (e.g, Ojha et al., 2015). With CRISM set to be the prime tool for Mars mineralogical surface studies for years to come, and no replacement firmly planned, its dataset requires further processing and optimisation to characterise artefacts of detector origin. This is currently being pursued, as shown by the recent release of Map-projected

Targeted Reduced Data Records (MTRDRs) (Seelos et al., 2016). Unfortunately the release of this dataset has come too late to be incorporated into this thesis, but this new data will provide a useful tool in the identification of areas of mineralogical interest on Mars and could result in further identification of recent impact-induced hydrothermal activity. The MTRDR dataset could also be used to identify new areas of interest on Mars, such as the transportation of deposits due to gully processes like that described in section 4.3.2 and Turner et al. (2016).

7.1.1 Considerations for Future Orbital Instrumentation

To enable further detailed study of the surface mineralogy of Mars, future instrumentation should focus on improving the spatial spectral resolution of measurements. Both high-resolution spatial and spectral datasets are vital for future missions to Mars, and need to be deployed about Mars for landing site investigations to take place. With both CRISM and HiRISE being in operation for nearly 10 years, the development and deployment of replacements should be a matter of priority.

Whilst dust coverage obscuring surface spectral signatures on Mars will always be an issue, CRISM has been able to show a diverse, hydrated mineralogy in numerous locations (Ehlmann et al., 2009; Milliken et al., 2010; Ehlmann and Edwards, 2014; Carter et al., 2014). Higher resolution datasets would give the ability to geologically characterise these areas to a further degree of understanding from Martian orbit. Current Earth observation satellites are able to acquire spectral data at <4 m spatial resolution (e.g., Kruse and Perry, 2013), meaning it is feasible to consider the possibility of a heritage-type instrument based on the current level of technology available. The wavelength range and spectral resolution of CRISM is ideal regarding mineral characterisation, therefore this should be used in future missions.

7.2 Capability of Back-Reflection X-ray Diffraction

The results shown in Chapters 5 and 6 demonstrate the capability of the back-reflection X-ray diffraction technique. The technique, which is insensitive to sample morphology has been demonstrated to be capable of successfully identifying a variety of oxides, feldspars, carbonates, sulphates and phyllosilicate whole rock and pellet samples. The two X-ray diffraction laboratory facilities used in Chapter 5 have enabled versatile analysis, with the pre-existing CCD facility enabling crystallite preferred orientation investigations and imaging of a part of the Debye-Scherrer diffraction cone, and the

bespoke SDD facility enabling the fast experimental acquisition times with greater signal-to-noise across the whole X-ray energy range. The overlap of X-ray fluorescence peaks upon X-ray diffraction peaks hindered the mineralogical analysis of experimental data, and therefore a method was devised to suppress X-ray fluorescence peaks and reveal underlying diffraction peaks. Demonstrated in Chapter 5 and Hansford et al. (2014), this method of tuning the X-ray tube voltage to just below an absorption edge energy whilst still above the corresponding characteristic X-ray fluorescence energy enables enough Bremsstrahlung photons up to the absorption edge energy to reveal the presence of an underlying diffraction peak, if present. This process of X-ray fluorescence suppression has allowed the identification of minerals using diffraction peaks that were initially obscured. This presence of X-ray fluorescence, whilst troublesome in terms of peak overlap, does give insights into the elements present in the sample, which does help focus mineralogical identification in X-ray diffraction data.

The results shown in Chapter 5 illustrate the difficulty in analysis of data returned by the back-reflection technique. The analysis of feldspar samples proved particularly troublesome, as the diffraction patterns are very similar for each member of the feldspar series resulting in tentative identification; however, the identification of specific feldspars is also difficult with a laboratory diffractometer. The identification of prehnite (figure 5.37), jarosite (figure 5.35), and hematite (figure 5.8) show the suitability of this instrument for deployment in a planetary environment, like Mars. Jarosite and hematite have been found on Mars by MER Opportunity at Meridiani Planum, suggesting the presence of past aqueous processes under acid-sulphate conditions (Klingelhöfer et al., 2004). Prehnite, found in orbital spectra in Chapter 4, is an indicator for alteration at elevated temperature and thus can indicate the presence of a hydrothermal system. The ability to detect and characterise an environment containing these minerals in-situ using the back-reflection technique could prove to be valuable for a planetary science mission.

Preferred orientation of crystallites occurs in both natural and prepared samples, but prepared, powder-pressed, samples typically show a higher degree of preferred orientation. The pre-existing CCD chamber was used to experimentally prove the presence of preferred orientation as a sample could be rotated about an axis perpendicular to the incident X-ray beam, whereas this was not possible for the bespoke SDD chamber. If the technique were to be developed into a compact, lightweight instrument for deployment on the arm of a planetary lander or rover then the investigation of preferred orientation could be carried out in a similar fashion to that shown in figure 5.21 by

manoeuvring the instrument with respect to the sample, as at least two diffraction measurements of the same sample area – with different sample orientations – are required to determine the presence of preferred orientation. In the setup of a manoeuvrable, compact, back-reflection X-ray diffraction instrument, mapping of diffraction and fluorescence of a sample surface could also be undertaken.

As shown in Chapter 5 the technique can distinguish between gypsum, bassanite and anhydrite, therefore an arm-mounted, manoeuvrable version of the instrument could be used to map sulphate minerals in veins, which is of particular interest in the Mars' surface studies (e.g., Schwenger et al., 2016). This can be simulated in a laboratory with the use of translation stages to produce raster datasets across a sample, as this would be ideal for analysis of a sulphate vein in a whole rock sample. Analysis of individual measurements could then be brought together to create a mineral map image of the sample. The acquisition of fluorescence measurements to provide elemental information in the same location as diffraction data is a significant advantage as fluorescence measurements are complementary to the diffraction analysis. The X-ray sample-incident spot-size will determine the spatial resolution of this diffraction and fluorescence sample mapping, and so a method of focusing the X-ray beam to reduce sample spot size and thus increase the resolution of measurements should be explored.

Back-reflection X-ray diffraction could be considered to be complementary to other instrument techniques, such as Raman spectroscopy. Raman spectroscopy can also be used with minimal sample preparation for geologic characterisation, and is selected for both the ExoMars rover (Edwards et al., 2012) and the Mars 2020 rover (Beegle et al., 2015; Clegg et al., 2015). Alternatively the back-reflection technique could be used as a precursor for more rigorous analysis with an instrument such as CheMin (Blake et al., 2012) or a more sophisticated version of the back-reflection instrument that uses compact monochromators to make higher-resolution measurements. The Planetary Instrument for X-ray Lithochemistry (PIXL), planned for the Mars 2020 rover, has a similar geometry to that required for the back-reflection X-ray diffraction technique studied in this thesis. Although the primary goal of PIXL is to map X-ray fluorescence (Allwood et al., 2015), X-ray diffraction data would be acquired and could also be analysed for mineralogical identification.

Chapter 6 shows some of the results taken at the Diamond Light Source where high-resolution back-reflection energy-dispersive X-ray diffraction was carried out for the first time. The results showed how quartz, siderite, dolomite, calcite and talc could be

identified and their unit cells determined; however, the analysis of mica (muscovite) and kaolinite wasn't as conclusive as there were large errors in the determined unit cell due to the difficulties in (hkl) peak assignments. However, the results highlight the capability of the back-reflection technique in a high resolution configuration, and whilst the degree of synchrotron monochromation is certainly not likely to be achieved in a non-synchrotron facility, there is the possibility for the future development of compact monochromators to obtain higher-resolution back-reflection X-ray diffraction compared to the data shown in Chapter 5. A laboratory-based high-resolution back-reflection energy-dispersive X-ray diffraction instrument is currently being planned at the University of Leicester (Hansford, 2016b). Ultimately, measurements that would be taken in-situ using an instrument based on the back-reflection technique by a rover mission would be guided using orbital datasets and analysis, like that shown in Chapter 4.

Future development of the analysis technique for the laboratory facilities should focus on exploring the statistical usability of chi-squared fit values where model inaccuracies are at a minimum, and validating the model results with independent analysis. Currently, the mineral-fitting routine iterates PoDFast simulations, altering the energy calibration of the experimentally acquired spectrum, along with simulation run time and mineral/element quantities per iteration to enhance the model and give a closer fit to the experimental data. This method does not accurately reproduce the experimental data enough for meaningful comparisons with chi-squared fitting values beyond iterative model improvements, therefore future work should focus on ascertaining the possibility of improvement of chi-squared fit values where model inaccuracies are at a minimum (i.e. >2.2 keV); however, with naturally occurring samples, or indeed samples prepared in a laboratory, there may be contributions from unknown contaminants causing small amounts of diffraction and/or fluorescence that make the highly-accurate modelling of experimental data impossible, resulting in chi-squared values that can only be used in a relative sense to extract best-fit parameters. To verify the constituents of a sample, and validate mineral-fitting results, independent analysis should be explored with techniques such as lab-based ADXRD and XRF.

Alternative, non-planetary techniques of back-reflection X-ray diffraction should also be considered for future applications, such as explosive (Luggar et al., 1997) and drug (Cook et al., 2009) characterisation using a portable, compact version of the technique, and heritage applications (Mendoza Cuevas et al., 2015). A synchrotron-based deployment of the technique could be used to make high-resolution measurements for

applications where sample integrity is of utmost importance, such as archaeological and cultural heritage studies. This could be undertaken to identify provenance and to ensure conservation of artefacts by monitoring material deterioration, as well as analysis of paintings, sculptures, and studies of artefacts such as pottery where it is anticipated that pigments and glazes can be identified (Hansford et al., 2017). If these avenues of application were to be pursued then research would need to be taken to fully ascertain the capability of the technique in these fields.

7.3 Final Comments

This study has highlighted the importance of complementary in-situ and orbital datasets regarding planetary exploration and scientific discovery. The use of orbital datasets to identify areas of scientific interest, as shown in Chapter 4, is actively being used to guide surface missions on Mars. The ability to subsequently characterise geological samples in-situ with a planetary lander or rover is of high importance regarding mission science goals and establishing a ground truth to orbital observations. Techniques like the back-reflection X-ray diffraction method studied and shown in Chapters 5 and 6, which are insensitive to sample morphology and therefore not requiring additional instrumentation/tools to prepare samples for analysis, are of great advantage in this endeavour.

Appendix A: Hydrothermal Activity Recorded in Post Noachian-aged Impact Craters on Mars

Table A.1 details all 158 impact craters ≥ 3 km diameter analysed in study presented in Chapter 4 of this thesis. The result is either positive (indicating the presence of hydrated minerals) or null (defined in section 4.2.4 of this thesis).

Appendix A: Hydrothermal Activity Recorded in Post Noachian-aged Impact Craters on Mars

Table A. 1. All 158 impact craters analysed in Chapter 4 of this thesis.

Crater ID (Robins and Hynek, 2012)	Name	Latitude (°N)	Longitude (°E)	Diameter (km)	Geological Unit (Tanaka et al., 2014)	Analysed CRISM Observations	Result
02-000005		43.974	-141.039	61.52	AHv	FRT0001C6EB FRT000182EA FRT00009E05 FRT00019F2D	NULL
02-000020		43.757	-137.836	33.48	AHv	FRT00009696	NULL
02-000068		37.166	-179.359	17.63	lAv	FRT000178B0	NULL
02-000084		48.41	-129.557	15.93	AHv	FRT00016C0B	NULL
02-000088		53.79	-131.026	15.65	AHv	HRL0001816B FRT00016A41 FRT00016C7C FRT00016EAB	NULL
02-000116	Domoni	51.403	-125.595	13.72	AHv	FRT000165CB FRT000169D3 FRT00017654	NULL
02-000166		40.529	-128.343	10.82	AHv	HRL000195F1	NULL
02-000175		44.138	-173.093	10.5	lAv	FRT0000900B FRT000169D3 FRT00017654	NULL
02-000195		40.418	-128.398	9.76	AHv	HRL000195F1	NULL
02-000204		49.556	-173.805	9.53	Av	HRL0001663D	NULL
02-000229		40.509	-137.488	8.64	AHv	FRS00027234	NULL

Appendix A: Hydrothermal Activity Recorded in Post Noachian-aged Impact Craters on Mars

02-000231	52.452	-173.612	8.57	Av	FRT0000A213	NULL
02-000237	43.014	-122.735	8.39	AHv	FRT00016406	NULL
					HRL0001663D	
02-000246	50.166	-173.716	8.18	Av	HRL00018004	NULL
02-000284	52.558	-129.824	7.33	AHv	FRT0001656B	NULL
03-000009	54.935	-84.355	58.78	AHv	FRT00009684	NULL
					FRT00017CAD	
					FRT000181DB	
					FRT00024857	
					HRL0000ABBB	
03-000072	60.712	-101.436	21.6	AHv	HRS0001B74E	NULL
					FRT00019493	
03-000073	60.172	-108.882	21.52	AHv	HRL00019F5A	NULL
03-000077	43.216	-94.317	21.24	AHv	HRL00021D7F	NULL
					FRT000092E0	
					HRL000096EF	
03-000082	44.628	-106.984	20.91	AHv	HRL000098C3	NULL
03-000099	30.803	-62.393	19.41	AHv	FRT0001FCA9	NULL
03-000132	58.338	-85.738	16.62	AHv	HRS0000B780	NULL
03-000142	54.509	-88.294	15.94	AHv	FRT00016D5A	NULL
03-000174	57.569	-97.433	13.91	AHv	HRL00018740	NULL
03-000190	59.476	-96.361	13.07	AHv	FRT00017306	NULL
03-000205	32.633	-105.947	12.43	AHv	HRS0001C725	NULL

Appendix A: Hydrothermal Activity Recorded in Post Noachian-aged Impact Craters on Mars

						FRT000247B6	
03-000226		55.345	-106.445	11.73	AHv	FRT0002498F	NULL
03-000228		57.332	-105.228	11.62	AHv	HRS0000A2D3	NULL
03-000308		39.883	-102.628	8.92	AHv	HRS0000C885	NULL
						FRT00018DFD	
03-000332		43.046	-119.242	8.51	AHv	FRT000184EA	NULL
03-000416	Chatturat	35.385	-94.926	7.19	AHv	FRT00009392	NULL
05-000047		57.952	58.673	52.81	AHi	FRT0000C860	NULL
						FRT000171C6	
05-000055	Davies	45.958	0.144	49.37	AHi	FRT00018335	NULL
05-000136		53.044	57.852	34.34	mAl	FRT00009A4F	NULL
05-000211		53.768	41.45	27.18	mAl	HRS0000A05B	NULL
						FRT0000BFA6	
						FRT0001B619	
						FRT00018705	
						HRL0001B89D	
05-000375		52.415	39.861	20.01	AHi	HRL000194F4	POSITIVE
05-000662		61.031	24.13	12.09	mAl	FRT00018AE9	NULL
05-000673		47.826	3.504	11.99	mAl	HRL00016715	NULL
						FRT00014235	
						FRT00016475	
						FRS00029DDA	
06-000016	Nier	42.788	106.109	46.3	eAb	FRS0002BACA	NULL

Appendix A: Hydrothermal Activity Recorded in Post Noachian-aged Impact Craters on Mars

						FRT0000A14C	
						FRT00018D20	
06-000022		43.395	117.367	39.55	Av	FRT00024180	NULL
06-000040		42.954	115.671	31.54	Av	FRT00010764	NULL
						FRT000084CA	
						FRT00017C76	
06-000057	Vivero	48.97	118.854	27.12	eAb	HRS00018B7D	NULL
06-000075		39.063	116.279	23.26	AHi	FRT000098DC	NULL
						FRT0000A467	
						FRT0000AFB7	
						FRT0000C1BF	
						FRT0000C5B5	
						FRT0000C494	
						FRT0000CCE5	
06-000077		58.083	62.162	23.09	AHi	FRT0000D05A	NULL
						FRT00009BC5	
06-000079	Bacolor	32.992	118.593	22.63	AHv	HRL000188EF	NULL
06-000114		41.53	87.717	17.28	mAl	FRT0000C17A	NULL
06-000123		36.111	87.904	16.64	mAl	HRL0000B3A6	NULL
06-000145		50.264	118.019	15.02	eAb	FRT00016E6D	NULL
						HRL0000B28F	
06-000162		34.88	117.448	14.28	AHv	HRS000123ED	NULL
06-000166		43.843	89.518	14.01	mAl	FRT00009A8B	NULL
06-000205		51.961	62.884	12.45	mAl	FRT00017870	NULL

Appendix A: Hydrothermal Activity Recorded in Post Noachian-aged Impact Craters on Mars

						FRT0000B0C6	
06-000230		34.22	109.592	11.08	AHv	FRT00008C9E	NULL
06-000234		58.251	89.608	10.82	mAl	FRT00009536	NULL
06-000247		31.505	116.253	10.59	AHv	FRT000094D3	NULL
06-000248		37.431	115.372	10.58	Av	FRT00016E02	NULL
06-000262		36.379	107.743	10.23	eAb	FRT0000A908	NULL
						FRT000016B4	
06-000284		34.926	111.577	9.65	eAb	HRL0001DACB	NULL
06-000293		47.238	82.51	9.43	mAl	FRT00016B52	NULL
06-000315		43.227	83.813	9.01	mAl	FRT00017BE8	NULL
06-000323		46.693	90.068	8.83	mAl	HRS00018D25	NULL
06-000324		32.406	111.27	8.76	AHv	FRT00010386	NULL
06-000343		31.81	114.325	8.52	AHv	FRT00009B8B	NULL
06-000352		61.379	78.461	8.33	mAl	FRT000166B6	NULL
06-000445		39.599	88.111	7.04	mAl	FRT0000846F	NULL
						FRT0000ADA4	
						FRT00008A1E	
						FRT00016E5E	
						FRT00017252	
						HRL00008177	
						HRL00008661	
						HRL0001FD49	
07-000008	Stokes	55.621	171.287	62.49	AHi	HRL000183FB	POSITIVE

Appendix A: Hydrothermal Activity Recorded in Post Noachian-aged Impact Craters on Mars

						HRL000194A3	
						HRS0001B728	
						FRT0000CCD7	
						FRT00007D00	
						FRT0000952D	
						HRL00018EDE	
07-000025	Kufra	40.357	120.301	37.48	AHi	HRS0001045C	NULL
						FRT00009776	
						FRT000169F3	
07-000033	Chincoteague	41.199	124.128	34.03	Av	HRL000194E7	NULL
07-000042		42.882	157.79	30.43	mAl	FRT0000A364	NULL
07-000053		34.797	157.998	27	AHv	FRT0000C61C	NULL
07-000062		53.395	164.27	24.34	mAl	FRT0001659C	NULL
07-000083		30.725	143.44	21.67	AHv	FRT00016DFE	NULL
07-000088		39.36	179.278	20.98	lAv	FRT000086B5	NULL
						FRT000099F5	
07-000099		38.595	137.227	19.03	Av	HRL000132C5	NULL
						FRT00016EC8	
07-000177		34.649	125.608	12.94	Av	FRT000167B2	NULL
07-000184		34.706	120.535	12.49	Av	FRT0000B172	NULL
07-000189		30.67	137.379	12.3	Av	FRT000085C8	NULL
						FRT00009592	
07-000209		50.753	123.907	11.08	mAl	HRL0001BB3B	NULL
07-000223		48.977	158.664	10.46	mAl	HRL00016642	NULL

Appendix A: Hydrothermal Activity Recorded in Post Noachian-aged Impact Craters on Mars

07-000225		34.646	123.546	10.36	AHi	FRT0001708B	NULL
07-000229	Loja	41.214	136.215	10.15	mAl	FRT000144A6	NULL
07-000240		45.047	159.438	9.66	mAl	FRT00017722	NULL
						FRT0001BBA2	
07-000253		53.842	127.808	9.23	mAl	FRT00017328	NULL
07-000255		36.567	155.464	9.19	AHv	HRL000D1D3	NULL
07-000271		55.839	164.359	8.91	mAl	FRT00016FCD	NULL
07-000275		43.101	157.946	8.78	mAl	FRT0000A364	NULL
						FRT0000AC34	
						FRT0000C287	
						FRT000054E0	
						FRT000085BA	
						FRT0000963B	
						FRT00018C69	
						HRL00003481	
						HRL0000B73D	
						HRL0000BC5C	
						HRL0000D0F1	
08-000002	Nicholson	0.194	-164.516	107.36	AHi	HRL00016F6E	NULL

Appendix A: Hydrothermal Activity Recorded in Post Noachian-aged Impact Craters on Mars

						FRT00010EC6	
						FRT000236FC	
						FRT00024BF2	
						HRL0000379F	
						HRL000063FB	
						HRL00008372	
						HRL0000AAF5	
						HRL00021F2A	
08-000003	Pettit	12.252	-173.836	92.49	AHi	HRS00019D90	NULL
08-000006		15.438	-178.426	59.5	AHi	FRT00009766	NULL
08-000038		10.041	-152.462	34.32	AHv	HRS00011CDD	NULL
08-000053		10.578	-174.671	30.7	AHi	HRS0001EB96	NULL
						FRT00009344	
						FRT00009BE8	
						FRT0000CA62	
08-000060	Tooting	23.203	-152.22	27.86	AHi	FRT0000A17D	NULL
						FRT000148E9	
						HRL00004481	
						HRL00008246	
						HRL0000BFEB	
						HRL0001645D	
						HRL00017B5B	
08-000063		24.416	-142.162	27.09	AHtu	HRL00017FFB	NULL
08-000072		28.649	-152.973	26.12	lAv	FRT0000B848	NULL

Appendix A: Hydrothermal Activity Recorded in Post Noachian-aged Impact Craters on Mars

08-000085		13.691	-159.698	23	AHv	FRT0000C9F8 FRT000093A5	NULL
08-000133		21.58	-175.775	15.04	lAv	FRT00009957	NULL
08-000155		14.185	-157.669	13.42	AHv	FRT0000B4DF FRT00006044 HRL00007F73 HRL00008E72 HRL000087A9	NULL
08-000178		10.652	-135.227	12.26	lAv	HRL00009874 HRL0000AAF1 HRL000189C5	NULL
08-000281		14.175	-146.991	8.71	AHtu	HRS00002F08 FRT00006421 FRT00009816 FRT0001FCB4	NULL
09-000000	Poynting	8.419	-112.738	69.7	AHi	FRT00017708 FRT0000884E	NULL
09-000001	Paros	21.985	-98.11	34.61	AHi	FRT0000BD5B FRT00003621 FRT00008D6D FRT0000A175	NULL
09-000004	Rahe	25.055	-97.473	26.79	AHv	FRT0000C360	NULL
09-000005		17.998	-93.811	25.52	AHv	FRT000176AE	NULL
09-000006		9.615	-119.076	23.59	AHv	FRT00009C14	NULL

Appendix A: Hydrothermal Activity Recorded in Post Noachian-aged Impact Craters on Mars

09-000007		17.976	-110.887	22.68	AHv	FRT000073E7	NULL
09-000010		14.016	-95.979	20.68	AHv	FRT00004088	NULL
09-000012		27.731	-124.536	19.66	AHv	FRT00011DD0	NULL
						FRT00005D5F	
						FRT0000ACA2	
09-000015		19.281	-99.922	19.18	AHv	HRL0000AB99	NULL
09-000020		20.917	-95.131	16.68	AHv	FRT0000956A	NULL
09-000022		29.777	-123.581	16.59	AHv	FRT00009571	NULL
09-000027	Karzok	18.407	-131.722	15.29	Ave	FRT000075F3	NULL
09-000038		20.552	-93.54	13.09	AHv	HRS0000A8D6	NULL
						FRT000075A9	
						FRT00007C91	
						FRT0002342A	
09-000059	Pangboche	17.283	-133.387	10.16	Ave	FRT00024470	NULL
09-000094		16.443	-118.791	8.02	AHv	FRT000097BA	NULL
09-000104		6.899	-120.658	7.56	AHv	FRT000172A4	NULL
						FRT00023535	
						FRT00024A55	
09-000110		26.197	-118.934	7.29	AHv	HRL00010944	NULL
						FRT00004119	
						FRT00016452	
10-000007	Fesenkov	21.664	-86.526	87.38	AHi	FRT00011A9A	NULL

Appendix A: Hydrothermal Activity Recorded in Post Noachian-aged Impact Craters on Mars

						FRT000078A1	
						FRT0000A0BD	
10-000130		26.033	-85.351	24.48	AHv	FRS00028CE3	NULL
						FRT00023648	
						FRT0002415C	
10-000219		15.208	-75.259	17.23	AHv	FRS000275BF	NULL
10-000247		21.986	-85.9	15.86	AHi	FRT00011A9A	NULL
10-000439	Aveiro	21.275	-78.959	9.87	AHv	FRT00013F5C	NULL
						FRT00009288	
10-000660		21.723	-80.944	7.26	AHv	FRT00011AF7	NULL
14-000111		10.665	134.442	28.17	AHv	FRT00017F8F	NULL
14-000598		29.665	116.555	9.25	AHv	HRS0000B62E	NULL
15-000004	Eddie	12.337	142.175	83.91	AHi	FRT0000988B	NULL
						FRT00009017	
						FRT00017320	
15-000008	Lockyer	27.843	160.53	71.35	AHi	HRS00011178	NULL
15-000017		9.557	150.153	54.84	AHv	HRL00005EF4	NULL
						FRT0000B0BE	
						FRT0000619D	
						FRT00017788	
						HRL000166A4	
15-000018		8.934	141.283	50.77	AHv	HRS0000AB65	POSITIVE

Appendix A: Hydrothermal Activity Recorded in Post Noachian-aged Impact Craters on Mars

						FRT00008412	
						FRT00009B7F	
						FRT0000A57F	
						FRT0000A846	
15-000029	Kotka	19.25	169.875	38.93	AHi	HRL0000C413	NULL
15-000050		3.043	140.321	29.4	AHI	FRT0000AA2F	NULL
15-000055		16.533	160.395	27.65	AHv	FRT00012702	NULL
15-000069		8.552	169.259	24.12	lAvf	FRT0000ACE8	NULL
						FRT0000B957	
15-000076		25.017	167.587	22.74	AHv	HRS0000BE0C	NULL
15-000089		14.58	155.607	20.76	AHv	FRT00016EC1	NULL
15-000103	Persbo	8.561	156.884	19.49	lAv	FRT0000D6C5	NULL
15-000119		8.755	143.014	17.35	AHv	FRT00008E84	NULL
15-000130		6.954	142.207	16.06	AHv	HRL00021B67	NULL
15-000131		18.065	160.854	15.89	AHv	FRT0000B05A	NULL
15-000142		24.592	173.299	14.93	lAv	FRT0000B289	NULL
15-000165	Corinto	16.949	141.713	13.69	AHv	HRS00018E57	NULL
						FRT00006311	
15-000240	Zunil	7.697	166.191	10.26	lAvf	FRT0000B21F	NULL
15-000261		7.165	174.423	9.79	lAv	HRL0000536B	NULL
						FRT9991741C	
15-000263		27.605	175.199	9.63	lAv	HRS00018D13	NULL
15-000338		26.928	165.189	7.85	AHv	FRT00009643	NULL
15-000357		17.226	159.943	7.59	AHv	FRT00018C22	NULL

Appendix A: Hydrothermal Activity Recorded in Post Noachian-aged Impact Craters on Mars

05-002067	57.58	46.96	4.29	mAl	HRL0000AB48 FRT00008EF2	NULL
06-000460	31.46	118.37	6.88	AHv	FRT00009E55	NULL
06-000531	33.33	118.93	6.04	AHv	HRL0000B4EE	NULL
06-000790	58.07	66.6	4.43	mAl	FRT000234F6	NULL
06-000960	43.27	87.94	3.71	mAl	FRT00016BC3	NULL
07-000413	56.14	173.09	6.59	AHi	HRL000183FB	NULL
07-000414	52.09	167.09	6.58	mAl	FRT000096A3	NULL
07-000443	54.04	168.4	6.25	mAl	HRS00018B20	NULL
07-000551	53.55	164.45	5.32	mAl	FRT0001759C	NULL
07-000808	36.8	133.22	3.9	Av	FRT00016D12	NULL
07-000875	53.76	122.01	3.69	mAl	HRL00021D51	NULL
07-000906	34.93	122.37	3.61	AHi	FRT00016C2D	NULL
14-000875	26.94	129.63	6.75	AHv	FRT000093B3	NULL
15-000566	13.07	158.81	5.23	AHv	HRL00010ED1	NULL

Appendix B: Back-Reflection Energy-Dispersive X-ray Diffraction

Diffraction

This appendix contains the datasets detailed in table 5.1 that were acquired using the laboratory-based back-reflection technique explored in Chapter 5 of this thesis.

B.1 Quartz

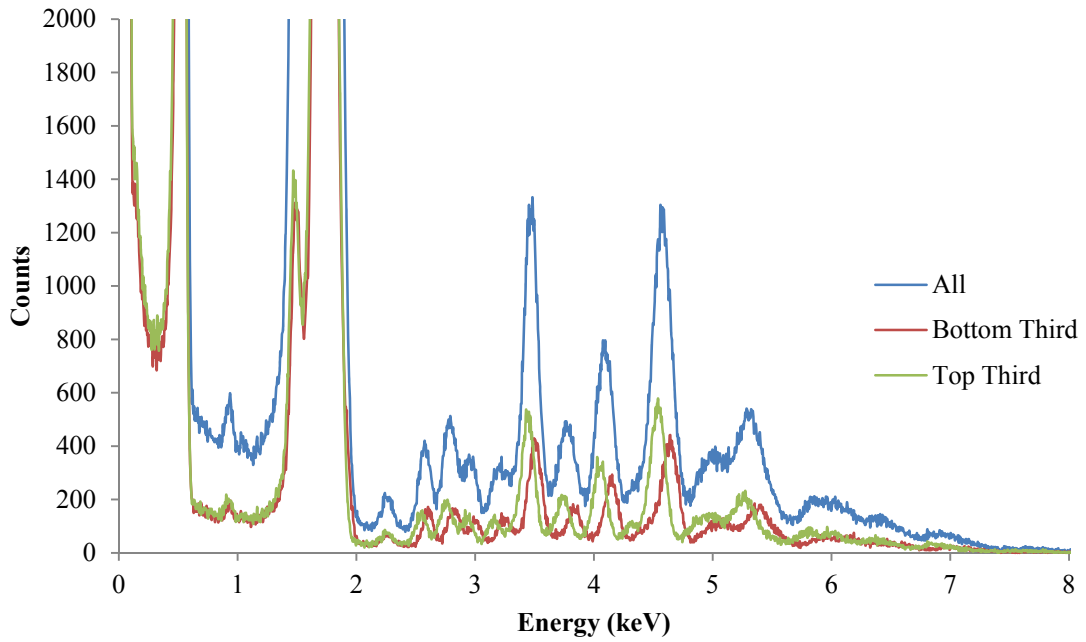


Figure B.1. 8 kV Quartz pellet data obtained using the pre-existing CCD facility as outlined in table 5.1. The data is split into the bottom and top thirds of the CCD to enable diffraction peak identification. For model plot comparison see figure 5.2 in section 5.4.1.1.

B.2 Goethite

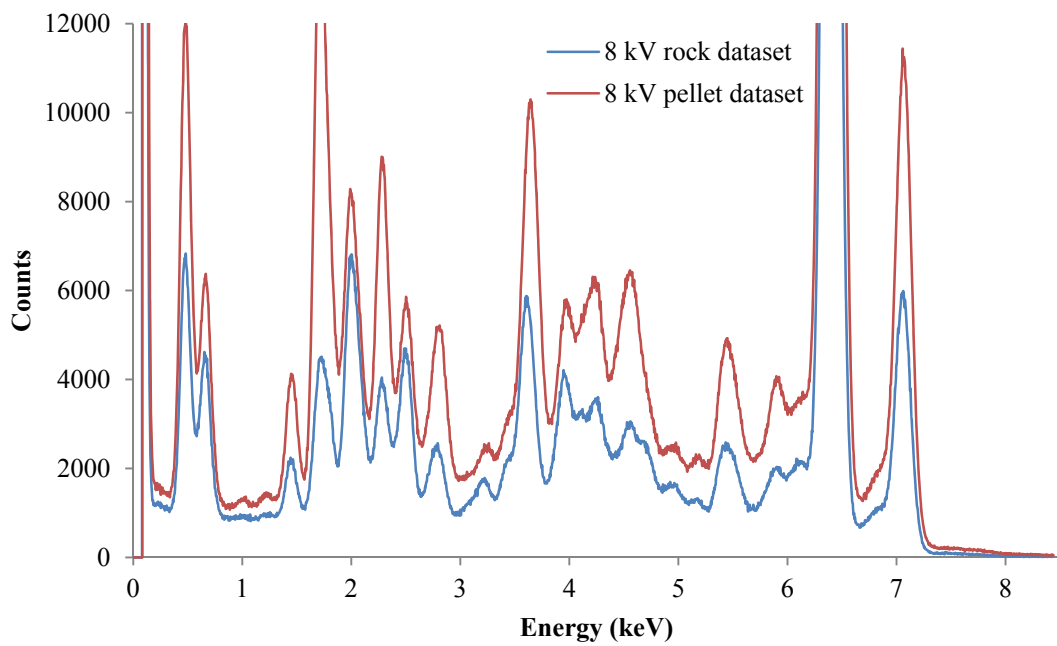


Figure B.2. 8 kV Goethite pellet and rock data obtained using the bespoke SDD facility as outlined in table 5.1. For model plot comparisons see figures 5.5 and 5.6 in Chapter 5.4.1.2.

B.3 Hematite

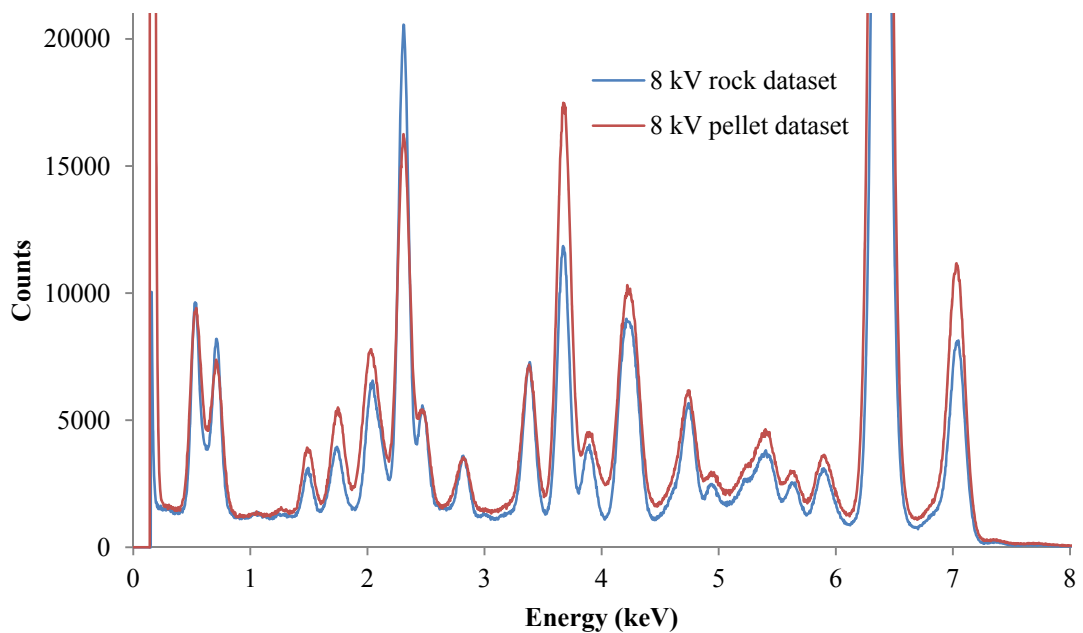


Figure B.3. 8 kV Hematite pellet and rock data obtained using the bespoke SDD facility as outlined in table 5.1. For model plot comparisons see figures 5.7 and 5.8 in section 5.4.1.3.

B.4 Evje

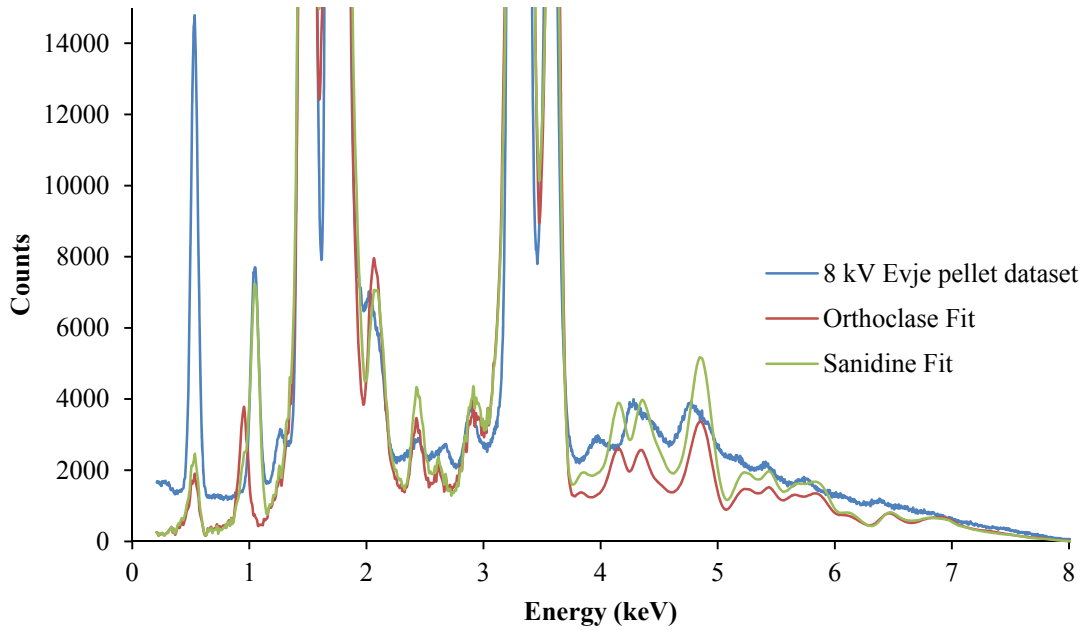


Figure B.4. 8 kV Evje pellet data obtained using the bespoke SDD facility as outlined in table 5.1, with orthoclase and sandine fits produced by the mineral-fitting routine with data from Tseng et al. (1995) and Keefer and Brown (1978). For additional K-suppression dataset see figure 5.10 in section 5.4.1.4.

B.5 Iveland

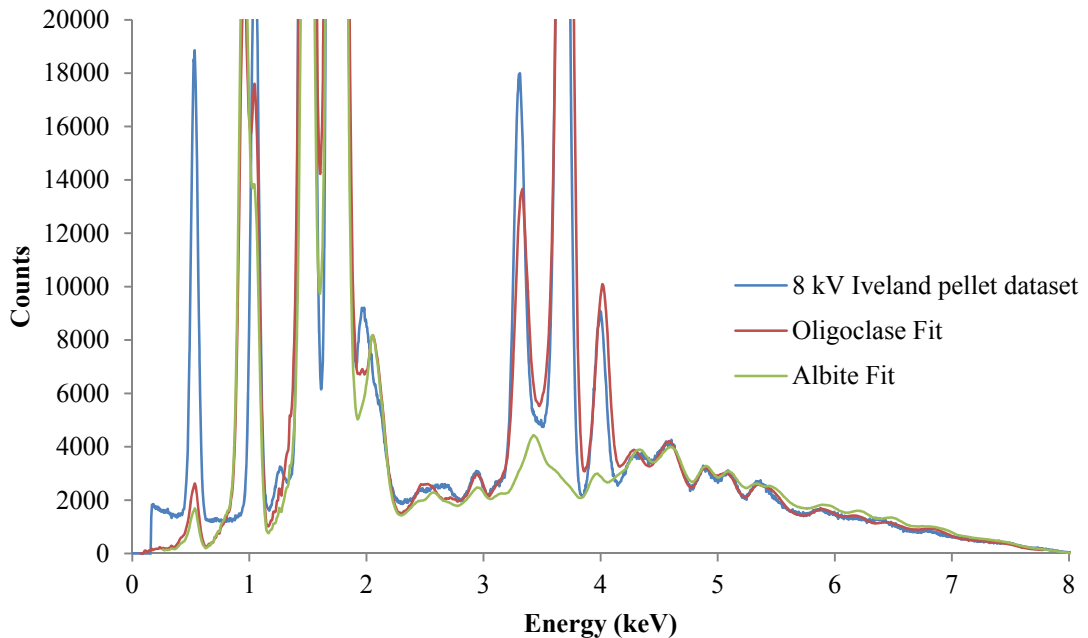


Figure B.5. 8 kV Iveland pellet data obtained using the bespoke SDD facility as outlined in table 5.1, with albite and oligoclase fits produced by the mineral fitting routine with data from Armbruster et al. (1990) and Philips (1971). For Ca-suppression dataset see figure 5.14 in section 5.4.1.6.

B.6 Brastad

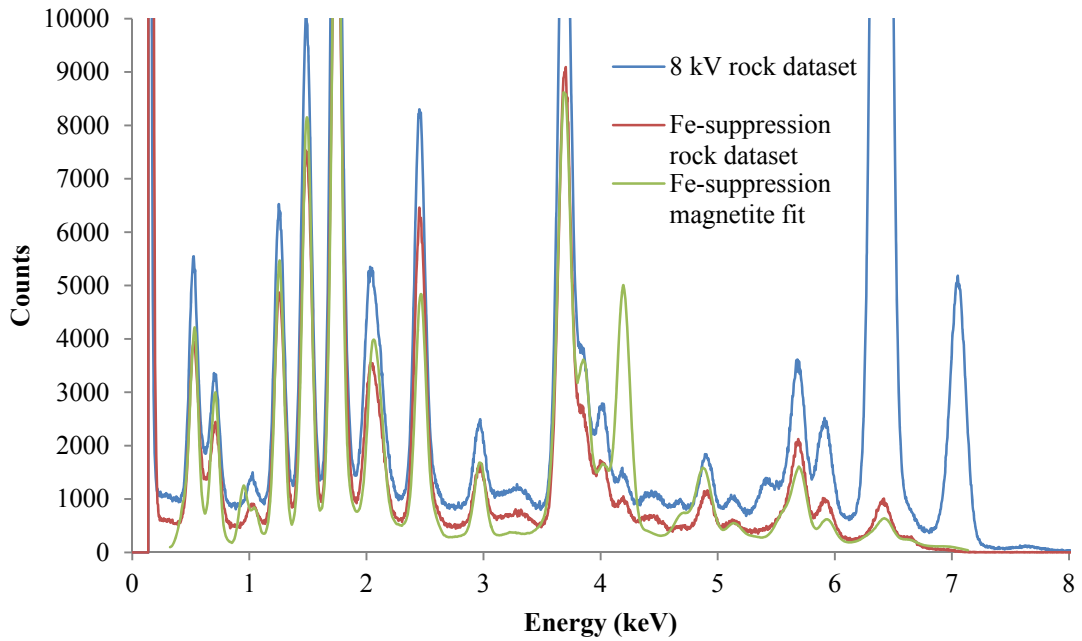


Figure B.6. 8 kV and Fe-suppression Brastad rock datasets obtained using the bespoke SDD facility as outlined in table 5.1. An Fe-suppression model created using the mineral-fitting routine using data from Wechsler et al. (1984). Additional fluorescence from O, Na, Mg, Al, Si and Ca is included in the fit, along with Zr. Rayleigh scattering effects are also included. For Ca-suppression dataset see figure 5.16 in section 5.4.1.6.

B.7 Hope

Figures B.7 and B.8 contain datasets acquired of Hope using the pre-existing CCD setup, with events incident on the top and bottom thirds of the CCD plotted individually for diffraction peak identification. Figure B.9 contains the 8 kV Hope dataset compared to calcite diffraction of fluorescence models produced by PoDFluX (Hansford, 2009). For Ca-suppression dataset see figure 5.18 in section 5.4.2.

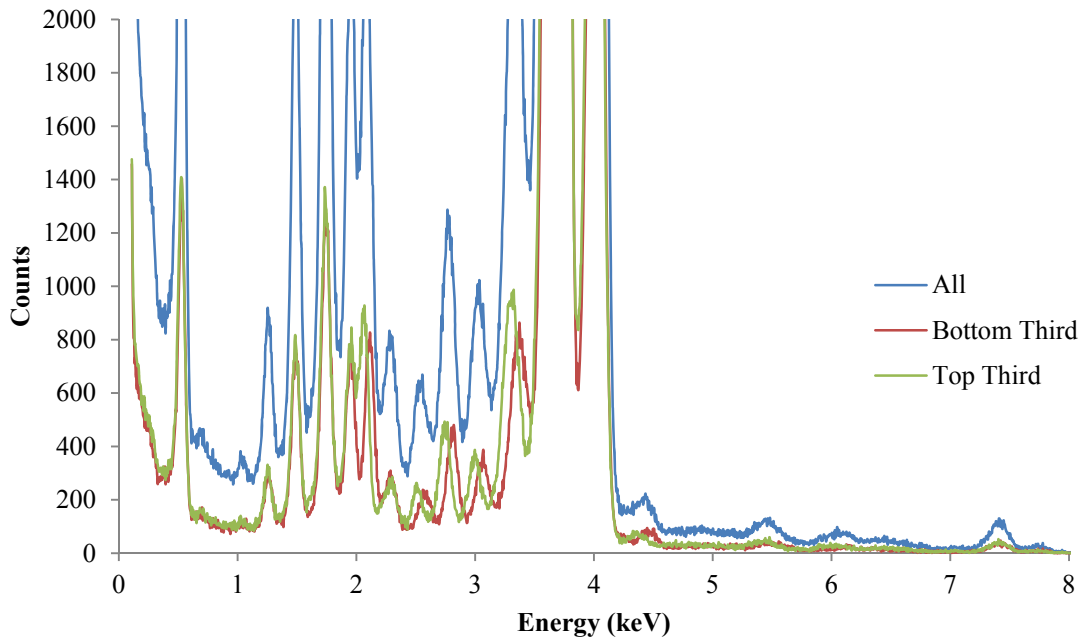


Figure B.7. Hope rock 8 kV dataset obtained using the pre-existing CCD facility as outlined in table 5.1.

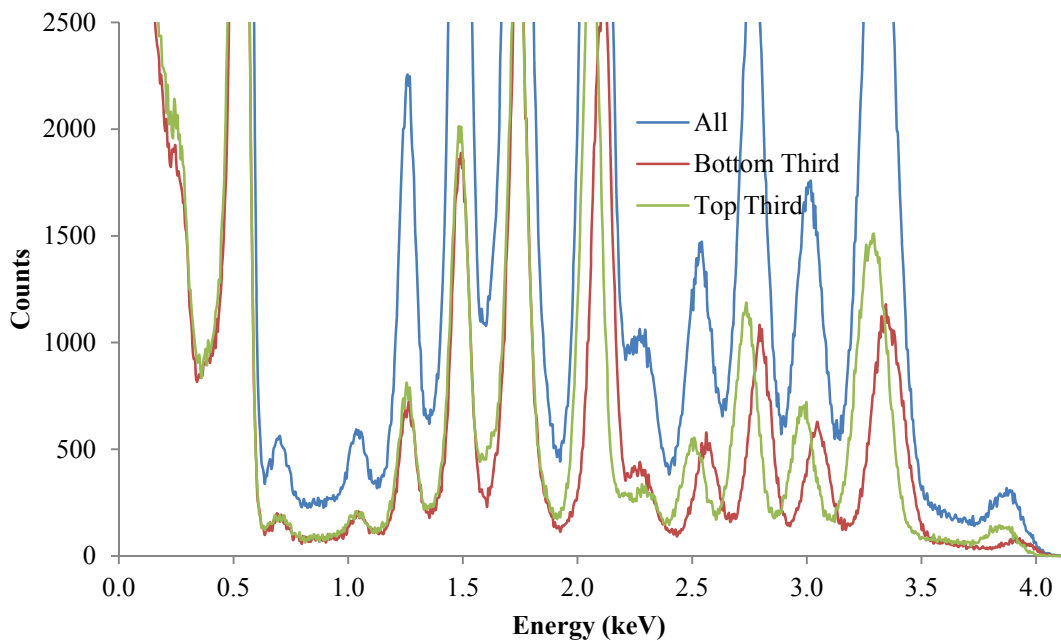


Figure B.8. Hope rock Ca-suppression dataset obtained using the pre-existing CCD facility as outlined in table 5.1.

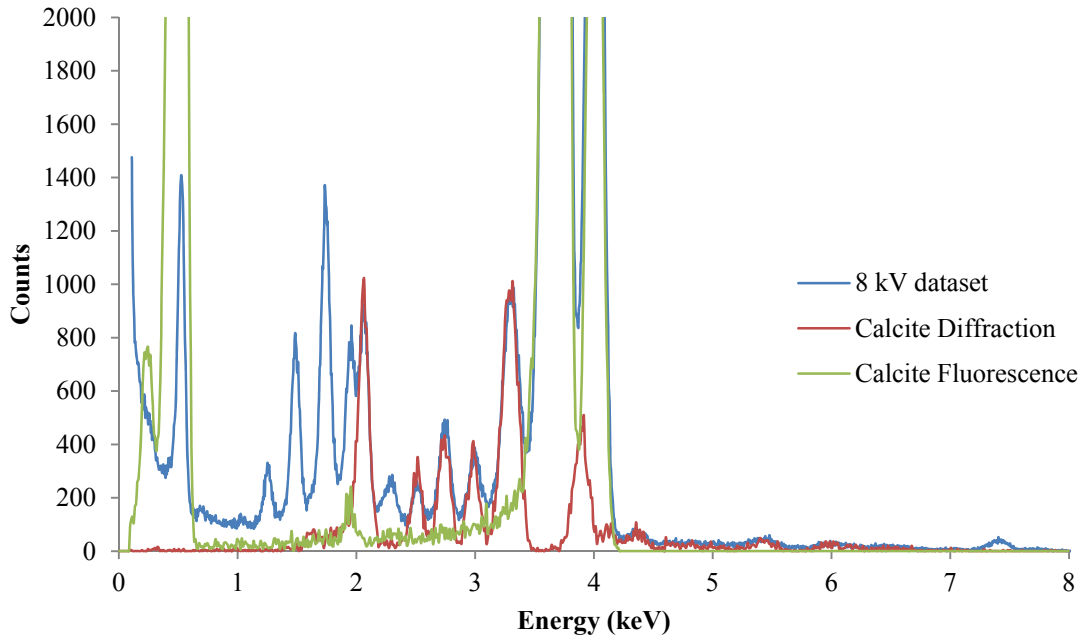


Figure B.9. Hope rock 8 kV dataset obtained using the pre-existing CCD facility as outlined in table 5.1 compared to PoDFluX diffraction and fluorescence models created using data from Sitepu (2009).

B.8 BastilleA

Figures B.10 and B.11 contain datasets acquired of BastilleA using the pre-existing CCD setup, with events incident on the top and bottom thirds of the CCD plotted individually for diffraction peak identification. Figure B.12 contains the 8 kV BastilleA dataset compared to calcite diffraction of fluorescence models produced by PoDFluX (Hansford, 2009). For Ca-suppression dataset see figure 5.18 in section 5.4.2.

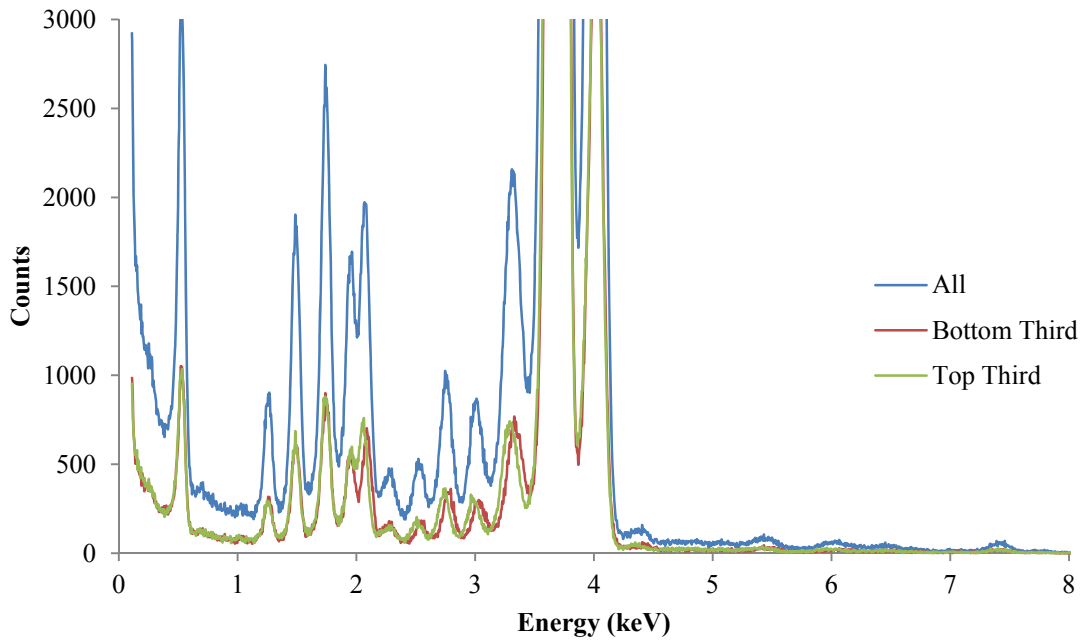


Figure B.10. BastilleA rock 8 kV dataset obtained using the pre-existing CCD facility as outlined in table 5.1.

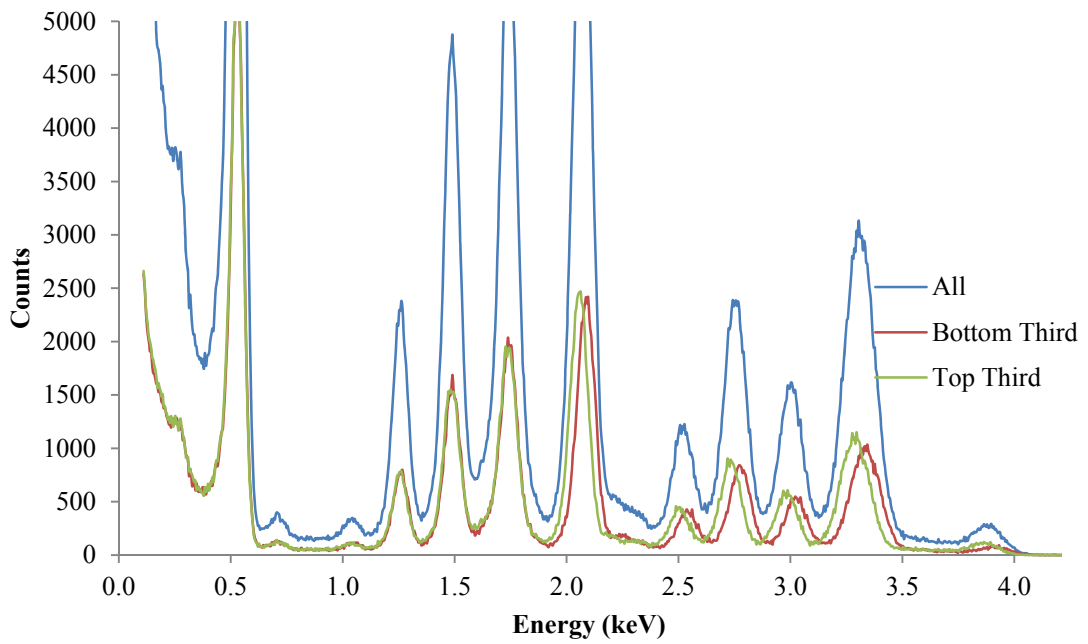


Figure B.11. BastilleA rock Ca-suppression dataset obtained using the pre-existing CCD facility as outlined in table 5.1.

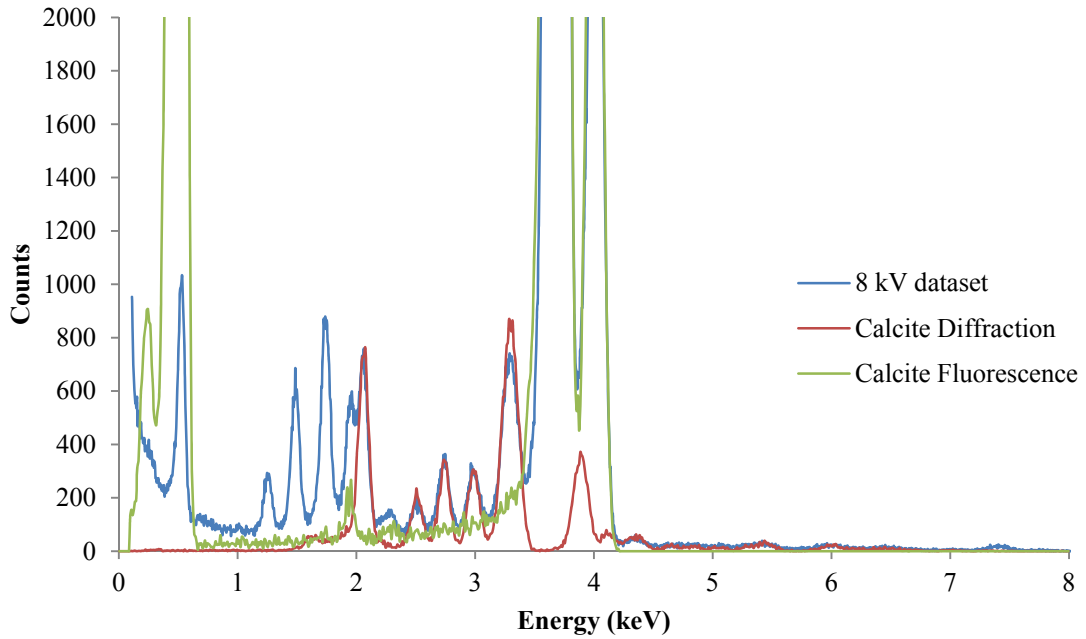


Figure B.12. BastilleA rock 8 kV dataset obtained using the pre-existing CCD facility as outlined in table 5.1 compared to PoDFluX diffraction and fluorescence models created using data from Sitepu (2009).

B.9 MindelA

Figures B.13 and B.14 contain datasets acquired of MindelA using the pre-existing CCD setup, with events incident on the top and bottom thirds of the CCD plotted individually for diffraction peak identification. Figure B.15 contains the 8 kV MindelA dataset compared to dolomite diffraction of fluorescence models produced by PoDFluX (Hansford, 2009). For Ca-suppression dataset see figure 5.19 in section 5.4.2.

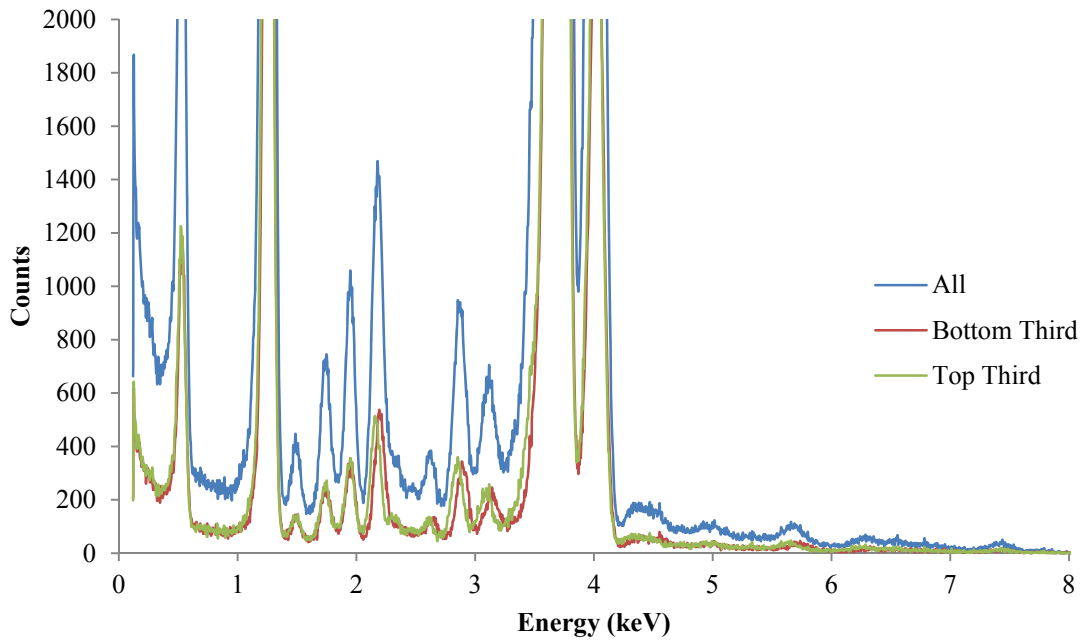


Figure B.13. MindelA rock 8 kV dataset obtained using the pre-existing CCD facility as outlined in table 5.1.

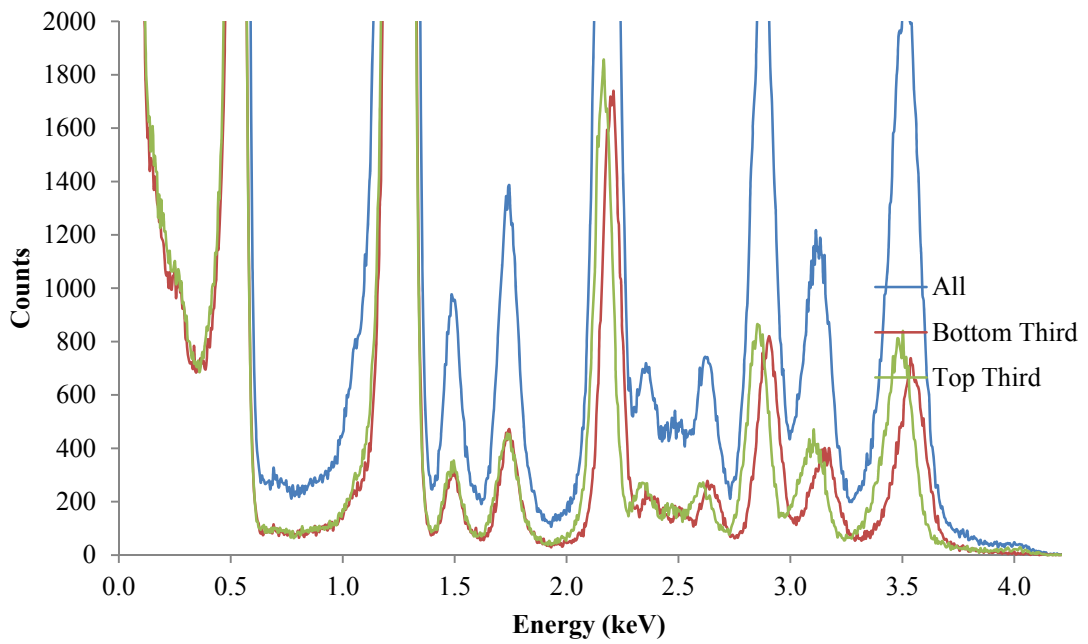


Figure B.14. MindelA rock Ca-suppression dataset obtained using the pre-existing CCD facility as outlined in table 5.1.

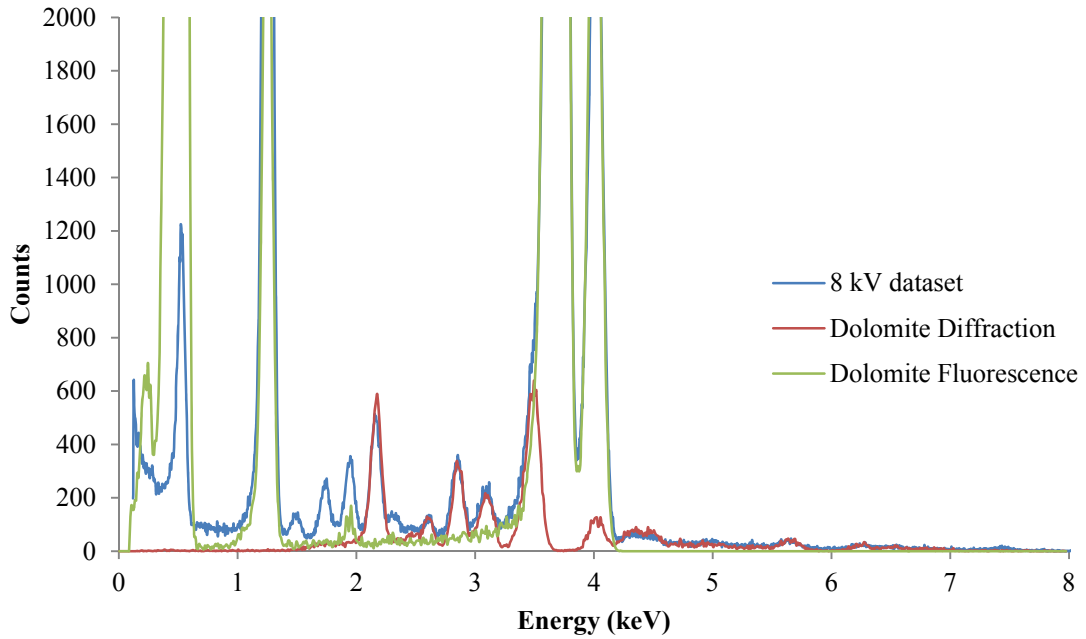


Figure B.15. MindelA rock 8 kV dataset obtained using the pre-existing CCD facility as outlined in table 5.1 compared to PoDFluX diffraction and fluorescence models created using data from Ross and Reeder (1992).

B.10 MindelB

Figures B.16 and B.17 contain datasets acquired of MindelB using the pre-existing CCD setup, with events incident on the top and bottom thirds of the CCD plotted individually for diffraction peak identification. Figure B.18 contains the 8 kV MindelB dataset compared to dolomite diffraction of fluorescence models produced by PoDFluX (Hansford, 2009). For Ca-suppression dataset see figure 5.19 in section 5.4.2.

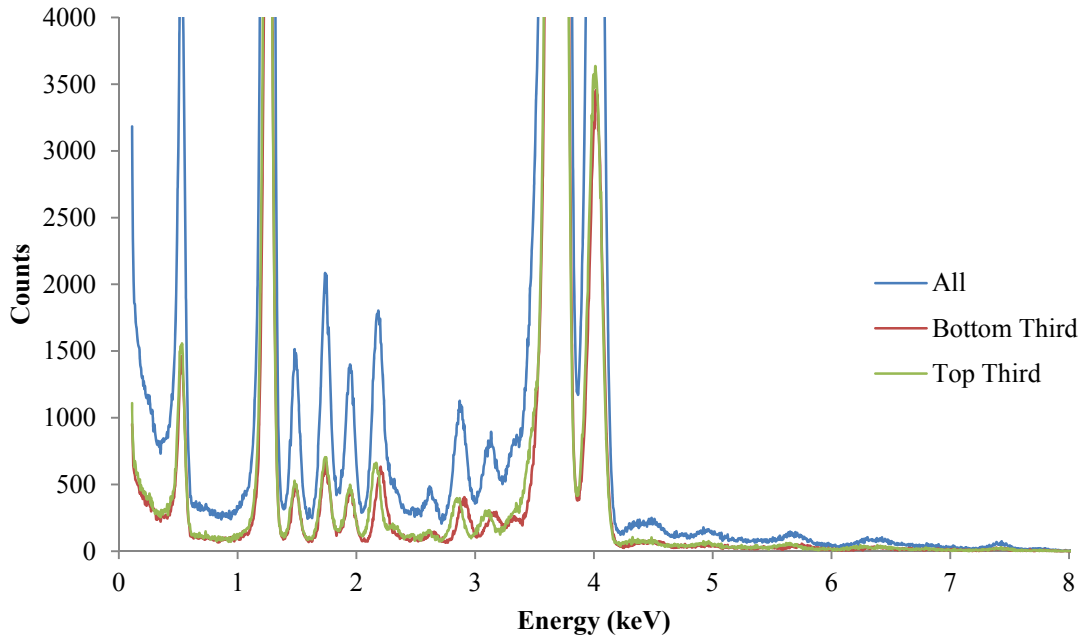


Figure B.16. MindelB rock 8 kV dataset obtained using the pre-existing CCD facility as outlined in table 5.1.

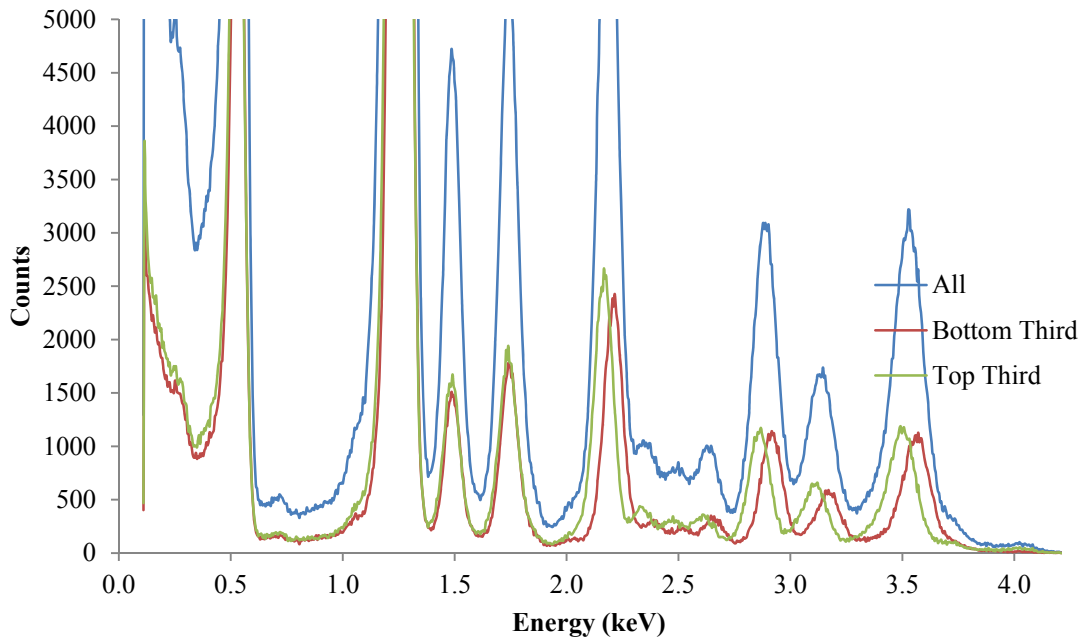


Figure B.17. MindelB rock Ca-suppression dataset obtained using the pre-existing CCD facility as outlined in table 5.1.

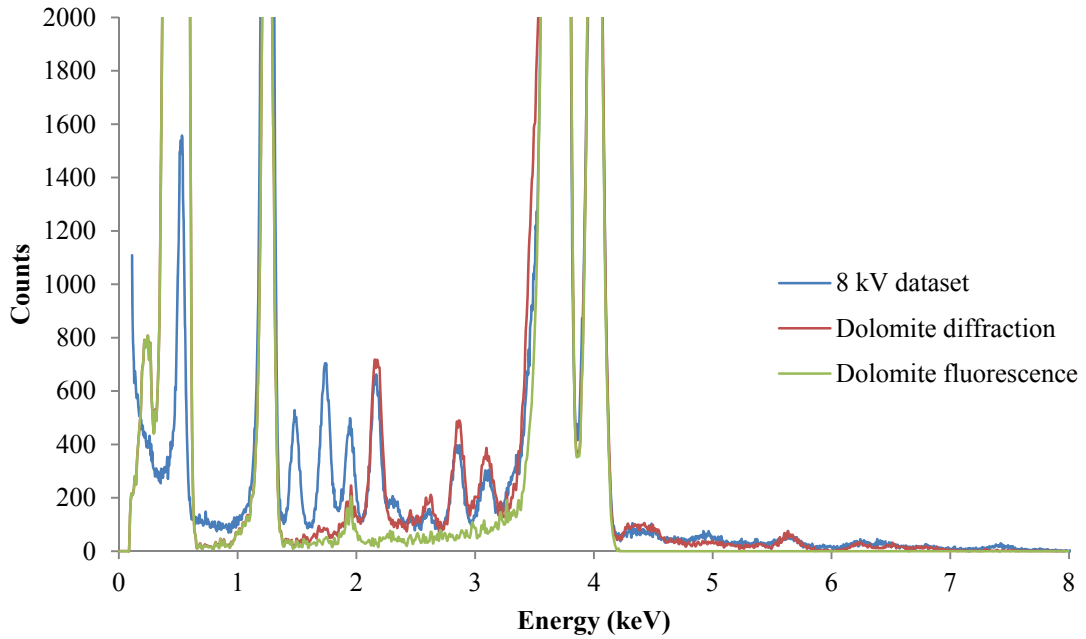


Figure B.18. MindelB rock 8 kV dataset obtained using the pre-existing CCD facility as outlined in table 5.1 compared to PoDFluX diffraction and fluorescence models created using data from Ross and Reeder (1992).

B.11 JDo-1

Figures B.19 and B.20 contain datasets acquired of JDo-1 using the pre-existing CCD setup, with events incident on the top and bottom thirds of the CCD plotted individually for diffraction peak identification. Figure B.21 contains the 8 kV JDo-1 dataset compared to dolomite diffraction of fluorescence models produced by PoDFluX (Hansford, 2009). For Ca-suppression dataset see figure 5.20 in section 5.4.2.

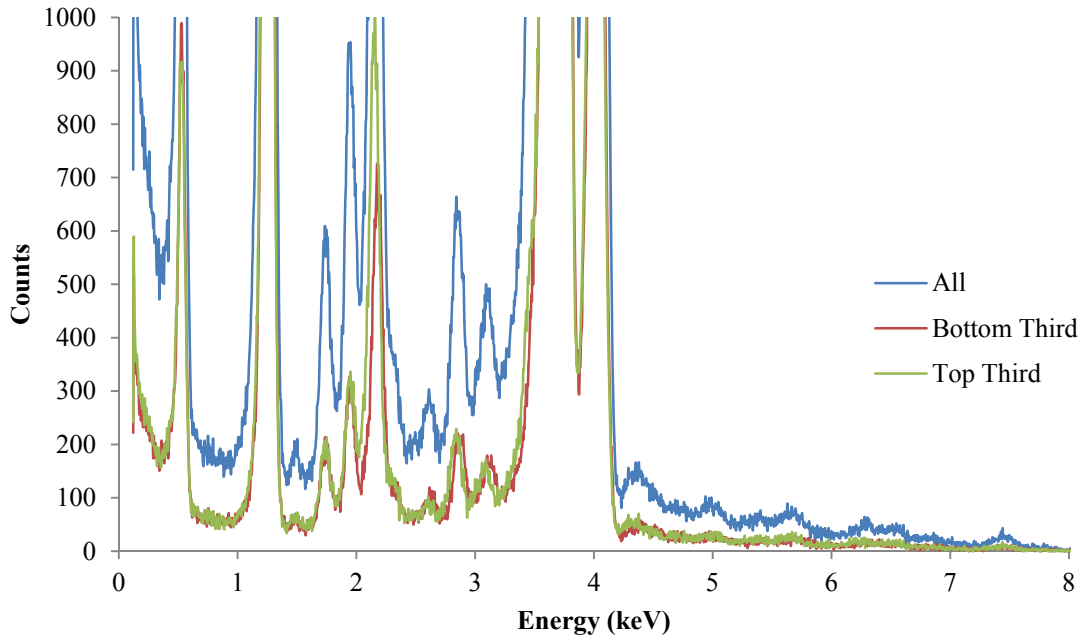


Figure B.19. JDo-1 pellet 8 kV dataset obtained using the pre-existing CCD facility as outlined in table 5.1.

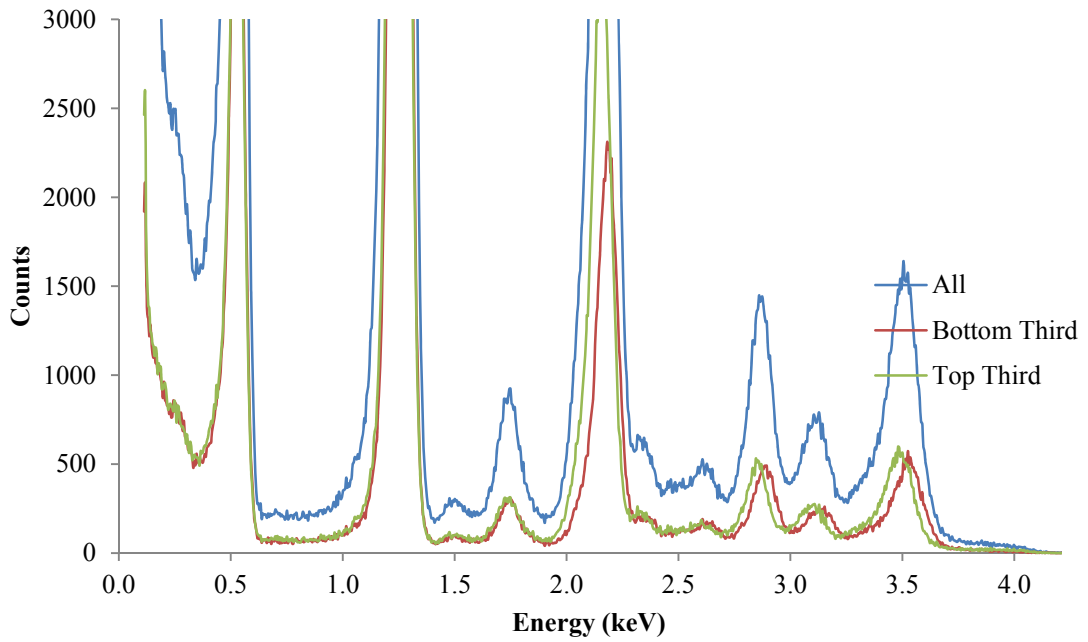


Figure B.20. JDo-1 pellet Ca-suppression dataset obtained using the pre-existing CCD facility as outlined in table 5.1.

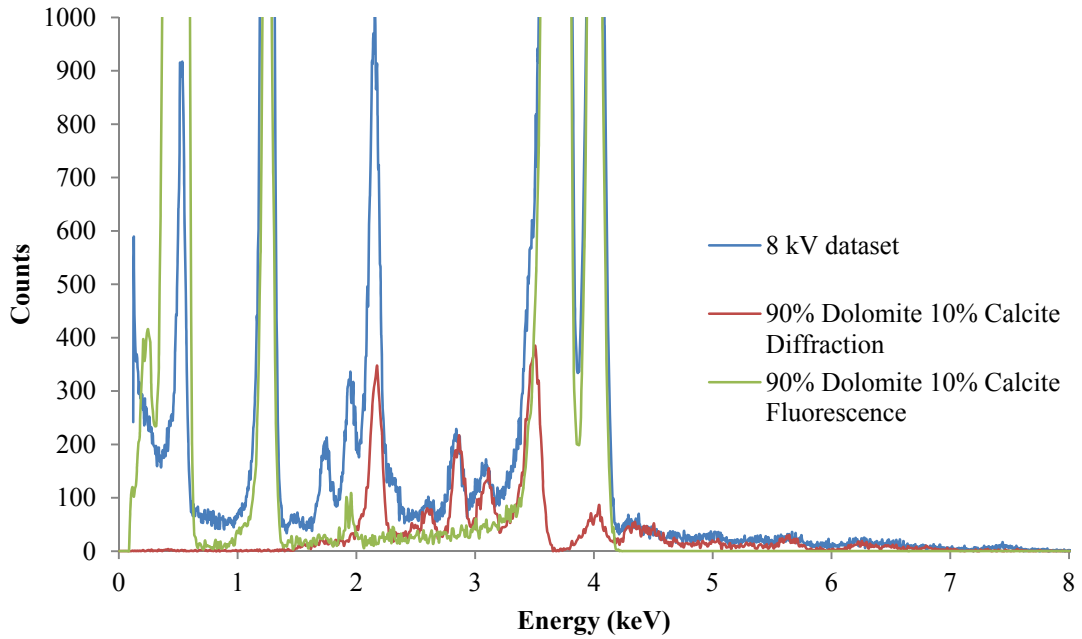


Figure B.21. JDo-1 pellet 8 kV dataset obtained using the pre-existing CCD facility as outlined in table 5.1 compared to PoDFluX diffraction and fluorescence models created using data from Ross and Reeder (1992) and Sitepu (2009).

B.12 WatchetB

Figures B.22-B.24 contain datasets acquired of the first WatchetB pellet, with the second WatchetB pellet datasets shown in figures B.27 and B.28. WatchetB rock datasets are shown in figures B.29 and B.30. Experimental parameters for each acquisition is detailed in table 5.1 and where applicable, top and bottom CCD events are plotted individually for diffraction peak identification. Diffraction and fluorescence model comparisons to experimental acquisitions are included in figures B.25, B.26, and B.31.

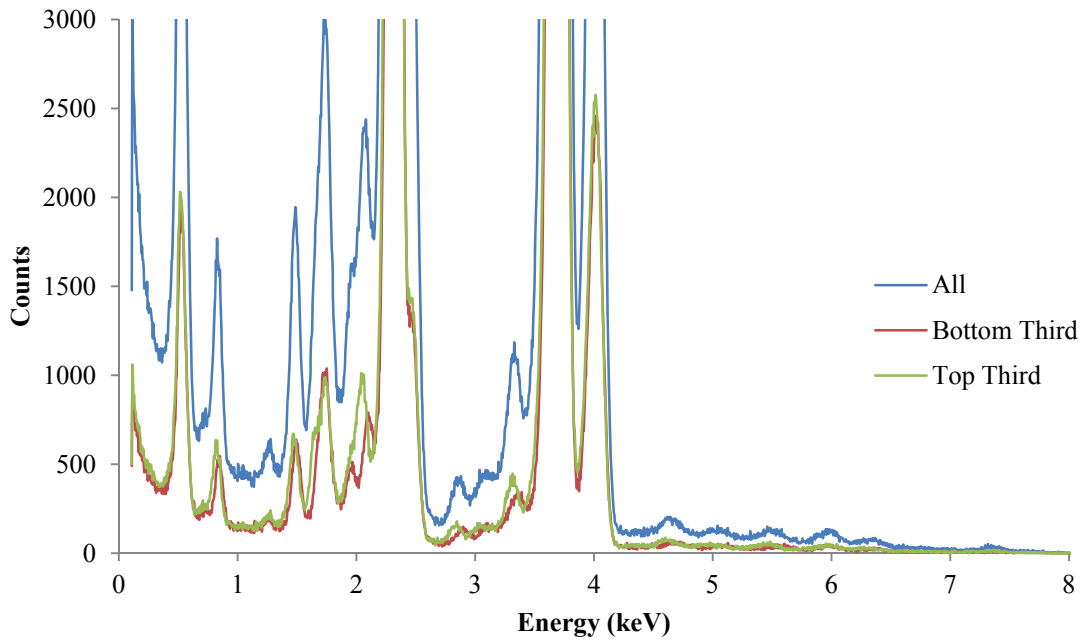


Figure B.22. First WatchetB pellet 8 kV dataset obtained using the pre-existing CCD facility as outlined in table 5.1.

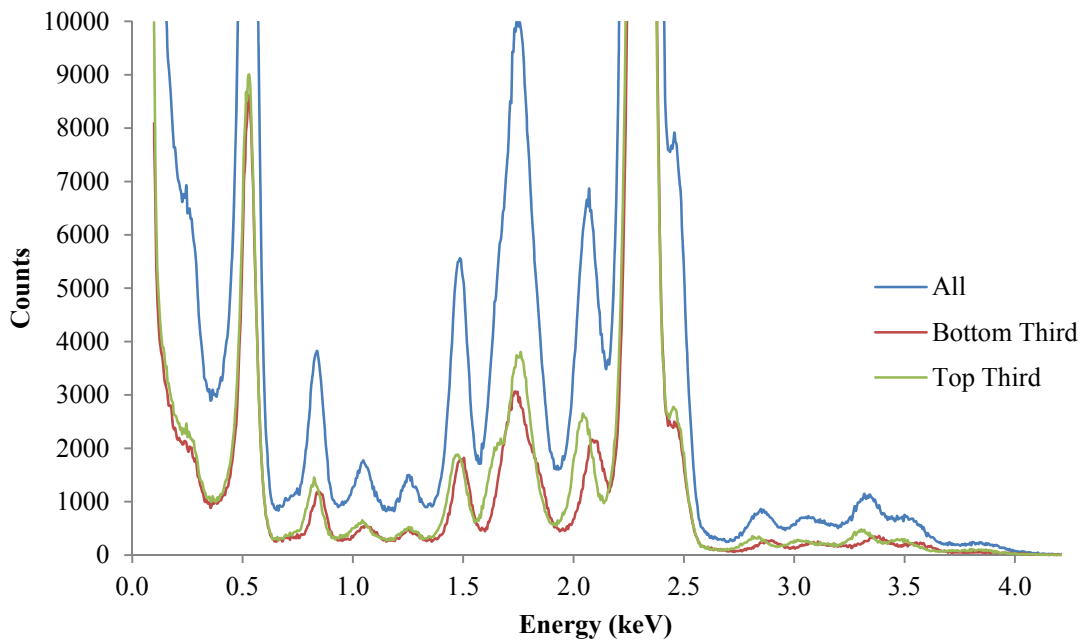


Figure B.23. First WatchetB pellet Ca-suppression dataset obtained using the pre-existing CCD facility as outlined in table 5.1.

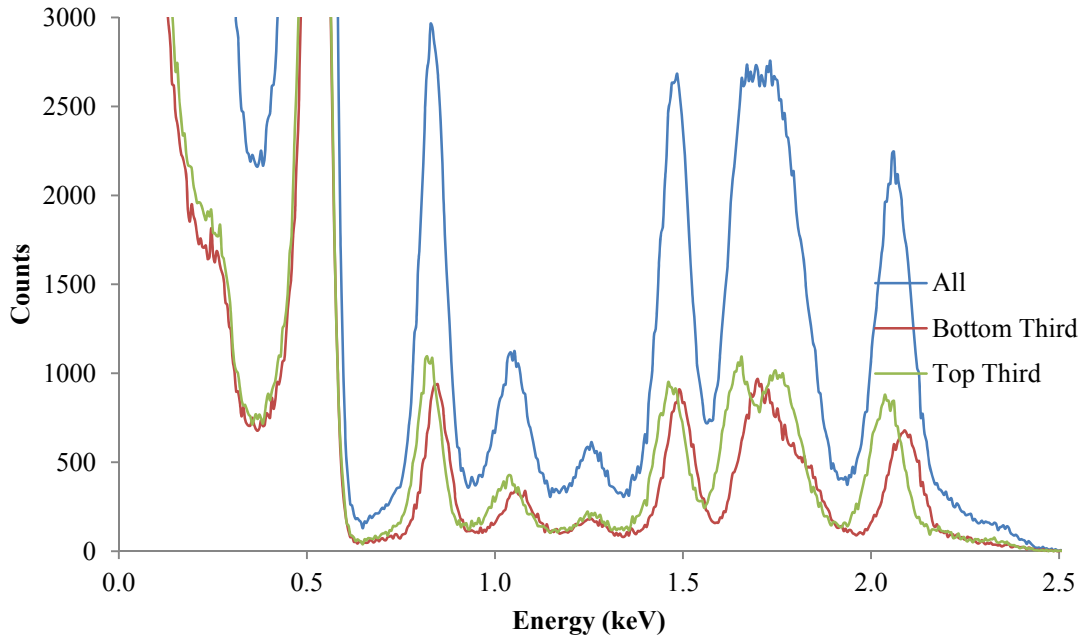


Figure B.24. First WatchetB pellet S-suppression dataset obtained using the pre-existing CCD facility as outlined in table 5.1.

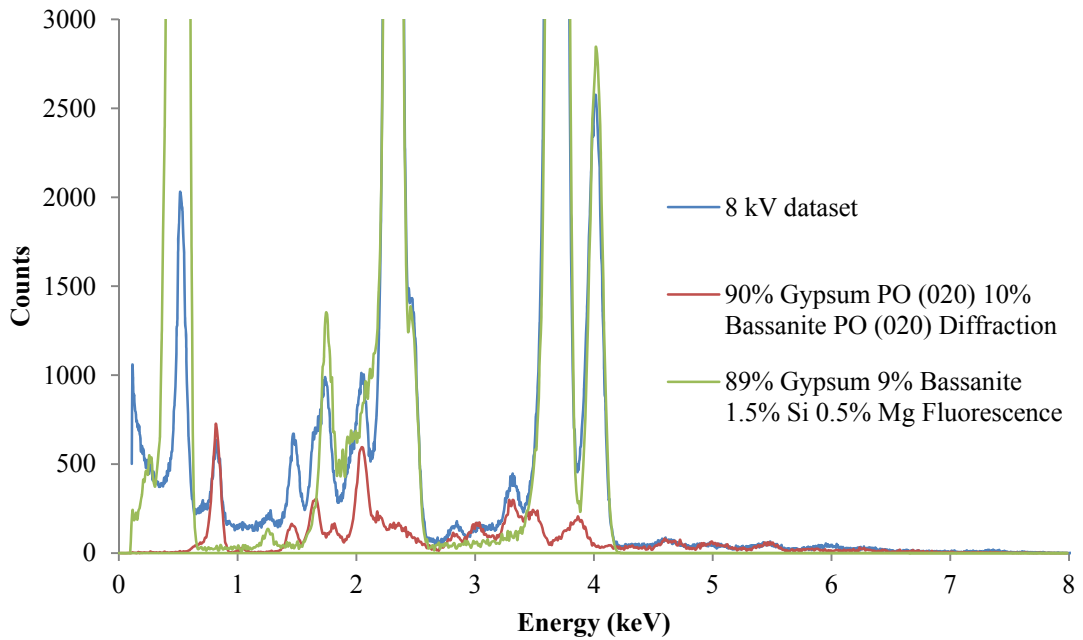


Figure B.25. 8 kV dataset acquired of the first WatchetB pellet compared to PoDFluX models for gypsum and bassanite diffraction and fluorescence using information from Boeyens and Ichharam (2002) and Ballirano et al. (2001). The diffraction model incorporated a preferred orientation effect along the (020) plane.

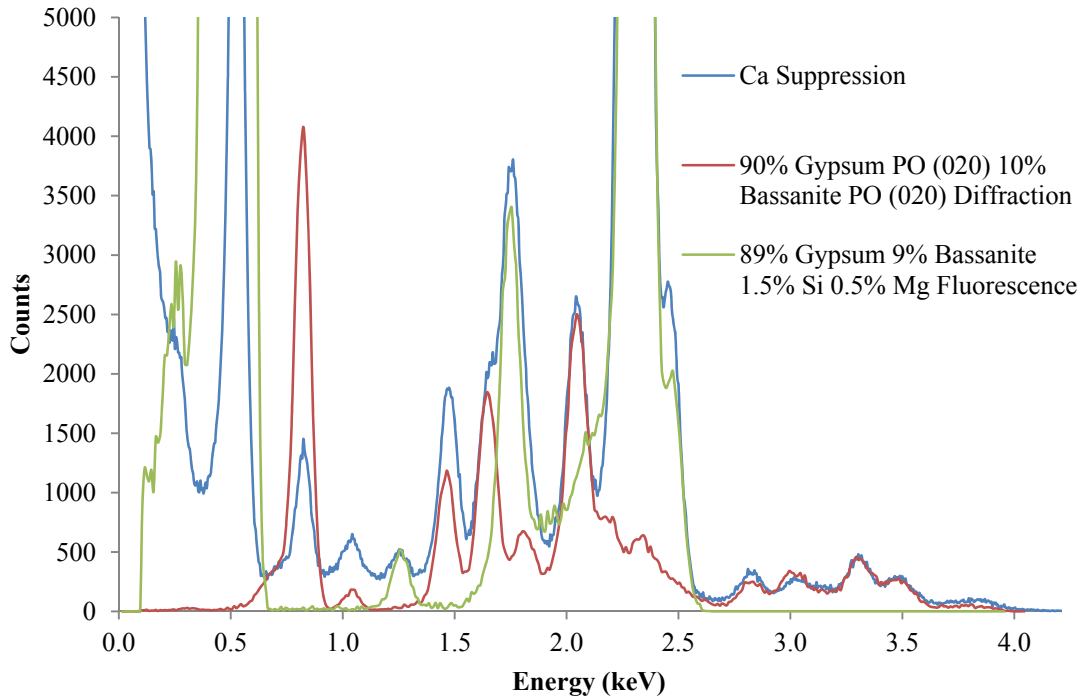


Figure B.26. Ca-suppression dataset acquired of the first WatchetB pellet compared to PoDFluX models for gypsum and bassanite diffraction and fluorescence using information from Boeyens and Ichharam (2002) and Ballirano et al. (2001). The diffraction model incorporated a preferred orientation effect along the (020) plane.

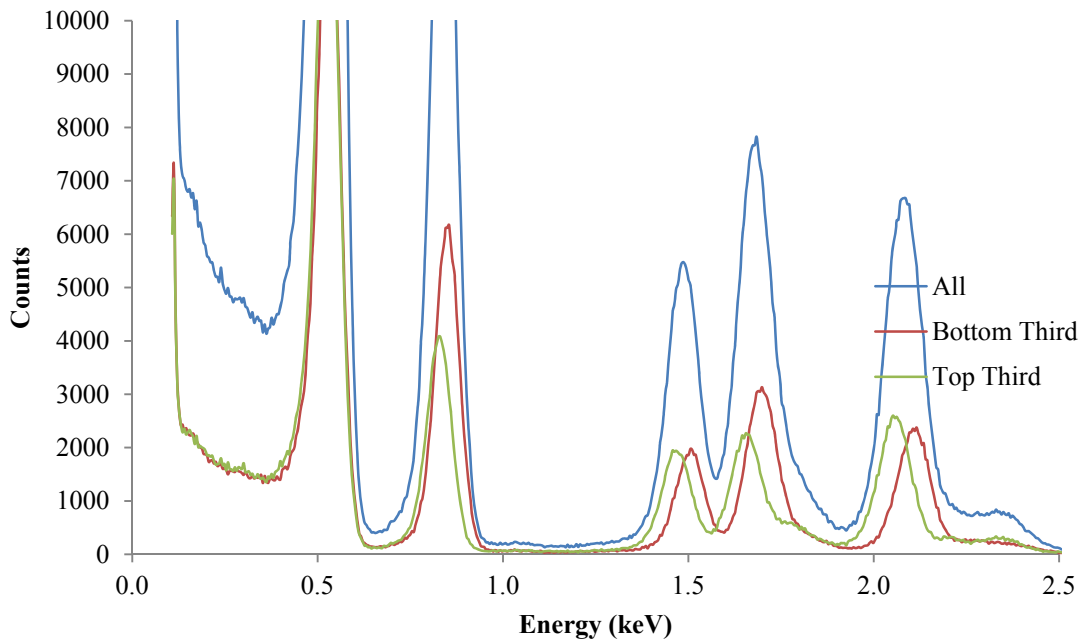


Figure B.27. Second WatchetB pellet S-suppression dataset obtained using the pre-existing CCD facility as outlined in table 5.1.

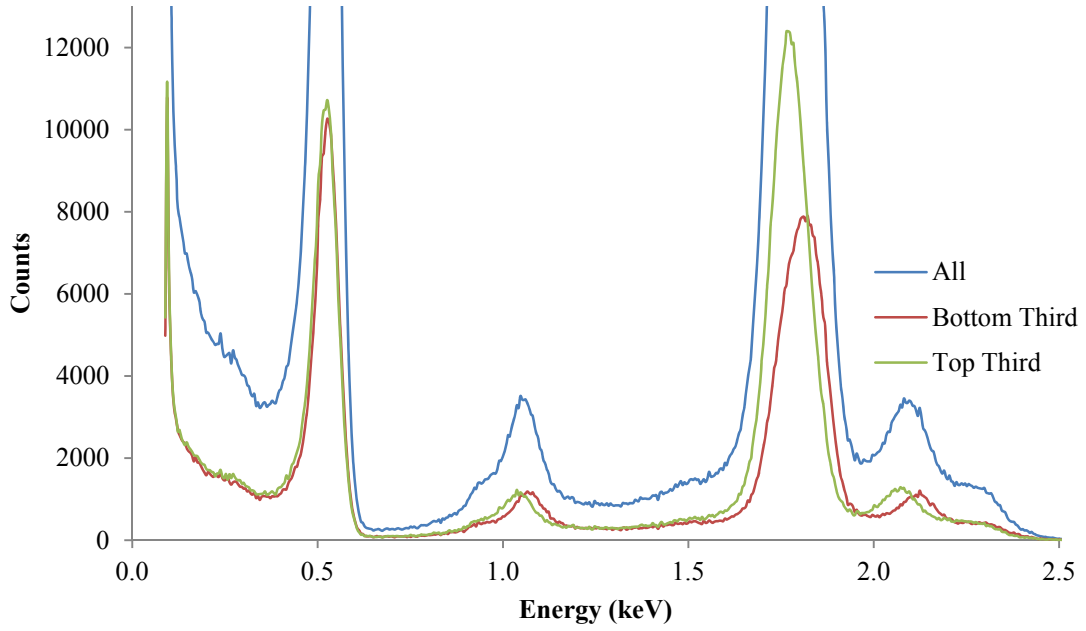


Figure B.28. WatchetB second pellet S-suppression second pellet S-suppression dataset obtained using the pre-existing CCD facility as outlined in table 5.1. This dataset was taken two days after the S-suppression dataset in figure B.27, as discussed in section 5.4.3.1.

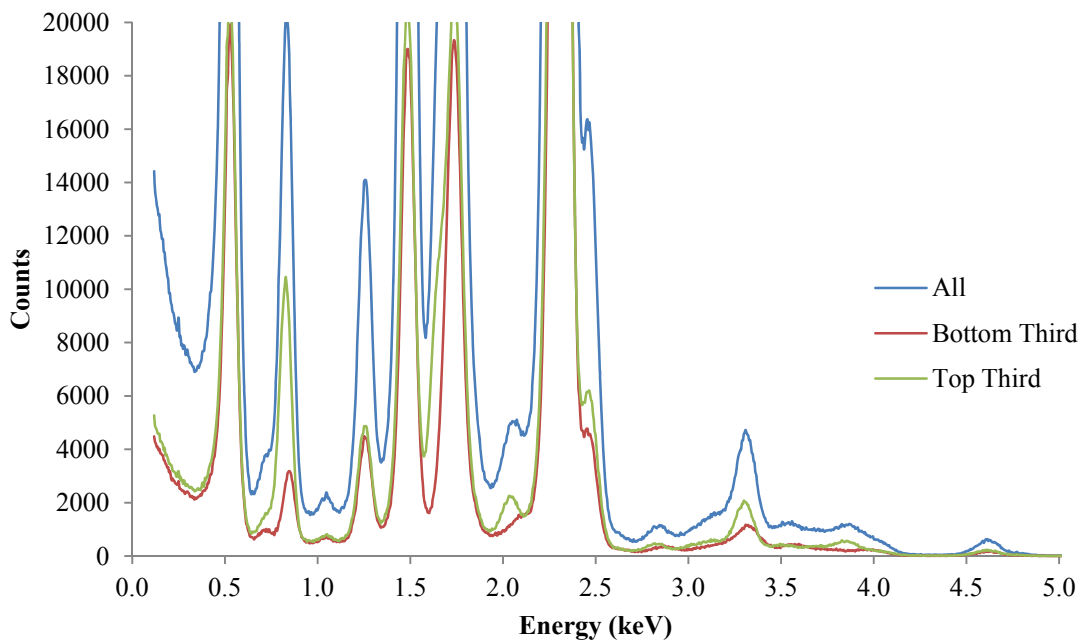


Figure B.29. WatchetB rock Ca-suppression dataset obtained using the pre-existing CCD facility as outlined in table 5.1.

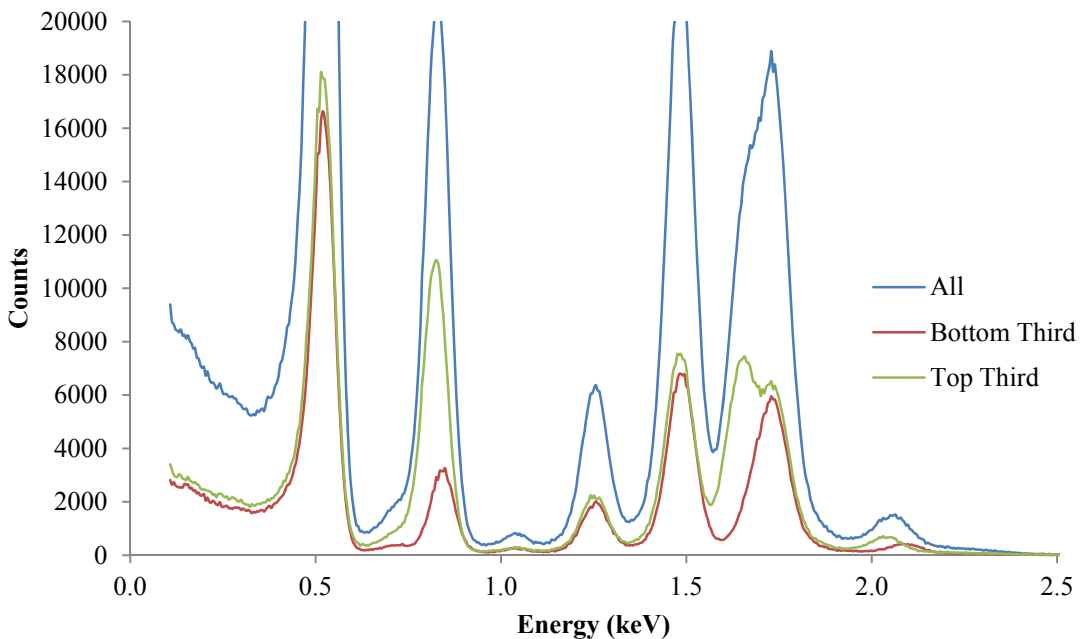


Figure B.30. WatchetB rock S-suppression dataset obtained using the pre-existing CCD facility as outlined in table 5.1.

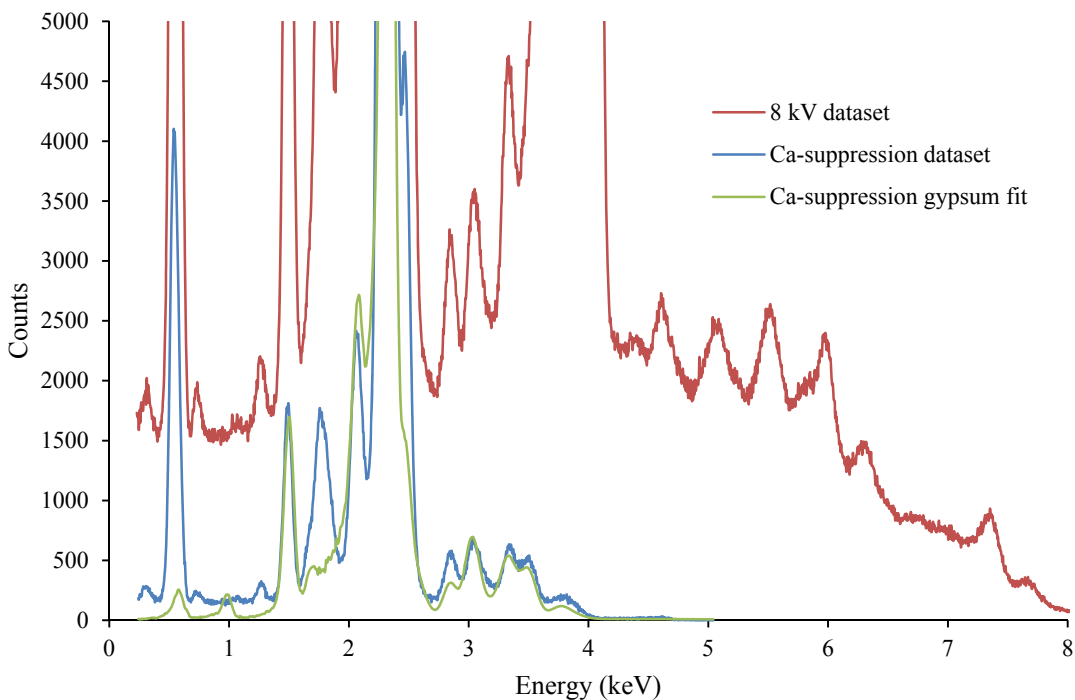


Figure B.31. WatchetB 8 kV and Ca-suppression rock datasets obtained using the bespoke SDD facility as outlined in table 5.1, compared to a Ca-suppression gypsum fit produced using the mineral fitting routine with data from Boeyens and Ichharam (2002)

B.13 WatchetC

Figures B.32-B.34 contain datasets acquired of the first WatchetC pellet, with the second WatchetC pellet datasets shown in figures B.37 and B.38. WatchetC rock datasets are shown in figures B.39, B.40 and B.41. Experimental parameters for each acquisition is detailed in table 5.1 and where applicable, top and bottom CCD events are plotted individually for diffraction peak identification. Diffraction and fluorescence model comparisons to experimental acquisitions are included in figures B.35, B.36, and B.42.

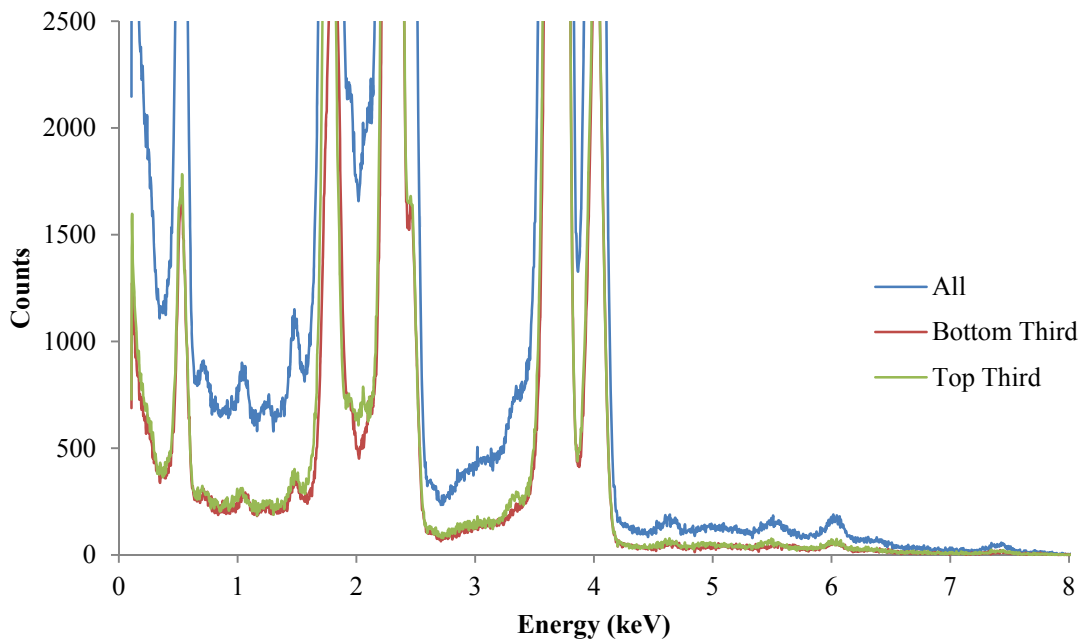


Figure B.32. First WatchetC pellet 8 kV dataset obtained using the pre-existing CCD facility as outlined in table 5.1.

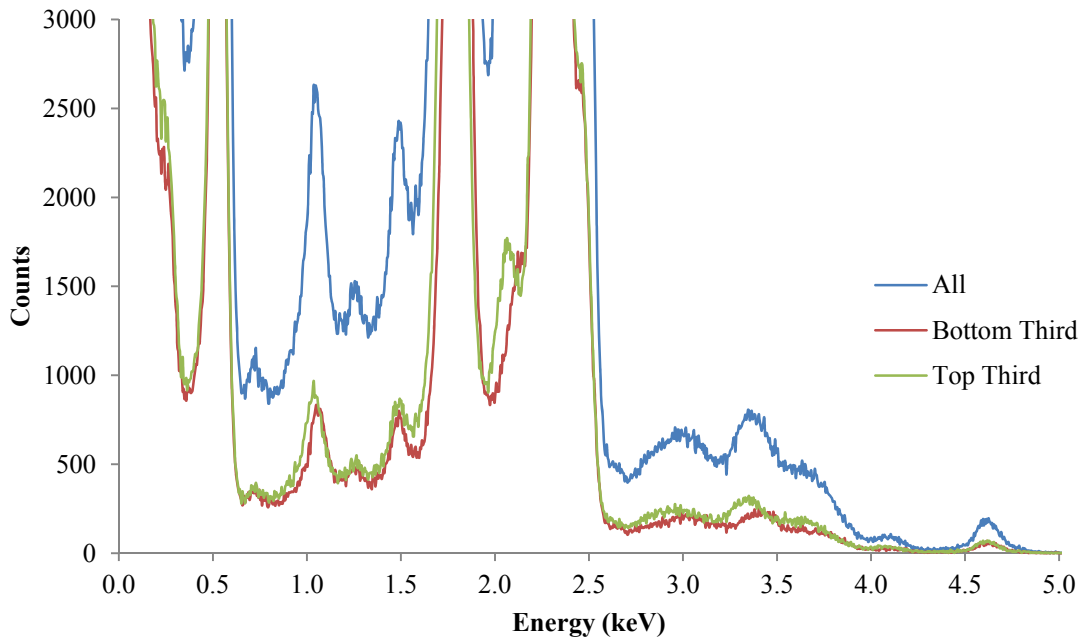


Figure B.33. First WatchetC pellet Ca-suppression dataset obtained using the pre-existing CCD facility as outlined in table 5.1.

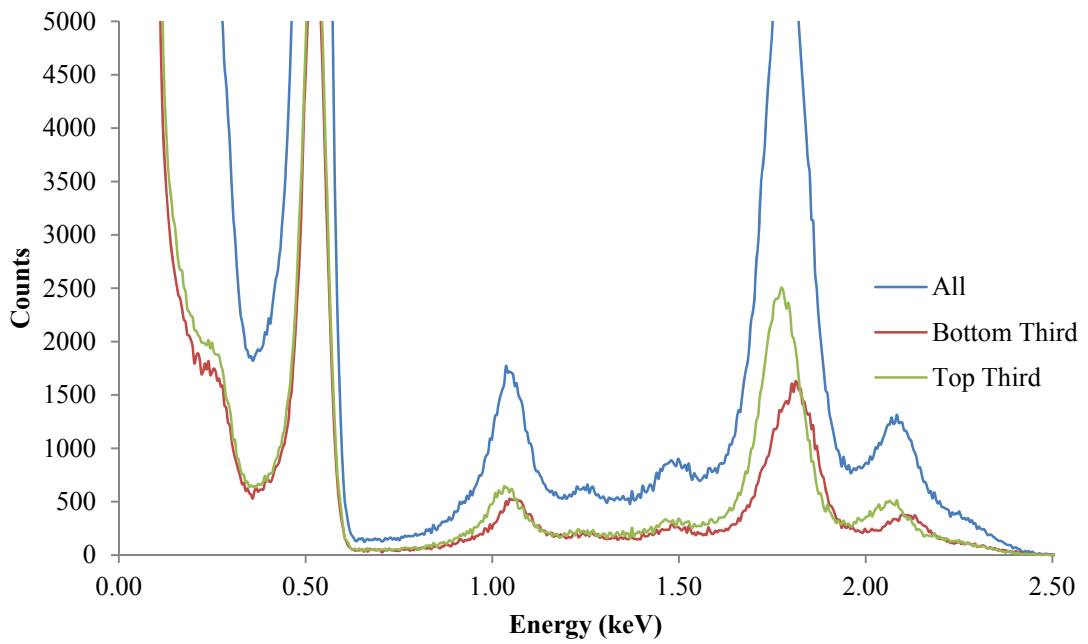


Figure B.34. First WatchetC pellet S-suppression dataset obtained using the pre-existing CCD facility as outlined in table 5.1.

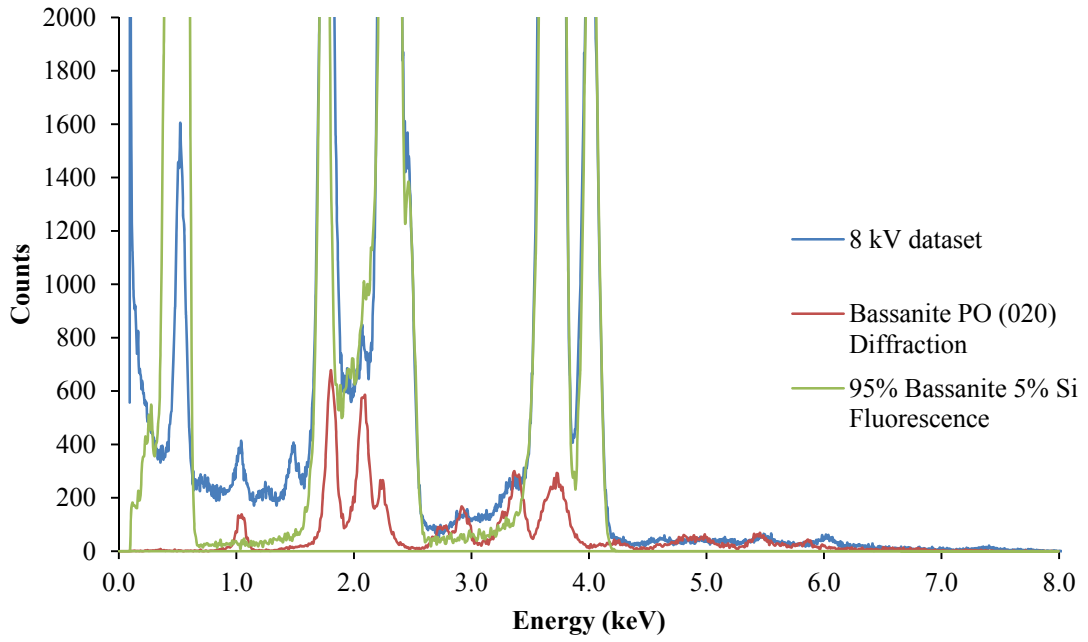


Figure B.35. 8 kV dataset acquired of the first WatchetC pellet compared to PoDFluX models for bassanite diffraction and fluorescence using information from Ballirano et al. (2001). The diffraction model incorporated a preferred orientation effect along the (020) plane.

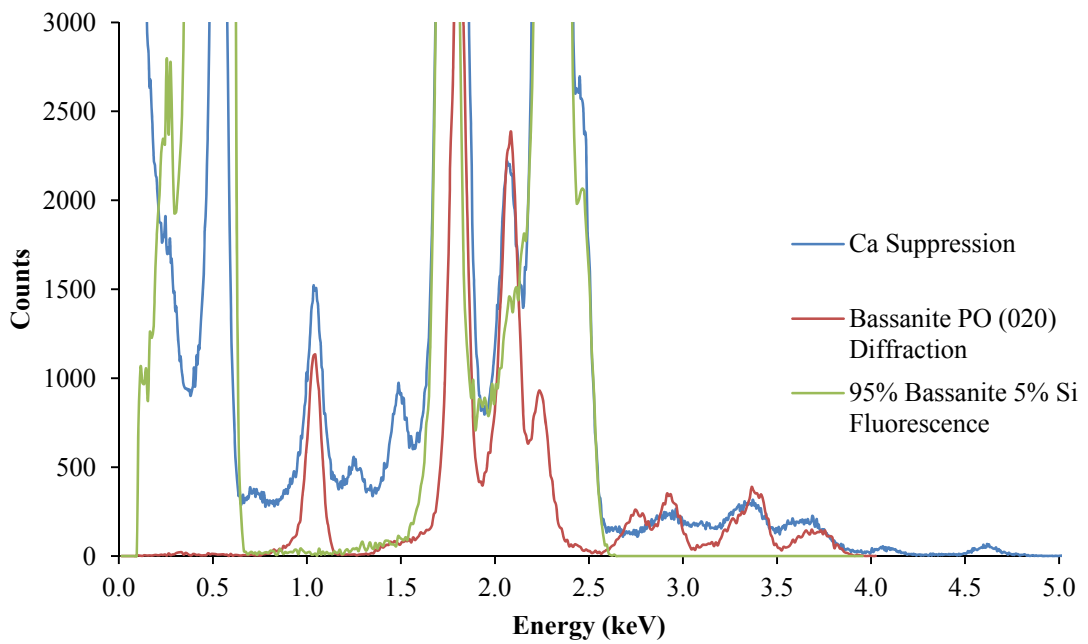


Figure B.36. Ca-suppression dataset acquired of the first WatchetC pellet compared to PoDFluX models for bassanite diffraction and fluorescence using information from Ballirano et al. (2001). The diffraction model incorporated a preferred orientation effect along the (020) plane.

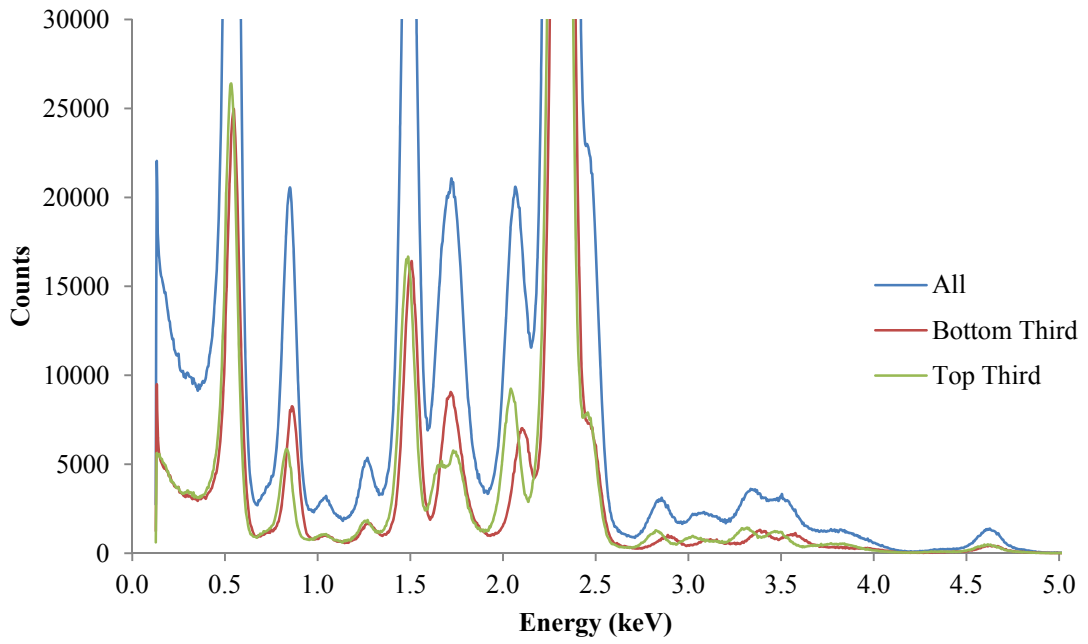


Figure B.37. Second WatchetC pellet Ca-suppression dataset obtained using the pre-existing CCD facility as outlined in table 5.1.

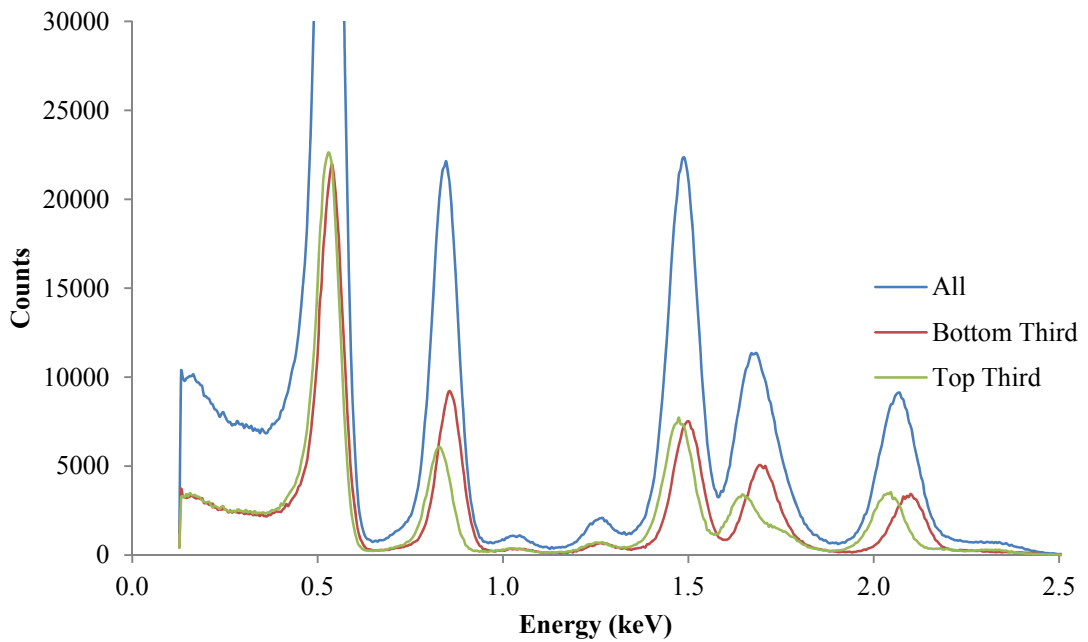


Figure B.38. Second WatchetC pellet S-suppression dataset obtained using the pre-existing CCD facility as outlined in table 5.1.

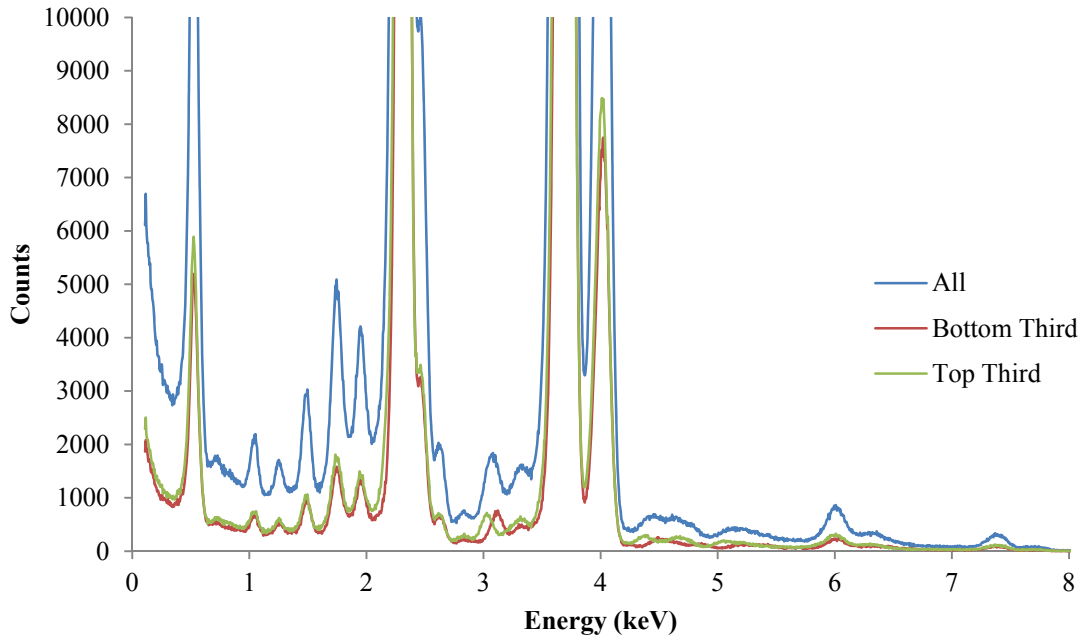


Figure B.39. WatchetC rock 8 kV dataset obtained using the pre-existing CCD facility as outlined in table 5.1.

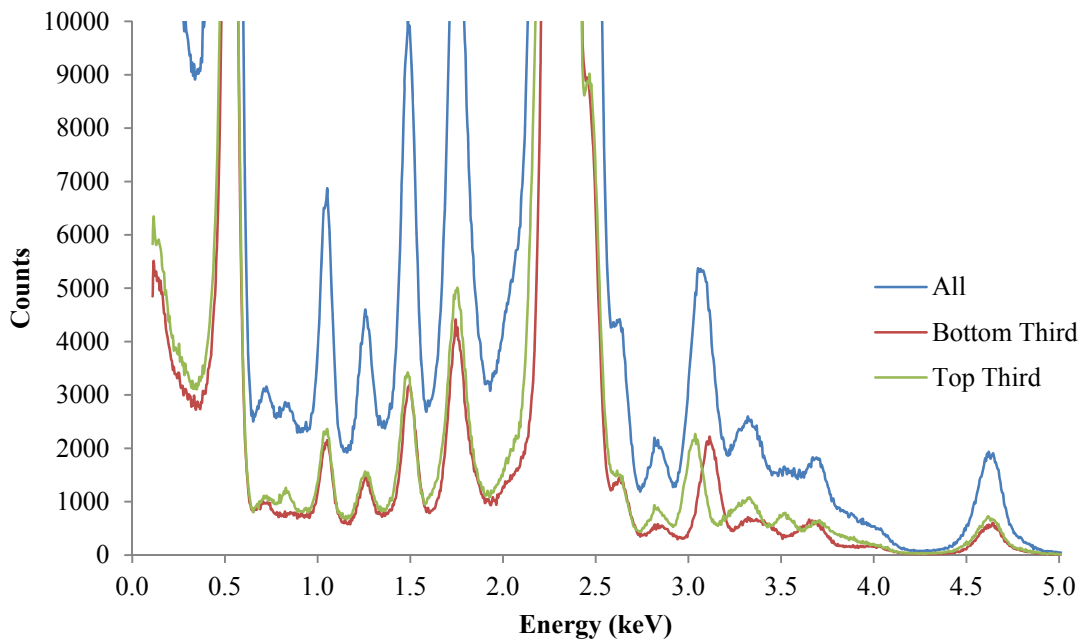


Figure B.40. WatchetC rock Ca-suppression dataset obtained using the pre-existing CCD facility as outlined in table 5.1.

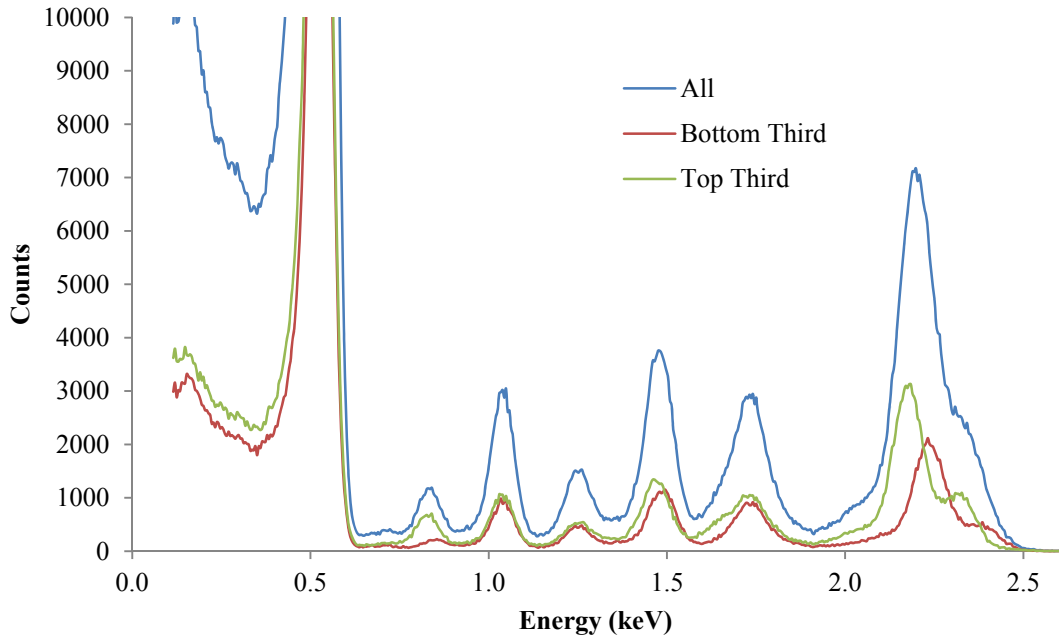


Figure B.41. WatchetC rock S-suppression dataset obtained using the pre-existing CCD facility as outlined in table 5.1.

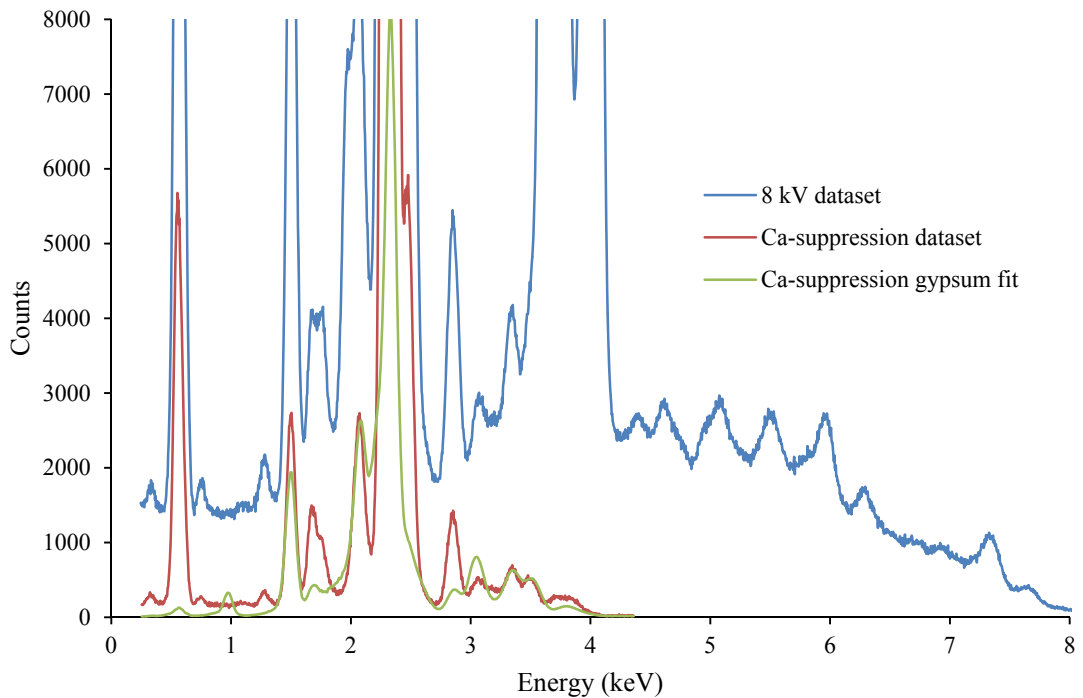


Figure B.42. WatchetC 8 kV and Ca-suppression rock datasets obtained using the bespoke SDD facility as outlined in table 5.1, compared to a Ca-suppression gypsum fit produced using the mineral fitting routine with data from Boeyens and Ichharam (2002).

B.14 Thackaringa

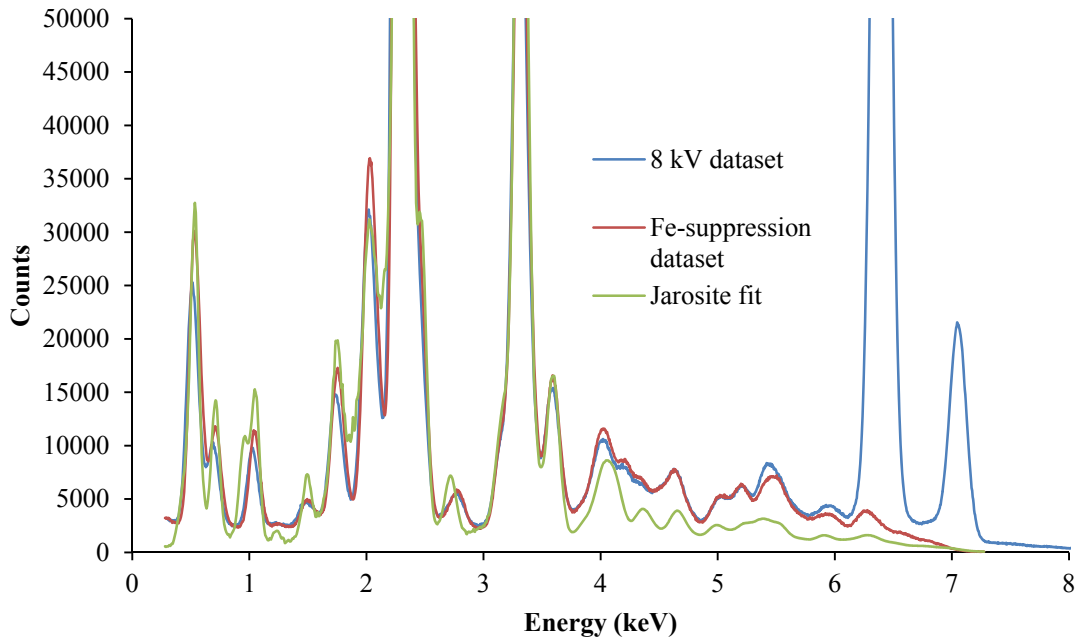


Figure B.43. Thackaringa 8 kV, Fe- and S-suppression rock datasets obtained using the bespoke SDD facility as outlined in table 5.1, compared to a Fe-suppression jarosite fit produced using the mineral fitting routine with data from Menchetti and Sabelli (1976).

B.15 Wave Hill

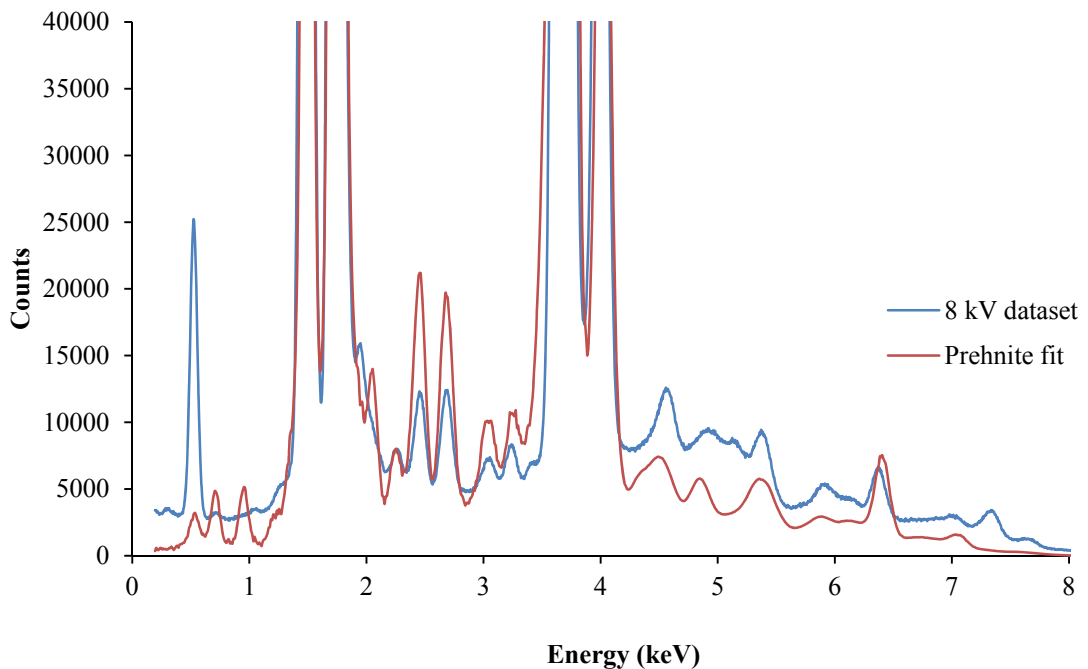


Figure B.44. Wave Hill 8 kV rock dataset obtained using the bespoke SDD facility as outlined in table 5.1, compared to a 8 kV prehnite fit produced using the mineral fitting routine with data from Detrie et al. (2009).

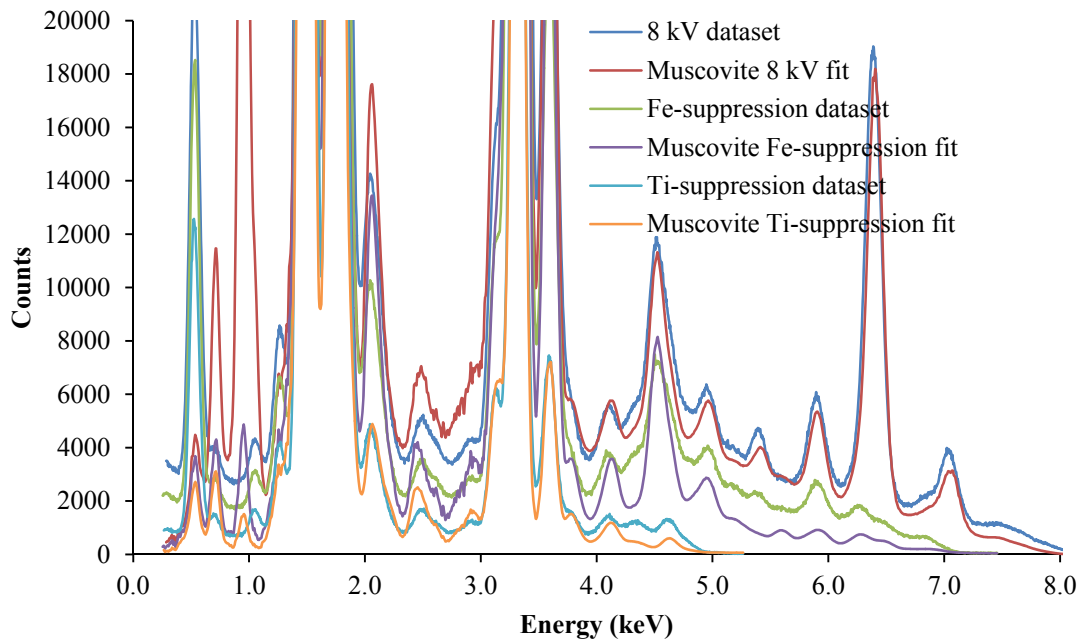
B.16 Mica

Figure B.45. Mica 8 kV, Fe-, Ti- and K-suppression pellet datasets obtained using the bespoke SDD facility as outlined in table 5.1, compared to muscovite fits produced using the mineral fitting routine with data from Rothbauer (1971).

Appendix C: High-Resolution Back-Reflection Energy-Dispersive X-ray Diffraction

This appendix details the diffraction peaks for the samples analysed in Chapter 6: High-Resolution Back-Reflection Energy-Dispersive X-ray Diffraction. For context please see the chapter and section referred to for each sample. In each table the experimental d -spacing, assigned Miller indices, calculated d -spacing from the fitted unit cell and a d -spacing difference between the experimental and calculated datasets are detailed.

C.1 Quartz

Table C.1 details the diffraction peaks for the quartz powder pellet sample shown in section 6.2.1 of this thesis.

Table C.1. Diffraction peaks identified from data shown in figure 6.3. The calculated d -spacings were determined using the fitted unit cell for quartz shown in table 6.1. The average absolute d -spacing difference was determined to be 0.000037.

Monochromator Energy (eV)	Experimental d -spacing (Å)	Miller Indices (hkl)	Calculated d -spacing (Å)	d -spacing difference (Å)
2525.134	2.457054	110	2.456939	0.000115
2719.724	2.281290	102	2.281342	-0.000052
2773.991	2.236670	111	2.236695	-0.000025
2915.955	2.127796	200	2.127772	0.000025
3133.83	1.979889	201	1.979879	0.000009
3412.899	1.818020	112	1.817944	0.000075
3711.431	1.671806	202	1.671787	0.000019
3739.878	1.659091	103	1.659097	-0.000006
3857.585	1.608474	210	1.608444	0.000030
4024.945	1.541601	211	1.541631	-0.000030
4270.702	1.452900	113	1.452895	0.000005
4373.935	1.418613	300	1.418514	0.000099
4489.286	1.382166	212	1.382165	0.000001
4512.895	1.374936	203	1.374968	-0.000032
4522.622	1.371980	301	1.372049	-0.000070
4817.916	1.287899	104	1.287880	0.000018
4940.354	1.255984	302	1.256006	-0.000022

C.2 Dolomite

Tables C.2 and C.3 detail the dolomite and calcite diffraction peaks for the JDo-1 pellet sample shown in section 6.2.2 of this thesis.

Table C.2. Dolomite diffraction peaks identified from data shown in figure 6.4. The calculated d -spacings were determined using the fitted unit cell for dolomite shown in table 6.2. The average absolute d -spacing difference was determined to be 0.000495.

Monochromator Energy (eV)	Experimental d-spacing (Å)	Miller Indices (hkl)	Calculated d-spacing (Å)	d-spacing difference (Å)
2146.601	2.890229	1 0 4	2.887929	0.002300
2321.196	2.672881	0 0 6	2.670375	0.002506
2441.199	2.541516	0 1 5	2.540324	0.001193
2578.414	2.406292	1 1 0	2.406136	0.000156
2827.347	2.194469	1 1 3	2.193776	0.000692
3001.999	2.066819	0 2 1	2.066372	0.000447
3076.321	2.016895	2 0 2	2.016670	0.000225
3355.841	1.848926	0 2 4	1.848593	0.000333
3436.945	1.805302	0 1 8	1.805155	0.000147
3471.328	1.787423	1 1 6	1.787535	-0.000110
3551.231	1.747212	2 0 5	1.746908	0.000304
3957.536	1.567856	2 1 1	1.567628	0.000228
4014.373	1.545660	1 2 2	1.545591	0.000069
4232.639	1.465964	2 1 4	1.465910	0.000054
4297.345	1.443893	2 0 8	1.443965	-0.000071
4335.389	1.431224	1 1 9	1.431122	0.000102
4388.783	1.413814	1 2 5	1.413628	0.000186
4466.76	1.389136	3 0 0	1.389183	-0.000047
4646.072	1.335529	0 0 12	1.335188	0.000341
4782.927	1.297319	2 1 7	1.297603	-0.000280
4887.538	1.269555	0 2 10	1.270162	-0.000610

Table C.3. Calcite diffraction peaks identified from data shown in figure 6.4. The calculated d -spacings were determined using the fitted unit cell for calcite shown in table 6.3. The average absolute d -spacing difference was determined to be 0.000611.

Monochromator Energy (eV)	Experimental d-spacing (Å)	Miller Indices (hkl)	Calculated d-spacing (Å)	d-spacing difference (Å)
2486.131	2.495593	1 1 0	2.494486	0.001107
2717.101	2.283492	1 1 3	2.284304	-0.000810
2964.198	2.093172	2 0 2	2.094149	-0.000980
3219.93	1.926955	0 2 4	1.927100	-0.000140
3244.776	1.912203	0 1 8	1.911978	0.000224
3309.627	1.874739	1 1 6	1.874994	-0.000250
3818.189	1.625068	2 1 1	1.625591	-0.000520
3866.58	1.604732	1 2 2	1.603886	0.000846

C.3 Siderite

Tables C.4 and C.5 detail the siderite and hematite diffraction peaks for the siderite powder pellet sample shown in section 6.2.3 of this thesis.

Table C.4. Siderite diffraction peaks identified from data shown in figure 6.5. The calculated d -spacings were determined using the fitted unit cell for siderite shown in table 6.4. The average absolute d -spacing difference was determined to be 0.000176.

Monochromator Energy (eV)	Experimental d-spacing (Å)	Miller Indices (hkl)	Calculated d-spacing (Å)	d-spacing difference (Å)
2233.533	2.777764	104	2.778116	-0.000352
2653.999	2.337775	110	2.337482	0.000293
2920.715	2.124329	113	2.124355	-0.000026
3170.694	1.956873	202	1.956765	0.000109
3468.836	1.788707	024	1.788595	0.000112
3591.815	1.727473	018	1.727088	0.000385
3603.719	1.721767	116	1.721875	-0.000108
4074.89	1.522708	211	1.522621	0.000087
4135.556	1.500374	122	1.500427	-0.000053
4341.441	1.429230	1 0 10	1.429280	-0.000050
4368.134	1.420497	214	1.420459	0.000037
4467.651	1.388859	208	1.389058	-0.000199
4516.906	1.373716	119	1.373460	0.000256
4533.597	1.368659	125	1.368223	0.000436
4598.425	1.349366	300	1.349546	-0.000180
4874.41	1.272974	0 0 12	1.273033	-0.000060
4953.402	1.252676	217	1.252920	-0.000245

Table C.5. Hematite diffraction peaks identified from data shown in figure 6.5. The calculated d -spacings were determined using the fitted unit cell for hematite shown in table 6. The average absolute d -spacing difference was determined to be 0.000639.

Monochromator Energy (eV)	Experimental d-spacing (Å)	Miller Indices (hkl)	Calculated d-spacing (Å)	d-spacing difference (Å)
3869.144	1.603669	018	1.603703	-0.000034
4259.946	1.456568	300	1.456224	0.000344
4716.513	1.315585	1 0 10	1.315262	0.000322
3656.015	1.697143	116	1.698998	-0.001855

C.4 Kaolinite

Table C.6 details the kaolinite diffraction peaks for the kaolin powder pellet sample shown in section 6.2.4 of this thesis.

Table C.6. Kaolinite diffraction peaks identified from data shown in figure 6.6. The calculated d -spacings were determined using the fitted unit cell for kaolinite shown in table 6.7. The average absolute d -spacing difference was determined to be 0.000257.

Monochromator Energy (eV)	Experimental d-spacing (Å)	Miller Indices (hkl)	Alternate Miller Indices (hkl)	Calculated d-spacing (Å)	d-spacing difference (Å)
2602.089	2.384403	003		2.384193	0.000210
2650.062	2.341247	2 0 -2	1 -3 1	2.342063	-0.000816
3115.368	1.991620	2 0 -3	1 -3 2	1.991324	0.000296
3469.754	1.788234	004		1.788145	0.000089
3728.217	1.664280	-2 4 0		1.664437	-0.000158
3829.275	1.620364	0 -5 2		1.620567	-0.000203
3913.396	1.585537	1 3 -4		1.586017	-0.000480
4024.154	1.541904	-1 3 4	2 -2 4 2 0 3 3 1 -3	1.541209	0.000695
4337.544	1.430513	005		1.430516	-0.000002
4629.256	1.340380	1 3 -5		1.340205	0.000175
4750.234	1.306247	1 -3 -5	2 0 4	1.306575	-0.000328
4830.599	1.284518	-4 0 2		1.284487	0.000031
4839.105	1.282260	0 -6 3		1.282158	0.000102
4982.882	1.245265	-2 6 2*		1.245282	-0.000017

*Estimate; was not used in unit-cell fit.

C.5 Mica

Tables C.7 and C.8 detail the mica and quartz diffraction peaks for the mica powder pellet sample shown in section 6.2.5 of this thesis.

Table C.7. Mica diffraction peaks identified from data shown in figure 6.7. The calculated d -spacings were determined using the fitted unit cell for mica shown in table 6.9. The average absolute d -spacing difference was determined to be 0.000345.

Monochromator Energy (eV)	Experimental d-spacing (Å)	Miller Indices (hkl)	Calculated d-spacing (Å)	d-spacing difference (Å)
2486.995	2.494726	0 0 8	2.493928	0.000798
2601.903	2.384573	133	2.384353	0.000220
3110.675	1.994624	0 0 10	1.995142	-0.000520
3584.46	1.731017	-1 3 9	1.731433	-0.000420
3731.833	1.662667	-2 0 10	1.662989	-0.000320
3763.742	1.648573	1 3 9	1.647608	0.000965
4069.091	1.524878	-1 3 11	1.524646	0.000232
4089.695	1.517196	1 1 12	1.517124	0.000072
4269.414	1.453338	0 2 13	1.453174	0.000164
4353.284	1.425342	0 0 14	1.425102	0.000240
4383.192	1.415617	1 1 13	1.415337	0.000280
4452.115	1.393705	-1 1 14	1.393700	0.000005
4587.225	1.35266	-1 3 13	1.352204	0.000455
4631.439	1.339748	2 0 12	1.339647	0.000101
4977.613	1.246583	0 0 16	1.246964	-0.000380

Table C.8. Quartz diffraction peaks identified from data shown in figure 6.7. The calculated d -spacings were determined using the fitted unit cell for quartz shown in table 6.10. The average absolute d -spacing difference was determined to be 0.000078.

Monochromator Energy (eV)	Experimental d-spacing (Å)	Miller Indices (hkl)	Calculated d-spacing (Å)	d-spacing difference (Å)
2773.729	2.236882	1 1 1	2.236757	0.000125
2915.992	2.127769	200	2.127767	0.000002
3413.056	1.817936	112	1.818083	-0.000150
3711.531	1.671761	2 0 2	1.671895	-0.000130
4025.044	1.541563	211	1.541649	-0.000087
4488.937	1.382274	212	1.382225	0.000048
4512.214	1.375144	203	1.375104	0.000039
4522.228	1.372099	301	1.372062	0.000037

C.6 Talc

Tables C.9 – C.11 detail the talc, magnesite and dolomite diffraction peaks for the mica powder pellet sample shown in section 6.2.6 of this thesis.

Table C.9. Talc diffraction peaks identified from data shown in figure 6.8. The calculated d -spacings were determined using the fitted unit cell for talc shown in table 6.12. The average absolute d -spacing difference was determined to be 0.000284.

Monochromator Energy (eV)	Experimental d -spacing (Å)	Miller Indices (hkl)	Calculated d -spacing (Å)	d -spacing difference (Å)
2258.74	2.746772	-1 1 3	2.746607	0.000164
2653.787	2.337961	0 0 4	2.337673	0.000288
3196.112	1.941313	2 -2 2	1.942662	-0.001350
3317.382	1.870357	0 0 5	1.870139	0.000219
3980.704	1.558732	0 0 6	1.558449	0.000283
4059.896	1.528331	0 6 0	1.528872	-0.000540
4117.501	1.506952	-3 -3 2	1.506832	0.000120
4279.477	1.449921	-3 -3 3	1.450385	-0.000460
4340.125	1.429663	2 4 3	1.429878	-0.000220
4474.246	1.386812	3 -3 2	1.386586	0.000226
4517.781	1.37345	-2 2 6	1.373304	0.000146
4645.824	1.3356	0 0 7	1.335813	-0.000210
4703.804	1.319139	-2 6 1	1.319592	-0.000450
4721.765	1.314122	-4 0 2	1.313945	0.000177
4787.227	1.296154	2 -6 1	1.296418	-0.000260
4876.121	1.272527	-1 7 0	1.271967	0.000560
4885.29	1.270139	1 7 0	1.269935	0.000204

Table C.10. Magnesite diffraction peaks identified from data shown in figure 6.8. The calculated d -spacings were determined using the fitted unit cell for magnesite shown in table 6.13. The average absolute d -spacing difference was determined to be 0.000473.

Monochromator Energy (eV)	Experimental d -spacing (Å)	Miller Indices (hkl)	Calculated d -spacing (Å)	d -spacing difference (Å)
2472.653	2.509193	0 0 6	2.510293	-0.001100
3641.882	1.703728	0 1 8	1.704019	-0.000290
4117.501	1.506952	2 1 1	1.506998	-0.000046
4402.614	1.409373	1 0 10	1.409876	-0.000500
4573.507	1.356717	1 1 9	1.355970	0.000747
4645.824	1.3356	3 0 0	1.335750	-0.000150

Table C.11. Dolomite diffraction peak energies identified from data shown in figure 6.8. The calculated d -spacings were determined using the fitted unit cell for dolomite shown in table 6.14. The average absolute d -spacing difference was determined to be 0.000720.

Monochromator Energy (eV)	Experimental d-spacing (Å)	Miller Indices (hkl)	Calculated d-spacing (Å)	d-spacing difference (Å)
2151.01	2.884307	1 0 4	2.884938	-0.000630
2324.596	2.668972	0 0 6	2.667885	0.001087
3098.183	2.002665	1 0 7	2.004256	-0.001590
3487.238	1.77927	0 0 9	1.778590	0.000679
3964.992	1.564908	1 2 -1	1.565832	-0.000920
4297.155	1.443957	2 0 8	1.442469	0.001488
4340.125	1.429663	1 1 -9	1.429679	-0.000016
4517.781	1.37345	0 1 11	1.373693	-0.000240
4653.32	1.333449	0 0 12	1.333943	-0.000490
4787.227	1.296154	1 2 -7	1.296203	-0.000049

Appendix D: Publications List

Published:

Hansford, G.M., Turner, S.M.R., Staab, D., and Vernon, D., 2014. The suppression of fluorescence peaks in energy-dispersive X-ray diffraction. *Journal of Applied Crystallography*, 47(5), 1708-1715.

<http://onlinelibrary.wiley.com/doi/10.1107/S160057671401927X/abstract>

Turner, S.M.R., Bridges, J.C., Grebby, S. and Ehlmann, B.L., 2016. Hydrothermal activity recorded in post Noachian-aged impact craters on Mars. *Journal of Geophysical Research: Planets*, 121(4), pp.608-625.

<http://onlinelibrary.wiley.com/doi/10.1002/2015JE004989/abstract>

Submitted for Publication:

Hansford, G.M., Turner, S.M.R., Degryse, P. and Shortland, A.J., 2017. High-resolution X-ray diffraction with no sample preparation. Submitted to *Acta Crystallographica Section A*.

Abstracts:

Turner, S.M.R., Bridges, J.C., and Grebby, S., 2013. CRISM investigations of impact craters in the Amazonis Planitia region of Mars. 3rd UK in Aurora Meeting.

http://www.ras.org.uk/images/stories/meetings/mars_abstracts_20130208.pdf

Turner, S.M.R., Hansford, G.M., Bridges, J.C., Ambrosi, R.M., and Vernon, D., 2013. A Study of Sulphate Minerals using a Novel X-Ray Diffraction Technique. Abstract #EPSC2013-379. European Planetary Science Congress 2013.

<http://meetingorganizer.copernicus.org/EPSC2013/EPSC2013-379-2.pdf>

Turner, S.M.R., Bridges, J.C., and Grebby, S., 2013. Near-Infrared CRISM Investigations of Amazonian Impact Craters on Mars: Comparisons to the Nakhlite Alteration Minerals. Abstract #EPSC2013-383. European Planetary Science Congress 2013.

<http://meetingorganizer.copernicus.org/EPSC2013/EPSC2013-383-1.pdf>

Williams, M., Bennel, K., Williams, H.R., Bridges, J.C., Ambrosi, R.M., Bannister, N.P., Turner, S., Sykes J., and Schroeven-Deceuninck, H., 2013. Autonomous Hopping Robotic Vehicle for Planetary Science and Exploration. Abstract #EPSC2013-464. European Planetary Science Congress 2013.

<http://meetingorganizer.copernicus.org/EPSC2013/EPSC2013-464.pdf>

Turner, S.M.R., Bridges, J.C., and Grebby, S., 2013. Near-Infrared CRISM Investigations of Hydrothermally Altered Amazonian Impact Craters on Mars. Status and Developments in Geological Remote Sensing, Geological Remote Sensing Group 2013.

Turner, S.M.R., Bridges, J.C., Grebby, S., and Ehlmann, B.L., 2014. CRISM Investigations of Amazonian-aged Impact Craters on Mars: Linking Impact Induced Hydrothermal Activity and the Nakhlite Martian Meteorites. Fermor Meeting 2014: Comparative Planetology.

Turner, S.M.R., Bridges, J.C., Grebby, S., and Ehlmann, B.L., 2014. Near Infrared CRISM Investigations of hydrothermally altered Amazonian Impact craters on Mars. 25 Years of Remote Sensing, Geological Remote Sensing Group Silver Anniversary Conference 2014.

Turner, S.M.R., Bridges, J.C., Grebby, S., and Ehlmann, B.L., 2015. Hydrothermal Minerals within Impact Craters in Amazonian-Aged Terrains on Mars. Abstract #2061. 46th Lunar and Planetary Science Conference.

<http://www.hou.usra.edu/meetings/lpsc2015/pdf/2061.pdf>

Turner, S.M.R., Hansford, G.M., and Bridges, J.C., 2015. A Study of Sulphate Minerals Using a Novel X-ray Diffraction Technique. Abstract #2222. 46th Lunar and Planetary Science Conference.

<http://www.hou.usra.edu/meetings/lpsc2015/pdf/2222.pdf>

Turner, S.M.R., Bridges, J.C., Grebby, S., and Ehlmann, B.L., 2015. Hydrothermal Minerals within Impact Craters in Amazonian-Aged Terrains on Mars. 4th UK in Aurora Meeting

<http://www2.le.ac.uk/departments/physics/people/johnbridges/aurorameeting>

Turner, S.M.R., Hansford, G.M., and Bridges, J.C., 2015. A Study of Sulphate Minerals Using a Novel X-ray Diffraction Technique. 4th UK in Aurora Meeting
<http://www2.le.ac.uk/departments/physics/people/johnbridges/aurorameeting>

Hansford, G.M., Turner, S.M.R., Karim, N., and Hall, J., 2015. Completely Non-Destructive High-Resolution XRD Analysis of Cultural Heritage Objects. Denver X-ray Conference, 64th Annual Conference on Applications of X-ray Analysis.
<http://www.dxcicdd.com/15/abstracts/S21.pdf>

McEwen, A., Chojnacki, M., Miyamoto, H., Hemmi, R., Weitz, C., Williams, R., Quantin, C., Flahaut, J., Wray, J., Turner, S., Bridges, J., Grebby, S., Leung, C., and Rafkin, S., 2015. Landing Site and Exploration Zone in Eastern Melas Chasma. p.1007. First Landing Site/Exploration Zone Workshop for Human Mission to the Surface of Mars.
<http://www.hou.usra.edu/meetings/explorationzone2015/pdf/1007.pdf>

Turner, S.M.R., Hansford, G.M., and Bridges, J.C., 2016. X-ray Diffraction on Unprepared Rock Samples: A Study of Sulphate Minerals. Abstract #2274. 47th Lunar and Planetary Science Conference.
<http://www.hou.usra.edu/meetings/lpsc2016/pdf/2274.pdf>

Turner, S.M.R., Bridges, J.C., Grebby, S., and Ehlmann, B.L., 2016. Hydrothermal Activity Recorded in Post Noachian-Aged Impact Craters on Mars. Abstract #2915. 47th Lunar and Planetary Science Conference.
<http://www.hou.usra.edu/meetings/lpsc2016/pdf/2915.pdf>

References

- Abramov, O., and Kring, D.A., 2005. Impact-induced hydrothermal activity on early Mars. *J. Geophys. Res.*, 110, E12S09. doi:10.1029/2005JE002453.
- Adams, J.B., 1975. Interpretation of visible and near-infrared diffuse reflectance spectra of pyroxenes and other rock-forming minerals. *Infrared Raman spectroscopy of lunar and terrestrial minerals*, pp.91-116.
- Albee, A.L., Palluconi, F.D. and Arvidson, R.E., 1998. Mars global surveyor mission: overview and status. *Science*, 279(5357), pp.1671-1672.
- Albee, A.L., Arvidson, R.E., Palluconi, F. and Thorpe, T., 2001. Overview of the Mars global surveyor mission. *Journal of Geophysical Research: Planets (1991–2012)*, 106(E10), pp.23291-23316.
- Allwood, A., Clark, B., Flannery, D., Hurowitz, J., Wade, L., Elam, T., Foote, M. and Knowles, E., 2015, March. Texture-specific elemental analysis of rocks and soils with PIXL: The Planetary Instrument for X-ray Lithochemistry on Mars 2020. In *2015 IEEE Aerospace Conference* (pp. 1-13). IEEE.
- American Mineralogist Crystal Structure Database, 2016. Available at: <http://rruff.geo.arizona.edu/AMS/amcsd.php> (last accessed 25th August 2016).
- Angel, R.J., Carpenter, M.A., and Finger, L.W., 1990. Structural variation associated with compositional variation and order-disorder behavior in anorthite-rich feldspars. *American Mineralogist*, 7(5), pp.150-162.
- Armbruster, T., Bürgi, H.B., Kunz, M., Gnos, E., Broenniman, S. and Lienert, C., 1990. Variation of displacement parameters in structure refinements of low albite. *American Mineralogist*, 75(1-2), pp.135-140.
- Arvidson, R.E., Squyres, S.W., Bell, J.F., Catalano, J.G., Clark, B.C., Crumpler, L.S., De Souza, P.A., Fairén, A.G., Farrand, W.H., Fox, V.K., Gellert, R., Ghosh, A.,

References

- Golombek, M.P., Grotzinger, J.P., Guinness, E.A., Herkenhoff, K.E., Jolliff, B.L., Knoll, A.H., Li, R., McLennan, S.M., Ming, D.W., Mittlefehldt, D.W., Moore, J.M., Morris, R.V., Murchie, S.L. Parker, T.J., Paulsen, G., Rice, J.W., Ruff, S.W., Smith, M.D. and Wolff, M.J., 2014. Ancient aqueous environments at Endeavour crater, Mars. *Science*, 343(6169), p.1248097.
- Ballirano, P., Maras, A., Meloni, S. and Caminiti, R., 2001. The monoclinic I2 structure of bassanite, calcium sulphate hemihydrate ($\text{CaSO}_4 \cdot 0.5 \text{H}_2\text{O}$). *European Journal of Mineralogy*, 13(5), pp.985-993.
- Barnhart, C.J., Nimmo, F., and Travis, B. J., 2010. Martian post-impact hydrothermal systems incorporating freezing. *Icarus*, 208, pp.101-117.
- Beegle, L., Bhartia, R., White, M., DeFlores, L., Abbey, W., Wu, Y.H., Cameron, B., Moore, J., Fries, M., Burton, A., Edgett, K.S., Ravine, M.A., Hug, W., Reid, R., Nelson, T., Clegg, S., Wiens, R., Asher, S., and Sobron P., 2015, March. SHERLOC: scanning habitable environments with raman & luminescence for organics & chemicals. In *2015 IEEE Aerospace Conference* (pp. 1-11). IEEE.
- Bergstrom, J. W., W. A. Delamere, and A. S. McEwen (2004), MRO High Resolution Imaging Science Experiment (HiRISE): Instrument test, calibration, and operating constraints, paper presented at 55th International Astronautical Federation Congress, Int. Astron. Congr., Vancouver, B.C., Canada.
- Bezou, C., Nonat, A., Mutin, J.C., Christensen, A.N. and Lehmann, M.S., 1995. Investigation of the crystal structure of $\gamma\text{-CaSO}_4$, $\text{CaSO}_4 \cdot 0.5 \text{H}_2\text{O}$, and $\text{CaSO}_4 \cdot 0.6 \text{H}_2\text{O}$ by powder diffraction methods. *Journal of Solid State Chemistry*, 117(1), pp.165-176.
- Bibring, J. -P., Langevin, Y., Mustard, J.F., Poulet, F., Arvidson, R., Gendrin, A., Gondet, B., Mangold, N., Pinet, P., Forget, F. and the OMEGA team, 2006. Global mineralogical and aqueous mars history derived from OMEGA/Mars Express data, *Science*, 312, pp.400-404, doi:10.1126/science.1122659.

References

- Binder, A.B., Arvidson, R.E., Guinness, E.A., Jones, K.L., Morris, E.C., Mutch, T.A., Pieri, D.C. and Sagan, C., 1977. The geology of the Viking Lander 1 site. *Journal of Geophysical Research*, 82(28), pp.4439-4451.
- Birle, J.D. and Tettenhorst, R., 1968. Refined muscovite structure. *Mineralogical Magazine*, 36(282), pp.883-886.
- Bish, D.L. and Von Dreele, R.B., 1989. Rietveld refinement of non-hydrogen atomic positions in kaolinite. *Clays and Clay Minerals*, 37(4), pp.289-296.
- Bish, D.L., Blake, D.F., Vaniman, D.T., Chipera, S.J., Morris, R.V., Ming, D.W., Treiman, A.H., Sarrazin, P., Morrison, S.M., Downs, R.T., Achilles, C.N., Yen A.S., Bristow, T.F., Crisp, J.A., Morookian, J.M., Farmer, J.D., Rampe, E.B., Stolper, E.M., Spanovich, N. and MSL Science Team, 2013. X-ray diffraction results from Mars Science Laboratory: Mineralogy of Rocknest at Gale crater. *Science*, 341(6153), p.1238932.
- Bish, D., Blake, D., Vaniman, D., Sarrazin, P., Bristow, T., Achilles, C., Dera, P., Chipera, S., Crisp, J., Downs, R.T., Farmer, J., Gailhanou, M., Ming, D., Morookian, J.M., Morris, R., Morrison, S., Rampe, E., Treiman, A. and Yen, A., 2014. The first X-ray diffraction measurements on Mars. *IUCrJ*, 1, pp.514-522, doi:10.1107/S2052252514021150.
- Bishop, J., Madejova, J., Komadel, P. and Froschl, H., 2002a. The influence of structural Fe, Al, and Mg on the infrared OH bands in spectra of dioctahedral smectites, *Clay Miner.*, 37, pp.607-616, doi:10.1180/0009855023740063.
- Bishop, J. L., Murad, E., and Dyar, M.D., 2002b. The influence of octahedral and tetrahedral cation substitution on the structure of smectites and serpentines as observed through infrared spectroscopy, *Clay Miner.*, 37, pp.617-628, doi:10.1180/0009855023740064.

References

- Bishop, J.L., Lane, M.D., Dyar, M.D. and Brown, A.J., 2008. Reflectance and emission spectroscopy of four groups of phyllosilicates: Smectites, kaolinite-serpentines, chlorites, and micas, *Clay Miner.*, *43*, pp.35-54, doi:10.1180/claymin.2008.043.1.03.
- Blake, D. F., 2000. Remote X-ray Diffraction and X-ray Fluorescence analysis on planetary surfaces. *Advances in X-ray Analysis*, *43*, pp.487-496.
- Blake, D., Vaniman, D., Achilles, C., Anderson, R., Bish, D., Bristow, T., Chen, C., Chipera, S., Crisp, J., Des Marais, D., Downs, R.T., Farmer, J., Feldman, S., Fonda, M., Gailhanou, M., Ma, H., Ming, D.W., Morris, R.V., Sarrazin, P., Stolper, E., Treiman, A., and Yen, A., 2012. Characterization and Calibration of the CheMin Instrument on Mars Science Laboratory. *Space Science Reviews*, *170*(1-4), pp.341-399.
doi:10.1007/s11214-012-9905-1
- Blake, R.L., Hessevick, R.E., Zoltai, T. and Finger, L.W., 1966. Refinement of hematite structure. *American Mineralogist*, *51*(1-2), p.123.
- Boeyens, J.C.A. and Ichharam, V.V.H., 2002. Redetermination of the crystal structure of calcium sulphate dihydrate, $\text{CaSO}_4 \cdot 2\text{H}_2\text{O}$. *Zeitschrift für Kristallographie-New Crystal Structures*, *217*(JG), pp.9-10.
- Bragg, W.L., 1913. The Diffraction of Short Electromagnetic Waves by a Crystal. *Proceedings of the Cambridge Philosophical Society* **17**, pp.43–57.
- Bridges, J.C. and Grady, M.M., 2000. Evaporite mineral assemblages in the nakhlite (martian) meteorites. *Earth and Planetary Science Letters*, *176*(3), pp.267-279.
- Bridges, J.C. and Schwenzer, S.P., 2012. The nakhlite hydrothermal brine on Mars. *Earth Planet. Sci. Lett.* *359-360*, pp.117-123.
- Bridges, J.C., Schwenzer, S.P., Leveille, R., Westall, F., Wiens, R. C., Mangold, N., Bristow, T., Edwards, P. and Berger, G., 2015. Diagenesis and clay mineral formation at Gale Crater, Mars, *J. Geophys. Res. Planets*, *120*, pp.1-19,
doi:10.1002/2014JE004757.

References

- Brigatti, M.F., Frigieri, P. and Poppi, L., 1998. Crystal chemistry of Mg-, Fe-bearing muscovites-2M1. *American Mineralogist*, 83(7-8), pp.775-785.
- Buchsteiner, A. and Stüsser, N., 2009. Optimizations in angular dispersive neutron powder diffraction using divergent beam geometries. *Nuclear Instruments and Methods in Physics Research Section A: Accelerators, Spectrometers, Detectors and Associated Equipment*, 598(2), pp.534-541.
- Bultel, B., Quantin-Nataf, C., Andréani, M., Clénet, H. and Lozac'h, L., 2015. Deep alteration between Hellas and Isidis Basins, *Icarus*, 260, pp.141-160, doi:10.1016/j.icarus.2015.06.037.
- Buras, B., Chwaszczewska, J., Szarras, S. and Szmid, Z., 1968. Fixed angle scattering (FAS) method for X-ray crystal structure analysis. Report 894/II/PS, Institute of Nuclear Research, Warsaw.
- Burns, R. G., 1970. Mineralogical applications of crystal field theory, Cambridge University Press, London.
- Burns, R. G., 1993. Origin of electronic spectra of minerals in the visible to near-infrared region. in: C. M. Pieters, P. A. J. Englert, (Eds.), Remote Geochemical Analysis: Elemental and Mineralogical Composition. Cambridge University Press, New York, 3-29.
- Carr, M.H., 1996. *Water on Mars*. Oxford University Press, New York, USA.
- Carr, M.H., 2006. *The surface of Mars*. Cambridge University Press, Cambridge, UK.
- Carbone, M., Ballirano, P. and Caminiti, R., 2008. Kinetics of gypsum dehydration at reduced pressure: an energy dispersive X-ray diffraction study. *European Journal of Mineralogy*, 20(4), pp.621-627.
- Carter, J. and Poulet, F., 2012. Orbital identification of clays and carbonates in Gusev crater, *Icarus*, 219, pp.250-253, doi: 10.1016/j. icarus.2012.02.024.

References

- Carter, J., Poulet, F., Bibring, J.-P. and Murchie, S., 2010. Detection of hydrated silicates in crustal outcrops in the northern plains of Mars, *Science*, 328, 1682, doi:10.1126/science.1189013.
- Carter, J., Poulet, F., Bibring, J.-P., Mangold, N., and Murchie, S., 2013. Hydrous minerals on Mars as seen by the CRISM and OMEGA imaging spectrometers: Updated global view, *J. Geophys. Res. Planets*, 118, pp.831-858, doi: 10.1029/2012JE004145.
- Carter, J., Quantin, C., Thollot, P., Loizeau, D., Ody, A., and Lozach, L., 2016. Oxia Planum, a Clay-laden Landing Site Proposed for the ExoMars Rover Mission: Aqueous Mineralogy and Alteration Scenarios. In *Lunar and Planetary Science Conference* (Vol. 47, p. 2064).
- Changela, H.G. and Bridges, J.C., 2010. Alteration assemblages in the nakhlites: Variation with depth on Mars, *Meteorit. Planet. Sci.*, 45, pp.1847-1867.
- Chevrier, V., & Mathé, P. E., 2007. Mineralogy and evolution of the surface of Mars: A review. *Planetary and Space Science*, 55(3), pp.289-314.
- Christensen, P.R. and Moore, H.J., 1992. *The Martian Surface Layer*, MARS, edited by Kieffer, H.H., Univ. Arizona Press, Tucson, pp. 686-729
- Christensen, P.R., Bandfield, J.L., Bell III, J.F., Gorelick, N., Hamilton, V.E., Ivanov, A., Jakosky, B.M., Kieffer, H.H., Lane, M.D., Malin, M.C. and McConnochie, T., McEwen, A.S., McSween Jr, H.Y., Mehall, G.L., Moersch, J.E., Neelson, K.H., Rice Jr, J.W., Richardson, M.I., Ruff, S.W., Smith, M.D., Titus, T.N. and Wyatt, M.B., 2003. Morphology and composition of the surface of Mars: Mars Odyssey THEMIS results. *Science*, 300(5628), pp.2056-2061.
- Cibin, G., 2014. Back-reflection experiment schematic at the Diamond Light Source. Email received 9th December 2014.
- Clark, R. N., Gallagher, A. J., And Swayze, G. A., 1990: Material absorption band depth mapping of imaging spectrometer data using the complete band shape least-

squares algorithm simultaneously fit to multiple spectral features from multiple materials. In: Proceedings of the Third Airborne Visible/Infrared Imaging Spectrometer (AVIRIS) Workshop, JPL Publication 90-54, pp. 176-186.

Clark, B.C., Morris, R.V., McLennan, S.M., Gellert, R., Jolliff, B., Knoll, A.H., Squyres, S.W., Lowenstein, T.K., Ming, D.W., Tosca, N.J., Yen, A., Christensen, P.R., Gorevan, S., Brückner, J., Calvin, W., Dreibus, G., Farrand, W., Klingelhofer, G., Waenke, H., Zipfel, J., Bell III, J.F., Grotzinger, J., McSween, H.Y. and Rieder, R., 2005. Chemistry and mineralogy of outcrops at Meridiani Planum. *Earth and Planetary Science Letters*, 240(1), pp.73-94.

Clark, R.N., Swayze, G.A., Wise, R., Livo, K.E., Hoefen, T.M., Kokaly, R.F. and Sutley, S.J., 2007. USGS Digital Spectral Library splib06a, U.S. Geol. Surv. Data, 231.

Clark, R. N., 1999. Chapter 1: Spectroscopy of Rocks and Minerals, and Principles of Spectroscopy, in *Manual of Remote Sensing, Volume 3, Remote Sensing for the Earth Sciences*, (A.N. Rencz, ed.) John Wiley and Sons, New York, p 3- 58.

Clegg, S.M., Wiens, R.C., Maurice, S., Gasnault, O., Sharma, S.K., Misra, A.K., Newell, R., Forni, O., Lasue, J., Anderson, R.B. and Nowak-Lovato, K.L., Fouchet, T., Angel, S.M., Rull, F., Johnson, J.R., and the SuperCam Science Team, 2015. Remote geochemical and mineralogical analysis with supercam for the Mars 2020 rover. In *Lunar and Planetary Science Conference* (Vol. 46, p. 2781).

Cloutis, E.A., Hawthorne, F.C., Mertzman, S.A., Krenn, K., Craig, M.A., Marcino, D., Methot, M., Strong, J., Mustard, J.F., Blaney, D.L., Bell, J.F.I. and Vilas, F., 2006. Detection and discrimination of sulfate minerals using reflectance spectroscopy, *Icarus*, 184, pp.121-157, doi:10.1016/j. icarus.2006.04.003.

Cockell, C.S., Balme, M., Bridges, J.C., Davila, A. and Schwenzer, S.P., 2012. Uninhabited habitats on Mars, *Icarus*, 217, pp.184-193, doi:10.1016/j.icarus.2011.10.025.

References

- Collins, D.R. and Catlow, C.R.A., 1991. Energy-minimized hydrogen-atom positions of kaolinite. *Acta Crystallographica Section B: Structural Science*, 47(5), pp.678-682.
- Cook, E.J., Pani, S., George, L., Hardwick, S., Horrocks, J.A., and Speller, R.D., 2009. Multivariate Data Analysis for Drug Identification Using Energy-Dispersive X-ray Diffraction. *IEEE Transactions on Nuclear Science*, 56(3), pp.1459-1464.
- Cullity, B. D., and Stock, S. R., 2001. *Elements of X-ray Diffraction* (third edition). Upper Saddle River, NJ: Prentice hall.
- Daubar, I.J. and Kring, D.A., 2001. Impact-induced hydrothermal systems: Heat sources and lifetimes. In *Lunar and Planetary Science Conference* (Vol. 32, p. 1727).
- Deer, W.A., Howie, R.A. and Zussman, J., 1992. An introduction to the rock-forming minerals (Vol. 696). London: Longman.
- Detrie, T.A., Ross, N.L., Angel, R.J. and Gatta, G., 2009. Equation of state and structure of prehnite to 9.8 GPa. *European Journal of Mineralogy*, 21(3), pp.561-570.
- Diamond, 2016. Diamond Light Source Ltd. Available at: <http://www.diamond.ac.uk/Home.html> (Accessed 1st June 2016).
- Dickson, J.L., Head, J.W. and Kreslavsky, M., 2007. Martian gullies in the southern mid-latitudes of Mars: Evidence for climate-controlled formation of young fluvial features based upon local and global topography, *Icarus*, 188(2), pp.315-323.
- Dollase, W.A., 1986. Correction of intensities for preferred orientation in powder diffractometry: application of the March model. *Journal of Applied Crystallography*, 19(4), pp.267-272.
- Dyar, M.D., Gunter, M.E., and Tasa, D., 2007. *Mineralogy and Optical Mineralogy*. Mineralogical Society of America, Chantilly, Virginia, USA.

References

- Eckert, M., 2012. Max von Laue and the discovery of X-ray diffraction in 1912. *Annalen der Physik*, 524(5), pp.A83-A85. doi:10.1002/andp.201200724
- Edwards, H.G., Hutchinson, I. and Ingley, R., 2012. The ExoMars Raman spectrometer and the identification of biogeological spectroscopic signatures using a flight-like prototype. *Analytical and bioanalytical chemistry*, 404(6-7), pp.1723-1731.
- Effenberger, H., Mereiter, K. and Zemmann, J., 1981. Crystal structure refinements of magnesite, calcite, rhodochrosite, siderite, smithonite, and dolomite, with discussion of some aspects of the stereochemistry of calcite type carbonates. *Zeitschrift für Kristallographie-Crystalline Materials*, 156(1-4), pp.233-244.
- Ehlmann, B.L. and Edwards, C.S., 2014. Mineralogy of the Martian Surface. *Annu. Rev. Earth Planet. Sci.*, 42, 291-315, doi:10.1146/annurev-earth-060313-055024.
- Ehlmann, B.L., Mustard, J.F., Clark, R.N., Swayze, G.A. and Murchie, S.L., 2011a. Evidence for low-grade metamorphism, hydrothermal alteration, and diagenesis on Mars from phyllosilicate mineral assemblages, *Clays Clay Miner.*, 590(4), pp.359-377, doi:10.1346/CCMN.2011.0590402.
- Ehlmann, B.L., Mustard, J.F., Murchie, S.L., Bibring, J.-P., Meunier, A., Fraeman, A.A. and Langevin, Y., 2011b. Subsurface water and clay mineral formation during the early history of Mars, *Nature*, 479, 53-60, doi:10.1038/nature10582.
- Ehlmann, B.L., Mustard, J.F., Murchie, S.L., Poulet, F., Bishop, J.L., Brown, A.J., Calvin, W.M., Clark, R.N., Des Marais, D.J., Milliken, R.E., Roach, L.H., Roush, T.L., Swayze, G.A. and Wray, J.J., 2008., Orbital identification of carbonate-bearing rocks on Mars, *Science*, 322, pp.1828-1832, doi:10.1126/science.1164759.
- Ehlmann, B.L., Mustard, J.F., Swayze, G.A., Clark, R.N., Bishop, J.L., Poulet, F., Des Marais, D.J., Roach, L.H., Milliken, R.E., Wray, J.J., Barnouin-Jha, O. and Murchie, S.L., 2009. Identification of hydrated silicate minerals on Mars using MRO-CRISM: Geologic context near Nili Fossae and implications for aqueous alteration, *J. Geophys. Res.*, 114, E00D08, doi:10.1029/2009JE003339.

References

- ESA, 2015. Four Candidate Landing Sites for ExoMars 2018. Available at: <http://exploration.esa.int/mars/54708-four-candidate-landing-sites-for-exomars-2018/> (Accessed 15th August 2016).
- ESA, 2016a. ExoMars TGO reaches Mars orbit while EDM Situation under assessment. Available at: http://www.esa.int/Our_Activities/Space_Science/ExoMars/ExoMars_TGO_reaches_Mars_orbit_while_EDM_situation_under_assessment (Accessed 15th February 2017).
- ESA, 2016b. Schiaparelli crash site in colour. Available at: http://www.esa.int/Our_Activities/Space_Science/ExoMars/Schiaparelli_crash_site_in_colour (Accessed 15th February 2017).
- ESA, 2016c. The ExoMars Programme 2016-2020. Available at: <http://exploration.esa.int/mars/46048-programme-overview/> (Accessed 25th August 2016).
- Facchinelli, A., Bruno, E. and Chiari, G., 1979. The structure of bytownite quenched from 1723 K. *Acta Crystallographica Section B: Structural Crystallography and Crystal Chemistry*, 35(1), pp.34-42.
- Filiberto, J. and Schwenzer, S.P., 2013. Alteration mineralogy of Home Plate and Columbia Hills-Formation conditions in context to impact, volcanism, and fluvial activity, *Meteorit. Planet. Sci.*, 48, pp.1937-1957, doi:10.1111/maps.12207.
- FitzGerald, J.D., Parise, J.B. and MacKinnon, I.D., 1986. Average structure of an An₄₈ plagioclase from the Hogarth Ranges. *American Mineralogist*, 71(11-12), pp.1399-1408.
- Friedrich, W. and Knipping, P., 1952. Experimenteller Teil. *Naturwissenschaften*, 39(16), pp.364-368. doi:10.1007/BF00646958

Gaffey, S.J., 1987. Spectral reflectance of carbonate minerals in the visible and near infrared (0.35–2.55 μm): Anhydrous carbonate minerals, *J. Geophys. Res.*, 92, pp.1429-1440, doi:10.1029/JB092iB02p01429.

Gatta, G.D., Merlini, M., Valdrè, G., Liermann, H.P., Nénert, G., Rothkirch, A., Kahlenberg, V. and Pavese, A., 2013. On the crystal structure and compressional behavior of talc: a mineral of interest in petrology and material science. *Physics and Chemistry of Minerals*, 40(2), pp.145-156.

Gatti, E., and Rehak, P., 1984. Semiconductor drift chamber-An application of a novel charge transport scheme. *Nuclear Instruments and Methods in Physics Research*, 225(3), pp.608-614.

Giessen, B.C., and Gordon, G.E., 1968. X-ray diffraction: new high-speed technique based on X-ray spectrography. *Science*, 159(3818), pp.973-975.

Girolami, G.S., 2016. *X-ray Crystallography* (first edition). University Science Books, Mill Valley, California.

Golombek, M.P., Grant, J.A., Farley, K.A., Willford, K., Chen, A., Otero, R.E., and Ashley, J.W., 2016. Downselection of Landing Sites Proposed for the Mars 2020 Rover Mission. In Lunar and Planetary Science Conference (Vol. 47, p. 2324).

Gooding, J.L., Wentworth, S.J. and Zolensky, M.E., 1991. Aqueous alteration of the Nakhla meteorite, *Meteoritics*, 26, pp.135-143, doi:10.1111/j.1945-5100.1991.tb01029.x.

Grant, J.A., Irwin, R.P., Grotzinger, J.P., Milliken, R.E., Tornabene, L.L., McEwen, A.S., Weitz, C.M., Squyres, S.W., Glotch, T.D. and Thomson, B.J., 2008. HiRISE imaging of impact megabreccia and sub-meter aqueous strata in Holden Crater, Mars. *Geology*, 36(3), pp.195-198.

Grebby, S.R., 2011. *Novel applications of airborne LiDAR and multispectral data for high-resolution geological mapping of vegetated ophiolitic rock and sedimentary cover*,

Troodos Range, Cyprus. PhD Thesis, University of Leicester. Available at: <https://lra.le.ac.uk/handle/2381/9697> (Accessed 15th August 2016).

Gross, C., Wendt, L., Combe, J.-P., Jodlowski, P., Marzo, G.A., Roush, T.L., McCord, T., Halbach, P. and Neukum, G., 2012. Investigating the phyllosilicate bearing Micoud crater in the northern plains of Mars. In Lunar and Planetary Science Conference (Vol. 43, p. 1795).

Gross, C., Poulet, F., Michalski, J., Horgan, B., and Bishop, J.L., 2016. Mawrth Vallis – Proposed Landing Site for ExoMars 2018/2020. In Lunar and Planetary Science Conference (Vol. 47, p. 1421).

Grotzinger, J.P., Sumner, D.Y., Kah, L.C., Stack, K., Gupta, S., Edgar, L., Rubin, D., Lewis, K., Schieber, J., Mangold, N., Milliken, R., Conrad, P.G., DesMarais, D., Farmer, J., Siebach, K., Calef III, F., Hurowitz, J., McLennan, S.M., Ming, D., Vaniman, D., Crisp, J., Vasavada, A., Edgett, K.S., Malin, M., Blake, D., Gellert, R., Mahaffy, P., Wiens, R.C., Maurice, S., Grant, J.A., Wilson, S., Anderson, R.C., Beegle, L., Arvidson, R., Hallet, B., Sletten, R.S., Rice, M., Bell III, J., Griffes, J., Ehlmann, B., Anderson, R.B., Bristow, T.F., Dietrich, W.E., Dromart, G., Eigenbrode, J., Fraeman, A., Hardgrove, C., Herkenhoff, K., Jandura, L., Kocurek, G., Lee, S., Leshin, L.A., Leveille, R., Limonadi, D., Maki, J., McCloskey, S., Meyer, M., Minitti, M., Newsom, H., Oehler, D., Okon, A., Palucis, M., Parker, T., Rowland, S., Schmidt, M., Squyres, S., Steele, A., Stopler, E., Summons, R., Treiman, A., Williams, R., Yingst, A. and MSL Science Team, 2014. A habitable fluvio-lacustrine environment at Yellowknife Bay, Gale Crater, Mars. *Science*, 343(6169), p.1242777.

Hamilton, V.E., Christensen, P.R. and McSween, H.Y., 1997. Determination of Martian meteorite lithologies and mineralogies using vibrational spectroscopy, *J. Geophys. Res.*, 102(E11), pp.25593-25603, doi:10.1029/97JE01874.

Haidon, C., 2013. University of Leicester, Department of Geology Watchet Bay X-ray diffraction sample analysis. Email received 5th June 2013.

Hansford, G.M., 2009. PoDFluX: A new Monte Carlo ray-tracing model for powder diffraction and fluorescence. *Review of Scientific Instruments*, 80(7), pp.073903.

Hansford, G.M., 2011a. Back-reflection energy-dispersive X-ray diffraction: a novel diffraction technique with almost complete insensitivity to sample morphology. *Journal of Applied Crystallography*, 44(3), pp.514-525.

Hansford, G.M., 2011b. Optimization of a simple X-ray diffraction instrument for portable and planetary applications. *Nuclear Instruments and Methods in Physics Research Section A: Accelerators, Spectrometers, Detectors and Associated Equipment*, 632(1), pp.81-88.

Hansford, G.M., 2012. Further optimisation of a simple X-ray diffraction instrument for portable and planetary applications. *Nuclear Instruments and Methods in Physics Research Section A: Accelerators, Spectrometers, Detectors and Associated Equipment*, 690, pp.117-124.

Hansford, G.M., 2013. X-ray diffraction without sample preparation: Proof-of-principle experiments. *Nuclear Instruments and Methods in Physics Research Section A: Accelerators, Spectrometers, Detectors and Associated Equipment*, 728, pp.102-106.

Hansford, G.M., Turner, S.M.R., Staab, D., and Vernon, D., 2014. The suppression of fluorescence peaks in energy-dispersive X-ray diffraction. *Journal of Applied Crystallography*, 47(5), pp.1708-1715.

Hansford, G.M., 2015. PoDFast and the mineral-fitting routine. Email received 8th October 2015.

Hansford, G.M., 2016a. Diamond Peak fitting IDL program. Email received 12th May 2016.

Hansford, G.M., 2016b. Laboratory-based high-resolution back-reflection X-ray diffraction facility. Email received 10th August 2016.

References

- Hansford, G.M., Turner, S.M.R., Degryse, P. and Shortland, A.J., 2017. High-resolution X-ray diffraction with no sample preparation. Submitted to *Acta Crystallographica Section A*.
- Hartmann, W.K. and Raper, O., 1974. The New Mars: The Discoveries of Mariner 9. *NASA Special Publication*, 337.
- Hartmann, W.K. and Neukum, G., 2001 Cratering chronology and the evolution of Mars. *Space Science Reviews*, 96, pp.165-194.
- He, B.B., 2011. *Two-dimensional X-ray Diffraction*. John Wiley & Sons, Hoboken: NJ, USA.
- Head, J.N., Melosh, H.J. and Ivanov, B.A., 2002. Martian meteorite launch: High-speed ejecta from small craters, *Science*, 298(5599), pp.1752-1756.
- Heldmann, J.L. and Mellon, M.T., 2004. Observations of Martian gullies and constraints on potential formation mechanisms, *Icarus*, 168(2), pp.285-304.
- Heldmann, J.L., Carlsson, E., Johansson, H., Mellon, M.T. and Toon, O.B., 2007. Observations of Martian gullies and constraints on potential formation mechanisms: II. The northern hemisphere, *Icarus*, 188(2), pp.324-344.
- Henke, B.L., Gullikson, E.M. and Davis, J.C., 1993. X-ray interactions: photoabsorption, scattering, transmission, and reflection at E= 50-30,000 eV, Z= 1-92. *Atomic data and nuclear data tables*, 54(2), pp.181-342.
- Hicks, L.J., Bridges, J.C. and Gurman, S.J., 2014. Ferric saponite and serpentine in the nakhlite martian meteorites. *Geochim. Cosmochim. Acta*, 136, pp.194-210, doi:10.1016/j.gca.2014.04.010.
- Hill, K.S., Hansford, G.M., Vernon, D., Talboys, D.L., Ambrosi, R.M., Bridges, J.C., and Hutchinson, I.B., 2011. The Mars-XRD Instrument for ExoMars: Combined X-ray

References

- Diffraction and Fluorescence Measurements. In Lunar and Planetary Science Conference (Vol. 42, p. 2107).
- Hunt, G. R., 1977. Spectral Signatures of Particulate Minerals in the Visible and Near Infrared. *Geophysics* 42, 3, 501-513.
- Imperial College London, 2016. Feldspar. Available at:
<https://wwwf.imperial.ac.uk/earthscienceandengineering/rocklibrary/viewminrecord.php?mineral=feldspar> (Accessed 23rd August 2016).
- Jenkins, R., 1999. *X-Ray Fluorescence Spectrometry* (second edition), John Wiley & Sons, New York, USA.
- Johns Hopkins University, 2013. An Illustrated Guide to CRISM Observing Modes. Available at:
http://crism.jhuapl.edu/instrument/images/observing_modes_poster_v5.pdf (Accessed 16th June 2016).
- Kämpfe, B., Luczak, F., and Michel, B., 2005. Energy Dispersive X-Ray Dffraction. *Particle & Particle Systems Characterization*, 22(6), pp.391-396.
doi:10.1003/ppsc.200501007
- Keefer, K.D. and Brown, G.E., 1978. Crystal structures and compositions of sanidine and high albite in cryptoperthitic intergrowth. *American Mineralogist*, 63(11-12), pp.1264-1273.
- Keller, L., and McCarthy, G., 1985. North Dakota State Univ., Fargo, ND, USA. ICDD Grant-in-Aid.
- Kihara, K., 1990. An X-ray study of the temperature dependence of the quartz structure. *European Journal of Mineralogy*, pp.63-78.
- Klingelhöfer, G., Morris, R.V., Bernhardt, B., Schröder, C., Rodionov, D.S., De Souza, P.A., Yen, A., Gellert, R., Evlanov, E.N., Zubkov, B., Foh, J., Bonnes, U., Kankeleit, S.M.R. Turner PhD Thesis

References

- E., Gütllich, P., Ming, D.W., Renz, F., Wdowiak, T., Squyres, S.W. and Arvidson, R.E., 2004. Jarosite and hematite at Meridiani Planum from Opportunity's Mössbauer spectrometer. *Science*, 306(5702), pp.1740-1745.
- Klingelhöfer, G., DeGrave, E., Morris, R.V., Van Alboom, A., de Resende, V.G., De Souza Jr, P.A., Rodionov, D., Schröder, C., Ming, D.W., and Yen, A., 2006. Mössbauer spectroscopy on Mars: goethite in the Columbia Hills at Gusev crater. *Hyperfine Interactions*, 166(1), pp.549-554, doi: 10.1007/s10751-006-9329-y.
- Korochantseva, E.V., Schwenzer, S.P., Buikin, A.I., Hopp, J., Ott, U. and Trieloff, M., 2011. ⁴⁰Ar-³⁹Ar and cosmic-ray exposure ages of nakhlites—Nakhla, Lafayette, Governador Valadares—and Chassigny. *Meteoritics & Planetary Science*, 46(9), pp.1397-1417.
- Kruse, F.A. and Perry, S.L., 2013. Mineral mapping using simulated Worldview-3 short-wave-infrared imagery. *Remote Sensing*, 5(6), pp.2688-2703.
- Langevin, Y., Bibring, J.P., Montmessin, F., Forget, F., Vincendon, M., Douté, S., Poulet, F. and Gondet, B., 2007. Observations of the south seasonal cap of Mars during recession in 2004–2006 by the OMEGA visible/near-infrared imaging spectrometer on board Mars Express. *Journal of Geophysical Research: Planets*, 112(E8).
- Larsson, A.K. and Christy, A.G., 2008. On twinning and microstructures in calcite and dolomite. *American Mineralogist*, 93(1), pp.103-113.
- Laue, M., 1952a. Eine quantitative Prüfung der Theorie für die Interferenz-Erscheinungen bei Röntgenstrahlen. *Naturwissenschaften*, 39(16), pp.368-372. doi:10.1007/646959
- Laue, M., 1952b. Theoretischer Teil. *Naturwissenschaften*, 39(16), pp.361-363. doi:10.1007/BF00646957
- Lechner, P., Eckbauer, S., Hartmann, R., Krisch, S., Hauff, D., Richter, R., Soltau, H., Strüder, L., Fiorini, C., Gatti, E. and Longoni, A., 1996. Silicon drift detectors for high

References

- resolution room temperature X-ray spectroscopy. *Nuclear Instruments and Methods in Physics Research Section A: Accelerators, Spectrometers, Detectors and Associated Equipment*, 377(2), pp.346-351.
- Luggar, R.D., Horrocks, J.A., Speller, R.D. and Lacey, R.J., 1997. Low angle X-ray scatter for explosives detection: a geometry optimization. *Applied radiation and isotopes*, 48(2), pp.215-224.
- Malin, M.C. and Edgett, K.S., 2000. Evidence for recent groundwater seepage and surface runoff on Mars. *Science*, 288(5475), pp.2330-2335.
- Malin, M.C., Bell, J.F., Cantor, B.A., Caplinger, M.A., Calvin, W.M., Clancy, R.T., Edgett, K.S., Edwards, L., Haberle, R.M., James, P.B., Lee, S.W., Ravine, M.A., Thomas, P.C. and Wolff, M.J., 2007. Context camera investigation on board the Mars Reconnaissance Orbiter. *Journal of Geophysical Research: Planets*, 112(E5).
- Marinangeli, L., Hutchinson, I., Baliva, A., Stevoli, A., Ambrosi, R., Critani, F., Delhez, R., Scandelli, L., Holland, A., Nelms, N. and the Mars-XRD Team, 2007. An European XRD/XRF Instrument for the ExoMars Mission. In Lunar and Planetary Science Conference (Vol. 38, p. 1322).
- Marinangeli, L., Hutchinson, I.B., Stevoli, A., Adami, G., Ambrosi, R., Amils, R., Assis Fernandes, V., Baliva, A., Basilevsky, A.T., Benedix, G., Bland, P., Böttger, A.J., Bridges, J., Caprarelli, G., Cressy, G., Critani, F., d'Alessandro, N., Delhez, R., Domeneghetti, C., Fernandez-Remolar, D., Filippone, R., Fioretti, A.M., Garcia Ruiz, J.M., Gilmore, M., Hansford, G.M., Iezzi, G., Ingley, R., Ivanov, M., Marseguerra, G., Moroz, L., Pellicciari, C., Petrinca, P., Piluso, E., Pompilio, L., Sykes, J., Westall, F. and the Mars-XRD team, 2011. The mineralogy and chemistry analyser (Mars-XRD) for the ExoMars 2018 mission. Proceedings of the EPSC-DPS Joint Meeting, 2-7 October, Nantes, France.
- Marzo, G.A., Davila, A.F., Tornabene, L.L., Dohm, J.M., Fairén, A.G., Gross, C., Kneissl, T., Bishop, J.L., Roush, T.L. and McKay, C.P., 2010. Evidence for Hesperian impact-induced hydrothermalism on Mars. *Icarus*, 208(2), pp.667-683.

References

McEwen, A.S., Eliason, E.M., Bergstrom, J.W., Bridges, N.T., Hansen, C.J., Delamere, W.A., Grant, J.A., Gulick, V.C., Herkenhoff, K.E., Keszthelyi, L., Kirk, R.L., Mellon, M.T., Squyres, S.W., Thomas, N. and Weitz, C.M., 2007. Mars reconnaissance orbiter's high resolution imaging science experiment (HiRISE). *Journal of Geophysical Research: Planets*, 112(E5).

McGuire, P.C., Bishop, J.L., Brown, A.J., Fraeman, A.A., Marzo, G.A., Morgan, M.F., Murchie, S.L., Mustard, J.F., Parente, M., Pelkey, S.M., Roush, T.L., Seelos, F.P., Smith, M.D., Wendt, L. and Wolff, M.J., 2009. An improvement to the volcano-scan algorithm for atmospheric correction of CRISM and OMEGA spectral data. *Planetary and Space Science*, 57(7), pp.809-815.

McLennan, S.M., Anderson, R.B., Bell, J.F., Bridges, J.C., Calef, F., Campbell, J.L., Clark, B.C., Clegg, S., Conrad, P., Cousin, A. and Des Marais, D.J., Dromart, G., Dyar, M.D., Edgar, L.A., Ehlmann, B.L., Fabre, C., Forni, O., Gasnault, O., Gellert, R., Grant, J.A., Grotzinger, J.P., Gupta, S., Herkenhoff, K.E., Hurowitz, J.A., King, P.L., Le Mouélic, S., Leshin, L.A., Lèveillé, R., Lewis, K.W., Mangold, N., Maurice, S., Ming, D.W., Morris, R.V., Nachon, M., Mewsom, H.E., Ollila, A.M., Perret, G.M., Rice, M.S., Schmidt, M.E., Schwenzer, S.P., Stack, K., Stöpler, E.M., Sumner, D.Y., Treiman, A.H., VanBommel, S., Vaniman, D.T., Vasavada, A., Wiens, R.C., Wingst, R.A. and MSL Science Team, 2014. Elemental geochemistry of sedimentary rocks at Yellowknife Bay, Gale crater, Mars. *Science*, 343(6169), p.1244734.

Melosh, H. J., 1989. *Impact Cratering: A Geologic Process*, Oxford Univ. Press, New York.

Menchetti, S. and Sabelli, C., 1976. Crystal chemistry of the alunite series: crystal structure refinement of alunite and synthetic jarosite. *Neues Jahrbuch für Mineralogie, Monatshefte*, pp.406-417.

Mendoza Cuevas, A., Bernardini, F., Gianoncelli, A. and Tuniz, C., 2015. Energy dispersive X-ray diffraction and fluorescence portable system for cultural heritage applications. *X-Ray Spectrometry*, 44(3), pp.105-115.

References

Merlini, M. and Hanfland, M., 2013. Single-crystal diffraction at megabar conditions by synchrotron radiation. *High Pressure Research*, 33(3), pp.511-522.

Meteoritical Bulletin Database, 2016. Available at:

<http://www.lpi.usra.edu/meteor/index.php>

(Accessed 10th August 2016).

Milliken, R.E., Grotzinger, J.P. and Thomson, B.J., 2010. Paleoclimate of Mars as captured by the stratigraphic record in Gale Crater, *Geophys. Res. Lett.*, 37, L04201, doi:10.1029/2009GL041870.

Ming, D.W., Mittlefehldt, D.W., Morris, R.V., Golden, D.C., Gellert, R., Yen, A., Clark, B.C., Squyres, S.W., Farrand, W.H., Ruff, S.W., Arvidson, R.E., Klingelhöfer, G., McSween, H.Y., Rodionov, D.S., Schöder, C., de Souza Jr, P.A. and Wang, A., 2006. Geochemical and mineralogical indicators for aqueous processes in the Columbia Hills of Gusev crater, Mars. *Journal of Geophysical Research: Planets*, 111(E2).

Moore, D.M. and Reynolds, R.C., 1997. *X-ray Diffraction and the Identification and Analysis of Clay Minerals (second edition)*. Oxford: Oxford university press.

Morris, R.V., Ruff, S.W., Gellert, R., Ming, D.W., Arvidson, R.E., Clark, B.C., Golden, D.C., Siebach, K., Klingelhöfer, G., Schröder, C., Fleischer, I., Yen, A.S. and Squyres, S.W., 2010. Identification of carbonate-rich outcrops on Mars by the Spirit rover. *Science*, 329(5990), pp.421-424.

Murchie, S.L., Arvidson, R., Bedini, P., Beisser, K., Bibring, J. P., Bishop, J., Boldt, J., Cavender, P., Choo, T., Clancy, R. T., Darlington, E. H., Des Marais, D., Espiritu, R., Fort, D., Green, R., Guinness, E., Hayes, J., Hash, C., Heffernan, K., Hemmler, J., Heyler, G., Humm, D., Hutcheson, J., Izenberg, N., Lee, R., Lees, J., Lohr, D., Malaret, E., Martin, T., McGovern, J.A., McGuire, P., Morris, R., Mustard, J., Pelkey, S., Rhodes, E., Robinson, M., Roush, T., Schaefer, E., Seagrave, G., Seelos, F., Silverglate, P., Slavney, S., Smith, M., Shyong, W.J., Strohbahn, K., Taylor, H., Thompson, P., Tossman, B., Wirzburger, M. and Wolff, M., 2007. Compact Reconnaissance Imaging

Spectrometer for Mars (CRISM) on Mars Reconnaissance Orbiter (MRO). *J. Geophys. Res.*, *112*, E05S03, doi:10.1029/2006JE002682.

Murchie, S.L., Mustard, J.F., Ehlmann, B.L., Milliken, R.E., Bishop, J.L., McKeown, N.K., Noe Dobrea, E.Z., Seelos, F.P., Buczkowski, D.L., Wiseman, S.M., Arvidson, R.E., Wray, J.J., Swayze, G., Clark, R.N., Des Marais, D.J., McEwen, A.S. and Bibring, J.-P., 2009a. A synthesis of Martian aqueous mineralogy after 1 Mars year of observations from the Mars Reconnaissance Orbiter, *J. Geophys. Res.*, *114*, E00D06, doi:10.1029/2009JE003342.

Murchie, S.L., Seelos, F.P., Hash, C.D., Humm, D.C., Malaret, E., McGovern, J.A., Choo, T.H., Seelos, K.D., Buczkowski, D.L., Morgan, M.F., Barnouin-Jha, O.S., Nair, H., Taylor, H.W., Patterson, G.W., Harvel, C.A., Mustard, J.F., Arvidson, R.E., McGuire, P., Smith, M.D., Wolff, M.J., Titus, T.N., Bibring, J.-P. and Poulet, F., 2009b. Compact Reconnaissance Imaging Spectrometer for Mars investigation and data set from the Mars Reconnaissance Orbiter's primary science phase, *J. Geophys. Res.*, *114*, E00D07, doi:10.1029/2009JE003344.

Murchie, S., Guinness, E. and Slavney, S., 2012. Mars Reconnaissance Orbiter, CRISM Data Product Software Interface Specification, Version 1.3.7.1. NASA PDS. Available at: http://pds-geosciences.wustl.edu/mro/mro-m-crisp-2-edr-v1/mrocr_0001/document/crisp_dpsis.pdf (Accessed 16th June 2016).

Mustard, J.F., Poulet, F., Gendrin, A., Bibring, J.P., Langevin, Y., Gondet, B., Mangold, N., Bellucci, G. and Altieri, F., 2005. Olivine and pyroxene diversity in the crust of Mars. *Science*, *307*(5715), pp.1594-1597.

Mustard, J.F., Murchie, S.L., Pelkey, S.M., Ehlmann, B.L., Milliken, R.E., Grant, J.A., Bibring, J.P., Poulet, F., Bishop, J., Dobrea, E.N., Roach, L., Seelos, F., Arvidson, R.E., Wiseman, S., Green, R., Hash, C., Humm, D., Malaret, E., McGovern, J.A., Seelos, K., Clancy, T., Clark, R., Marais, D.D., Izenberg, N., Knudson, A., Langevin, Y., Martin, T., McGuire, P., Morris, R., Robinson, M., Roush, T., Smith, M., Swayze, G., Taylor, H., Titus, T. and Wolff, M., 2008. Hydrated silicate minerals on Mars observed by the CRISM instrument on MRO, *Nature*, *454*, pp.305-309, doi:10.1038/nature07097.

References

Mutch, T.A., Arvidson, R.E., Binder, A.B., Guinness, E.A. and Morris, E.C., 1977. The geology of the Viking Lander 2 site. *Journal of Geophysical Research*, 82(28), pp.4452-4467.

NASA, 2007. Mars Global Surveyor (MGS) Spacecraft Loss of Contact. Available at: http://www.nasa.gov/pdf/174244main_mgs_white_paper_20070413.pdf (Accessed 22nd August 2016).

NASA, 2012. CRISM Spectral Library. Available at: http://pds-geosciences.wustl.edu/missions/mro/spectral_library.htm (Accessed 15th August 2016).

NASA, 2016. Mars Fact Sheet. Available at: <http://nssdc.gsfc.nasa.gov/planetary/factsheet/marsfact.html> (Accessed 24th August 2016).

NASA JPL, 2016. 2020 Landing Site for Mars Rover Mission. Available at: <http://marsnext.jpl.nasa.gov/index.cfm> (Accessed 15th August 2016).

NASA MEPAG, 2016. High-level summary of Mars Science Goals, Objectives, Investigations, and Priorities: 2015 Active Version. Available at: http://mepag.nasa.gov/reports/CombinedGoals_June18_FINAL.xlsx (Accessed 15th August 2016).

Natl. Bur. Stand., 1981. Silicon Oxide (quartz, low). National Bureau of Standards (U.S.), Monograph 25-18, p61.

Nesse, W., 2011. *Introduction to Mineralogy* (second edition). Oxford University Press, USA.

Norrish, K. and Taylor, R., 1962. Quantitative analysis by X-ray diffraction. *Clay Miner. Bull*, 5(28), pp.98-109.

- Nyquist, L.E., Bogard, D.D., Shih, C.Y., Greshake, A., Stöffler, D. and Eugster, O., 2001. Ages and Geologic Histories of Martian Meteorites, *Space Science Reviews*, 96, pp.105-164.
- O'Dwyer, J.N., and Tickner, J.R., 2008. Quantitative mineral phase analysis of dry powders using energy-dispersive X-ray diffraction. *Applied Radiation and Isotopes*, 66, pp.1359-1362. doi:10.1016/j.apradiso.2008.03.014.
- Ojha, L., Wilhelm, M.B., Murchie, S.L., McEwen, A.S., Wray, J.J., Hanley, J., Massé, M. and Chojnacki, M., 2015. Spectral evidence for hydrated salts in recurring slope lineae on Mars. *Nature Geoscience*, 8(11), pp.829-832.
- Osinski, G.R., Tornabene, L.L., Banerjee, N.R., Cockell, C.S., Flemming, R., Izawa, M.R., McCutcheon, J., Parnell, J., Preston, L.J., Pickersgill, A.E., Pontefract, A., Sapers, H.M. and Southam, G., 2013. Impact-generated hydrothermal systems on Earth and Mars. *Icarus*, 224(2), pp.347-363.
- Pelkey, S.M., Mustard, J.F., Murchie, S., Clancy, R.T., Wolff, M., Smith, M., Milliken, R., Bibring, J.P., Gendrin, A., Poulet, F., Langevin, Y. and Gondet, B., 2007. CRISM multispectral summary products: Parameterizing mineral diversity on Mars from reflectance. *Journal of Geophysical Research: Planets*, 112(E8).
- Perdikatsis, B. and Burzlaff, H., 1981. Strukturverfeinerung am Talk $Mg_3[(OH)_2Si_4O_{10}]$. *Zeitschrift für Kristallographie-Crystalline Materials*, 156(1-4), pp.177-186.
- Perdikatsis, V., 2000. A New Method for Estimation and Correction of the Degree of Preferred Orientation of Calcite and Dolomite in Limestone and Marbles. *In Materials Science Forum* (Vol. 321, pp. 128-132). Trans Tech Publications.
- Phillips, M.W. and Colville, A.A., Ribbe, P.H. (1971): The crystal structures of two oligoclases: A comparison with low and high albite. *ZK*, 133, pp.43-65.

- Pieters, C. M., 1983. Strength of mineral absorption features in the transmitted component of near-infrared reflected light: First results from RELAB. *J. Geophys. Res.*, 88, B11, 9534-9544.
- Pilati, T., Demartin, F. and Gramaccioli, C.M., 1998. Lattice-dynamical estimation of atomic displacement parameters in carbonates: calcite and aragonite CaCO_3 , dolomite $\text{CaMg}(\text{CO}_3)_2$ and magnesite MgCO_3 . *Acta Crystallographica Section B: Structural Science*, 54(5), pp.515-523.
- Poulet, F., Bibring, J.P., Mustard, J.F., Gendrin, A., Mangold, N., Langevin, Y., Arvidson, R.E., Gondet, B. and Gomez, C., 2005. Phyllosilicates on Mars and implications for early Martian climate. *Nature*, 438(7068), pp.623-627.
- Poulet, F., Gomez, C., Bibring, J.P., Langevin, Y., Gondet, B., Pinet, P., Belluci, G. and Mustard, J., 2007. Martian surface mineralogy from Observatoire pour la Minéralogie, l'Eau, les Glaces et l'Activité on board the Mars Express spacecraft (OMEGA/MEx): Global mineral maps. *Journal of Geophysical Research: Planets*, 112(E8).
- Rathbun, J.A. and Squyres, S.W., 2002. Hydrothermal systems associated with Martian impact craters. *Icarus*, 157(2), pp.362-372.
- Robbins, S.J. and Hynek, B.M., 2012. A new global database of Mars impact craters ≥ 1 km: 1. Database creation, properties, and parameters. *Journal of Geophysical Research: Planets*, 117(E5).
- Robinson, D. and Bevins, R.E., 1999. Patterns of regional low-grade metamorphism in metabasites, in *Low-Grade Metamorphism*, edited by M. Frey and D. Robinson, pp.143-168, Blackwell Sci., Oxford, U.K.
- Ross, N.L. and Reeder, R.J., 1992. High-pressure structural study of dolomite and ankerite. *American Mineralogist*, 77(3-4), pp.412-421.
- Rothbauer, R., 1971. Untersuchung eines 2M1-muskovits mit neutronenstrahlen. *Neues Jahrbuch für Mineralogie Monatshefte*, 4, pp.143-154.

Rothery, D.A., 1987. Improved discrimination of rock units using Landsat Thematic Mapper imagery of the Oman ophiolite. *Journal of the Geological Society*, 144(4), pp.587-597.

Ruff, S.W. and Christensen, P.R., 2002. Bright and dark regions on Mars: Particle size and mineralogical characteristics based on Thermal Emission Spectrometer data. *Journal of Geophysical Research: Planets*, 107(E12).

Salby, M. L., 1995. Fundamentals of Atmospheric Physics. Vol. 61. Academic press.

Schade, U. and Wasch, R., 1999. Near-infrared reflectance spectra from bulk samples of the two Martian meteorites Zagami and Nakhla. *Meteoritics & Planetary Science*, 34(3), pp.417-424.

Schon, S.C., Head, J.W. and Fassett, C.I., 2009. Unique chronostratigraphic marker in depositional fan stratigraphy on Mars: Evidence for ca. 1.25 Ma gully activity and surficial meltwater origin. *Geology*, 37(3), pp.207-210.

Shu-Cheng, Y., Jiann-Shing, L., Shu-Fang, T. and Chui-Long, L., 1999. Synthesis and structural features of a flux-grown hematite. *Journal-Geological Society of China-Taiwan*, 42(3), pp.349-358.

Schulze, D.G. and Schwertmann, U., 1984. The influence of aluminium on iron oxides: X. Properties of Al-substituted goethites. *Clay Minerals*, 19(4), pp.521-539.

Schwenzer, S.P. and Kring, D.A., 2009. Impact-generated hydrothermal systems capable of forming phyllosilicates on Noachian Mars. *Geology*, 37(12), pp.1091-1094.

Schwenzer, S.P. and Kring, D.A., 2013. Alteration minerals in impact-generated hydrothermal systems—Exploring host rock variability. *Icarus*, 226(1), pp.487-496.

Schwenzer, S.P., Bridges, J.C., Wiens, R.C., Conrad, P.G., Kelley, S.P., Leveille, R., Mangold, N., Martín-Torres, J., McAdam, A., Newsom, H., Zorzano, M.P., Rapin, W., Spray, J., Treiman, A.H., Westall, F., Fairén, A.G., and Meslin, P.-Y., 2016. Fluids

during diagenesis and sulfate vein formation in sediments at Gale crater, Mars.

Meteoritics & Planetary Science, 1-28.

Shih, C. -Y., Nyquist, L. E., Reese, Y. and Wiesmann, H., 1998. The Chronology of the Nakhilite, Lafayette: Rb-Sr and Sm-Nd Isotopic Ages. In *Lunar and Planetary Science Conference* (Vol. 29, p. 1145).

Sitepu, H., 2009. Texture and structural refinement using neutron diffraction data from molybdate (MoO_3) and calcite (CaCO_3) powders and a Ni-rich Ni 50.7 Ti 49.30 alloy. *Powder Diffraction*, 24(04), pp.315-326.

Smith, D.E., Zuber, M.T., Frey, H.V., Garvin, J.B., Head, J.W., Muhleman, D.O., Pettengill, G.H., Phillips, R.J., Solomon, S.C., Zwally, H.J., Banerdt, W.B., Duxbury, T.C., Golombek, M.P., Lemoine, F.G., Neumann, G.A., Rowlands, D.D., Aharonson, O., Ford, P.G., Ivanov, A.B., Johnson, C.L., McGovern, P.J., Abshire, J.B., Afzal, R.S. and Sun, X., 2001. Mars Orbiter Laser Altimeter: Experiment summary after the first year of global mapping on Mars, *J. Geophys. Res.*, 106(E10), pp.23689-23722, doi:10.1029/2000JE001364.

Smith, D. E., Neumann, G. A., Arvidson, R., Guinness, E., Slavney, S., 2003. Mars Global Surveyor Laser Altimeter Mission Experiment Gridded Data Record. MGS-M-MOLA-5-MEGDR-L3- V1.0 ed., NASA Planetary Data System.

Smith, D.R., Holland, A.D., Hutchinson, I., Abbey, A.F., Pool, P., Burt, D., and Morris, D., 2004. Low noise charge injection in the CCD22, *Proc. SPIE5501*, High-Energy Detectors in Astronomy, 189. doi:10.1117/12.551393.

Squyres, S.W., Grotzinger, J.P., Arvidson, R.E., Bell, J.F., Calvin, W., Christensen, P.R., Clark, B.C., Crisp, J.A., Farrand, W.H., Herkenhoff, K.E., Johnson, J.R., Klingelhöfer, G., Knoll, A.H., McLennan, S.M., McSween, H.Y., Morris, R.V., Rice, J.W., Rieder, R. and Soderblom, L.A., 2004. In situ evidence for an ancient aqueous environment at Meridiani Planum, Mars, *Science*, 306, 1709 – 1713, doi:10.1126/science.1104559.

References

Squyres, S.W., Arvidson, R.E., Bollen, D., Bell, J.F., Brueckner, J., Cabrol, N.A., Calvin, W.M., Carr, M.H., Christensen, P.R., Clark, B.C., Crumpler, L., Des Marais, D.J., d'Uston, C., Economou, T., Farmer, J., Farrand, W.H., Folkner, W., Gellert, R., Glotch, T.D., Golombek, M., Gorevan, S., Grant, J.A., Greeley, R., Grotzinger, J., Herkenhoff, K.E., Hviid, S., Johnson, J.R., Klingelhöfer, G., Knoll, A.H., Landis, G., Lemmon, M., Li, R., Madsen, M.B., Malin M.C., McLennan, S.M., McSween, H.Y., Ming, D.W., Moersch, J., Morris, R.V., Parker, T., Rice Jr, J.W., Richter, L., Rieder, R., Schröder, C., Sims, M., Smith, M., Smith, P., Soderblom, L.A., Sullivan, R., Tosca, N.J., Wänke, H., Wdowiak, T., Wolff, M., and Yen, A., 2006. Overview of the Opportunity Mars Exploration Rover Mission to Meridiani Planum: Eagle Crater to Purgatory Ripple. *Journal of Geophysical Research: Planets*, 111(E12).

Squyres, S.W., Arvidson, R.E., Ruff, S., Gellert, R., Morris, R.V., Ming, D.W., Crumpler, L., Farmer, J.D., Des Marais, D.J., Yen, A., McLennan, S.M., Calvin, W., Bell, J.F., Clark, B.C., Wang, A., McCoy, T.J., Schmidt, M.E. and de Souza, P.A., 2008. Detection of silica-rich deposits on Mars, *Science*, 320, 1063-1067, doi:10.1126/science.1155429.

Squyres, S.W., Arvidson, R.E., Bell III, J.F., Calef III, F., Clark, B.C., Cohen, B.A., Crumpler, L.A., de Souza Jr, P.A., Farrand, W.H., Gellert, R., Grant, J., Herkenhoff, K.E., Hurowitz, J.A., Johnson, J.R., Joliff, B.L., Knoll, A.H., Li, R., McLennan, S.M., Mittlefehldt, D.W., Parker, T.J., Paulsen, G., Rice, M.S., Ruff, S.W., Schröder, C., Yean, A.S., and Zacny, K., 2012. Ancient Impact and Aqueous Processes at Endeavour Crater, Mars, *Science*, 336, 570-576, doi:10.1126/science.1220476.

Stuart, B., 2004. Infrared Spectroscopy: Fundamentals and Applications. John Wiley & Sons.

Sun, V.Z. and Milliken, R.E., 2014. The geology and mineralogy of Ritchey crater, Mars: Evidence for post-Noachian clay formation. *Journal of Geophysical Research: Planets*, 119(4), pp.810-836.

References

- Sun, V.Z. and Milliken, R.E., 2015. Ancient and recent clay formation on Mars as revealed from a global survey of hydrous minerals in crater central peaks. *Journal of Geophysical Research: Planets*, 120(12), pp.2293-2332.
- Suzuki, Y., Morgan, P.E. and Niihara, K., 1998. Use of a high X-ray flux instrument for a mineral: X-ray powder diffraction pattern of CaMg (CO₃)₂. *Powder Diffraction*, 13(04), pp.216-221.
- Swanson, H.E. and Fuyat, R.K., 1953. ICDD PDF 05, 0586, Calcite. *Natl. Bur. Stand.(US), Circ, 539*, p.51.
- Swindle, T.D., Treiman, A.H., Lindstrom, D.J., Burkland, M.K., Cohen, B.A., Grier, J.A., Li, B. and Olson, E.K., 2000. Noble gases in iddingsite from the Lafayette meteorite: Evidence for liquid water on Mars in the last few hundred million years. *Meteoritics & Planetary Science*, 35(1), pp.107-115.
- Tanaka, K.L., 1986. The Stratigraphy of Mars. *Proc. 17th Lunar Planet. Sci. Conf., J. Geophys. Res.* **91**, suppl., 139-158.
- Tanaka, K.L., Robbins, S.J., Fortezzo, C.M., Skinner, J.A. and Hare, T.M., 2014. The digital global geologic map of Mars: Chronostratigraphic ages, topographic and crater morphologic characteristics, and updated resurfacing history. *Planetary and Space Science*, 95, pp.11-24.
- Tanner, B. K., 1995. Introduction to the Physics of Electrons in Solids. Cambridge University Press.
- Thomson, B.J., Bridges, N.T., Milliken, R., Baldrige, A., Hook, S.J., Crowley, J.K., Marion, G.M., de Souza Filho, C.R., Brown, A.J. and Weitz, C.M., 2011. Constraints on the origin and evolution of the layered mound in Gale Crater, Mars using Mars Reconnaissance Orbiter data. *Icarus*, 214(2), pp.413-432.

References

- Tornabene, L. L., Osinski, G. R. and McEwen, A. S., 2009. Parautochthonous megabreccias and possible evidence of impact-induced hydrothermal alteration in Holden Crater, Mars. In *Lunar and Planetary Science Conference* (Vol. 40, p. 1766).
- Treiman, A.H., 2005. The nakhlite meteorites: Augite-rich igneous rocks from Mars. *Chemie der Erde-Geochemistry*, 65(3), pp.203-270.
- Tseng, H.Y., Heaney, P.J. and Onstott, T.C., 1995. Characterization of lattice strain induced by neutron irradiation. *Physics and Chemistry of Minerals*, 22(6), pp.399-405.
- Turner, S.M.R., Bridges, J.C., Grebbly, S. and Ehlmann, B.L., 2016. Hydrothermal activity recorded in post Noachian-aged impact craters on Mars. *Journal of Geophysical Research: Planets*, 121(4), pp.608-625.
- USGS, 1991. Mars Global Digital Image Mosaic 1. Available at: <ftp://pdsimage2.wr.usgs.gov/pub/pigpen/mars/viking/> (Accessed 10th August 2016).
- USGS, 2003. MGS MOLA Global Dataset. Available at: <ftp://pdsimage2.wr.usgs.gov/pub/pigpen/mars/mola/> (Accessed 24th August 2016).
- USGS, 2011. Valles Marineris Hemisphere Enhanced. Available at: http://astrogeology.usgs.gov/search/map/Mars/Viking/valles_marineris_enhanced (Accessed 24th August 2016).
- USGS, 2012. Mars Nomenclature. Available at: <ftp://pdsimage2.wr.usgs.gov/pub/pigpen/mars/Nomenclature/> (Accessed 24th August 2016).
- Vaniman, D.T., Bish, D.L., Ming, D.W., Bristow, T.F., Morris, R.V., Blake, D.F., Chipera, S.J., Morrison, S.M., Treiman, A.H., Rampe, E.B., Rice, M., Achilles, C.N., Grotzinger, J.P., McLennan, S.M., Williams, J., Bell III, J.F., Newsom, H.E., Downs, R.T., Maurice, S., Sarrazin, P., Yen, A.S., Morookian, J.M., Farmer, J.D., Stack, K., Milliken, R.E., Ehlmann, B.L., Sumner, D.Y., Berger, G., Crisp, J.A., Hurowitz, J.A., Anderson, R., Des Marais, D.J., Stöpler, E.M., Edgett, K.S., Gupta, S., Spanovich, N.

and MSL Science Team, 2014. Mineralogy of a mudstone at Yellowknife Bay, Gale crater, Mars. *Science*, 343(6169), p.1243480.

Wang, A., Korotev, R.L., Jolliff, B.L., Haskin, L.A., Crumpler, L., Farrand, W.H., Herkenhoff, K.E., de Souza Jr, P., Kusack, A.G., Hurowitz, J.A. and Tosca, N.J., 2006. Evidence for phyllosilicates in Wolly Patch, an altered rock encountered at West Spur, Columbia Hills, by the Spirit rover in Gusev crater, Mars. *Journal of Geophysical Research: Planets*, 111, E02S16, doi:10.1029/2005JE002516.

Wechsler, B.A., Lindsley, D.H. and Prewitt, C.T., 1984. Crystal structure and cation distribution in titanomagnetites ($\text{Fe}_{3-x}\text{TixO}_4$). *American Mineralogist*, 69(7-8), pp.754-770.

Wenk, H.R., Joswig, W., Tagai, T., Korekawa, M. and Smith, B.K., 1980. The average structure of An 62-66 labradorite. *American Mineralogist*, 65(1-2), pp.81-95.

Werner, S.C. and Tanaka, K.L., 2011. Redefinition of the crater-density and absolute-age boundaries for the chronostratigraphic system of Mars. *Icarus*, 215(2), pp.603-607.

Wray, J.J., Noe Dobrea, E.Z., Arvidson, R.E., Wiseman, S.M., Squyres, S.W., McEwen, A.S., Mustard, J.F. and Murchie, S.L., 2009. Phyllosilicates and sulfates at Endeavour Crater, Meridiani Planum, Mars. *Geophysical Research Letters*, 36(21).

Yang, H., Lu, R., Downs, R.T. and Costin, G., 2006. Goethite, $\alpha\text{-FeO}(\text{OH})$, from single-crystal data. *Acta Crystallographica Section E: Structure Reports Online*, 62(12), pp.i250-i252.

Young, R.A. and Hewat, A.W., 1988. Verification of the Triclinic Crystal Structure of Kaolinite. *Clays Clay Miner.*, 36(3), pp.225-232.

Zurek, R.W. and Smrekar, S.E., 2007. An overview of the Mars Reconnaissance Orbiter (MRO) science mission. *Journal of Geophysical Research: Planets (1991–2012)*, 112(E5).